ABSTRACT

Title of dissertation: LIGHT SCATTERING PROPERTIES
OF ASTEROIDS AND COMETARY NUCLEI

Jian-Yang Li, Doctor of Philosophy, 2005

Dissertation directed by: Professor Michael F. A'Hearn
Associate Research Professor Lucy A. McFadden
Department of Astronomy

The photometric properties of asteroids and cometary nuclei, bodies important for understanding the origin of the Solar System, are controlled by the physical properties of their surfaces. Hapke's theory is the most widely used theoretical model to describe the reflectance of particulate surfaces, and has been applied to the disk-resolved photometric analyses of asteroid 433 Eros, comet 19P/Borrelly, and asteroid 1 Ceres, in this dissertation.

Near Earth Asteroid Rendezvous returned disk-resolved images of Eros at seven wavelengths from 450nm to 1050nm. The bidirectional reflectance of Eros's surface was measured from those images with its shape model and geometric data. Its single-scattering albedo, w, was found to mimic its spectrum, with a value of 0.33$\pm$0.03 at 550nm. The asymmetry factor of the single-particle phase function, g, is -0.25$\pm$0.02, and the roughness parameter, $\bar{\theta}$, is 28°$\pm$3°, both of which are independent of wavelength. The V-band geometric albedo of Eros is 0.23, typical for an S-type asteroid.

From the disk-resolved images of Borrelly obtained by Deep Space 1 (DS1), the

maps of its w, g, and $\bar{\theta}$ were constructed by modeling the reflectance of Borrelly terrain by terrain. w varies by a factor of 2.5, with an average of 0.057$\pm$0.009. g changes from -0.1 to -0.7, averaging -0.43$\pm$0.07. $\bar{\theta}$ is $\leq$35° for most of the surface, but up to 55° for some areas, with an average of 22$^\circ\pm$5°. The 1-D temperature measurement from DS1 can be well described by the standard thermal model assuming a dry surface, except for one area, where the discrepancy can be explained by a sublimation rate that is consistent with the observed water production rate.

HST images through three filters, covering more than one rotation of Ceres, were acquired. Its V-band lightcurve agrees with earlier observations very well. A strong absorption band centered at about 280nm is noticed, but cannot be identified. w of Ceres was modeled to be 0.073$\pm$0.002, 0.046$\pm$0.002, and 0.032$\pm$0.003 at 555nm, 330nm, and 220nm, respectively. The maps of w for Ceres at three wavelengths were constructed, with eleven albedo features identified. Ceres' surface was found to be very uniform.

LIGHT SCATTERING PROPERTIES OF ASTEROIDS AND COMETARY NUCLEI

by

Jian-Yang Li

Dissertation submitted to the Faculty of the Graduate School of the
University of Maryland, College Park in partial fulfillment
of the requirements for the degree of
Doctor of Philosophy
2005

Advisory Commmittee:

Professor Michael F. A'Hearn, Chair
Associate Research Professor Lucy A. McFadden
Professor J. Patrick Harrington
Professor Bruce Hapke
Professor Roald Z. Sagdeev
Doctor Anne J. Verbiscer

献给我的爸爸妈妈

ACKNOWLEDGMENTS

I own my gratitude to all people who made this thesis possible, and made my experience in graduate school wonderful.

First and the foremost, I would like to thank my two advisors, Mike A'Hearn and Lucy McFadden, for changing my view of the planetary system to a fantastic world that I enjoy staying in, looking at, and exploring for the rest of my life. Starting my graduate research work with some sort of language barrier as a foreign student, I was impressed by Mike's prompt responses to my questions that sometimes even myself had trouble in understanding from what I said. I gained great confidence from the conversations with Mike at the beginning, and received invaluable scientific advises from Mike continuously since then. As a mentor, Mike guided me by not only his scientific advises, but also his confidence, infinite enthusiasm, and a great sense of humor. And thank you Mike for introducing me into and letting me work for the exciting Deep Impact project!

Lucy, as one of the most important collaborators of Mike's, has been a great advisor not only in my research, but also in my scientific personality and even everyday life. With her help, I never afraid of talking to anybody or presenting my work anywhere. She introduced me to so many people who have helped or will help me greatly in my career. I have been deeply impressed by her enthusiasm to astronomy, skills of communication, and team work. I am grateful to Lucy for her help in the way that is probably more important for me than my research. So thank you Lucy for sitting with me before my first

presentation in the first DPS meeting I attended!

I would like to thank Doug Hamilton for allowing me to work on a dynamics project in the summer of 2000, which was my first project in astronomy, allowing me to taste, for the first time, the exciting feeling of being in the field that has attracted me since my childhood. The plot of the stable time scale of test particles in the giant planet region is still on the wall in my office. Thanks Doug!

I own many thanks to Pat Harrington, with whom I finished my second-year project on measuring the expansion of a planetary nebula. It was the fantastic HST images of the beautiful planetary nebula that allowed me finally realize that I did like astronomy, although I did not know if it was the "planetary" here that led me into the field of planetary sciences finally. I did not realize that I was going to use IDL to develop all software tools for my thesis work when Pat taught me some basic commands of IDL for the first time. Thank you Pat for the opportunity of working with you, and for your name in my first publication!

Thanks also go to Casey Lisse, who helped me greatly with his quick mind and patience when I just started my thesis work. Thank Dennis Wellnitz for his clear explanations to any questions I asked. I really enjoyed talking with him. Thank Bruce Hapke for his invaluable advises and comments since I started to learn the theories of light scattering and apply it to my work. Thank Anne Verbiscer for reading my thesis with great detail, and for checking all the references. And thank everybody who has helped me in my research.

In addition to all the important people in my career in astronomy, I am grateful to all the people who have helped me from other aspects. Thanks to the support from the

department, especially John Trasco, Mary Ann Phillips, Linda Diamond, for shielding us with a peaceful and easy environment. Thanks to all my friends who signed either or both of the two graduation gifts I received. Thanks to my best friends, Jianglai, Yuanzhen, Qing, for painting my life with colors, and for giving me confidence.

I owe a deep debt of thanks to my fiancée, Huaning, who witnesses the whole process of my thesis work, and every detail of the birth of this thesis. I would not have finished this thesis, and decided to devote my life to astronomy without her continuous support, understanding, encouragement, and forgiveness. I would not have been enjoying such a wonderful life that I am now without her. Thank you Huaning for the unique graduation gift you gave me, which was the best gift I ever received. And thank you for being with me anytime. I love you!

Finally, thank the world for having so many mysteries and so much fun; thank modern technology for enabling us to go to the Moon, Mars, Jupiter, Saturn, and beyond.

This thesis is dedicated to my parents!

TABLE OF CONTENTS

LIST OF TABLES

LIST OF FIGURES

Chapter 1

Introduction

1.1 History of Solar System Small Bodies

In addition to the Sun, the nine planets, and their moons in our solar system, there are many small bodies, such as asteroids, comets, and meteors, too small and too faint to be discovered and tracked easily. It is believed that these small bodies are the leftovers of the original building blocks that formed the nine planets and other large bodies in the early solar system. A huge amount of energy was released during the accretion of large bodies, speeding up the chemical reactions to change their compositions, produce differentiations to have segregation at different places within their bodies, and change the original physical states, *e.g.*, the crystalline or amorphous. Therefore large bodies were modified dramatically from the original planetesimals. However, small bodies did not release much energy from accretion, nor were they able to trap much energy, *e.g.* from radioactive decay, in their interiors, to change their properties physically or chemically. Therefore they are better tracers of the original environment and processes in the proto-planetary disk.

Asteroids are small interplanetary rocky bodies that formed and concentrated mainly in the reservoir between Jupiter and Mars (*e.g.*, McFadden, 1993). Many of them are in dynamical groups, or asteroid families, identified by their orbital proper elements, spreading from Earth-crossing asteroids to the Trojans (for current asteroid family identification,

see Bendjoya and Zappalà, 2002; Zappalà et al., 2002, and references therein). While not as visually spectacular as comets because they have no surface activity, it is relatively much easier to measure their physical parameters such as size, rotational state, albedo, *etc*. Therefore, many more studies have been carried out about the surface properties and the evolution of asteroids than of comets. The term comet usually refers to small bodies containing a large fraction of frozen volatile materials (Weissman et al., 2002), mainly water but with moderate amounts of methanol and carbon dioxide. They orbit the Sun on very eccentric orbits, and develop an unstable atmosphere when very close to the Sun, forming comae and long tails composed of volatile gases and a large amount of dust. Because of their sudden appearance and short but spectacular stay in the inner solar system, comets were a long-time mystery, until several decades ago people started to know more about their nature.

Although visually very different, asteroids and comets are considered to have formed through very similar processes during the formation of the Solar System. Because of the differentiation of materials within the planet formation disk, different materials are concentrated at different heliocentric distances. Heavy materials, usually with higher melting temperatures such as silicate-bearing minerals, have relatively higher fraction inside, and light materials, such as carbonaceous and volatile materials mainly concentrate outside, with their compositions changing gradually. The so-called planetesimals and cometesimals, mainly distinguished by their compositions, formed by collisional sticking from tiny particles that condensed from the gaseous disk in solar nebular. And due to their different compositions, different physical environments and perturbations from large proto-planets, the leftover planetesimals and cometesimals evolved following different paths thereafter

to form asteroids and comets.

Proto-asteroids mainly formed within Jupiter's orbit. Within the ice line of about 3 AU from the Sun, where water or water ice is unstable to evaporation, asteroids either contain little or have lost much of their volatile materials, and do not have a comet-like atmosphere or outgassing. The origin of asteroids was summarized by Bell et al. (1989, and references therein). The initial formation of asteroids, prior to the importance of collisional evolution, was probably very similar to that of comets, although their compositional materials were very different. The planetesimals in the central plane of the solar nebula, mainly at smaller heliocentric distances than the formation region of comets, and between Mars and Jupiter, formed asteroids through gravitational and collisional accretion. Because of the rapid formation of Jupiter, the formation of a single large body at the position of the current asteroid belt was curtailed due to the strong gravitational purterbations from the massive proto-Jupiter. We see many small bodies at this region rather than one large planet. Intense metamorphic heating due to gravitational accretion and radioactive decay (*e.g.,* Urey, 1955; Grimm and McSween, 1993; MacPherson et al., 1995; Huss et al., 2001, *etc.)* then produced differentiation in large asteroids of a few hundred kilometers in radius, which might then break up into many small asteroids during their complicated collisional evolution (*e.g.* Keil, 2002, and references therein). The gravitational heating mainly depends on their sizes. The radioactive heating depends on heliocentric distance in the sense that radioactive elements are more diluted by the presence of water and organics at larger heliocentric distances so the energy density is less. At the same time and thereafter, complex collisional evolution, controlled by the orbital dynamics, internal strength gradients, and the distribution of metal, as well as the

(sometimes chaotic) dynamical evolution, led to their current state.

Because they were mainly inside Jupiter's orbit, asteroids were not scattered away from their formation regions very strongly by Jupiter, and thus remained in relatively circular orbits compared to comets, except at some resonant positions where substantial mass loss occurred due to strong secular gravitational perturbations from Jupiter. Because asteroids have remained within a relatively small region since they formed, dynamical and collisional evolution keep playing a relatively important role among asteroids. Asteroidal dynamical families are considered to be fragments from collisional destruction of precursor bodies (see, *e.g.*, Richardson et al., 2002; Davis et al., 2002, for reviews). Their number, size distribution, and shapes are determined by collisional and dynamical evolution. According to the differences and similarities of their spectra, asteroidal taxonomic classes are defined (Gaffey and McCord, 1978; Tholen, 1984; Tholen and Barucci, 1989), believed to indicate the internal correlation within each family, and the different compositions and surface physical properties, therefore different formation environments and processes between families. The phase functions, defined as the brightness variation of an object with respect to phase angle, *i.e.*, the angle between the Sun and the observer as seen from the object, of many asteroids have been obtained from ground-based observations, although the range of phase angle was limited by geometry (see, *e.g.*, Bowell et al., 1989; Helfenstein and Veverka, 1989, and references therein). The phase functions of many asteroids can be modeled fairly well with both Hapke's model and Lumme and Bowell's model. Phase functions also show similarities within each dynamical group. The opposition effect is more prominent among bright asteroids like 44 Nysa (E), 133 Cyrene (SR), and 1862 Apollo (Q). While dark asteroids like 24 Themis (C), 419 Aurelia (F), and

253 Mathilde (C) usually do not show an obvious opposition surge, they have relatively steep phase functions, and less surface albedo variation (Clark et al., 1999). The spatial distribution of taxonomic classes shows that darker, redder, and more primitive objects such as C- and D-type asteroids, become more frequent at larger heliocentric distances, while brighter asteroids such as S-, E-, and M-types are found more frequently among the planet-crossing population at smaller heliocentric distances (*e.g.* Zellner and Bowell, 1977; Tholen, 1984; Tholen and Barucci, 1989, *etc)*. As shown in Table 1 of Bell et al. (1989), different asteroidal types represent various compositions and degrees of total metamorphic heating. Thus the spatial distribution of asteroidal taxonomic types implies the spatial distribution of physical environments and accretion processes in the early solar system.

Oort (1950) initiated important steps in the study of the origin of comets. He suggested a spherical cloud with a radius between radii 50,000 and 150,000 AU around the solar system, whence all "new" long-period comets come. A year later, Kuiper (1951) proposed a disk-like belt outside the orbit of Neptune, the so-called Kuiper Belt, which serves as the reservoir of short-period comets (Fernández, 1980). At the same time, Whipple (1950) argued that, rather than a cloud of interstellar dust (Lyttleton, 1948), every comet has a solidified core called the nucleus. He proposed his famous "dirty snowball" model for cometary nuclei, which was later augmented by the "rubble pile" model of Weissman (1986) and Weidenschilling (1994). Other models include the "fractal model" by Donn (1990) and the "icy-glue model" by Gombosi and Houpis (1986). However, the latter two have not been as widely accepted as the first two.

The origin of comets has been studied intensively from both observations and nu-

merical simulations since then, and summarized by Weidenschilling (1994, 1997). Comets are thought to form from the condensation and collisional coagulation of cometesimals in the central plane of the solar nebula outside proto-Jupiter, and the ice line, throughout the region of the giant planets to the radius of Kuiper Belt. At about kilometer size, gravitational accretion was responsible for the growth of bodies. The effect of this scenario on the structure of cometary nuclei is that nuclei would be composed of structural elements having a variety of scales with sizes ranging from about 10 to 100 m, and bodies would have low mechanical strength and macroscopic voids, both of which are consistent with the existence of active areas and the fragility of nuclei. The long-period and parabolic comets from the Oort Cloud also originated at small heliocentric distances inside proto-Neptune in the solar nebula, and then were scattered outward to very eccentric and distant orbits by the perturbations of giant planets (Safronov, 1969; Fernández and Ip, 1981). Due to the perturbations of passing stars and giant molecular clouds, comets scattered into the outer region were stirred from a flattened disk into a spherical cloud (Chakrabarti, 1992), to form the so-called Oort Cloud. When they are perturbed by the galactic tidal forces and/or passing stars or other massive stellar systems, and re-enter the inner solar system, they are discovered as “new” comets. Comets originally formed outside proto-Neptune’s orbit probably stay where they formed because there are not big perturbers out there. These might be the progenitors of today’s short period comets and Kuiper Belt Objects (KBO’s). Since comets spend most of their life in the outer solar system, and because they are very small, the properties of their nuclei remain almost pristine, except for the outermost layers of nuclei that probably have been heated during infrequent passages through small perihelion distances. The above scenario of the formation and

evolution of comets was supported by both numerical simulations of the dynamical evolution of a large number of test cometesimals in the giant planet cross region (Levison et al., 2001; Królikowska, 2001; Fernández and Gallardo, 1994; Chakrabarti, 1992; Duncan et al., 1988), and the observations that confirmed the existence of the Kuiper Belt (Jewitt and Luu, 1995). More detailed physical properties of comets, especially their nuclei, still need to be understood to evaluate these ideas.

However, because cometary nuclei are usually hidden in thick comae at small heliocentric distance where we can most readily observe, only a few cometary nuclei have been studied from ground-based or earth-orbiting telescopic observations in either optical or the IR (see, *e.g.*, Jewitt and Meech (1985); Brooke and Knacke (1986); Veeder et al. (1987); Birkett et al. (1987); Millis et al. (1988) for 49P/Arend-Rigaux, Jewitt and Meech (1985); Meech et al. (1986) for 1P/Halley, Jewitt and Meech (1987); Fernández et al. (2000) for 2P/Encke, Campins et al. (1987); Birkett et al. (1987); Jewitt and Meech (1988); Delahodde et al. (2001) for 28P/Neujmin 1, Jewitt and Meech (1988); A'Hearn et al. (1989) for 10P/Tempel 2, Lamy et al. (1998) for 19P/Borrelly, Lamy et al. (2001) for 9P/Tempel 1, and Lisse et al. (1999) for C/Hyakutake). None of these observations was able to resolve the nucleus (nuclear radius about 10 km, telescope resolution about 50 km), and these studies relied on models of coma to extract the nuclear brightness. So they are limited in accuracy and in providing us detailed information about the nuclear surface scattering properties. The only three *in situ* observations were performed for comet 1P/Halley by ESA's Giotto spacecraft (Reinhard, 1986; Keller et al., 1986) and the Soviet Union's Vega 1 and 2 spacecraft (Sagdeev et al., 1986a,b) during its 1986 apparition, for comet 19P/Borrelly by NASA's Deep Space 1 (DS1) spacecraft (Soderblom et al., 2004a)

in 2001, and for comet 81P/Wild 2 by NASA's Stardust spacecraft (Brownlee et al., 2003). These *in situ* observations were able to tell us much more concerning cometary nuclei than the sum of all ground-based observations, yielding detailed spectra, shape, surface features, active areas, and direct measurements of the chemical composition of the inner coma, and the nucleus itself.

Dynamical and physical properties of asteroids and comets show a strong correlation between these two kinds of small bodies in many aspects. Both of them have small sizes, irregular shapes, and low albedos (for C- and D-type asteroids). Sometimes it is hard to give unambiguous definitions to them (Hartmann et al., 1987; McFadden, 1993; Weissman et al., 2002), or to distinguish a dormant or an extinct comet from an asteroid. It was suggested that some asteroids might be the end state of comets, especially some near Earth asteroids (NEAs) (Wetherill, 1988; Coradini et al., 1997a,b). The transition between comets and asteroids has been discussed for some objects (see, *e.g.*, Silva and Cellone, 2001; Bus et al., 2001; Chamberlin et al., 1996; Fernández et al., 1997, 2001; McFadden et al., 1993, *etc.)*, with the direct evidence of cometary activity observed for some of them, such as (2060) Chiron, (4015) Wilson-Harrington (107P/Wilson-Harrington), and (7968) Elst-Pizarro (133P/Elst-Pizarro). A good review of the transition from comets to asteroids was given by Weissman et al. (2002). It was also suggested that comets and C- or D-type asteroids might have a common origin (Ziolkowski, 1995), or at least might have formed in similar conditions (Hartmann et al., 1987) and have undergone similar physical evolution (Weidenschilling, 1997; Weissman et al., 2002).

1.2 Motivation

Because of the close relationship between the properties of small bodies and the origin of the Solar System, it is important to understand asteroids and comets. What are they like, why are they so, and how did they form?

1.2.1 Asteroidal photometry

Since von Seeliger (1887) and Müller (1893) started to study the photometry of the Saturnian system, asteroidal photometry has become an important method to study the physical properties of asteroids. With the distance of an asteroid usually determined from astrometric measurements and calculations of its orbit, the brightness usually tells us the combined information about its size and reflectance. If the brightnesses in both the infrared and visible for an asteroid are obtained, then the standard thermal model (STM) (Brown, 1985; Lebofsky et al., 1986) will yield the size and albedo. The brightness change with respect to time, or lightcurve, is usually interpreted as the effect of varying apparent illuminated cross-section of a rotating non-spherical body. Some information about the shape of the asteroid can be obtained (See Chapter 3). The phase function contains important information about the physical properties of its surface.

To interpret asteroidal photometric data such as phase functions in general, Hapke (1981, 1984, 1986) and Lumme and Bowell (1981a,b) developed independent models to describe the photometric behaviors of actual regolith, by including effects of microstructure, multiple scattering and large-scale roughness. A good review about the photometry of solar system small bodies done prior to 1989 was given by Bowell et al. (1989).

Hapke's and Lumme and Bowell's models have been applied successfully to analyze disk-integrated and disk-resolved phase functions of many inner planets, moons and asteroids. The applications include the estimates of a variety of regolith optical properties, such as the average particle single-scattering albedo, particle transparency, and structural properties, such as particle size, shape distribution, soil compaction and large-scale roughness (Bowell et al., 1989; Helfenstein and Veverka, 1989), which are impossible to measure directly.

On the other hand, any photometric model can also be used in the opposite direction, that is, to use photometric theories to interpolate and extrapolate available photometric data to the geometries for which observations are not available or not possible, and thence to go further to combine with other data to infer some other physical properties of the body. For example, an accurate thermal model usually requires information about the whole phase function to calculate the Bond albedo (see Chapter 2). But even if only part of the phase function is observed, as long as photometric parameters can be modeled well, there will be no problem to calculate the Bond albedo.

Among those models used to interpret photometric data of asteroids, Hapke's theory is the most widely used approximate theory that correlates the physical properties of an asteroidal surface with its reflectance behavior and phase function, and it has been applied to almost all observed asteroids since it was developed (*e.g.* Helfenstein and Veverka, 1987, 1989; Simonelli et al., 1998; Clark et al., 2002, *etc.)*. It interprets the reflectance of particles as being determined by their size, shape, composition, and purity. The reflectance of a surface is modeled with the reflectance behavior of single particles, as well as the macroscopic roughness of the surface, compaction status, *etc*, all of which

hide important information about the evolutionary history of a surface. Hapke's theory has been summarized in his book (Hapke, 1993) that is often referred to in the planetary photometry communities as "Hapke's bible", although it is still an approximate model, and being continuously improved by new observations and laboratory experiments.

Despite the powerful theoretical tools available, it is sometimes very difficult to interpret a whole-disk phase curve unambiguously because of the irregular shape, unknown rotational state, and the limitation of Earth-based observations to a small range of phase angles (a few to about 20° for main belt asteroids, and smaller for more distant objects). One important property of the phase curves of most asteroids is the opposition effect, which provides porosity of surface texture, and the properties of amorphous or crystalline structure. (For observations of the opposition effect, see *e.g.*, Belskaya and Shevchenko (2000); for theories, see *e.g.*, Hapke (1986); Shkuratov and Helfenstein (2001)). However, the lack of photometric data at small phase angles makes the study of the opposition effect difficult. Another example is that a disk-integrated phase function observed over only a small range of phase can be fitted equally well with very different photometric parameter sets (see Fig. 2.7 and relevant text). Therefore, to constrain the physical parameters of an asteroidal surface better, we need observations from space to obtain a large range of phase angle and/or disk-resolved images. Experimental studies of meteoritic powders also provide important clues to constrain the physical properties of asteroids.

1.2.2 Cometary photometry

For comets, it is usually very hard to measure the brightness of bare nuclei because they are usually very faint when far from the Sun, and hidden in thick comae when close to

the Sun. Cometary nuclei are usually smaller than a hundred kilometers, and the smallest pixel scale at a comet ever reached from the ground when they are close to the Earth is only about 50 km, with only a few observations of IRAS-Araki-Alcock reaching 20 km. Thus the aperture-integrated brightness contains much signal from the coma. Aperture photometry of comets, through various broadband or narrowband filters, measures their activities and compositions within comae, indicating nuclear compositional properties (*e.g.* A'Hearn et al., 1995; Farnham and Cochran, 2002; Schleicher et al., 2003; Farnham and Schleicher, 2005, *etc.)*. Direct photometry of cometary nuclei is obtained only when they are far from the Sun without much coma contamination except for very inactive comets with very little coma (such as Neujmin 1 and Arend-Rigaux, and Encke in its post-perihelion phase). But for those cases comets are usually very faint ($\geq$ 20 mag), and the phase angles reached from the ground are very limited. A method has been developed to separate the signal from the nucleus from that of the coma when they have well developed comae (Lamy and Toth, 1995). In this method, the brightness of coma is modeled by a canonical $f(\theta)/r^n$ profile with respect to the cometocentric distance with an azimuthal angle parameter $f(\theta)$ and a power law index n (could be a function of the azimuthal angle, θ, too). Then it is extrapolated into the optocentric region that contains signal from both coma and nucleus. The signal from the coma in the central region can be estimated from the model, and the residual brightness in the central region is then a point spread function (PSF) formed by a point source, considered to be the nucleus. An example is shown in Fig. 1.1 for comet Hyakutake from Lisse et al. (1999). This method has been applied to several comets successfully (Lamy et al., 1998; Lisse et al., 1999; Lamy et al., 1999, 2001), although in some earlier attempts a simplified version

that did not take into account the azimuthal variation of the $1/r$ profile was used (*e.g.*, for Neujmin 1 and Arend-Rigaux). However, it is obviously model-dependent. If there is any fine structure that deviates from the power law model, the uncertainty in the estimated nuclear brightness will be large.

Due to the difficulty in obtaining the brightness of cometary nuclei, observations over a large range of phase angles have been made for just a few comets, such as comet Encke (Fernández, 1999) and comet Neujmin 1 (Delahodde et al., 2001). In addition, the phase functions of both comets were interpreted by some semi- or entirely empirical phase laws such as a linear law, the IAU-adopted (H, G) system (Bowell et al., 1989), the phase law of Lumme and Bowell (1981a,b), and Shevchenko's law (Belskaya and Shevchenko, 2000) (for Neujmin 1). None of them was interpreted physically, but some comparisons with asteroids were made. The phase-range of Encke was from 2° to about 117°. It was found that Encke's phase behavior was comparable with C-type asteroids. The phase range of Neujmin 1 in Delahodde et al. (2001) was fairly small, 0.6° to 15°, but the similarity of Neujmin 1 to D-type asteroids in terms of color was noticed. Its steep opposition surge might indicate a very porous surface. These studies were very important in understanding the physics occurring on the surface of nuclei, but limited in providing detailed, spatially resolved information about the surface of cometary nuclei, and the physical interpretation. A large scatter in the measurements of disk-averaged results was found.

Again, space missions are able to do a much more advanced job in obtaining the photometry of cometary nuclei as for asteroidal photometry. First of all, spacecraft can go deep inside coma, and observe nuclei directly. Second, disk-resolved images are made

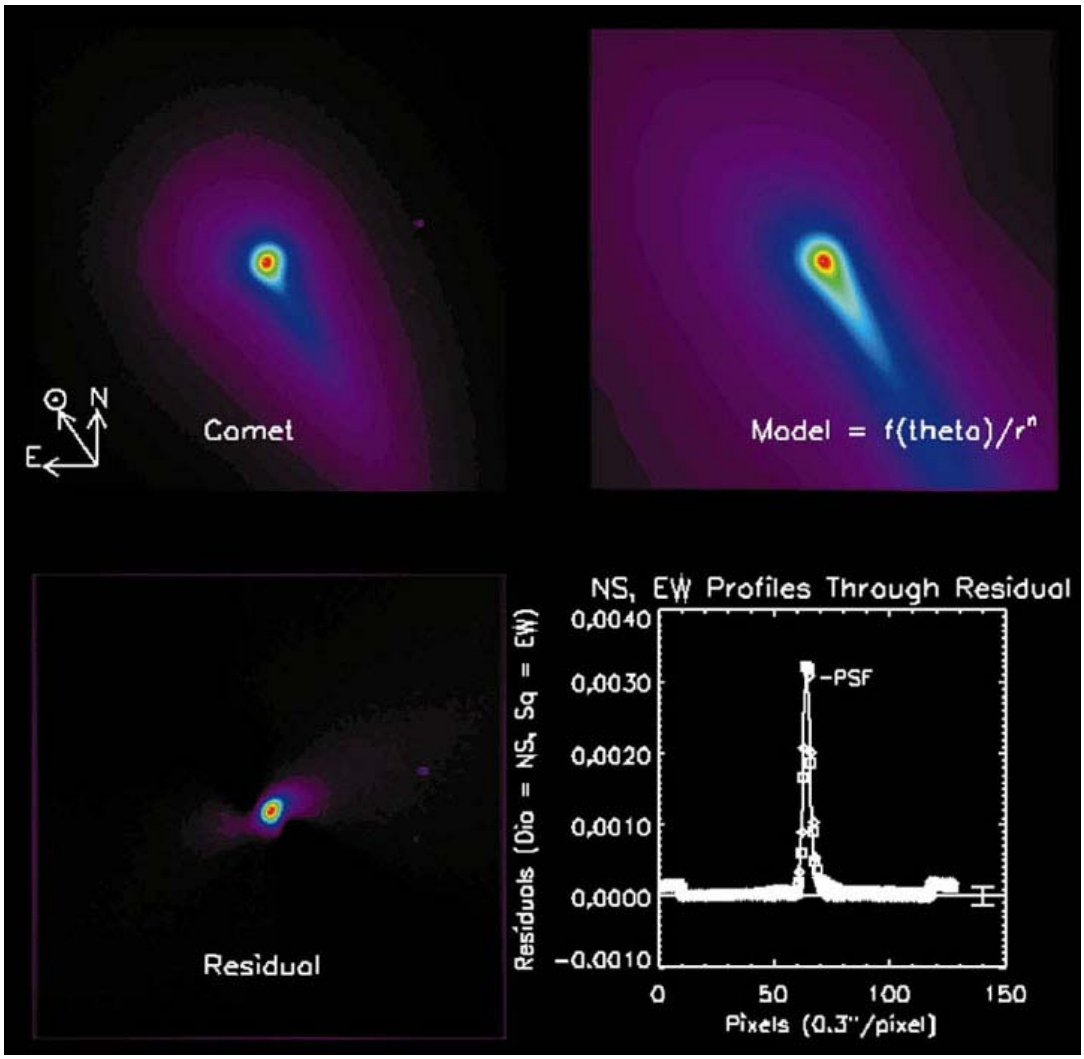

Figure 1.1 The nucleus extraction method applied to comet Hyakutake. By modeling (top right) and subtracting the coma from the original image (top left), the residual (bottom left) will only contain signal from the nucleus, with a PSF brightness profile (bottom right) (Lisse et al., 1999).

possible from *in situ* observations. And third, photometry at phase angles that are impossible to be reached from the ground can be obtained from spacecraft.

1.2.3 Down to my work

During recent years, many photometric and spectral observations have been made available from successful space missions to comets and asteroids. Galileo successfully encountered asteroids 951 Gaspra (Veverka et al., 1994) and 243 Ida and its moon Dactyl (Belton et al., 1996) *en route* to Jupiter. NEAR flew by a C-type asteroid 253 Mathilde (Veverka et al., 1999), and successfully rendezvoused with asteroid 433 Eros for a year (Cheng, 2002). Several comets have been visited by spacecraft, too. Comet 1P/Halley was visited by spacecraft at its last return to perihelion in 1986 (Reinhard, 1986; Keller et al., 1986; Sagdeev et al., 1986a,b). Comet 19P/Borrelly was imaged by Deep Space 1 (Soderblom et al., 2004a). Comet 81P/Wild 2 showed its dramatic and complicated surface to Stardust, which is returning to Earth the samples of dust collected in the coma (Brownlee et al., 2003). All of those space missions provided excellent photometric data that are otherwise impossible to be obtained from the ground, and helped to constrain the photometric properties of those targets dramatically. Once the well interpreted phase curves and detailed surface properties of a few cometary nuclei are available, it will provide better understanding for other cometary nuclei, and be valuable for the planning of future space missions to solar system small bodies.

Looking forward, many other missions are either going to comets or asteroids, or in preparation. Deep Impact, successfully launched on January 12, 2005, is heading to comet 9P/Tempel 1 to excavate a crater and see what is inside a comet (A'Hearn et al., 2005).

ESA's Rosetta is on its way to comet 67P/Churyumov-Gerasimenko and will rendezvous with it and put a lander on its surface (Wilson and Gimenez, 2004). Rosetta will also fly by two asteroids, (2867) Steins and (21) Lutetia, on its way to comet Churyumov-Gerasimenko. Dawn is in preparation, with its objective of orbiting asteroids 4 Vesta and 1 Ceres for about a year each (Russell et al., 2004).

Keeping all these in mind, I aimed my thesis work towards the photometric studies of asteroids and comets, with Hapke's theory as the primary theoretical tool to carry out all analyses, and spacecraft data as the primary input, including disk-resolved data of Eros from NEAR, disk-resolved images of Borrelly from DS1, and the HST images of Ceres.

1.3 Overview of Chapters

As the fundamental theory used throughout the dissertation, Hapke's theory of reflectance will be introduced in the next chapter. The problem of the disk-integrated phase function for irregular shapes will be studied numerically in Chapter 3 with forward modeling simulations. Then the photometric properties of three objects, asteroid (433) Eros, comet 19P/Borrelly, and asteroid (1) Ceres, will be studied, each in a chapter. Chapter 4 uses the excellent dataset of Eros returned from NASA's Near Earth Asteroid Rendezvous (NEAR) mission, coupled with the shape model determined by Thomas et al. (2002), to study the photometric properties of Eros. Its Hapke's parameters are determined, and the further implications of the photometric properties are discussed. All my software tools developed to perform disk-resolved photometric analysis are tested and confirmed with this excellent dataset. Chapter 5 describes an attempt to apply Hapke's theory to a cometary nucleus

with its shape model. I utilized about ten images from NASA's Deep Space 1 (DS1) spacecraft taken during its Borrelly flyby, and performed Hapke's analysis for the large photometrically distinguished terrains on Borrelly's surface one by one. Large photometric heterogeneity, unlike the uniformity of Eros, was observed, which is then correlated to its cometary activity through disk-resolved thermal modeling of Borrelly's surface. Chapter 6 takes the Hubble Space Telescope (HST) images of Ceres, with the resolution of about 60 km, to model the surface albedo maps of Ceres at three wavelengths. A uniform surface of Ceres is revealed, and the implication of the similarity of Ceres to icy satellites of giant planets is discussed. The last chapter, Chapter 7, is a summary of the whole dissertation, and discusses some possible future work.

Chapter 2

Light Scattering Theory

2.1 Basic Concepts and Theoretical Preparation

As a fundamental unit of the interaction between particulate medium and electromagnetic radiation, single-particle scattering is a starting point in understanding the properties of the light diffusely reflected from a particulate surface. A physically idealized and simplest particle is spherical with a uniform complex index of refraction interior, through which some important physical concepts are defined. In this section these basic concepts and physical quantities are reviewed, following the definitions in Hapke (1993).

2.1.1 Irradiance and radiance

The amount of radiative power at position $\mathbf{r}$ crossing unit area perpendicular to the direction of propagation Ω, traveling into unit solid angle about Ω, is called *radiance*, denoted by $I(\mathbf{r}, \Omega)$, or *specific intensity*.

On the other hand, if the radiation is collimated to direction Ω, then the radiative power crossing unit area perpendicular to the direction of propagation is called *irradiance*, denoted by J. Ideally, the radiative energy from a collimated light beam has zero solid angle width. In reality, since the distance between light source (*e.g.*, the Sun, stars) and most light scattering bodies (*e.g.*, planets, asteroids) are extremely large compared to the sizes of celestial bodies, this is always a good approximation. Irradiance has the same

unit as flux (W m^{-2}), but it only refers to the flux of a collimated source.

2.1.2 Cross sections

The *extinction cross section* is defined as the ratio of the removed power P_E from an incident collimated beam to the irradiance J of the incident beam.

$$\sigma_E = P_E/J \tag{2.1}$$

It has a unit of area, and can be understood as an equivalent area of the medium that intercepts and removes all incident energy it receives.

Let the part of the removed power P_E that is scattered be P_S, and the part that is absorbed be P_A, then the *scattering cross section* and *absorption cross section* are defined as, respectively,

$$\sigma_S = P_S/J \tag{2.2}$$

$$\sigma_A = P_A/J \tag{2.3}$$

Since $P_S + P_A = P_E$, we have $\sigma_S + \sigma_A = \sigma_E$. We can think that in the total extinction cross section σ_E, σ_S is responsible for scattering only, and σ_A is responsible for absorption only.

2.1.3 Particle single-scattering albedo

The fraction of the total amount of power scattered by a single particle into all directions in the total amount of power that is removed from the incident irradiation J is called *particle single-scattering albedo*, denoted by w. From the definition of cross sections, the

single-scattering albedo is defined as

$$w = P_S/P_E = \sigma_S/\sigma_E \tag{2.4}$$

If a collimated beam with irradiance $J(\Omega_0)$ travels along direction Ω_0 onto a particle, and let the scattered radiance be $I(r, \Omega; \Omega_0)$, as a function of distance r from the particle, and along direction Ω, then at the surface of the scattering particle, the total scattered flux, F, or $I(\Omega)$ integrated over all directions, can be related to the incident irradiance J by the single-scattering albedo (SSA hereafter)

$$F = \int_{4\pi} I(\Omega) d\Omega = wJ \tag{2.5}$$

The SSA is never larger than unity, and usually is a function of wavelength. It is directly determined by the physical properties of particles, such as composition, size, shape, *etc.* It is also affected by the packing status for particulate surfaces or particle aggregates, such as porosity, internal strength, *etc*.

2.1.4 Single-particle phase function

The *single-particle phase function* $p(\alpha)$ describes the angular distribution of the scattered radiance, $I(\Omega, \Omega_0)$, as a function of *phase angle* α, the angle between the direction of incident beam, Ω_0, and the direction of scattered light, Ω. The single-particle phase function is defined by

$$I(\Omega) = wJ(\Omega_0)\frac{p(\alpha)}{4\pi} \tag{2.6}$$

In this definition, $p(\alpha) = 1$ if particle scatters isotropically, and the 4π is a normalization factor so that Eq. 2.5 holds. For spherical particles, the scattered power is independent

of azimuth angle, and the normalization condition for single-particle phase function becomes

$$\frac{1}{2}\int_0^{\pi} p(\alpha)\sin\alpha d\alpha = 1 \tag{2.7}$$

Sometimes people may put the 4π factor into the single-particle phase function, and the normalization constant is therefore 1 in that case.

2.1.5 Incidence angle and emission angle

Now consider the condition of a semi-infinite medium with particulate surface. There are two geometrical concepts correlated to this condition, the *incidence angle* and the *emission angle*. For the geometry illustrated schematically in Fig. 2.1, the normal to the surface $\mathbf{N}$ is along the z axis, and the angle between the surface normal $\mathbf{N}$ and incident light is called *incidence angle*, i. After scattered by the surface, some rays emerge from the surface traveling towards the direction that makes an angle e with $\mathbf{N}$, this is called *emission angle*. The common plane of incident ray and $\mathbf{N}$ is the *plane of incidence*; the common plane of emerging ray and $\mathbf{N}$ is the *plane of emergence*; and the common plane of incident and emerging rays is the *scattering plane*. The angle between the plane of incidence and the plane of emergence is denoted by ψ. And as defined before, the *phase angle* α is the angle between incident ray and emergent ray. These four angles are related by geometry,

$$\cos\alpha = \cos i\cos e + \sin i\sin e\cos\psi \tag{2.8}$$

As a common notation, and used in this dissertation, the cosines of i and e are usually denoted by $\mu_0 = \cos i$, and $\mu = \cos e$, respectively.

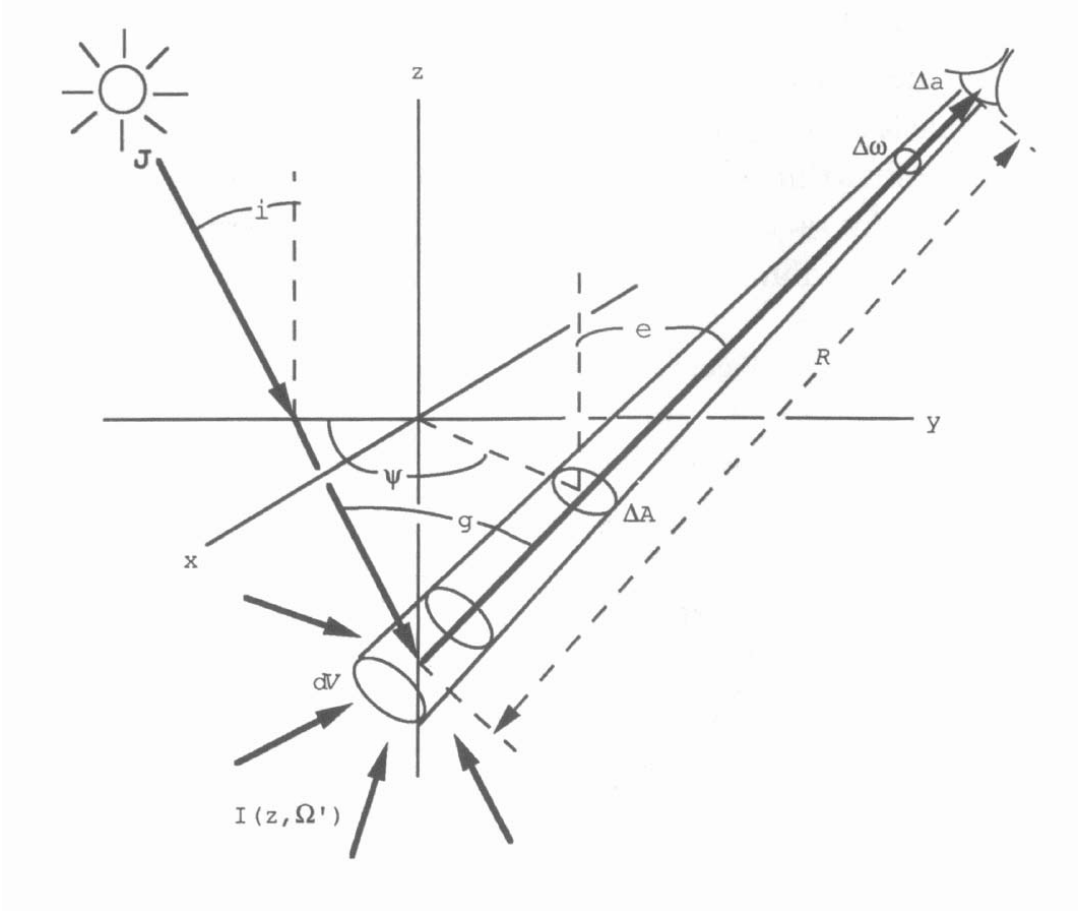

Figure 2.1 Schematic representation of the scattering geometry (From Hapke (1993) Fig. 8.4). The nominal surface of the medium is the x-y plane.

2.1.6 Reflectance

As defined in Hapke (1993), the term *reflectance* refers to the fraction of incident light diffusively scattered or reflected by a rough surface. A similar term, *reflectivity*, refers to the fraction that is specularly reflected from a smooth surface. Depending on geometry, there exist many kinds of reflectance. As initialized by Nicodemus (1970); Nicodemus et al. (1977), and summarized in Hapke (1993), people usually use two adjectives preceding the word reflectance to specify the geometry, the first describing the degree of collimation of the source, and the second that of the detector. The most commonly used adjectives include *directional*, *conical*, and *hemispherical*. If both adjectives are the same, a prefix *bi-* is used. Therefore, the *directional-hemispherical reflectance* refers to the total fraction of light reflected into the upper hemisphere when the surface is illuminated by a collimated source from above. This quantity determines the total reflected energy, therefore determines the temperature of the surface. The most commonly used reflectance, the *bidirectional reflectance*, $r(i, e, \alpha)$, refers to the fraction of light scattered into direction e when the surface is illuminated by collimated incident light in direction i. However, it must be noted that the bidirectional reflectance is a physically idealized concept. In reality, the solid angles for both collimated source and detector are finite, and what we can measure is actually biconical reflectance. But in most cases of remote sensing, the angular sizes of both source and detector are very small as seen from the object. The bidirectional reflectance is therefore a good approximation, and an important simplification in theoretical analysis.

Reflectance is a quantity that can be measured in observations or experiments.

Therefore to study the behavior of reflectance as a function of geometry and properties of incident light, and to study the correlation between reflectance and the basic physical quantities of particles such as the SSA are of great importance in understanding the physical properties, the evolutionary history, and the chemical composition, of surfaces of solid bodies.

2.2 Empirical Expressions of Reflectance

At a given phase angle, the reflectance of a surface is usually a function of phase angle α, incidence angle i, and emission angle e. For a spherical body, the i and e on its surface with respect to a fixed light source, and a fixed detector, change systematically from projected limb to terminator. The reflectance at one particular phase angle as a function of i and e determines the brightness change of the disk, and thus it is sometimes called *limb darkening* profile.

2.2.1 Lambert's law

The simplest empirical expression of bidirectional reflectance function is Lambert's law, in which reflectance is proportional to the cosine of incidence angle i,

$$r_L(i, e, \alpha) = \frac{1}{\pi} A_L \mu_0 \tag{2.9}$$

where A_L is a constant called Lambert albedo of the surface. If one calculates the total flux scattered into upper hemisphere,

$$F_S = \int_{2\pi} I(i, e, \alpha) \mu d\Omega = \int_{2\pi} r(i, e, \alpha) J \mu d\Omega = A_L J \mu_0 \tag{2.10}$$

then it is found that A_L is actually the directional-hemispherical reflectance of a Lambert surface, meaning the fraction of total incident energy that is scattered. A surface with $A_L = 1$ is called *perfectly diffuse surface*. Lambert's law is the simplest approximation of scattering. It adequately describes a bright surface with high albedo, but not as well for a dark surface.

2.2.2 Minnaert's law

Another approximation of bidirectional reflectance function, Minnaert's law, is a generalization of Lambert's law suggested by Minnaert (1941). The form of Minnaert's law is

$$r_M(i, e, \alpha) = A_M \mu_0^{\nu} \mu^{\nu-1} \tag{2.11}$$

where A_M is a constant called the *Minnaert albedo*, and ν is another constant, the *Minnaert index*. If $\nu = 1$, then Minnaert's law reduces to Lambert's law, and $A_M = A_L/\pi$. Minnaert's law empirically describes the variation of scattering of many surfaces over a limited range of angles. The Minnaert parameters are usually functions of phase angles (*e.g.* Veverka et al., 1989, *etc.)*.

2.2.3 Single-particle scattering

The exact solution of radiative transfer has been obtained for isolated perfectly spherical and homogeneous particles, known as Mie theory. In Hapke (1993), a simplified summary is provided. Readers are also referred to the works of Born and Wolf (1980); Stratton (1941); Van de Hulst (1957), and the books by Bohren and Huffman (1983) for more detailed derivations. The basic conclusions and equations are listed here for the purpose

of completeness.

The scattering behavior of single spherical particles depends on the ratio of particle size to the wavelength of incident light, expressed as $X = \pi D/\lambda$. If particle is much smaller than wavelength, i.e. $X \ll 1$, the scattering is called *Raleigh scattering*. For unpolarized incident light, the particle phase function is

$$p(\alpha) = \frac{3}{4}(1 + \cos^2 \alpha) \tag{2.12}$$

If particle size is in the same order of wavelength, the particle phase function is complicated, and depends on the single scattering albedo. If a particle is much larger than wavelength, then the scattering is close to geometric-optics scattering, with strong diffraction pattern appearing at large phase angles. The analytic expressions of single-particle phase function for the latter two cases are complicated and not listed here.

Spherical particles are idealization of real particles, which are actually very irregular in their shapes. It is not possible to derive a single simple expression for the single-particle phase funcion of irregular particles, instead, empirical expressions are usually used. There are two commonly used empirical single-particle phase function, the *Legendre polynomial series* and the *Henyey-Greenstein function*.

The Legendre polynomial representation of a single-particle phase function reads

$$p(\alpha) = \sum_{j=0}^{\infty} b_j P_j(\alpha) \tag{2.13}$$

where the b_j's are constants, and the $P_j(\alpha)$ are Legendre polynomials of order j. The combination of b_j's must satisfy the normalization condition (Eq. 2.7). This representation is most useful when single scattering is not far from isotropic, and only the first

few terms are important. The shapes of single-particle phase functions of single-term and double-term Legendre polynomial forms are shown in Fig. 2.2.

Henyey and Greenstein (1941) introduced an empirical phase function

$$p(\alpha) = \frac{1 - g^2}{(1 + 2g\cos\alpha + g^2)^{3/2}} \tag{2.14}$$

which is called *Henyey-Greenstein function*, or *HG function*, and will be the only single-particle phase function that is used in this dissertation for theoretical derivation and data modeling. The constant g in the HG function is the cosine asymmetry factor, of which a zero value gives isotropic scattering, a positive value forward-scattering, and a negative value backward-scattering (Fig. 2.3). Sometimes a *double HG function* is used, with one term describing the back-scattering lobe, and another term the forward-scattering lobe. One form introduced by McGuire and Hapke (1995) is,

$$p(\alpha) = \frac{1 + c}{2}\frac{1 - b^2}{1 - 2b\cos\alpha + b^2} + \frac{1 - c}{2}\frac{1 - b^2}{1 + 2b\cos\alpha + b^2} \tag{2.15}$$

where the constant b describes the amplitude of lobes, and is constrained within the range $0 \leq b < 1$, and the constant c is the weight factor, with no constraint except that $p(\alpha)$ has to be non-negative everywhere. The double HG function is highly flexible, and can fit particles of many kinds very well, and is widely used in practice (*e.g.* Domingue et al., 2002; Clark et al., 2002). McGuire and Hapke (1995) fitted many kinds of particles with double HG function, and summarized their b and c parameters in the plot as shown in Fig. 2.4, which correlates the physical properties of particles with two empirical parameters of their phase function to some extent.

There are two other forms of single-particle phase functions, which are for highly absorbing particles, and are not commonly used. Assume a spherical particle that is suf-

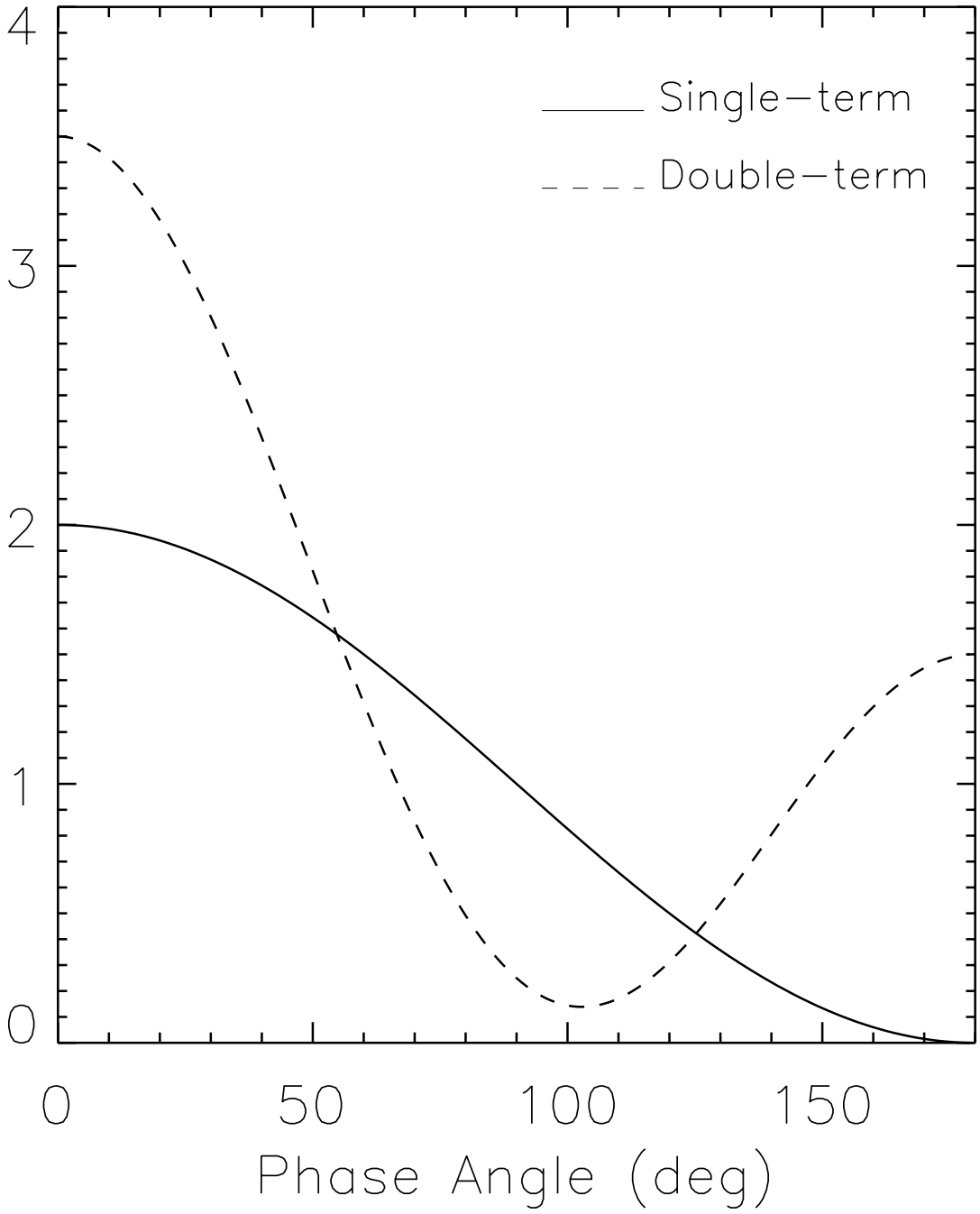

Figure 2.2 Single-term (solid line) and double-term (dashed line) Legendre polynomial forms of single-particle phase function. Parameters for single-term Legendre polynomial are 1 and 1, for double-term polynomial are 1, 1 for zeroth and first order terms, and 1.5 for second order term.

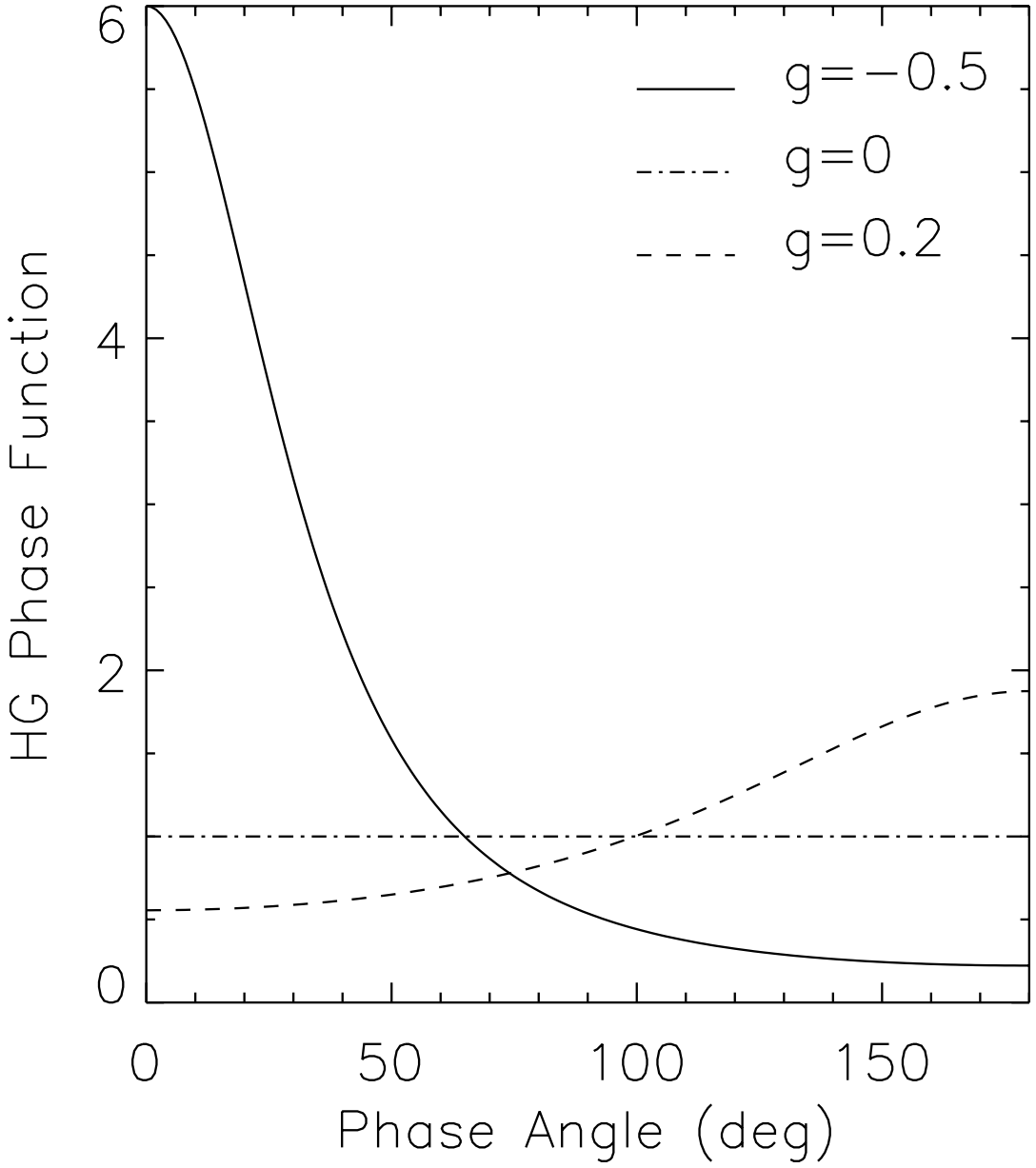

Figure 2.3 Examples of single-term HG functions with negative, zero, and positive asymmetry factors.

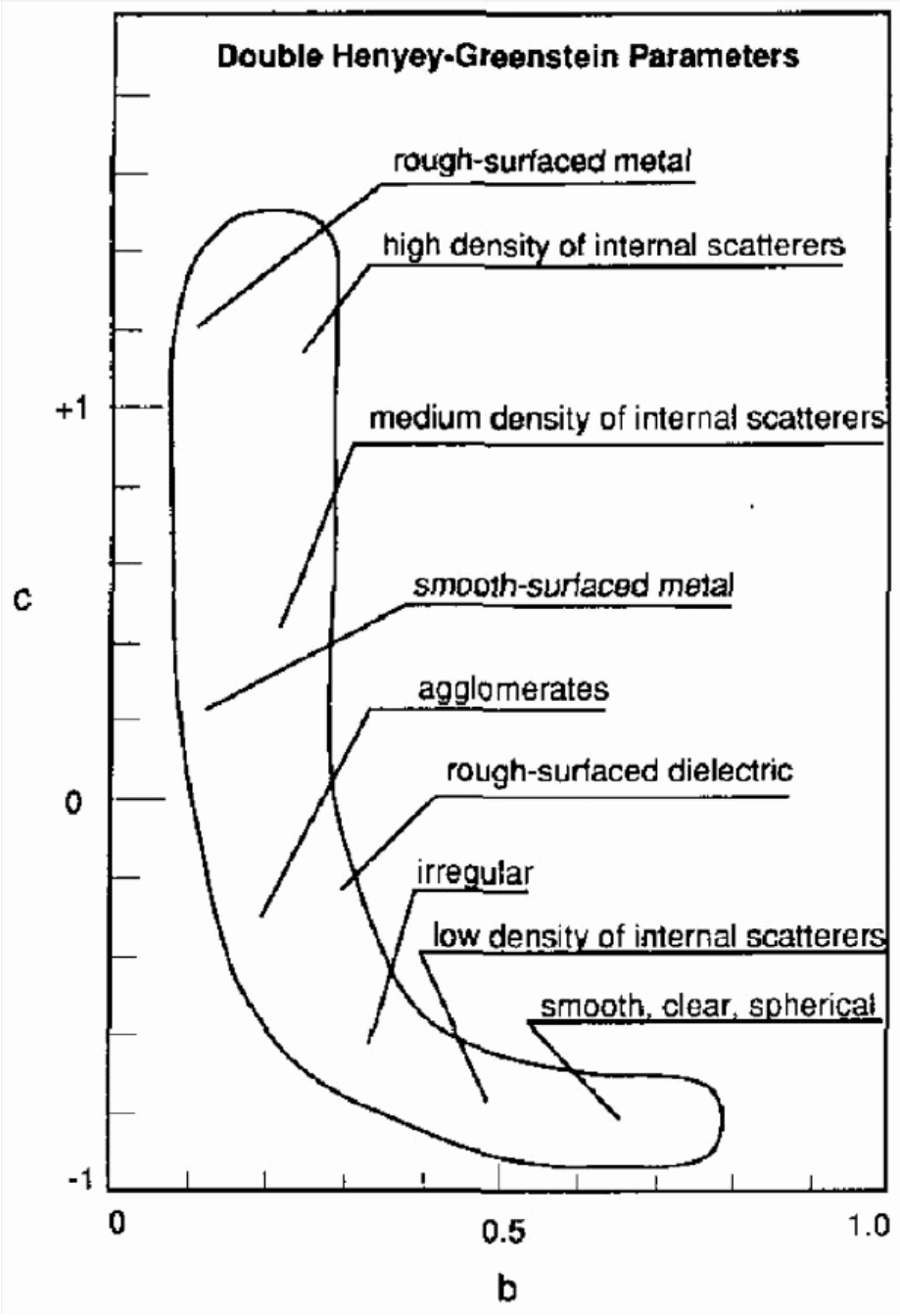

Figure 2.4 Plot to show the correlation between the b, c parameters of double-term HG function with physical properties of particles. Taken from McGuire and Hapke (1995).

ficiently absorbing so that internally transmitted light can be neglected, and the scattered light is all from surface scattering. By assuming two different scattering functions, the Lambert's law (Eq. 2.9) and the Lommel-Seeliger law (Eq. 2.20, see later sections), and integrating over the whole surface of the spherical particle, the phase functions are found to take the forms of

$$p(\alpha) = \frac{8}{3}\frac{\sin\alpha + (\pi-\alpha)\cos\alpha}{\pi} \tag{2.16}$$

$$p(\alpha) = \frac{3}{4(1-\ln 2)}\left[1 - \sin\frac{\alpha}{2}\tan\frac{\alpha}{2}\ln\left(\cot\frac{\alpha}{4}\right)\right] \tag{2.17}$$

where Eq. 2.16 corresponds to Lambert's law, and Eq. 2.17 corresponds to Lommel-Seeliger law. The plots of these two single-particle phase functions are shown in Fig. 2.5. The corresponding spheres are called *Lambert sphere* and *Lommel-Seeliger sphere*.

2.3 Hapke's Scattering Law

Hapke's scattering theory is an approximate solution of radiative transfer equation solved for a semi-infinite medium on the surface, as illuminated by a collimated beam with irradiance J at incidence angle i. The scattered radiance as detected at viewing angle e is, according to radiative transfer equation,

$$I = \int_0^\infty \left[\frac{w(\tau)}{4\pi}\int_{4\pi} p(\tau,\Omega',\Omega)I(\tau,\Omega')d\Omega' + \mathcal{F}(\tau,\Omega)\right]e^{-\tau/\mu}\frac{d\tau}{\mu} \tag{2.18}$$

The inner integral in the equation refers to multiple scattering happening at optical depth τ, where the direction of incident irradiance is at direction Ω'. It is integrated over all possible directions because the direction of incident irradiance due to previous scattering $I(\tau,\Omega')$ can be from anywhere. The second term in the outer integral, $\mathcal{F}(\tau,\Omega)$, is the

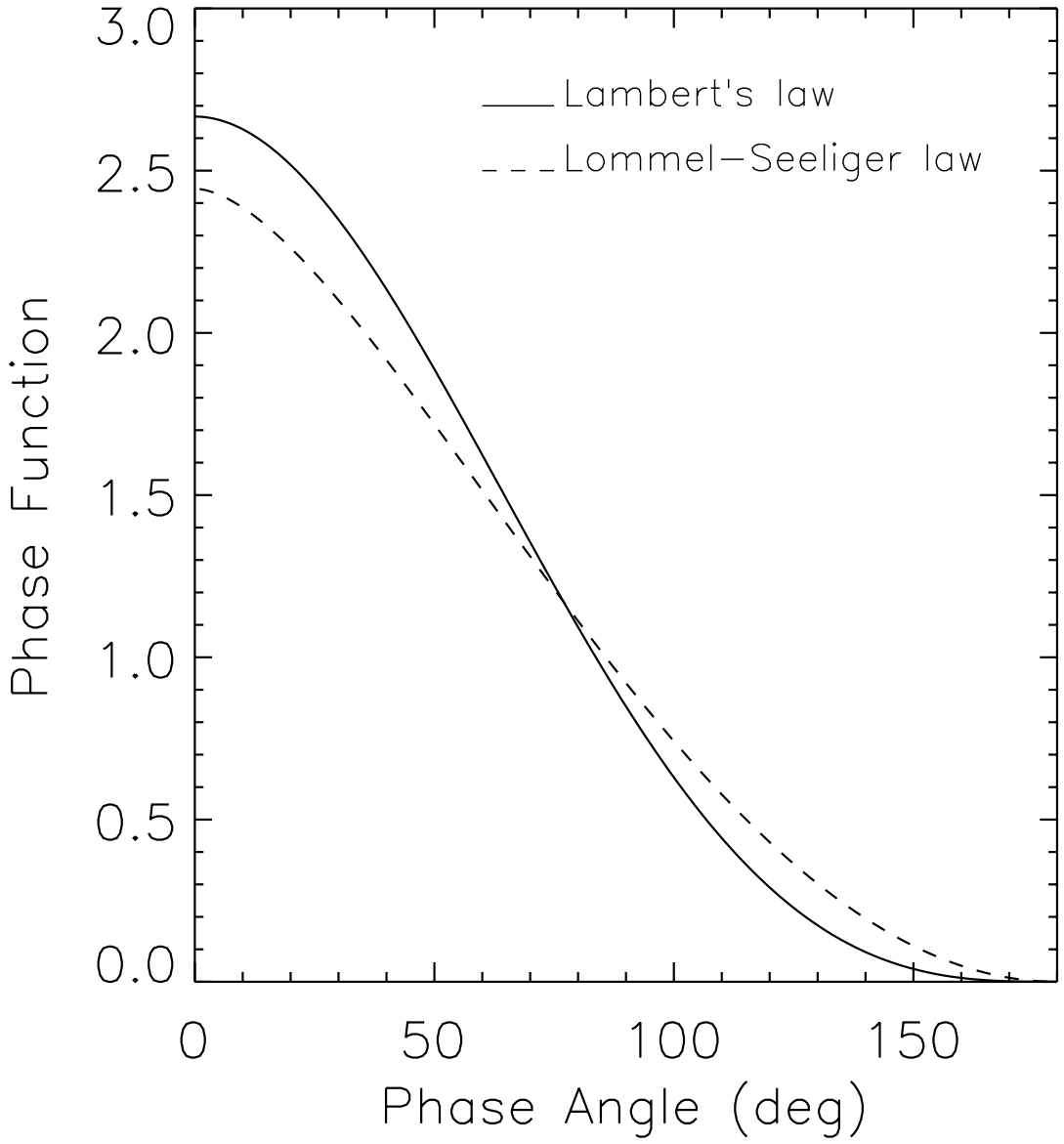

Figure 2.5 The phase function of an opaque sphere with its surface following Lambert's scattering law and Lommel-Seeliger scattering law, respectively.

single scattering term, where $\mathcal{F}$ is the source function,

$$\mathcal{F}(\tau, \Omega) = \frac{w(\tau)J}{4\pi} p(\tau, \alpha) e^{-\tau/\mu_0} \tag{2.19}$$

2.3.1 Single scattering, Lommel-Seeliger law

Assuming that p and w are independent of optical depth τ, and integrating the single scattering part of Eq. 2.18, the total radiance due to single scattering, I_s, is

$$I_s = J \frac{w}{4\pi} \frac{\mu_0}{\mu_0 + \mu} p(\alpha) \tag{2.20}$$

And the bidirectional reflectance due to single scattering is then

$$r_s = \frac{I_s}{J} = \frac{w}{4\pi} \frac{\mu_0}{\mu_0 + \mu} p(\alpha) \tag{2.21}$$

When $p(\alpha)$=1, *i.e.* isotropic, Eq. 2.20 is called *Lommel-Seeliger law*. For dark surface such as the Moon and Mercury, where multiple scattering is almost negligible, this scattering law describe the surfaces accurately.

2.3.2 Multiple scattering

The first term in Eq. 2.18 refers to multiple scattering, and the integral is extremely hard to evaluate, partly because it is entangled with the scattered radiance, an unknown, and partly because the single-particle phase function, which can only be described empirically, goes into the integral.

The simplest medium is composed of particles that scatter light istotropically and independently. The exact solution of this kind of medium is solved by Ambartsumian (1958) using a so-called embedded invariance, based on the fact that adding a new thin

layer to the surface of semi-infinite medium does not change the reflectance. The reflectance of such a medium is

$$r(i,e,\alpha) = \frac{w}{4\pi}\frac{\mu_0}{\mu_0+\mu}H(\mu_0)H(\mu) \tag{2.22}$$

where $H(x)$ is the Ambartsumian-Chandrasekhar H-function (Chandrasckhar, 1960), satisfying the integral equation

$$H(x) = 1 + \frac{w}{2}xH(x)\int_0^1 \frac{H(x')}{x+x'}dx' \tag{2.23}$$

The multiple scattering reflectance r_m in this case is therefore the total reflectance subtracted by single scattering reflectance

$$r_m(i,e,\alpha) = \frac{w}{4\pi}\frac{\mu_0}{\mu_0+\mu}[H(\mu_0)H(\mu)-1] \tag{2.24}$$

Hapke (1993) derived an approximated expression for the H-function by making simplified assumptions in solving the radiative transfer equation (Eq. 2.18)

$$H(x) \approx \frac{1+2x}{1+2\gamma x} \tag{2.25}$$

where $\gamma = \sqrt{1-w}$. Another and better version of the approximated H-function is derived recently in Hapke (2002) by linearizing the Eq. 2.23,

$$H(x) \approx \left[1 - wx\left(r_0 + \frac{1-2r_0x}{2}\ln\frac{1+x}{x}\right)\right]^{-1} \tag{2.26}$$

where $r_0 = (1-\gamma)/(1+\gamma)$. In our application of Hapke's theory to observational data, we used the most recent version of the H-function, *i.e.*, Eq. 2.26

The exact solution of reflectance for general anisotropic scattering particles has not been derived yet. The most recent, and the best, attempt to model the medium of

anisotropic scatterers is found in Hapke (2002). In this new model, the multiple scattering part is approximated by

$$r_m(i,e,\alpha) = \frac{w}{4\pi}\frac{\mu_0}{\mu_0+\mu}M(\mu_0,\mu) \tag{2.27}$$

where

$$M(\mu_0,\mu) = P(\mu_0)[H(\mu)-1] + P(\mu)[H(\mu_0)-1] + \mathcal{P}[H(\mu)-1][H(\mu_0)-1] \tag{2.28}$$

$P(\mu_0)$, $P(\mu)$, and $\mathcal{P}$ are the integrals of single-particle phase function

$$P(\mu_0) = \frac{1}{2\pi}\int_{e'=\pi/2}^{\pi}\int_{\varphi'=0}^{2\pi} p(\alpha')\sin e' de' d\varphi' \tag{2.29}$$

$$P(\mu) = \frac{1}{2\pi}\int_{i'=\pi/2}^{\pi}\int_{\varphi'=0}^{2\pi} p(\alpha')\sin i' di' d\varphi' \tag{2.30}$$

$$\mathcal{P} = \frac{1}{(2\pi)^2}\int_{i'=0}^{\pi/2}\int_{\varphi'_i=0}^{2\pi}\int_{e'=0}^{\pi/2}\int_{\varphi'_e=0}^{2\pi} p(\alpha')\sin e' de' d\varphi'_e \sin i' di' d\varphi'_i \tag{2.31}$$

Because of its complicated formulism, and the fact that many asteroids and almost all cometary nuclei are dark enough that the approximation of an isotropic single-particle phase function works fine, the new version of multiple scattering approximation is not incorporated into my work. Instead, we used the approximation for isotropic scatterers (Eq. 2.24).

Putting together the two components of reflectance, Hapke's bidirectional reflectance is

$$r(i,e,\alpha) = r_s + r_m = \frac{w}{4\pi}\frac{\mu_0}{\mu_0+\mu}[p(\alpha) + H(\mu_0)H(\mu) - 1] \tag{2.32}$$

Since the single scattering part is the exact solution of radiative transfer equation, and the multiple scattering part only refers to isotropic scattering, this representation gives good approximation to dark surfaces or a medium of isotropic scatterers. The photometric

analyses of many asteroids and satellites, including bright ones, using Hapke's model show good agreement between the model and observations over a broad range of phase angles (*e.g.* Helfenstein et al., 1994; Simonelli et al., 1998; Clark et al., 2002; Domingue et al., 2002, *etc.)*.

2.3.3 Opposition effect

For many solar system bodies and laboratory samples, the reflectance shows a non-linear increase at small phase angle close to opposition. This non-linear peak is usually called *opposition surge* or *opposition effect*, with a typical width of about 5° to 10° for asteroids. One mechanism that may cause the oppposition effect is that, when the phase angle is small, the emerging ray is close to the preferential path pre-selected by the incident ray. Or we can understand it by imagining the dramatic increase of the overlap between the cylinder of incident light and that of emerging light when phase angle decreases to zero. Therefore, this phenomenon presents itself only when the surface is particulate, and porous, and the mutual blocking between particles causes shadows that are larger than the wavelength, giving the name of this effect *shadow-hiding opposition effect*, or SHOE for short. This mechanism is studied by Hapke (1993), and an approximate analytic correction is added to Eq. 2.32 to take into account this effect. Because the SHOE is a single-scattering phenomenon, only the single scattering part of the bidirectional reflectance is affected, which takes the form of

$$r_s(i, e, \alpha) = \frac{w}{4\pi} \frac{\mu_0}{\mu_0 + \mu} p(\alpha)[1 + B_S(\alpha)] \tag{2.33}$$

where the opposition effect enters into the single scattering reflectance as term $B_S(\alpha)$,

$$B_S(\alpha) = \frac{B_{S0}}{1 + \frac{1}{h_S}\tan\frac{\alpha}{2}} \tag{2.34}$$

And the total bidirectional reflectance is now

$$r(i, e, \alpha) = \frac{w}{4\pi}\frac{\mu_0}{\mu_0 + \mu}\{[1 + B_S(\alpha)]p(\alpha) + H(\mu_0)H(\mu) - 1\} \tag{2.35}$$

Two parameters are introduced here to describe the SHOE. The first is the amplitude parameter, B_0, which is actually an empirical parameter. Theoretically, in a perfect case, the SHOE will give a unity amplitude parameter. But for real cases, this parameter is usually smaller than unity because of the finite size of particles and their imperfection from spherical uniform particles. The range of B_0 is $0 \leq B_0 \leq 1$. The second parameter is the width of opposition effect, h_S, which is determined by particle size, size distribution, packing status, but not likely the compositional properties or scattering properties such as phase function. If the particle size distribution follows a power law with an index of 4, which is of particular interest because it characterizes a comminution process, then the width parameter h_S for SHOE is proportional to $-\ln(1 - \phi)$, where ϕ is the ***filling factor***, the fraction of volume that is occupied by particles. For loosely packed powder, ϕ is close to 0, and the opposition peak is very narrow; for closely packed powder, however, the width will be very large, and the opposition effect is actually not pronounced from observational data. Therefore, an opposition surge with a few degrees is the evidence that there exists loosely packed regolith on the surface of an object.

If particle size is comparable with or smaller than wavelength, then the SHOE will not be present because there is no shadow between particles due to diffraction. But the constructive interference between the portions of a wave traveling in opposite directions

along the same multiple scattering paths within the medium will cause another kind of opposition effect, namely, the *coherent backscattering opposition effect,* or *CBOE*. The main difference between SHOE and CBOE is that SHOE is caused by the particles larger than wavelength, being a single scattering effect, and uncorrelated with the polarization signature of scattered light; but CBOE is caused by particles with comparable or smaller size than wavelength, being a multiple scattering effect as well as a single scattering effect, and affecting the polarization signature of scattered light. Or, in other words, SHOE is an effect of geometric optics, while CBOE is an effect of wave optics.

Because CBOE affects both single scattering and multiple scattering, a correction factor for the bidirectional reflectance is introduced by Hapke (2002), and the reflectance with consideration of CBOE, r_{CBOE}, is

$$r_{CBOE} = r[1 + B_C(\alpha)] \tag{2.36}$$

where r is the bidirectional reflectance without considering the CBOE. Hapke (2002) also provides an approximated expression for $B_C(\alpha)$,

$$B_C(\alpha) = B_{C0}\frac{1 + \frac{1-\exp[-(1/h_C)\tan(\alpha/2)]}{(1/h_C)\tan(\alpha/2)}}{2[1 + (1/h_C)\tan(\alpha/2)]^2} \tag{2.37}$$

Similar to SHOE, CBOE also needs the amplitude parameter, B_{C0}, and the width parameter, h_C, to describe it. The amplitude parameter B_{C0} is also an empirical parameter, with the physical constraint of $0 \leq B_{C0} \leq 1$. The width parameter h_C is determined by the optical properties of scatterers.

$$h_C = \lambda/4\pi\Lambda \tag{2.38}$$

λ is wavelength, and Λ is the transport mean free path in the medium, and is expressed as

$$\Lambda = [n\sigma Q_S(1- <\cos\theta>)]^{-1} \tag{2.39}$$

with n the number volume density of particles, σ the mean particle cross section, Q_S the mean particle scattering efficiency, and $<\cos\theta>$ the mean cosine of the scattering angle. An important property of CBOE is that the width of opposition surge depends on wavelength of incident light, providing an easy observational method of distinguishing between two mechanisms of opposition effect. The first application can be found in Clark et al. (2002).

2.3.4 Rough surface

Under all the above equations, an implicit but important assumption is that the surface is smooth on the scale that is much larger than particle size. This is obviously not true for the surfaces of solar system bodies. Hapke (1984) provided a correction to the above reflectance model to describe large scale surface roughness, based on the assumption that the macroscopically rough surface is made up of small, locally smooth facets that are large compared to the mean particle size and tilted with respect to each other. Assuming that the normals of those facets of a randomly rough surface are described by a distribution function $a(\vartheta, \zeta)d\vartheta d\zeta$, where ϑ is the zenith angle between a facet normal and the average normal direction of the whole surface, and ζ is the azimuth angle of the facet normal, we can reasonably assume that the orientations of these facets are independent of azimuth angle, and the distribution of facet normal is only a function of ϑ. It is further assumed

that the distribution function has the form of a Gaussian distribution

$$a(\vartheta, \zeta) d\vartheta d\zeta = \mathcal{A} e^{-\mathcal{B} \tan^2 \vartheta} d(\tan \vartheta) d\zeta \tag{2.40}$$

where $\mathcal{A}$ and $\mathcal{B}$ are two normalization constants so that

$$\int_0^{\pi/2} a(\vartheta) d\vartheta = 1 \tag{2.41}$$

The roughness of the surface is then characterized by its mean slope angle $\bar{\theta}$, or the *roughness parameter*

$$\tan \bar{\theta} = \frac{2}{\pi} \int_0^{\pi/2} a(\vartheta) \tan \vartheta d\vartheta \tag{2.42}$$

If the average normal direction is viewed as the zeroth-order approximation to describe a rough surface, then the roughness parameter $\bar{\theta}$ introduced by Hapke (1984) is a first-order correction superimposed onto the average orientation of a rough surface, indicating by how much most of the randomly oriented facets that compose the surface are tilted from the average normal direction. However, it has to be kept in mind that the directions of the normals of facets are assumed to be independent of azimuth angle, which means that if the distribution of rough features on the surface has some kind of anisotropic characteristics, then this description and the following equation may not be accurate. The assumption of a Gaussian distribution of the facet normals means that this parameter is probably not good in modeling surfaces that contains many disruptive features such as cracks or sharp edge craters. Furthermore, the size of the surface patch could also affect the roughness parameter if the roughness of the surface is not self-similar, meaning that different distribution functions need to be used at different scales.

In addition to the roughness parameter introduced by Hapke (1984, 1993), there are

some other methods to characterize large scale roughness, such as those in Van Diggelen (1959); Hameen-Anttila (1967) to describe impact craters, and the one presented by Buratti and Veverka (1985) to describe crater density. However, either because those methods are specifically referred to certain geographic environments, or are not directly related to a photometric model, they are not as widely used as the roughness parameter $\bar{\theta}$.

The method that corrects the Hapke's smooth surface photometric model for rough surfaces, introduced by Hapke (1984), is summarized here. The effect of roughness has three aspects: the illumination shadow, where for parts of the surface the incident light is blocked and we see shadows; the mutual blocking, where the emission ray is blocked and we do not see that part of surface; and the change of average incidence angle and emission angles. The first two effects cause the decrease of total scattered light from the surface, and is described by a correction function $S(i, e, \alpha)$, which should be less than or equal to 1, and decreases with increasing phase angle α. The last effect is accounted for by the effective incidence angle i_e and emission angle e_e, which are both functions of i, e, and α, and parameterized by $\bar{\theta}$. The expressions of their cosines, μ_{0e} and μ_e, and S are listed here, but details of derivation and the involved assumptions are not repeated here. Readers are referred to Hapke (1984, 1993).

If $e \geq i$,

$$\mu_{0e} \approx \chi(\bar{\theta}) \left[\cos i + \sin i \tan \bar{\theta} \frac{\cos \psi E_2(e) + \sin^2(\psi/2) E_2(i)}{2 - E_1(e) - (\psi/\pi) E_1(i)} \right] \tag{2.43}$$

$$\mu_e \approx \chi(\bar{\theta}) \left[\cos e + \sin e \tan \bar{\theta} \frac{E_2(e) - \sin^2(\psi/2) E_2(i)}{2 - E_1(e) - (\psi/\pi) E_1(i)} \right] \tag{2.44}$$

$$S(i, e, \psi) \approx \frac{\mu_e}{m u_e(0)} \frac{\mu_0}{\mu_{0e}(0)} \frac{\chi(\bar{\theta})}{1 - f(\psi) + f(\psi) \chi(\bar{\theta}) [\mu_0 / \mu_{0e}(0)]} \tag{2.45}$$

if $e \leq i$,

$$\mu_{0e} \approx \chi(\bar{\theta}) \left[\cos i + \sin i \tan \bar{\theta} \frac{E_2(i) - \sin^2(\psi/2) E_2(e)}{2 - E_1(i) - (\psi/\pi) E_1(e)} \right] \tag{2.46}$$

$$\mu_e \approx \chi(\bar{\theta}) \left[\cos e + \sin e \tan \bar{\theta} \frac{\cos\psi E_2(i) + \sin^2(\psi/2) E_2(e)}{2 - E_1(i) - (\psi/\pi) E_1(e)} \right] \tag{2.47}$$

$$S(i, e, \alpha) \approx \frac{\mu_e}{m u_e(0)} \frac{\mu_0}{\mu_{0e}(0)} \frac{\chi(\bar{\theta})}{1 - f(\psi) + f(\psi)\chi(\bar{\theta})[\mu/\mu_e(0)]} \tag{2.48}$$

where

$$\chi(\bar{\theta}) = \frac{1}{(1 + \pi \tan^2 \bar{\theta})^{1/2}} \tag{2.49}$$

$$E_1(x) = \exp\left(-\frac{2}{\pi} \cot \bar{\theta} \cot x \right) \tag{2.50}$$

$$E_2(x) = \exp\left(-\frac{1}{\pi} \cot^2 \bar{\theta} \cot^2 x \right) \tag{2.51}$$

$$f(\psi) = \exp\left(-2 \tan \frac{\psi}{2} \right) \tag{2.52}$$

Thus the bidirectional reflectance function of a rough surface, without considering the CBOE, is then

$$r_R(i, e, \alpha) = \frac{w}{4\pi} \frac{\mu_{0e}}{\mu_{0e} + \mu_e} \{ [1 + B(\alpha)] p(\alpha) + H(\mu_{0e}) H(\mu_e) - 1 \} S(i, e, \alpha) \tag{2.53}$$

2.4 Phase Function and Planetary Photometry

2.4.1 Geometric albedo and phase function

In planetary science, small bodies in the Solar System are usually hard to resolve from the ground even through the most powerful telescopes, thus it is important to study the integrated behavior of surface light scattering. Let the collimated irradiance from the Sun be J, then the total power scattered by a small area element dA with a normal $\mathbf{N}$, and toward a direction making a phase angle α, is $dP(i, e, \alpha) = Jr(i, e, \alpha)\mu dA$. The

total scattered power detected at direction Ω is then the integral of dP over the whole illuminated and visible area $A(i, v)$

$$P(\Omega) = \int_{A(i,v)} Jr(i, e, \alpha)\mu dA \tag{2.54}$$

The total scattered power over all directions is in turn the integral of $P(\Omega)$ over a solid angle of 4π.

In practice, it is often more convenient to use two physical quantities that are easier to measure: the *geometric albedo* or *physical albedo* A_p, and the *integral phase function* $\Phi(\alpha)$. The geometric albedo is defined as the ratio of the brightness of a body at $\alpha = 0$ to the brightness if the body is replaced by a perfect Lambert disk of the same size, and perpendicular to the line of sight, or

$$A_p \equiv \frac{\int_{A(i)} Jr(e, e, 0)\mu dA}{(J/\pi)\mathcal{A}} = \frac{\pi \int_{A(i)} r(e, e, 0)\mu dA}{\mathcal{A}} \tag{2.55}$$

where $\mathcal{A}$ is the projected cross-section of the body, and J/π is the power scattered by a perfect Lambert disk perpendicularly. The integral phase function is defined as the brightness of a body at any phase angle relative to its brightness at zero phase angle, or

$$\Phi(\alpha) \equiv \frac{\int_{A(i,v)} Jr(i, e, \alpha)\mu dA}{\int_{A(i)} Jr(e, e, 0)\mu dA} \tag{2.56}$$

With simple manipulation, we find that

$$\Phi(\alpha) = \frac{\pi}{\mathcal{A}A_p} \int_{A(i,v)} r(i, e, \alpha)\mu dA \tag{2.57}$$

The disk-averaged bidirectional reflectance at a direction making phase angle α is then

$$r(\alpha) = A_p\Phi(\alpha)/\pi \tag{2.58}$$

2.4.2 Bond albedo and phase integral

Another even more important physical quantity that is closely related to the thermal balance of a body is the *Bond albedo*, or *spherical albedo*, A_B, which is defined as the fraction of total incident irradiance scattered into all directions. With Eq. 2.54 and 2.58, A_B can be written as

$$\begin{aligned} A_B &\equiv \int_{4\pi} r(\alpha) d\Omega \\ &= A_p \int_{4\pi} \frac{1}{\pi} \Phi(\alpha) d\Omega \end{aligned} \tag{2.59}$$

The thermal radiation from an object is directly proportional to $1 - A_B$. The integral $\int_{4\pi} \Phi(\alpha)/\pi d\Omega$ is called *phase integral* q,

$$q = \frac{1}{\pi} \int_{4\pi} \Phi(\alpha) d\Omega = 2 \int_0^{\pi/2} \Phi(\alpha) \sin\alpha d\alpha \tag{2.60}$$

So $A_B = A_p q$.

2.4.3 Hapke's theory applied to planetary photometry

Using Hapke's bidirectional reflectance, the analytic expression of A_p and $\Phi(\alpha)$ can only be approximately derived for regular shapes such as spheres, or ellipsoids, and is done by Hapke (1984) only for a spherical body. From the bidirectional reflectance function of a smooth surface (Eq. 2.35), these two quantities are approximated as,

$$A_p \simeq r_0 \left(\frac{1}{2} + \frac{1}{6} r_0 \right) + \frac{w}{8} [(1 + B_{S0}) p(0) - 1] \tag{2.61}$$

$$\begin{aligned} \Phi(\alpha) \simeq \frac{r_0}{2A_p} \Bigg\{ \left[\frac{(1+\gamma)^2}{4} \{[1 + B_S(\alpha)] p(\alpha) - 1\} + (1 - r_0) \right] \times F(\alpha) \\ + \frac{4r_0}{3} G(\alpha) \Bigg\} \end{aligned} \tag{2.62}$$

where

$$F(\alpha) = 1 - \sin\frac{\alpha}{2}\tan\frac{\alpha}{2}\ln\left(\cot\frac{\alpha}{4}\right) \quad (2.63)$$

$$G(\alpha) = \frac{\sin\alpha + (\pi - \alpha)\cos\alpha}{\pi} \quad (2.64)$$

$F(\alpha)$ and $G(\alpha)$ result from the integration over a spherical surface, and are functions of only phase angle α. The first term of Eq. 2.62 describes a sphere covered by a Lommel-Seeliger scattering surface, modified by single-particle phase function and opposition effect. For low albedo bodies such as the Moon, this term dominates. The second term describes a sphere with Lambert scatterers covering its surface. High albedo bodies such as Venus or icy satellites of Jupiter and Saturn are mostly described by this term.

For spherical bodies with rough surface, Eq. 2.61, 2.62 are corrected for roughness parameter $\bar{\theta}$ as

$$A_p(\bar{\theta}) = \frac{w}{8}[(1 + B_{S0})p(0) - 1] + \mathcal{U}(w, \bar{\theta})r_0\left(\frac{1}{2} + \frac{1}{6}r_0\right) \quad (2.65)$$

$$\Phi(\alpha; \bar{\theta}) \simeq \Phi(\alpha; 0)\mathcal{K}(\alpha, \bar{\theta}) \quad (2.66)$$

where the two correction factors, $\mathcal{U}(w, \bar{\theta})$ and $\mathcal{K}(\alpha, \bar{\theta})$ are both numerically calculated and approximated by analytical expressions by Hapke (1993, p.353-354), and are not repeated here.

2.5 Data Modeling Techniques

The ultimate goal of a theoretical model is to describe the physics of real world. Finally, when photometric data are available from observations, we need to find the Hapke's parameter set that best models the observational data, and then study the physical properties

of the surface from those parameters. Hapke's model involves five or more parameters, including the SSA (w), photometric roughness ($\bar{\theta}$), the amplitude and width of opposition effect (B_{S0} and h_S for SHOE, and B_{C0} and h_C for CBOE), and one or more parameters to describe single-particle phase function $p(\alpha)$. The model we will stick with throughout this dissertation is a five-parameter version, which only considers the SHOE opposition effect, and adopts a one-term HG function involving one asymmetry parameter g to describe the single-particle phase function. The five parameters are summarized in Table 2.1. In this section, I will study the different effects of parameters in determining the shape of phase function and/or the magnitude of bidirectional reflectance at various phase angles, and discuss the main data modeling techniques I will follow in modeling both disk-integrated and disk-resolved photometric data with Hapke's theory.

2.5.1 Significance range of Hapke's parameters

The phase function and bidirectional reflectance as modeled by Hapke's theory are highly non-linear, and their five parameters are entangled with each other, making data modeling very difficult. But fortunately, these parameters affect different ranges of phase angles of the phase curve, or, from data modeling point of view, the reflectance data at different phase angles make different contributions in fitting the five parameters (Helfenstein and Veverka, 1989), so the five parameters can be constrained well if an appropriate scheme is used.

Let us consider disk-integrated photometry. If we define relative partial derivatives of the disk-averaged reflectance, which is a function of phase angle (Eq. 2.58), with

Table 2.1. A summary of the five Hapke's parameters in the version of Hapke's theory that I use throughout this thesis.

Parameter	Symbol	Meaning
Single scattering albedo	w	Fraction of total incident energy that is scattered by a single particle towards all directions
Asymmetry factor	g	Spatial energy distribution in a single particle scattering phase function
Opposition surge amplitude	B_0	Amplitude of opposition effect, SHOE only
Opposition surge width	h	Width of opposition effect, SHOE only
Roughness parameter	$\bar{\theta}$	Average deviation of local normal with respect to average

respect to its parameters, for example, the asymmetry factor, g, as

$$\frac{\partial \log r(\alpha)}{\partial g} \equiv \frac{\partial r(\alpha)}{\partial g} \times \frac{1}{r(\alpha)} \tag{2.67}$$

This quantity can be used to estimate the relative change of the reflectance caused by the perturbation of g. At a particular phase angle, the larger the absolute value of this quantity is, the greater the change of reflectance will be if g is perturbed by the same small amount; if this quantity is zero, then it means that any perturbations of g will not affect the reflectance at all. Therefore, for any given parameter, it can be constrained better by the data at phase angles where the absolute value of the relative partial derivative of that parameter is larger than where it is smaller. Furthermore, for reflectance data at a particular phase angle, the parameters with larger relative partial derivatives can be constrained better than parameters with smaller relative partial derivatives. If the relative partial derivative of a parameter is zero at some phase angle, then it will not be constrained by any data at that phase angle at all.

Taking Eros as an example, we plot such partial derivatives with respect to all five parameters corresponding to its Hapke's parameters as found by Domingue et al. (2002), w=0.43, B_0=1.0, h=0.022, g=-0.29, and $\bar{\theta}$=36°, in Fig. 2.6. The properties of the relative partial derivatives can be summarized as follows. The SSA, w, can be determined by the reflectance data at all phase angles, but the four other parameters have their own significant ranges. The data at opposition are crucial in fitting the amplitude of the opposition effect, B_0, but are useless for the width parameter h, which is mostly determined by the data at about the width of the opposition, i.e., at $\alpha \approx h$. Because of the exponential-like decay of the opposition effect with phase angle, neither of the opposition parameters

makes significant contribution at phase angles greater than several times the width of the opposition effect. In contrast to the opposition effect parameters, the global roughness parameter $\bar{\theta}$ is affected primarily by the reflectance data at higher phase angles, but almost unaffected by data around opposition. The most interesting parameter is the asymmetry factor g, which has no effect at a particular phase angle in the middle, about 62° for the assumed parameters here, if it is perturbed by a small amount. Therefore, according to the above properties, we can design a data modeling scheme, in which the SSA, w, and roughness parameter, $\bar{\theta}$, can be fitted first with disk-resolved images at phase angle about 62°, then we can use data at higher and lower phase angle but not close to zero to fit g, and finally use data close to opposition to model opposition parameters. For other asteroids, their Hapke's parameter may be different, therefore the fitting scheme can be different, but the various significance of data at different phase angles in fitting different Hapke's parameters can be analyzed similarly, and the scheme can be designed.

It has been noticed that, for an observed disk-integrated phase function alone, it is usually not possible to find a unique set of Hapke's parameters to model it (Domingue and Hapke, 1989), especially when phase angles are limited within a small range. For example, high roughness usually simulates the effects as high back-scattering in the overall shape of a phase function. In Fig. 2.7, we see that very different parameter sets can give out observationally indistinguishable phase curves at some small phase angles. However, if disk-resolved photometry is available, then all Hapke's parameters can be constrained better.

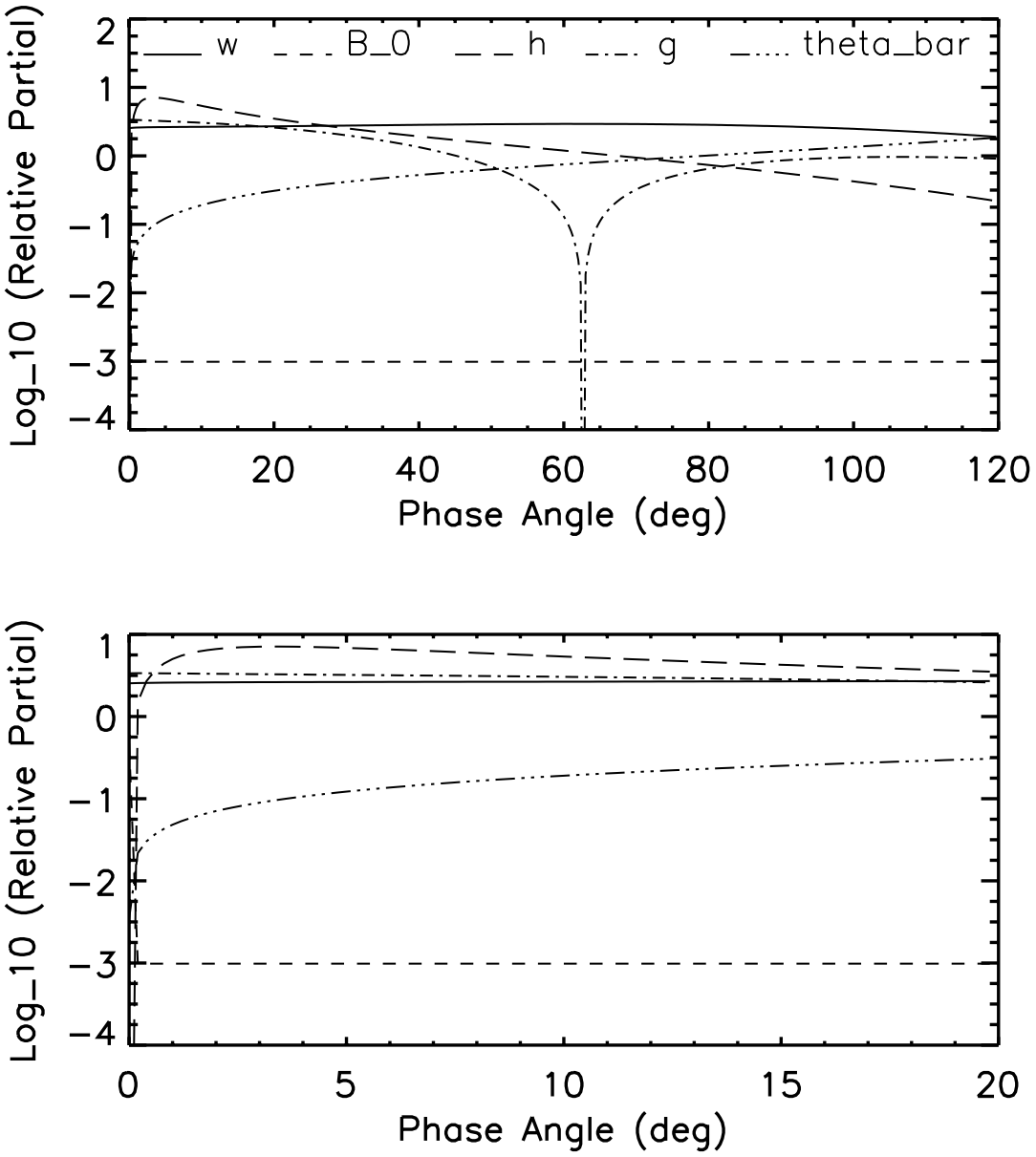

Figure 2.6 The relative partial derivatives as defined in Eq. 2.67 with respect to all five Hapke's parameters are plotted in upper panel. The lower panel is the close-up view of the upper panel at phase angles smaller than 20°, to show the effect of opposition parameters. The five Hapke's parameters are: w=0.43, B_0=1.00, h=0.022, g=-0.29, $\bar{\theta}$=36.

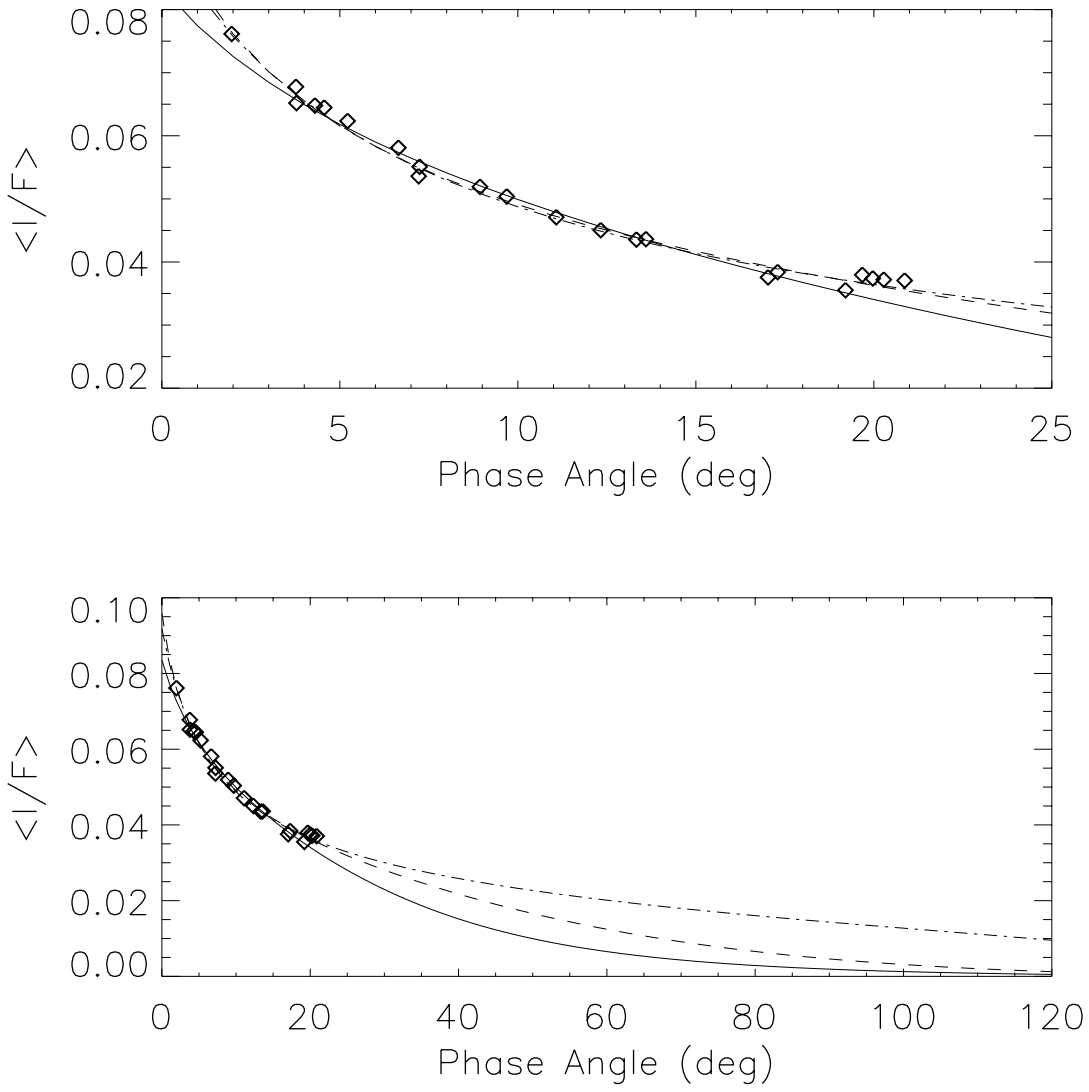

Figure 2.7 An example of the ambiguity of phase function modeling. Symbols are ground observations of average reflectance for asteroid 1 Ceres (Lagerkvist and Magnusson, 1995). Three very different sets of Hapke's parameters produce very similar phase functions within 20° phase angle, which is the highest phase angle reached from the ground for Ceres. All of the three sets of parameters fit data well. However, they are very different at large phase angles. The three sets of Hapke's parameters are listed in Table 2.2.

Table 2.2. The Hapke's parameters for the phase functions shown in Fig. 2.7. RMS stands for the root mean square error relative to the average of data.

Line	w	B_0	h	g	$\bar{\theta}$	RMS(%)
Solid	0.06	1.63	0.072	-0.42	18	1
Dashed	0.15	1.86	0.045	-0.18	40	0.7
Dash-dot	0.31	6.00	0.064	0.40	20	0.6

In disk-resolved photometry, the bidirectional reflectance can be measured directly from an image if the shape model of the object is available. The effects of various parameters can now be analyzed in a disk-resolved sense, where even at a particular phase angle, we have a variety of illumination and viewing geometries from the resolved disk if phase angle is not too small, and the shape of the object is not too simple. With reflectance data only within a small range of phase angle, the three phase parameters, B_0, h, and g cannot be modeled well in any case, as analyzed above, but the other two parameters, the SSA (w) and the roughness parameter ($\bar{\theta}$), can still be modeled because at any given phase angle, the disk limb darkening profile is solely and completely determined by the SSA and roughness parameter. Take a dark surface as an example, which is actually the simplest case, the multiple scattering term can be neglected, and the bidirectional reflectance is proportional to w and the term $S(i, e; \bar{\theta})\mu_{0e}(i, e; \bar{\theta})/(\mu_{0e}(i, e; \bar{\theta}) + \mu_e(i, e; \bar{\theta}))$. Therefore, the roughness parameter can be modeled from the limb darkening profile with fairly high accuracy. If the other three parameters are available or assumed, the SSA can be modeled as well. Thus with disk-resolved photometry available, we can eliminate the possible ambiguity between $\bar{\theta}$ and g in determining the overall shape of disk-integrated phase functions.

2.5.2 Least χ^2 Fitting

Throughout all of my thesis work in photometric analysis, both disk-integrated or disk-resolved, observational data are modeled using *least χ^2 fitting* data modeling technique, *i.e.*, models with all possible combinations of parameters within their ranges are tested by calculating the sums of the squares of the residuals between modeled values and data,

until the smallest sum is found for some combination of parameters, which is returned as the best modeled parameter set. The sum of the squares of residuals is the so called χ^2,

$$\chi^2 = \frac{1}{N}\sum_i \frac{(r_{i,model} - r_{i,measure})^2}{\sigma_i^2} \tag{2.68}$$

or if the error σ is not available,

$$\chi^2 = \frac{1}{N}\sum_i (r_{i,model} - r_{i,measure})^2 \tag{2.69}$$

where $r_{i,model}$ and $r_{i,measure}$ are the modeled and measured bidirectional reflectance for data point i, respectively, σ_i is the measurement error for data point i, and N is the total number of data points. The square root of χ^2 is taken as the *root mean square* or *RMS* error of the modeling (Eq. 2.69). The percentage RMS error relative to the average value of data is usually taken as an indicator of the goodness of the χ^2 fitting. One thing that has to be noted for the second definition of χ^2 (Eq. 2.69) is that, if the values of reflectance vary largely, then the χ^2 from this equation tends to be dominated by high reflectance, or bright areas on a surface. To avoid the bias, sometimes the relative χ^2 is used,

$$\chi^2 = \frac{1}{N}\sum_i \frac{(r_{i,model} - r_{i,measure})^2}{r_{i,measure}^2} = \frac{1}{N}\sum_i \left(\frac{r_{i,model}}{r_{i,measure}} - 1\right)^2 \tag{2.70}$$

Or, sometimes magnitudes, which is the logrithm of the reflectance, are used in modeling. In this dissertation, we only used the χ^2 defined in Eq. 2.69. But after modeling, the fit is checked for above bias by plotting modeled values as a function of measured values, and by plotting the ratios of model and observations as a function of all independent variables, to make sure that large systematic bias does not exist.

There are several computational methods to find the smallest χ^2 for data modeling. The two used in this dissertation are the *grid searching* and the *Levenberg-Marquardt*

(LM) method. The first one is very simple. All possible grid points in the parameter space are searched, the grid position with the smallest χ^2 wins, and the corresponding set of parameters is returned. With small steps for each parameter, the accuracy of this method increases, but the computational burden increases following a power low. The LM method is a gradient search method. It searches the steepest slope in parameter space, and follows the steepest slope until the minimum χ^2 is reached. This method is implemented in IDL by a library routine called `lmfit`, with the computational scheme following the one introduced in *Numerical Recipes in C* by Press et al. (1992).

It is shown in my work that for bright surfaces such as that of Eros, both of those two methods work well. But for dark surfaces such as that of Borrelly, the LM method seems not working as well as for bright surfaces. Therefore for Borrelly and Ceres, we actually used direct grid searching to find the best-fitted parameter set.

Chapter 3

Whole-Disk Phase Functions of Irregularly-Shaped Bodies

3.1 From Bidirectional Reflectance to Disk-Integrated Phase Function

It was not until less than a half century ago that human beings started to send spacecraft to explore the solar system. Spacecraft data of small bodies have been available for no more than two decades. Before that, the photometric properties of small bodies were studied only from the ground with whole-disk phase functions. A theoretical solution or approximation to the radiative transfer equation for a surface yields the bidirectional reflectance. To model ground-based observations, bidirectional reflectance needs to be integrated over the disk of an object. In this step, the shape and possible non-uniformity of photometric properties over the surface come into effect. It was back in the early 1900s that people realized that the change in total brightness of an asteroid is possibly due to its reflectance variation and/or non-spherical shape (Russell, 1906), and some methods were proposed to infer some properties of shapes and orbital geometries of asteroids. In recent years, lightcurve observations at various geometries have become an important way to infer the shapes of source bodies (see, *e.g.*, Kaasalainen and Torppa, 2001; Kaasalainen et al., 2001, *etc*). However, not until recently when more and more asteroids and comets were visited by spacecraft, did people realize the large diversity of the shapes of small bodies (Fig. 3.1).

In addition to the lightcurves, how to take into account the irregular shape of an

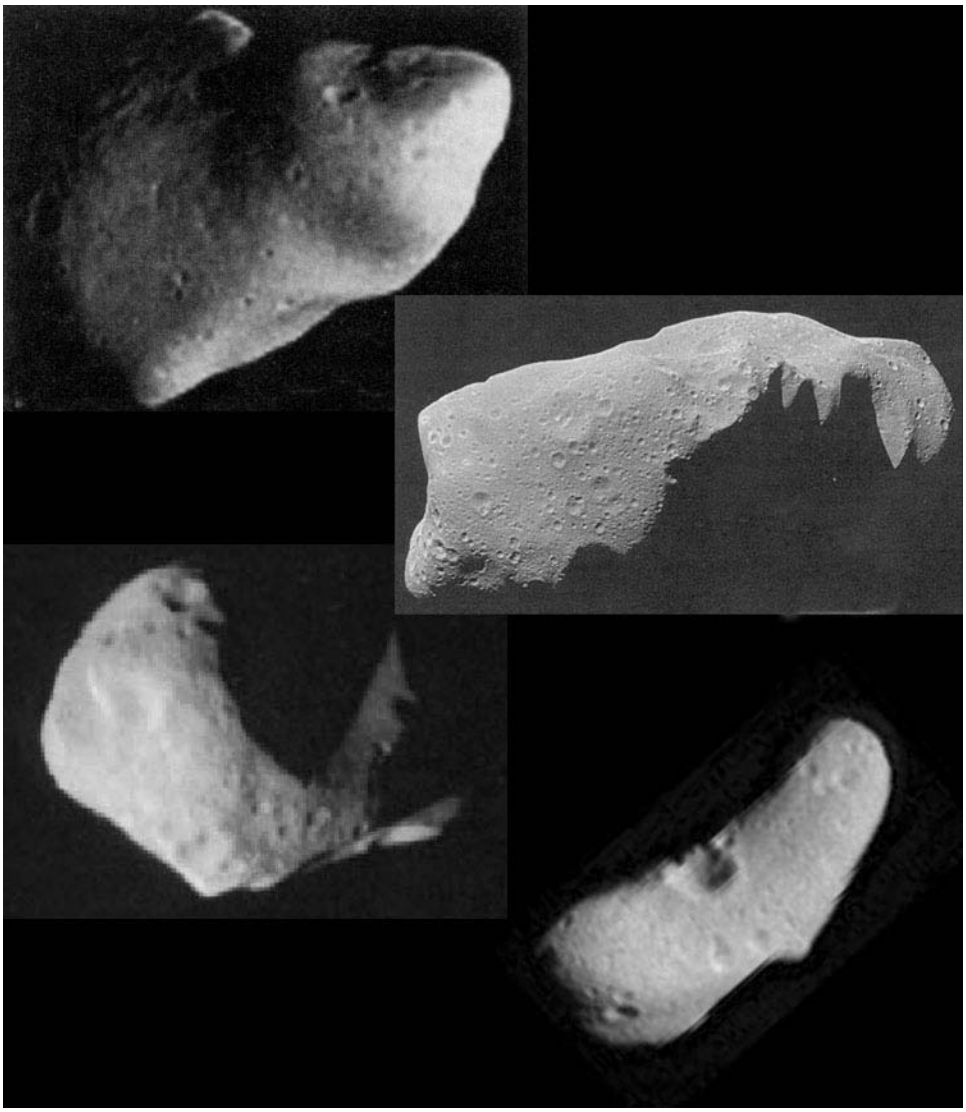

Figure 3.1 The images of asteroids 951 Gaspra (Belton et al., 1992), 243 Ida (Belton et al., 1994), 253 Mathilde (Veverka et al., 1999), and 433 Eros (our work) (from top to bottom).

object is also a problem in photometric modeling to whole-disk phase functions. To construct a phase function from lightcurves obtained at various phase angles, usually the average brightness of each lightcurve is calculated to represent the average brightness of the object at that phase angle. But as shown later, the amplitudes of lightcurves usually change with viewing geometry, and even at a constant phase angle, the average is not necessarily a constant, but rather depends on shape. To model the ground-based phase function, if a shape is needed, a sphere is usually assumed for the unknown shape of the object because of its simplicity in analytical analysis. But obviously in some cases this assumption could cause a very large error, because the shape of an asteroid can be far from a sphere, possibly very irregular with large craters or depressions with their sizes comparable with the size of the body. For example, as shown in Fig. 3.1, the shape of Eros is like a bent rod, with two large craters with sizes about 1/4 of the size of Eros; Mathilde has a very large depression that is almost 4/5 of its size. Many other shapes have been detected for asteroids, including very elongated shapes, and even contact binaries.

In this chapter, the effect of some irregular shapes of asteroids is studied with numerical simulations. Assuming particular photometric properties for a surface, as well as a particular non-spherical shape, we used Hapke's theory to calculate the bidirectional reflectance for the spatially resolved surface, then numerically integrate bidirectional reflectance over the whole visible and illuminated surface under various geometries to simulate lightcurves of this body. Taking those lightcurves as our "data", we constructed disk-integrated phase functions by the methods commonly used in research. Finally, the simulated phase functions were modeled, with Hapke's disk-integrated phase function for spherical shape (Eq. 2.61-2.66). The modeled Hapke's parameters can be compared to

the “original” or “true” Hapke’s parameters we assumed, from which we can investigate and evaluate the goodness of the method we used in constructing phase functions, and the uncertainties of modeled parameters caused by the assumption of a spherical shape for that particular non-spherical shapes. In the following section, the effect of a non-spherical shape on the lightcurve and disk-integrated phase function is first conceptually analyzed, as well as the conjuncted effect with illumination and viewing geometry. In the next section an ellipsoidal shape is assumed to study this most common approximation of asteroid shape in terms of photometric parameter retrieval. Then Eros’s shape is taken as a real case of very irregular shapes to study the impact on photometric modeling. The simulative studies for Eros also have an application in the next chapter to photometrically modeling Eros with NEAR data.

3.2 Effects of Shapes

3.2.1 Shape and lightcurve

The most direct consequence of non-spherical shape is a rotational lightcurve. A spherical object will not change its illuminated and visible cross-section when rotating, thus producing no lightcurve unless there are some photometric variations over the surface. Except for some special cases such as Iapetus (Squyres and Sagan, 1983, *etc*), it has been generally thought that non-spherical shape is usually more important for determining lightcurve shape than are photometric variations, especially at large phase angles when shadows dominate the total brightness of an asteroid (Kaasalainen and Torppa, 2001). Therefore rotational lightcurves are important tools for inferring the characteristics of its

source body shape.

Since the early days of lightcurve studies, it has been believed that the polar orientation can be determined from lightcurve observations at various phase angles (Russell, 1906), but it was also thought that determining the shape of an asteroid from its lightcurves is not possible. Lightcurve inversion, namely determining the shape from the lightcurves it produces, was studied first in both laboratory and numerical simulations (*e.g.* Barucci and Fulchignoni, 1983; Barucci et al., 1989), where models of asteroids with various shapes, compositions, and surface photometric properties were used to simulate lightcurves under different geometries. The lightcurve inversion to a 2-D shape was discussed by Ostro and Connelly (1984), and the opposition lightcurves in terms of asteroidal shape were subsequently discussed (Ostro and Connelly, 1986). Following the pioneering work of Russell in 1906, Wild (1989, 1991) developed a formalism to infer the surface albedo distribution from lightcurves observed at different phase angles and aspect angles, which is the angle between the direction of the rotational angular velocity and the direction of the Sun. A detailed consideration and method to find the 3-D shapes and albedo variations of asteroids from lightcurves has been discussed by Kaasalainen et al. (1992a) for strictly convex shapes, and its application was discussed and tested in a following paper (Kaasalainen et al., 1992b). This method was then optimized to determine the 3-D convex hull for arbitrary shapes (Kaasalainen and Torppa, 2001), as well as the rotational period, pole orientation, and scattering properties simultaneously from lightcurves observed at various aspects and phase angles (Kaasalainen et al., 2001). The inversion problem for highly non-convex and binary asteroids is also under investigation currently (*e.g.* Ďurech and Kaasalainen, 2003). Although radar observation has been

a very effective way of determining the shape of small bodies in the solar system (Ostro, 2003), due to the $1/r^4$ radar power dependence on the distance of target from the Earth, and inherent constraint to 0° phase, lightcurve inversion is still an important tool to studying the shapes of solar system bodies.

For our study of the effect of irregular shapes on phase functions, we want to understand how lightcurves change with respect to aspect angle and phase angle, so that we can construct phase functions in a better way to reduce the uncertainty in photometric modeling. We do not have to consider the lightcurve inversion problem; rather we are considering what kind of lightcurves are produced by a particular non-spherical shape under various aspects and phase angles.

To answer the question of how aspect angle affects the lightcurves of an irregularly shaped body, first, let us take a triaxial ellipsoid (with three axes $a > b > c$) as the shape model, and assume a uniform surface so that the lightcurve will be mainly determined by the projected cross-section of illuminated and visible surface. Another necessary assumption is the polar orientation, which is taken as aligned with the shortest axis c so that the rotational axis is along the direction of the largest angular momentum, corresponding to a stable rotational state. Although some comets are observed in excited rotational states (*e.g.* comet Halley), almost all asteroids are found to have relaxed to the short-axis rotational mode. The lightcurves produced by an ellipsoid with $a : b : c$=2.7:1.4:1, the axial ratio of the best fit ellipsoid for Eros, are shown in Fig. 3.2 for phase angles α=0°, 30°, and 60°, and the polar axis is assumed perpendicular to both the direction to the Sun and the direction to the observer. They basically have a doubly-peaked sinusoidal shape, with each peak occurring roughly when the maximum cross-section is seen, if the phase

angle is small. The lightcurve amplitude represents the approximate projected axial ratio (2.7/1.4=1.9≈0.7 mag at 0° phase angle in this case), and depending on phase angle.

Another very useful plot in understanding the change of lightcurves with respect to aspect angle is shown in Fig. 3.3, where lightcurve maxima and minima are plotted as functions of aspect angle for a triaxial ellipsoid with $a : b : c$=2.7:1.4:1, and viewed at 0° phase angle. At 0° (and 180°) aspect angle, when the object is viewed pole-on, there is not any cross-sectionalal change during rotation, and a zero lightcurve amplitude is found. The projected cross-section in this case is πab, the largest possible projected cross-section for this shape, thus the brightness at these two aspect angles are higher than at any other aspect angle. At 90° aspect angle, when the object is viewed equator-on, the projected cross-sectional change is the largest, yielding the largest lightcurve amplitude. But since the projected cross-section varies from πac to πbc in this case, the maximum brightness of the lightcurve then reaches its minimum. What this plot tells us about lightcurves is that, even at one phase angle, the maximum, mean, and minimum of one lightcurve do not necessarily represent the true maximum, mean, and minimum of the brightness of the object at that phase angle. This problem becomes more severe and complicated when phase angle is large so that the illuminated and visible area diverges more from the projected cross-section. A question to ask is, for such an ellipsoidal shape model, what is its average cross-section of many random shots from any aspects and phase angles. A calculation done by Weissman and Lowry (2003) for biaxial ellipsoids with axes $a > b$ shows that the average is close to a large fraction k of the maximum cross-section πab, were k=0.924 for a/b=1.5, 0.892 for a/b=2, and 0.866 for a/b=3.

Lightcurves for arbitrary shapes will be much more complicated. Their main prop-

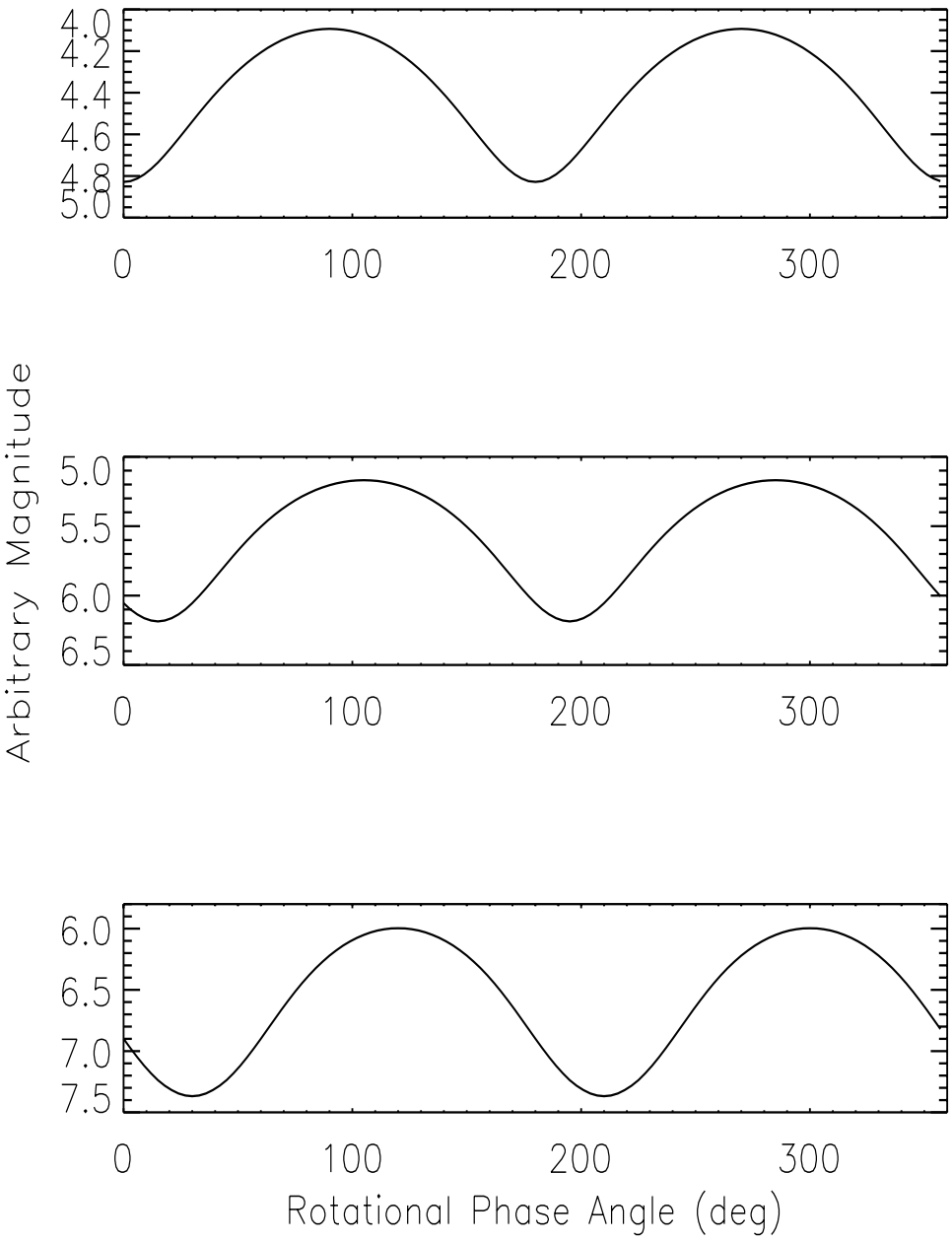

Figure 3.2 Examples of doubly-peaked lightcurves. They are produced by a triaxial ellipsoid with uniform surface, and axial ratios of the best fit ellipsoid for Eros. The photometric parameters of the surface are assumed to be those of Eros as published by Domingue et al. (2002) (Table 3.1). Object is illuminated and viewed equator-on. Phase angles, α, are 0°, 30°, and 60°, for upper, middle, and lower panel, respectively.

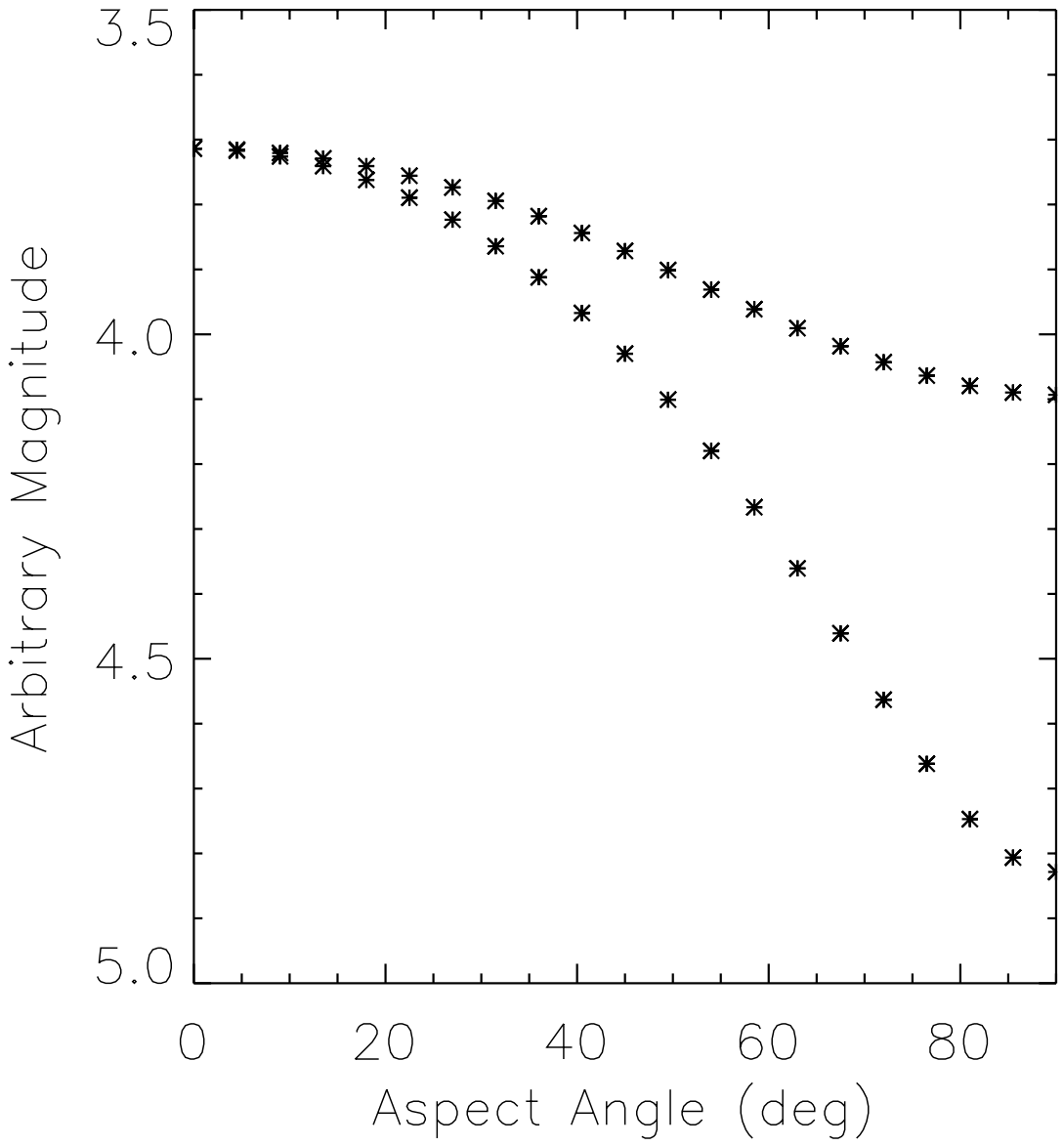

Figure 3.3 Plot of lightcurve maxima and minima as functions of aspect angle. The shape model is taken to be the best fit ellipsoid of Eros, and the photometric parameters are listed in Table 3.1. Solar phase angle is 0°.

erties such as the correlation between lightcurve amplitude and projected axial ratio, the amplitude variations with respect to aspect angle, *etc.*, are still very similar to those discussed above for ellipsoidal shapes. But with divergence from an ellipsoidal shape, and possibly large shadows formed by large concavities, the lightcurves may no longer be sinusoidal, with asymmetric shapes or even a single peak, and small scale oscillations. An example of such a lightcurve is shown in Fig. 3.4, calculated with Eros's real shape (Fig. 3.1), Hapke's parameters as assumed before, and illuminated and viewed in equatorial plane. Therefore real shapes have to be considered case by case, and we are not going to draw any further general conclusions here.

3.2.2 Construction of disk-integrated phase function

Because of the non-zero lightcurve amplitude for any non-spherical shapes, and the complicated behavior with respect to aspect and phase angles, the construction of a phase function is not as simple as for a sphere. For example, if lightcurves of an ellipsoid under all possible aspect angles are plotted with respect to phase angle, as shown in Fig. 3.5, at any given phase angle, we have to find a way to calculate an "average" or "effective" brightness, so that a definitive phase function can be constructed. The first idea that most people come up with would be to take the means of lightcurves at various phase angles. However, as shown in Fig. 3.3, different lightcurve magnitudes and amplitudes will appear even at one phase angle if they are observed at different aspects. There will not be a single method that is good for all cases, and different methods are used by different people. For example, lightcurve means over each rotational period were used to represent the average reflectance of the disk, either over time (*e.g.* Helfenstein et al., 1996), or

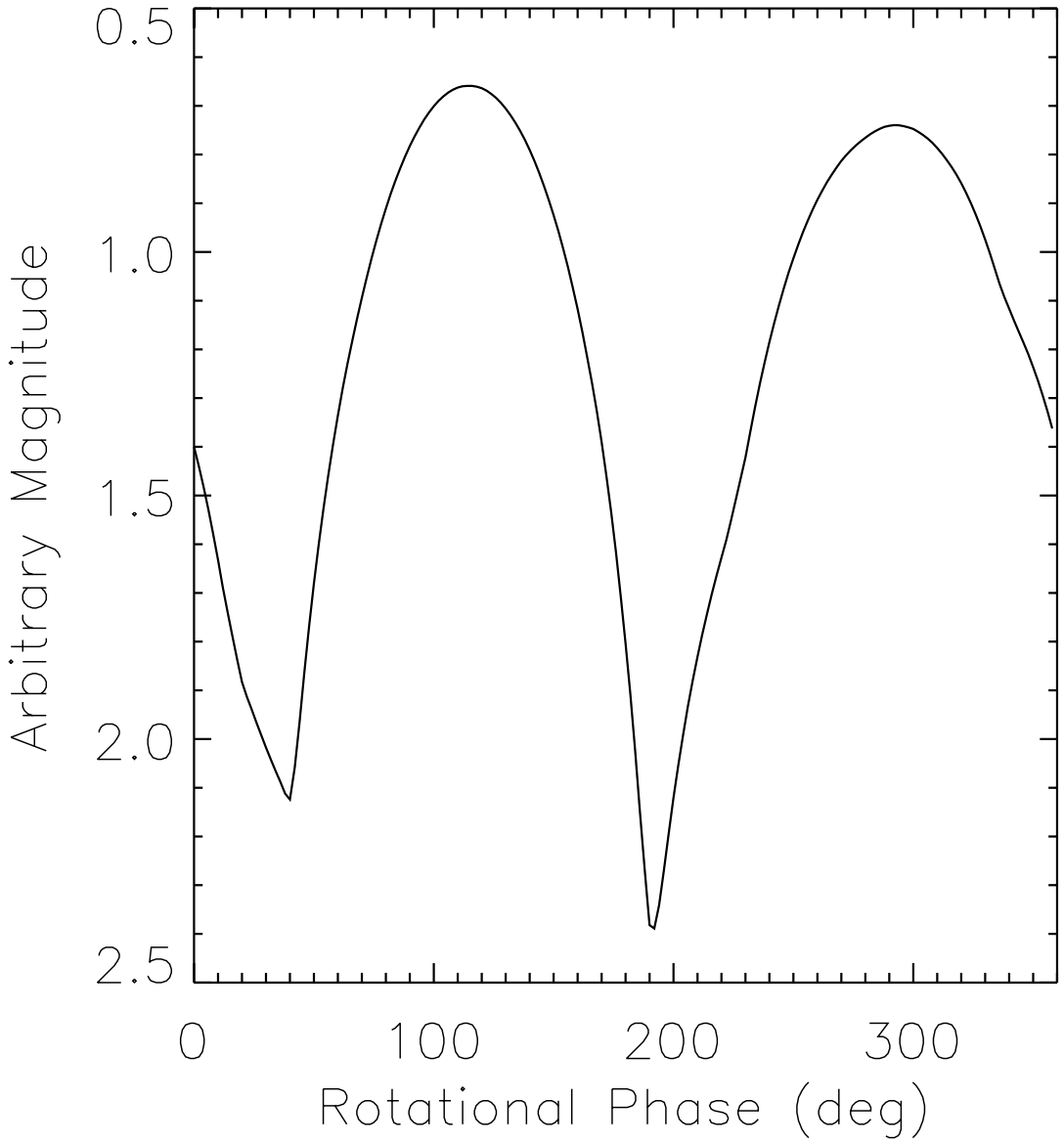

Figure 3.4 A lightcurve produced by Eros's shape, with the same photometric parameters as assumed for Fig. 3.2, and illuminated and viewed within its equatorial plane.

over the cross-sections (Domingue et al., 2002) if shape is available. Lightcurve maxima and minima were also used sometimes to construct a phase function to compare the fitted photometric parameters with those from lightcurve means (Helfenstein et al., 1994).

In our numerical simulations, we are able to produce lightcurves under all possible aspects at any phase angle, and the phase function constructed by all three methods stated above are studied. But one difference between numerical simulations and real observations has to be kept in mind, namely that in real observations it is not possible to obtain lightcurves at all possible aspects for any single phase angle. Therefore the results presented in this chapter are not necessarily accurate for all real observations. The numerical simulations rather show a method to help modeling real observations photometrically. We can take the real shape, or an approximated shape to the best knowledge we have, and put it into the geometries of observations, then insert modeled photometric parameters to see if observed lightcurves are best modeled with them, or what the discrepancy is and how to improve parameters. In this sense, we call our numerical simulation a *forward modeling* method.

3.3 Numerical Simulations with Ellipsoidal Shape

In this section, the phase functions of ellipsoidal shapes constructed using the three methods described in the last section will be compared with the phase function produced by a spherical shape with the radius equal to the effective radius of the ellipsoids, and with the same photometric parameters.

Three phase functions constructed from the maxima, means, and minima of the

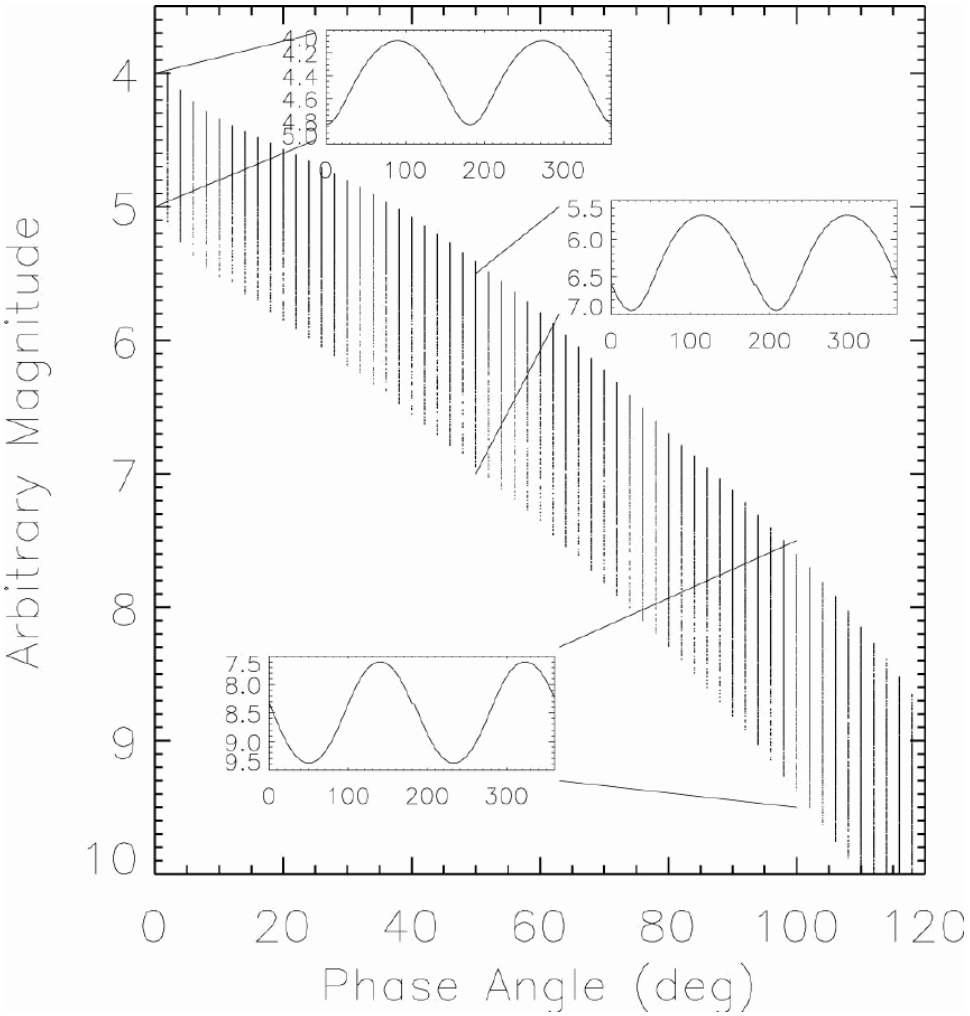

Figure 3.5 Lightcurves of an ellipsoid at all possible aspect angles are plotted with respect to phase angle. Three insets show the lightcurves at phases 0°, 50°, and 100°, respectively, all illuminated and viewed in the equatorial plane, At each phase angle, the brightness of the object varies, therefore a definitive phase function has to be constructed with some method.

lightcurves of an ellipsoid are shown in Fig. 3.6, assuming Eros's published photometric parameters as deduced by Domingue et al. (2002) (also listed in Table 3.1). A phase function produced by a sphere with the same set of photometric parameters is also plotted. As one can see in Fig. 3.6, if the body is ellipsoidal, then the broadening of the phase function by a non-zero lightcurve amplitude is almost the same at all phase angles from zero to at least 150°. In other words, the three lightcurves have very similar shapes, leading to nearly parallel phase curves. This means that a phase function constructed from lightcurve means can effectively "smooth" out the effect of a non-spherical body on the phase function, and acts as a reasonably good approximation to an average phase function to be modeled.

A best-fit of Hapke's parameters was carried out using χ^2 minimization for the curves of both lightcurve maxima and means (Fig. 3.7), and the modeled parameters are listed in Table 3.1. Although the phase functions, from both lightcurve maxima and lightcurve means, have shapes very similar to the phase function from a spherical shape with the same set of photometric parameters, the modeling is still unable to recover the original parameters accurately, although the starting parameters are within the error bars of the fit. The modeled geometric albedo is recovered very well because it is tied down by the brightness at very small phase angle. The SSA, w, and asymmetry factor, g, seem to be anti-correlated, with underestimated w and overestimated backscattering g yielding a correct geometric albedo. The amplitude parameter of the opposition effect is a little bit underestimated, maybe because the averages of lightcurves under different aspect angles at small phase angles smooth out the opposition surge a little bit. The width parameter of the opposition surge is the least constrained because it is usually the hardest parameter to

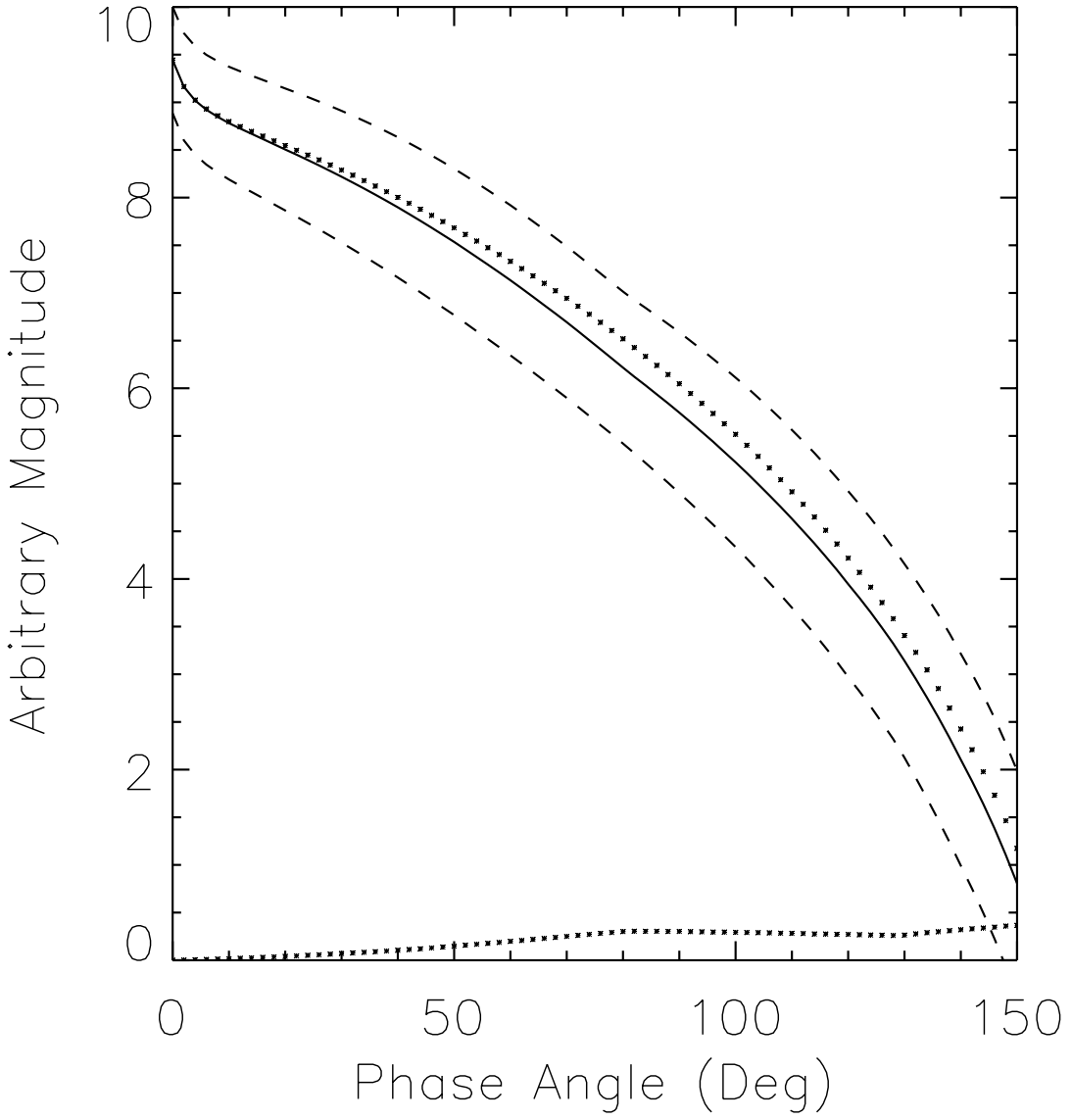

Figure 3.6 The three phase functions constructed from lightcurve maxima, minima (two dashed lines), and means (solid line), in an arbitrary magnitude scale. The dotted line almost aligned with lightcurve mean phase function is the phase function produced by a uniform sphere with same photometric parameter set. The dotted line at bottom illustrates the difference between the lightcurve mean phase function and the phase function from a sphere.

Table 3.1. Fit the midpoint phase function and upper limit phase function, constructed from the theoretical brightnesses of a triaxial ellipsoidal body with the published Eros's photometric parameters. The axial ratios of the shape model are 2.731:1.408:1.

	w	B_0	h	g	$\bar{\theta}$	A_p
"Original"[a]	0.43	1.00	0.022	-0.27	36	0.29
Midpoint	0.36	0.89	0.017	-0.36	34	0.30
Upper limit	0.40	0.73	0.011	-0.35	29	0.30

[a]Domingue et al. (2002)

be modeled due to the small range of data that are sensitive to this parameter. The roughness parameter is recovered well. Thus we conclude that caution has to be used when constructing a phase function from ground-based lightcurves. Although an ellipsoidal shape can be approximated relatively well by a spherical shape in terms of photometric modeling, the modeled parameters could still be substantially different from the true ones and require large error bars. With more diverse shapes of the small bodies in the solar system in reality, one may have to deal with solutions on a case by case basis even though their shapes may be relatively regular.

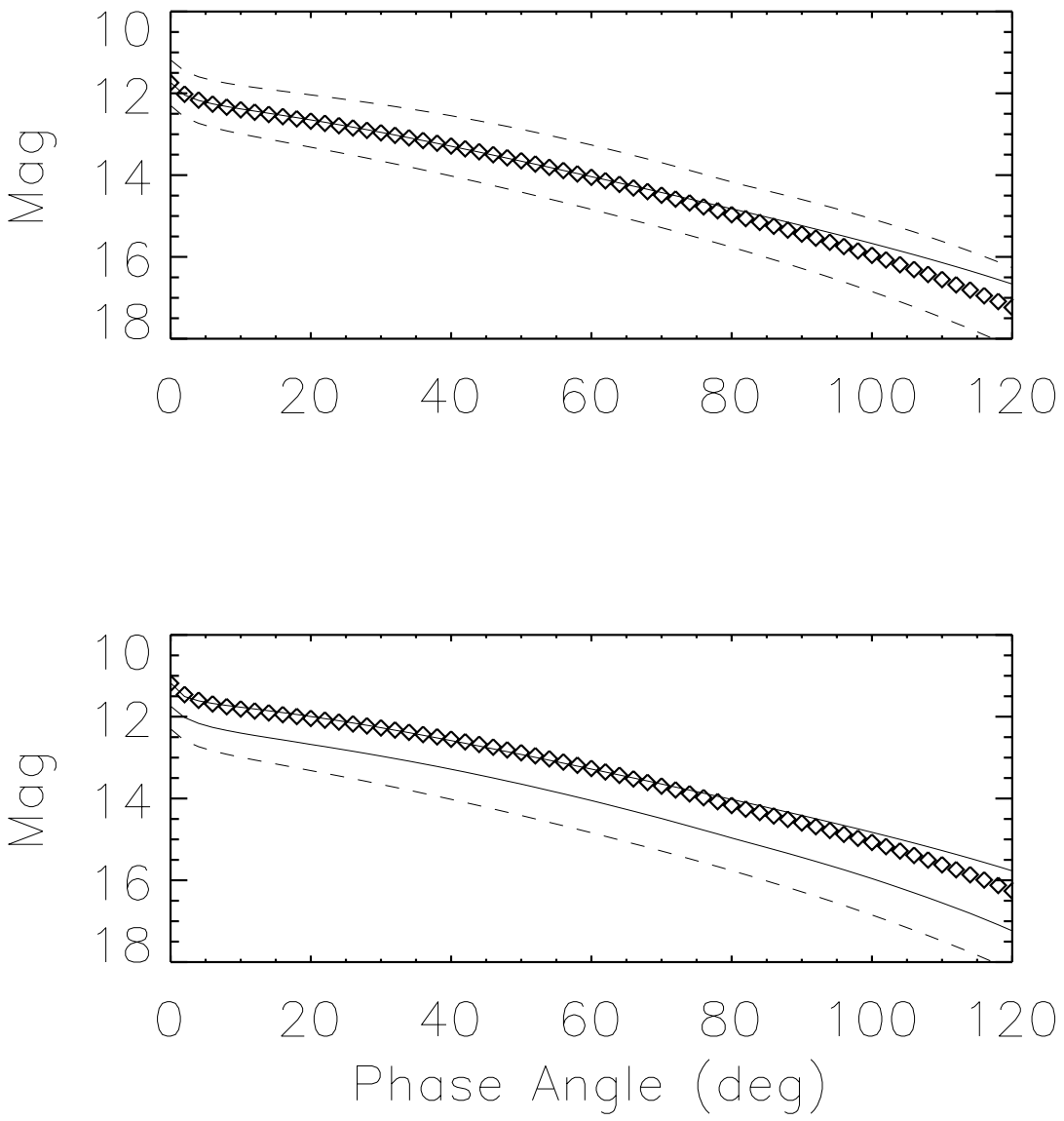

Figure 3.7 Hapke's modeling for lightcurve mean phase function (upper panel) and lightcurve maximum phase function (lower panel). Symbols show the phase function to be modeled, and solid lines show the models. Solid and dashed lines show theoretical phase functions constructed from numerically calculated lightcurves.

3.4 Numerical Simulations with Eros's Shape

As the second part of these simulative studies, the question we wanted to answer was: For a specific irregular shape, is it possible to recover the photometric parameters by fitting the phase functions constructed from the maxima, the means, and/or the minima of disk-integrated lightcurves by assuming a spherical shape? And if the answer is positive, how to do it? Or if the answer is negative, quantitatively how far from the fitted parameters are the correct ones? To answer these questions, we took Eros's real shape in simulations. Eros is the only solar system small body with its shape precisely determined. We hoped to demonstrate that our forward modeling procedure would be an effective way to study the effect of its irregular shape on photometric modeling, and our results regarding Eros can give us some hints for other small bodies with irregular but very different shapes. Another important aspect of this study is that, since the photometric properties of Eros will be analyzed with disk-resolved images obtained by the NEAR Shoemaker spacecraft in the next chapter, the forward modeling actually provides a way to correct the results of disk-integrated photometric modeling, and to compare them with those of disk-resolved modeling.

To do simulations, the published photometric parameters of Eros at 550 nm from Domingue et al. (2002) were used (Table 3.2), as well as its 10,152-triangular-plate shape model (Thomas et al., 2002; Carcich, 2001). According to Hapke's reflectance theory (Hapke, 1993), the local bidirectional reflectance in small area elements on the surface can be calculated if the shape is known so that the illumination and viewing geometry is specified. The theoretical disk-integrated lightcurves can then be obtained by integrating

over the visible and illuminated surface as the body rotates. We calculated the theoretical lightcurves under all possible illumination and viewing geometries of Eros by rotating the body-fixed pole orientation with respect to the scattering plane to all possible directions. In Fig. 3.8, the lightcurve mean phase function is compared with the phase function from a spherical shape and the same photometric parameters. Unlike the case of ellipsoidal shapes, here the lightcurve amplitude increases dramatically with phase, due to large shadows, and the deviation between the lightcurve-mean phase function and the phase function from a spherical body increases dramatically with phase starting at about 80°.

These theoretical phase functions were next fit with the formalism of a disk-integrated phase function for a sphere (Eq. 2.61-2.66) for phases less than 60° because ground-based observations of Eros can only cover this range of phase angles. Since the shape of Eros is relatively close to a biaxial ellipsoid, at any illumination and viewing geometry corresponding to the lightcurve maxima, its cross-sections with respect to the Sun are almost the same (Fig. 3.3). Therefore the lightcurve maxima define a fairly smooth phase function as shown in Fig. 4.1 in the next chapter. Since the lightcurve can vary greatly with polar orientation with respect to the observer, even at a constant phase angle, the lightcurve minima are very scattered. Therefore, we only focus on the theoretical phase function constructed from the lightcurve maxima, as well as the lightcurve means that we calculated (Fig. 3.9).

The results from fitting the theoretical phase functions are listed in Table 3.2, as well as the "original" parameters. Neither of the theoretical phase functions constructed from the lightcurve maxima or lightcurve means resulted in a correct recovery of all the originally assumed photometric parameters. On the other hand, they provide some clues

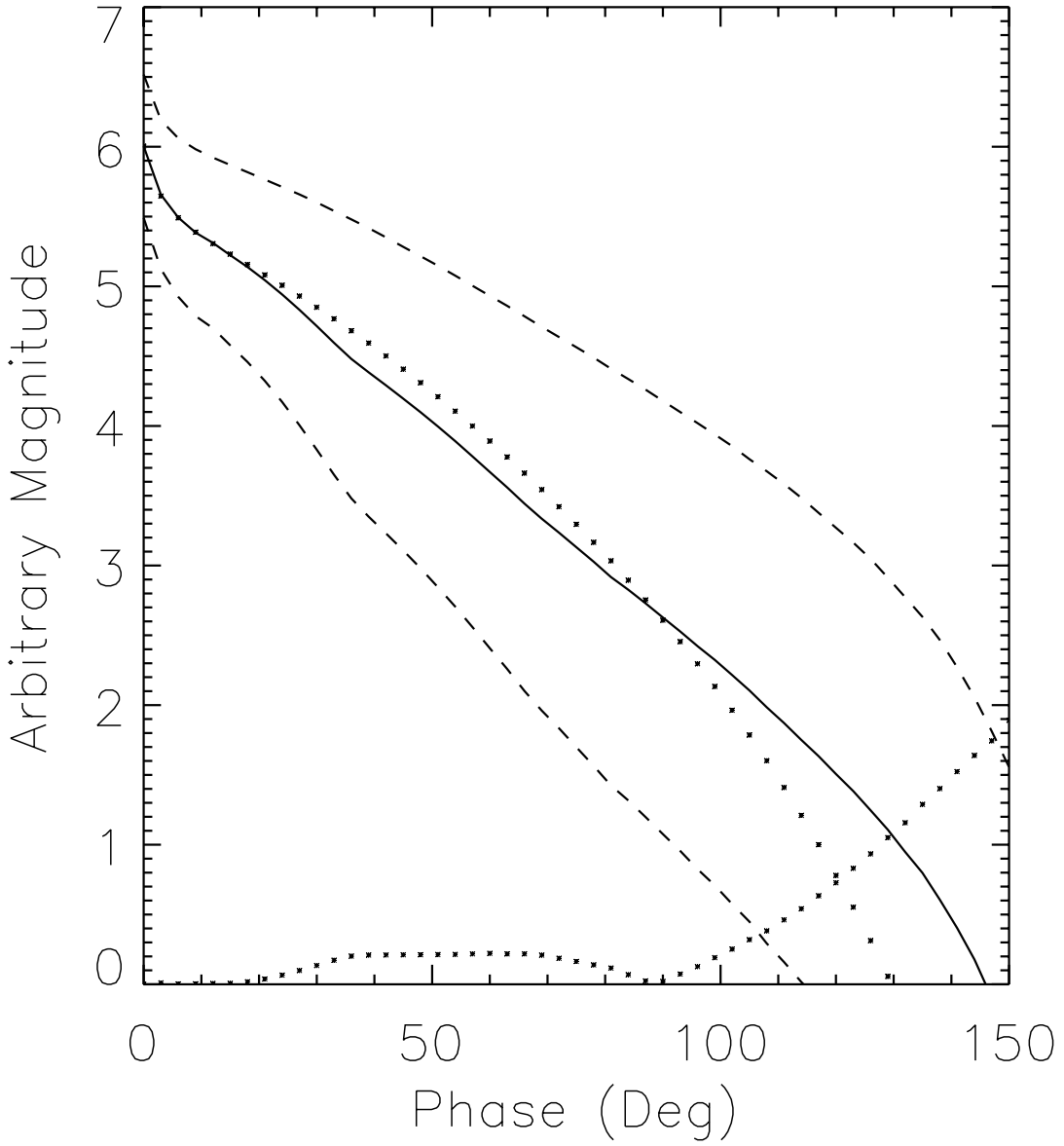

Figure 3.8 The phase function constructed from lightcurve means (solid line) is compared with the phase function produced by a sphere with same photometric parameters (upper dotted line). Deviation (bottom dotted line) starts increasing dramatically at about 80° phase angle.

Table 3.2. The results of fitting the theoretical phase functions constructed from the lightcurve maxima and lightcurve means calculated from Eros's shape model (Thomas et al., 2002) and the published Hapke's parameters at 550 nm (Domingue et al., 2002) (marked in the table as "original parameters"). The last row lists the Hapke's parameters fitted to the lightcurve maxima from ground-based observations of Eros (Fig. 4.2, see next chapter).

	w	B_0	h	g	$\bar{\theta}$	A_{geo}
"Original" parameters[a]	0.43	1.00	0.022	-0.29	36	0.29
Theoretical lightcurve maxima	0.63	0.98	0.020	-0.14	38	0.29
Theoretical lightcurve means	0.48	1.29	0.031	-0.25	23	0.33
Observed lightcurve maxima	0.59	1.42	0.010	-0.20	42	0.37

[a]Domingue et al. (2002)

to how wrong the fitted parameters are and how to estimate the correct values from the fitted ones.

Comparing the results from lightcurve means, we find that the SSA w is fitted slightly larger than the correct value by about 15%. For the asymmetry factor g, the fitted result is slightly less backscattering than its true value by about the same amount as the SSA was overestimated. Both the amplitude, B_0, and the width, h, of the opposition effect tend to be overestimated by about 30%, and the global roughness parameter

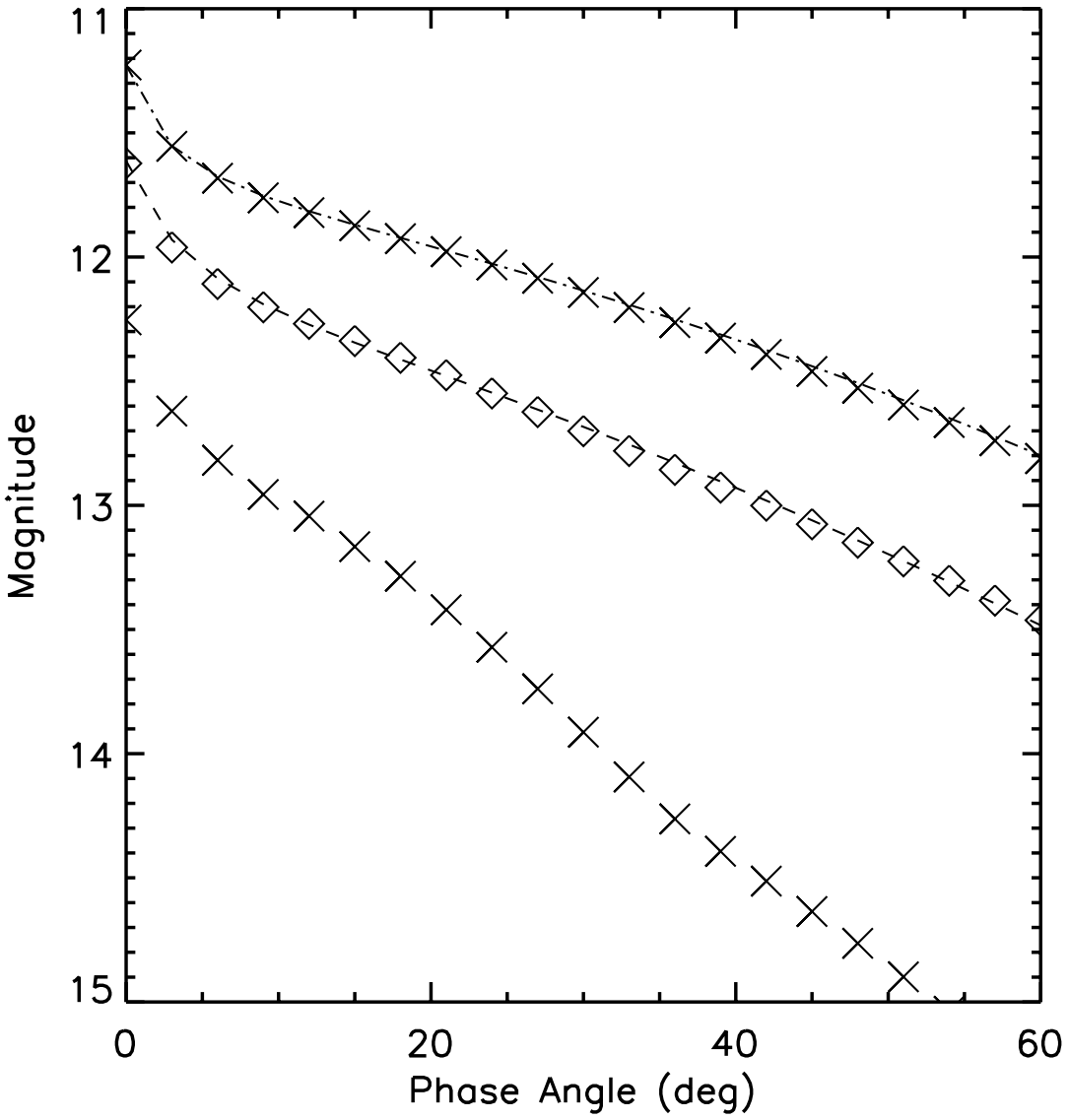

Figure 3.9 The Hapke's modeling of the theoretical phase functions from lightcurve means and maxima. Symbols show the theoretical phase functions, and dashed line and dash-dot line show the fits to the two phase functions. Their modeled parameters are listed in Table 3.2.

$\bar{\theta}$ is estimated incorrectly as well. However, for the lightcurve maxima, it is surprising that the opposition effect is preserved very well, with the fitted amplitude B_0 and width h less than 3% and 10% away from the correct values, respectively. The global roughness parameter $\bar{\theta}$ could be recovered from the lightcurve maxima as well. The SSA and g cannot be recovered as well from the maxima of the lightcurves, with more than 50% off from the correct values. For Eros's disk-integrated photometric data, because it is impossible to construct a smooth phase function from lightcurve means, we have to rely on the lightcurve maxima. Therefore, as indicated by the results from our simulations, when analyzing the phase function constructed from the lightcurve maxima, accurate opposition parameters are expected, but the SSA will be overestimated by more than 50%. This conclusion is only for the shape of Eros, or other asteroids with similar shapes and Hapke's parameters. As mentioned earlier, usually similar analysis has to be carried out for different asteroids case by case.

3.5 Summary and Discussions

Our simulations indicate that shape is very important in determining the disk-integrated photometric characteristics as are physical properties. When studying the photometric properties of small bodies from ground-based unresolved data, the effect of shape has to be carefully estimated, evaluated, and removed as much as possible. Our simulations show that if the shape of an object is close to an ellipsoid, then the phase function constructed from lightcurve means is closely approximated by a disk-integrated Hapke's phase function assuming a spherical shape. However, if the shape is very irregular like

that of Eros, then the means of the lightcurves can be approximated by a spherical model only at small phases. For the case of Eros, when phase is larger than about 80°, the deviation is large and a good recovery of Hapke's parameters is difficult. Photometric modeling of the theoretical phase functions constructed from lightcurve means and maxima with Eros's real shape model provides some indications for modeling the real phase function of Eros from observations, and will be used in the next chapter.

The effect of shapes of small bodies on their lightcurves and phase functions is a broad topic. As lightcurve inversion techniques are still being developed and improved, it usually requires a large amount of data to fully reconstruct the shape. The effect of non-spherical shape on phase function has been touched even less because of the large diversity of shapes of the small bodies in the solar system. More simulations with more different shape parameters should be done in the future to cover more parameter space. Statistical method is probably an effective way to theoretically study this topic. Some attempts have been made, such as Muinonen (1998), who proposed to describe any shape by random Gaussian shapes, and applied this representation to lightcurve inversion (Muinonen and Lagerros, 1998). However, before any general conclusions are drawn, in the real case of solar system small bodies, the best way to deal with this problem is probably the forward modeling procedure in comparison with observed lightcurves and phase functions, and may be coupled with iterations in photometric modeling for a better recovery of photometric parameters from the disk-integrated phase function.

Chapter 4

Asteroid 433 Eros

4.1 Background

Asteroid (433) Eros is a near-Earth asteroid in an orbit with semi-major axis 1.46 AU, and eccentricity 0.22. The spectrum of Eros shows the typical absorption features for S-type asteroids (Tholen, 1984), including the diagnostic 1 μm and 2 μm bands for pyroxene and the 1μm band for olivine. The size of Eros is close to a biaxial ellipsoid, with two axes about 33 km and 13 km across.

The Near Earth Asteroid Rendezvous (NEAR) is the first NASA Discovery Program mission launched in February 1996. It flew past a C-type asteroid (253) Mathilde, and then was successful in rendezvous with and orbiting of the asteroid Eros for one year, starting in February 2000. NEAR produced the largest-to-date dataset of spatially resolved images and spectra for an asteroid in its year-long orbiting of Eros. The multi-spectral imager (MSI) onboard NEAR spacecraft acquired images at seven wavelengths from 450 nm to 1050 nm, covering the whole surface of Eros with resolution up to several meters per pixel at phase angles between 50° and 110°. The near-infrared spectrometer (NIS) obtained spectra of the whole surface of Eros at phase angles from near opposition to about 120°. The high resolution shape model of Eros was constructed from these data (Thomas et al., 2002). The photometric properties of Eros in the near-infrared through 2.2 μm have been studied by Clark et al. (2002) using the NIS data. Domingue et al.

(2002) have used the MSI images at 550 nm, together with the earlier ground-based observations at V-band, to study the photometric properties of Eros at 550 nm wavelength. The composition of surface materials of Eros has been examined from its spectrum and color and their temperature dependence (McFadden et al., 2001; Bell et al., 2002; Murchie et al., 2002a; Lucey et al., 2002; Izenberg et al., 2003).

However, we noticed that previous approaches to studying the photometric properties of Eros at visible wavelengths were actually in a disk-integrated sense, *i.e.*, the MSI images containing the whole disk of Eros were used in constructing the disk-integrated phase function, and the shape model was coupled with the rotational model of Eros to compute the cross-sections to guarantee the accuracy of the disk-averaged reflectance as a function of phase angle. To improve the photometric models of Eros at visible wavelength, and to take full advantage of the disk-resolved images, we analyzed all available data of Eros, including all MSI images taken at seven wavelengths and at comparable resolutions, and all earlier ground-based observations at V-band. The theoretical simulations of the disk-integrated phase function analysis with Eros's shape model is studied in Chapter 3. Some important results are to be used in the following analysis. This part of my work, as well as part of the work in the last chapter, have been published (Li et al., 2004).

4.2 Ground-Based Phase Function

4.2.1 Data description

Historically, Eros was observed intensively during three apparitions in 1951-52, 1974-75, and 1981-82 (*e.g.*, Beyer, 1953; Tedesco, 1976; Harris et al., 1995, 1999, *etc.)*. Observations near opposition were carried out in 1993 at phase angles less than 6° (Krugly and Shevchenko, 1999), which are very important in measuring the opposition effect. The early lightcurve data before 1993 were extracted from Asteroid Photometric Catalog V1.0 (Lagerkvist and Magnusson, 1995) in NASA Planetary Data System (PDS) online archives, and the data for 1993 observations were obtained directly from Lagerkvist, C.-I.. Lightcurves covering more than 0.8 rotational period are included in our study, plotted in Fig. 4.1 as a function of solar phase angle. As the phase angle was nearly constant during the time span of each lightcurve measurement, the lightcurve is very close to a vertical line in the plot. Since Eros's shape is nearly a biaxial ellipsoid, a smooth phase function can be defined by the lightcurve maxima (as stated in Chapter 3), even if they were measured at very different pole orientations with respect to the observers, as indicated from the very different lightcurve amplitudes. However, this geometric effect makes it difficult to define a smooth phase function from the lightcurve means, unless the shape model is known as well as the pole orientations, so that the lightcurves can be corrected for different cross-sections to calculate the disk-average reflectance (Domingue et al., 2002).

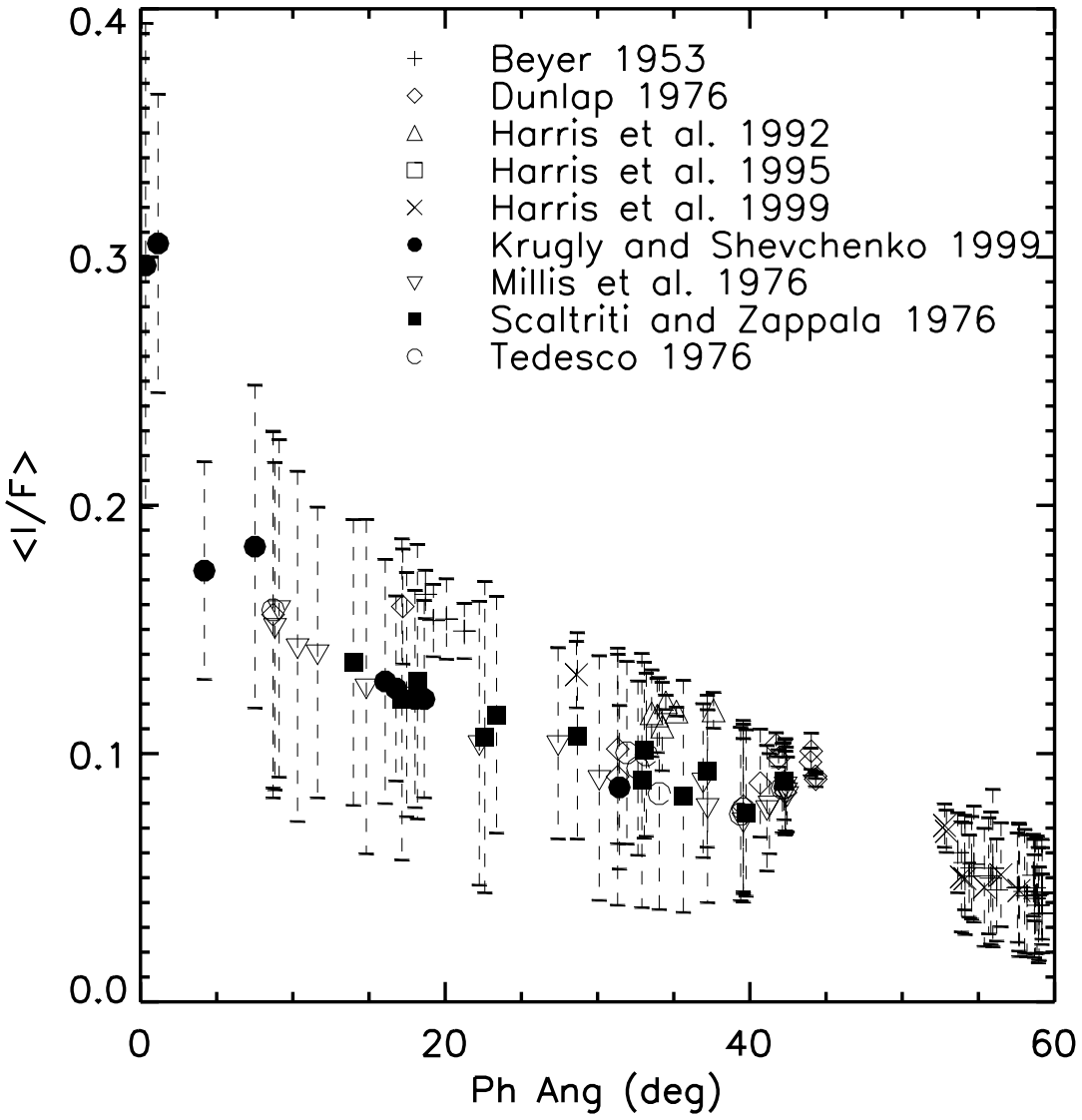

Figure 4.1 The ground-based lightcurves of Eros plotted against phase angle in the linear $< I/F >$ scale. The equivalent cross-section calculated from the volume of Eros was used to convert the original data in magnitude scale to reflectance. The dashed lines are the lightcurves with two ends at the lightcurve maxima and minima. The symbols are at the means of the lightcurves. Due to the reason stated in last chapter, the scatter of lightcurve minima is very large, but lightcurve maxima can define a very smooth phase function.

4.2.2 Results from disk-integrated phase function

Although as shown in last chapter, the disk-integrated phase function from lightcurve means is the best for the purpose of photometric modeling, it is not possible to get a well defined phase function from Eros's lightcurve means. Instead, we fitted the phase function from Eros's lightcurve maxima following the least χ^2 fitting scheme (Chapter 2.5.2). The fitting result is plotted in Fig. 4.2, as well as the theoretical lightcurve maxima predicted from the earlier photometric model (Domingue et al., 2002) and shape model (Thomas et al., 2002) for comparison. The modeled parameters are listed in the last row of Table 3.2, of which only the opposition effect parameters were kept as our final values, since no improvement for them is possible from fitting the MSI data which have phase angle greater than 55°, and our forward simulations show that they can be retrieved from lightcurve maxima fairly well (Chapter 3.4). The fitted values for other three parameters can be compared with the following results from the MSI data as a qualitative cross-check.

To estimate the uncertainty of the result, we focused on two aspects: 1) the measurement errors of the reflectance data and the corresponding geometric parameters; and 2) the fitting errors due to the errors of input data and the imperfection of the theoretical model. For ground-based observations, measurement errors mainly come from the observational errors. Another possible error source was introduced in converting the brightness from magnitude scale to reflectance scale, where the maximum cross-section of Eros calculated from its shape model was used. At high phase angles, the lightcurve maxima do not exactly occur at the maximum cross-section with respect to the Sun, in which case this would result in error in the converted disk-averaged reflectance. Fortunately the ground-

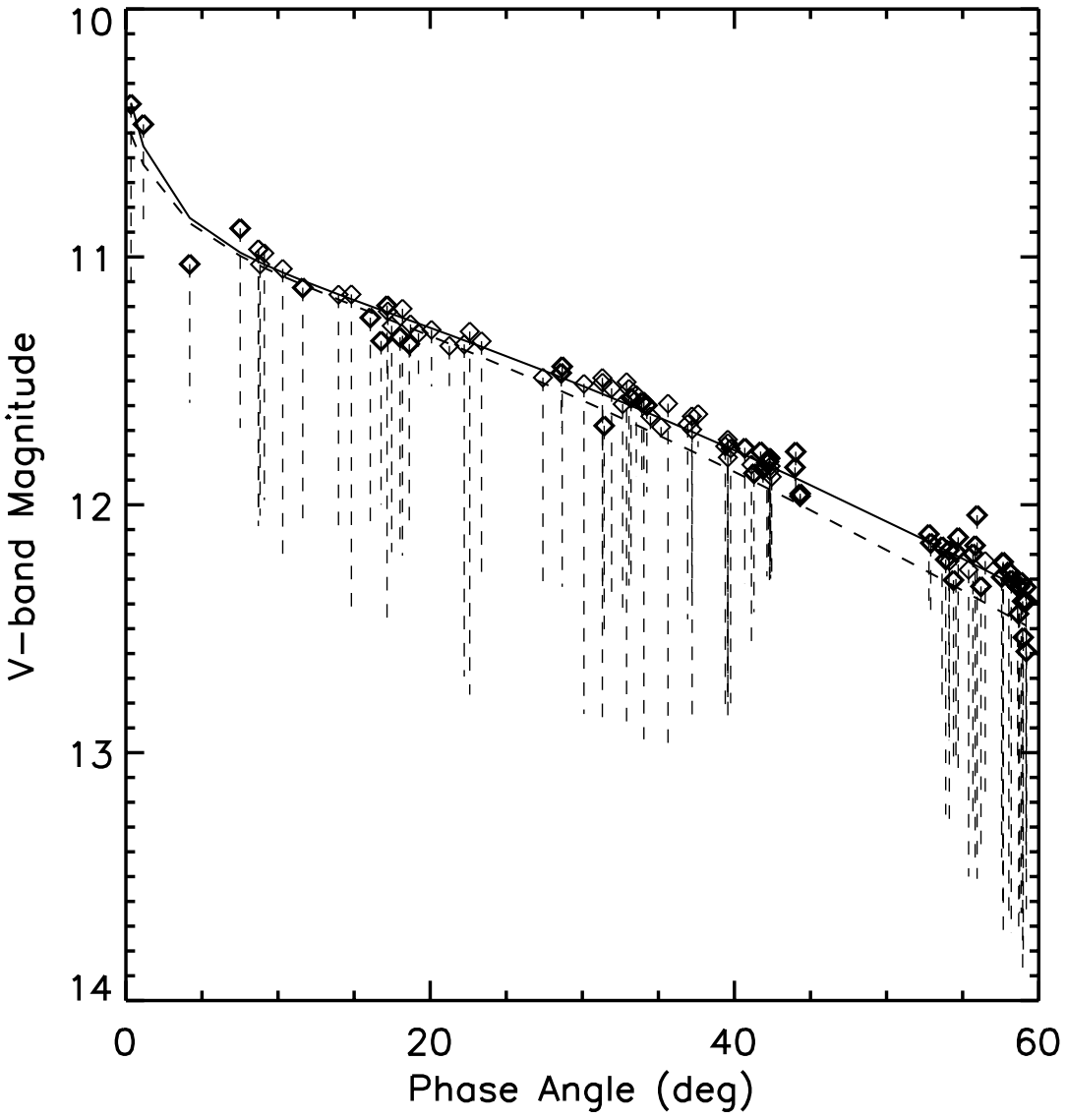

Figure 4.2 The fit to the lightcurve maxima from ground-based observations, plotted in magnitude scale to emphasize the lightcurves at high phase angles. The diamonds are the lightcurve maxima used in the fit, the vertical dashed lines show the lightcurves. The solid line is our fit to the lightcurve maxima, and the dashed line represents the lightcurve maxima predicted from the earlier photometric model (Domingue et al., 2002) and shape model (Thomas et al., 2002).

based lightcurves were only used to estimate the opposition effect parameters, where the data at large phase angles are less important. Overall, the error in ground-based data was taken to be less than 3%, and seemed realistic for error in the combined ground-based photometry plus resultant uncertainty in the magnitudes of lightcurve maxima. The fit itself is also good as seen from the plot (Fig. 4.2), with RMS error of 0.0040, or about 4% of the average reflectance. The 1-σ error bars of the amplitude and the width of the opposition effect are 0.1 and 0.003, respectively, or 7% and 40% relatively. These large error bars are mainly due to the lack of good data near opposition.

4.3 Disk-Resolved Photometry

4.3.1 NEAR MSI data

To perform disk-resolved photometric analysis for Eros at visible wavelengths, we took all NEAR MSI images from NEAR online data archives in NASA PDS (Taylor, 2001), and then selected part of them according to three criteria: 1) The images are all taken around similar spacecraft range to the center of Eros to ensure comparable resolution in each dataset; 2) Eros's disk covers more than 70% of each image frame so that limb effects are tiny and the geometry of the surface within each image frame does not change much; and 3) The images are already deblurred and radiometrically calibrated to reflectance unit I/F (Murchie et al., 1999, 2002b), where I is the observed intensity and πF is the incident flux. In this unit a 100%-reflecting Lambertian disk would have an I/F of 1.0 if illuminated normal to its surface. This unit of reflectance is widely used by observers, and used hereafter in this dissertation. But it is different from what is defined by Hapke

(1993) as stated in Chapter 2, where the F represents the incident solar flux. There is a π factor difference between the two conventional definitions of I/F, and it has to be accounted for in data modeling in order to retrieve the correct Hapke's parameters.

4.3.2 Model disk-resolved photometry

From the selected MSI images, the reflectance I/F values were averaged across Eros's disk in each image as one measurement of bidirectional reflectance. Eros's 89,398-plate shape model (Carcich, 2001) and corresponding SPICE data (NEAR Science Data Center, 2001) from NASA PDS online archives were then used to calculate the the average incidence angles, emission angles, and phase angles, corresponding to each selected image, or each bidirectional reflectance measurement. Next, the bidirectional reflectance data with incidence angles or emission angles greater than 75° were disregarded for the reason that they may contain large uncertainties in either the reflectance values or the measurements of the illumination and viewing geometries or both, due to the misalignment between the modeled images and real images. These bidirectional reflectance data are grouped into nine datasets from seven different filters, and at three different spacecraft (S/C) ranges for the images taken at 550 nm wavelength (Table 4.1).

The dataset at 550 nm wavelength and S/C range about 100 km is shown in Fig. 4.3 and 4.4 as an example. The image footprint size when taken at 100 km S/C range is about 4.5 km across, of which the relative size with respect to the disk of Eros is shown in Fig. 4.5. In these datasets, the images almost uniformly cover all the surface of Eros. Given the image footprint size of about 5 km, and the size of Eros about $33\times11\times11$ km, the images in each dataset have large overlapped areas, thus it is secure to say that the whole

Table 4.1. The datasets used and the least-square fitting results. Values in parentheses are preset and fixed in the fit. The error bars listed in the table are the 1-σ uncertainties given by the fitting routine `lmfit` to indicate the goodness of the fit itself, not the error bars of the resultant photometric models. The 1-σ uncertainties for $\bar{\theta}$'s are all less than 0.1, and are not listed in the table. The opposition effect parameters B_0 and h were preset to 1.42 and 0.010, respectively, and kept unchanged in the fitting process.

Dataset No.	Wavelength (nm)	S/C Range (km)	# of images	w	g	$\bar{\theta}$ (deg)	RMS Error
1	550	47-58	145	0.321±0.008	-0.26±0.05	23.0	0.0028
2	550	89-105	199	0.347±0.008	-0.23±0.02	29.6	0.0032
3	550	187-206	196	0.33±0.02	(-0.24)	31.1	0.0033
4	450	89-105	175	0.320±0.005	-0.23±0.02	26.0	0.0030
5	760	89-105	227	0.468±0.008	-0.25±0.02	29.6	0.0043
6	950	90-110	835	0.444±0.004	-0.27±0.01	27.6	0.0039
7	900	100-104	44	0.44±0.01	-0.22±0.03	28.0	0.0027
8	1000	98-105	173	0.458±0.007	-0.24±0.02	28.2	0.0039
9	1050	101-104	45	0.41±0.03	(-0.24)	32.1	0.011

surface of Eros is uniformly sampled at a variety of illumination and viewing geometries. However, for the two datasets only containing less than 50 images, the above statement may not be true, and the uncertainties of the final fitted photometric parameters from them will be larger. The phase angle coverage of the MSI images is from 53° to 110°, so it is not possible to model opposition effect from MSI data, but other three photometric parameters can be improved for ground-based results.

4.3.3 Results from disk-resolved photometry

The fitted parameters for the nine MSI datasets are listed in Table 4.1, where the opposition effect parameters were preset to be the values found from the ground-based phase function and are not listed. For some datasets the numbers in parentheses were also preset and kept fixed because free fitting caused unphysical values for those parameters. The photometric parameters from the three datasets at 550 nm wavelength were averaged with their fitted 1-σ error estimates as weights to find the final values, which are listed in Table 4.2 and compared with earlier photometric models of Eros and two other S-type asteroids, Gaspra and Ida, and the average S-type asteroids. The goodness of fitting the MSI data at wavelength of 550 nm and S/C range of 100 km is shown in Fig. 4.6 and 4.7 as an example for all nine datasets.

Overall our modeled values are consistent with past values, and within the ranges of values inferred from Eros's spectra and the models obtained at other wavelengths. As for disk-integrated photometric analysis, error has to be estimated from two aspects, the measurement error and the modeling error. Measurement error includes image calibration error, and the errors in the the calculated incident and emission angles. The phase angle

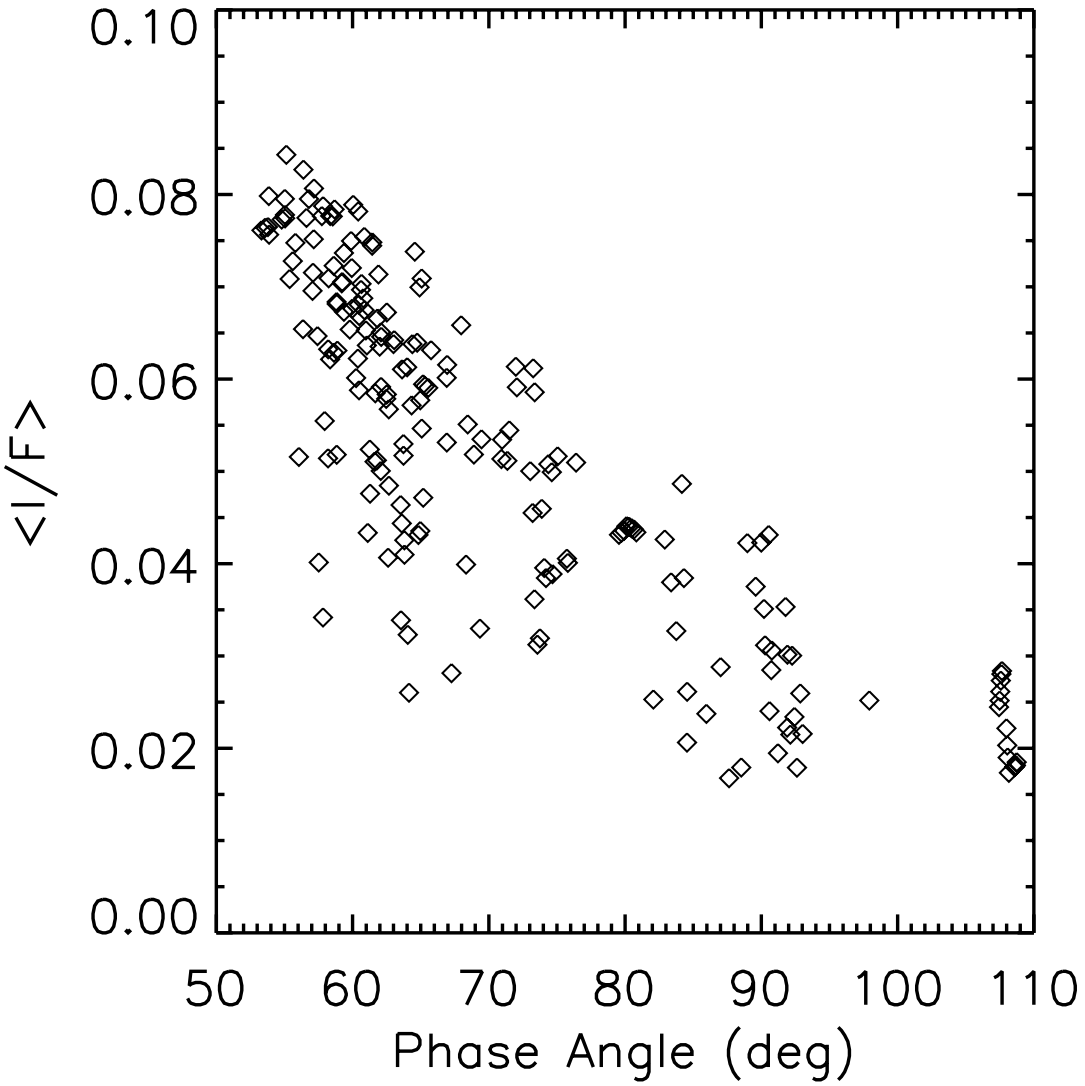

Figure 4.3 The bidirectional reflectance data from MSI images at wavelength 550 nm and S/C range of about 100 km are plotted against phase angle in the left panel.

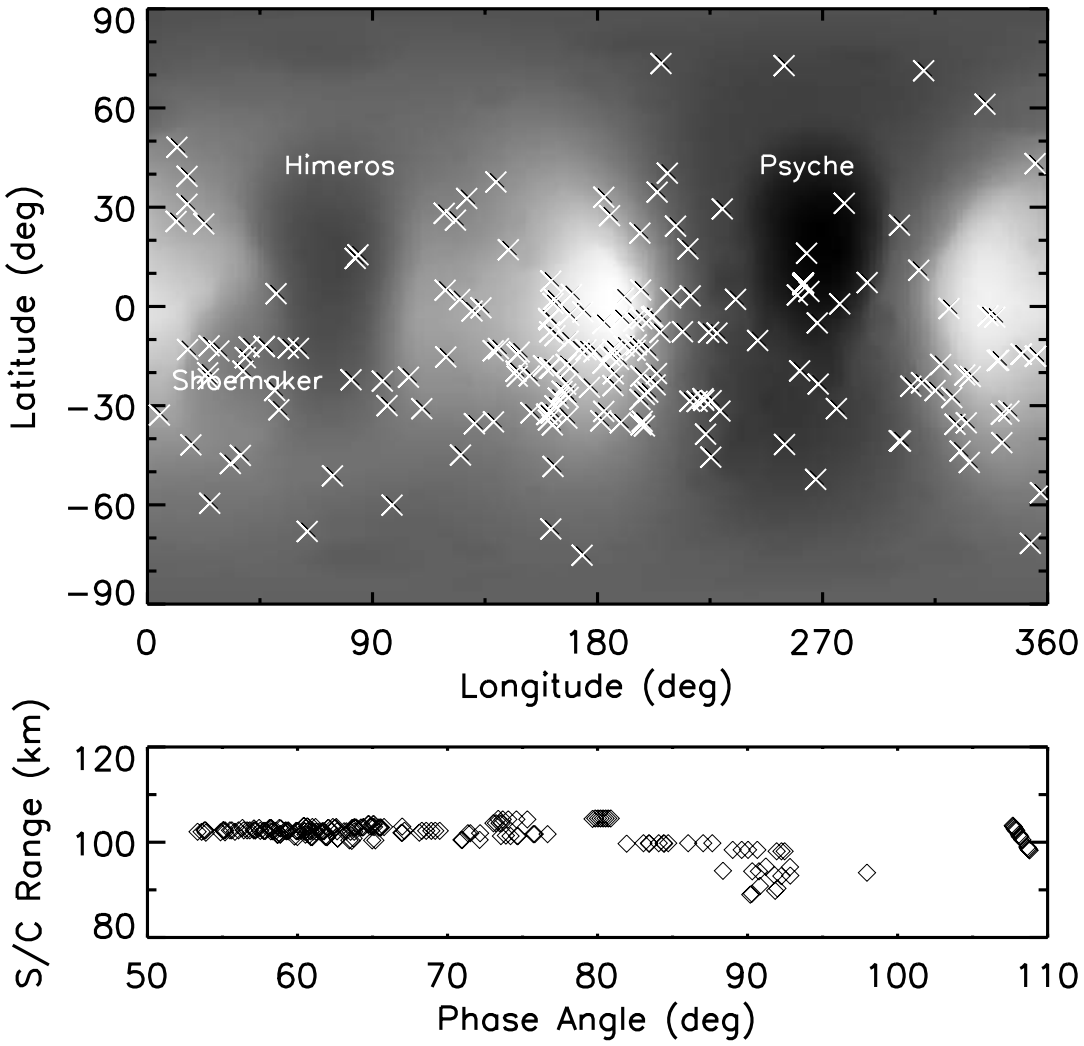

Figure 4.4 The upper panel shows the coverage of the MSI images at 550 nm wavelength and about 100 km S/C range on the surface of Eros. The position centers of the MSI images are superimposed on the surface map of Eros, where bright tone means high altitude, and dark tone means low altitude. In the lower panel, the spacecraft range of these data points are plotted as a function of phase angle.

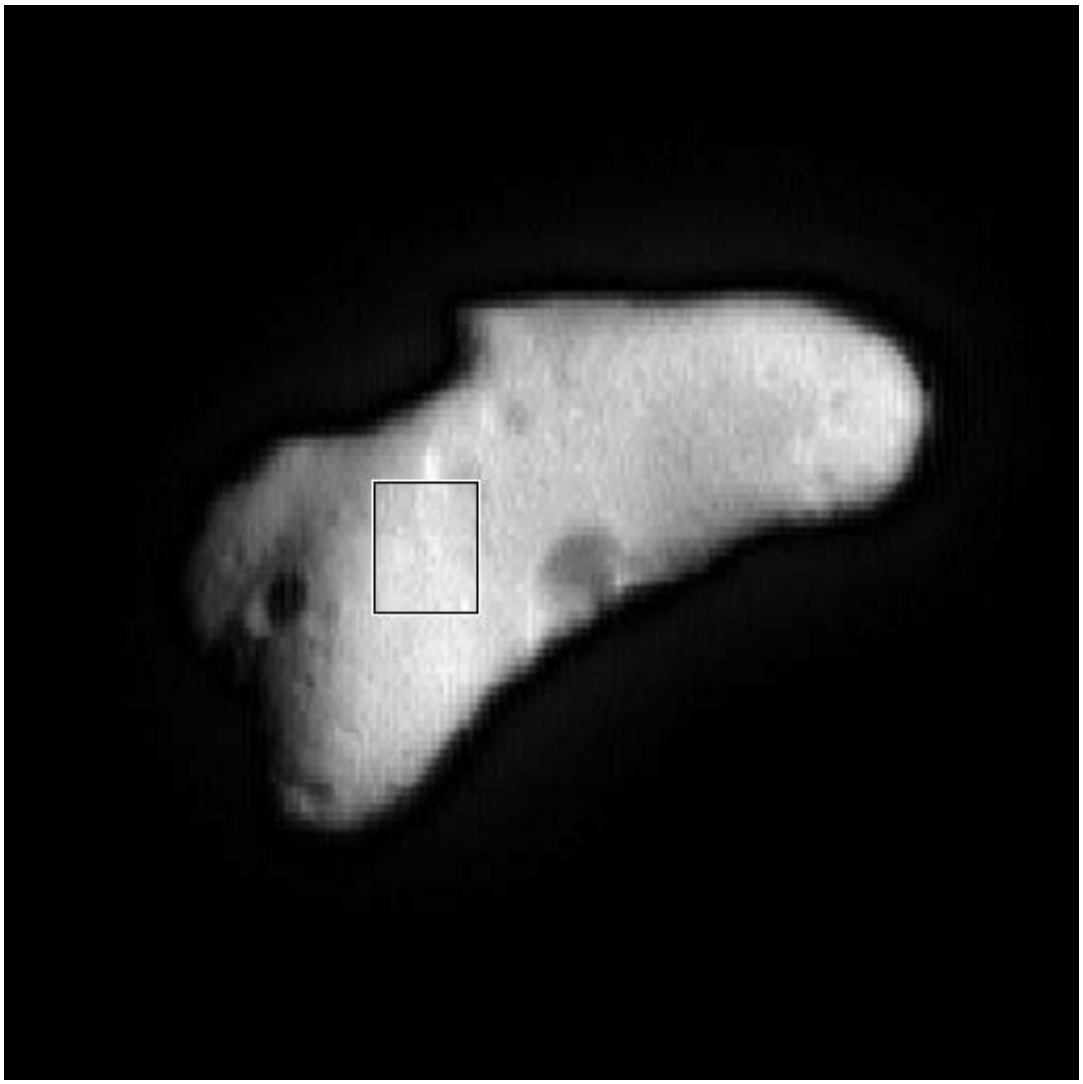

Figure 4.5 The relative size of the image footprint used to derive the data in left panel with respect to the size of Eros's disk is shown. The image footprint size is about 5 km by 4 km.

Table 4.2. The comparison of our photometric model of Eros with the earlier results of Eros, and with other objects.

Objects	w	B_0	h	g	$\bar{\theta}$	A_{geo}	A_{Bond}
Eros[a]	0.33±0.03	1.4±0.1	0.010±0.004	-0.25±0.02	28±3	0.23	0.093
Eros[b]	0.43	1.0	0.022	-0.29	36	0.29	0.12
Eros[c]	0.42	1.0	0.022	-0.26	24	0.26	0.13
Gaspra[d]	0.36	1.63	0.06	-0.18	29	0.22	0.11
Ida[e]	0.22	1.53	0.020	-0.33	18	0.21	0.071
Avg S-type[f]	0.23	1.32	0.02	-0.35	20	0.22	0.084

[a]This work, 550 nm

[b]Domingue et al. (2002), 550 nm

[c]Clark et al. (2002), 950 nm

[d]Helfenstein et al. (1994), 560 nm

[e]Helfenstein et al. (1996), 560 nm

[f]Helfenstein and Veverka (1989); Helfenstein et al. (1996), V-band

error is miniscule because the local phase angles only depend on Eros's shape or any local features very slightly. Murchie et al. (1999, 2002b) have demonstrated that the absolute reflectance of the calibrated MSI images is accurate to within 5%, which we took as the error of the average reflectance measured from MSI images. The inaccuracy or the uncertainties in the shape model should be small, and so are the errors of the SPICE data for calculating the local geometries. Because of the cosine dependence on the reflectance to incident and emission angles, errors are large for extreme geometries. The uncertainty is estimated to be 2% here.

The goodness of the fit can be estimated from the value of χ^2 as defined in Eq. 2.69, or the root mean square (RMS) error, which is actually the χ. The uncertainties of the fitted parameters can be inferred from the output σ's from the fitting routine `lmfit`, which were estimated from the partial derivatives of the theoretical model with respect to each parameter. Fig. 4.6 shows the goodness of the fit to the MSI reflectance data at 550 nm and S/C range about 100 km, with the RMS error 0.0032, or 6% of the average reflectance. A linear fit of $< I/F >_{fit}$ as a function of $< I/F >_{observed}$ results in a line with a slope of 0.95, basically implying no systematic bias in the fit. The peak-to-peak residual of about 40% of the average $< I/F >$ yields a 1-σ error bar of about 8% to the fitted parameters. Therefore although as given by the fitting routine that the 1-σ error bars of the SSA w, the asymmetry factor g, and the roughness parameter $\bar{\theta}$ are very tiny, the actual total error should be around 10%. The ratio between the fitted reflectance and the measured reflectance is also plotted as a function of incidence angle, emission angle, and phase angle in Fig. 4.7. The scatter for a few data points are large, but most of them are concentrated between 0.8 and 1.2. Overall, there is no systematic bias with the

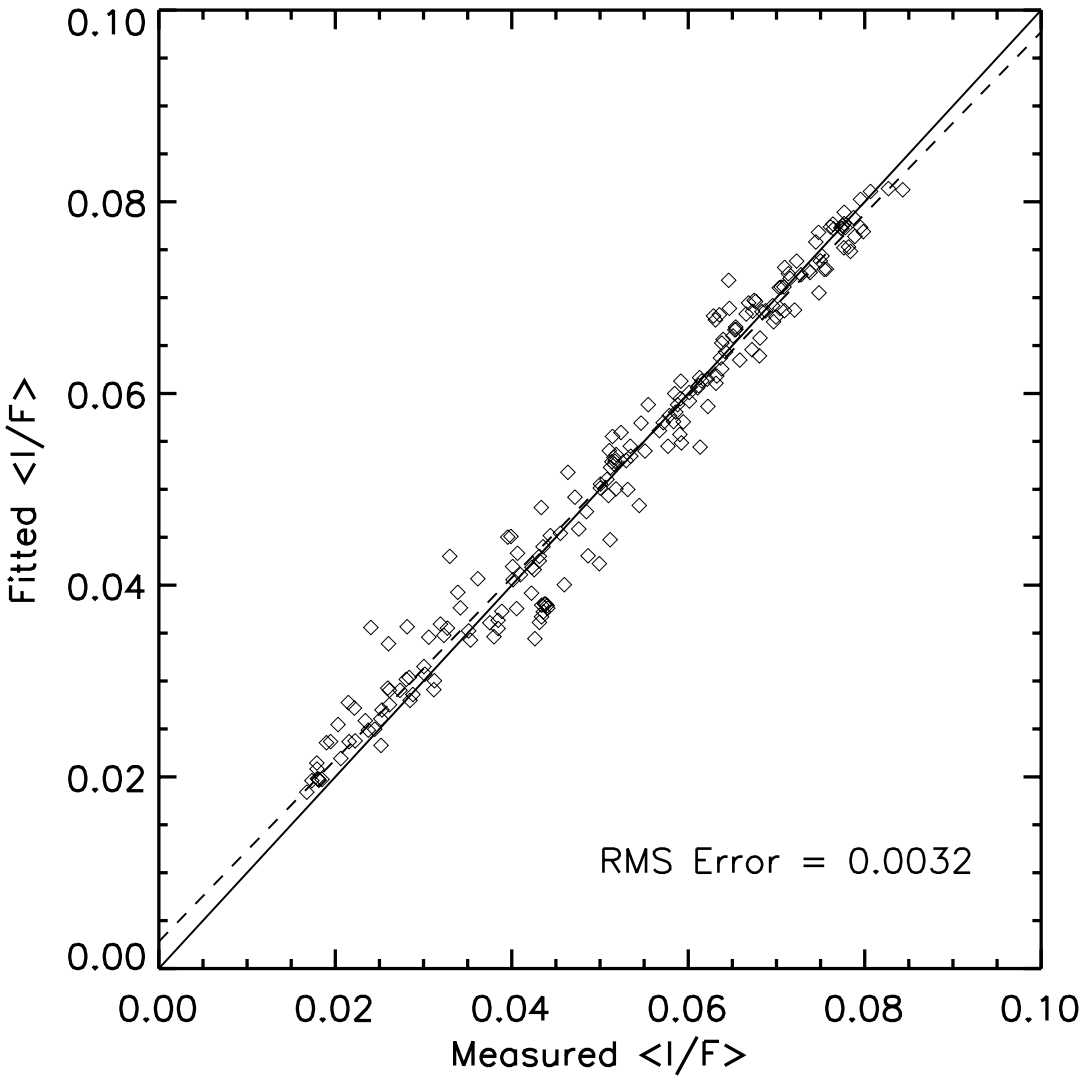

Figure 4.6 The goodness of fit between measured and fitted reflectance values for MSI data at 550 nm wavelength and 100 km S/C range. The solid line denotes a perfect correlation. The dashed line is the linear fit to the actual results.

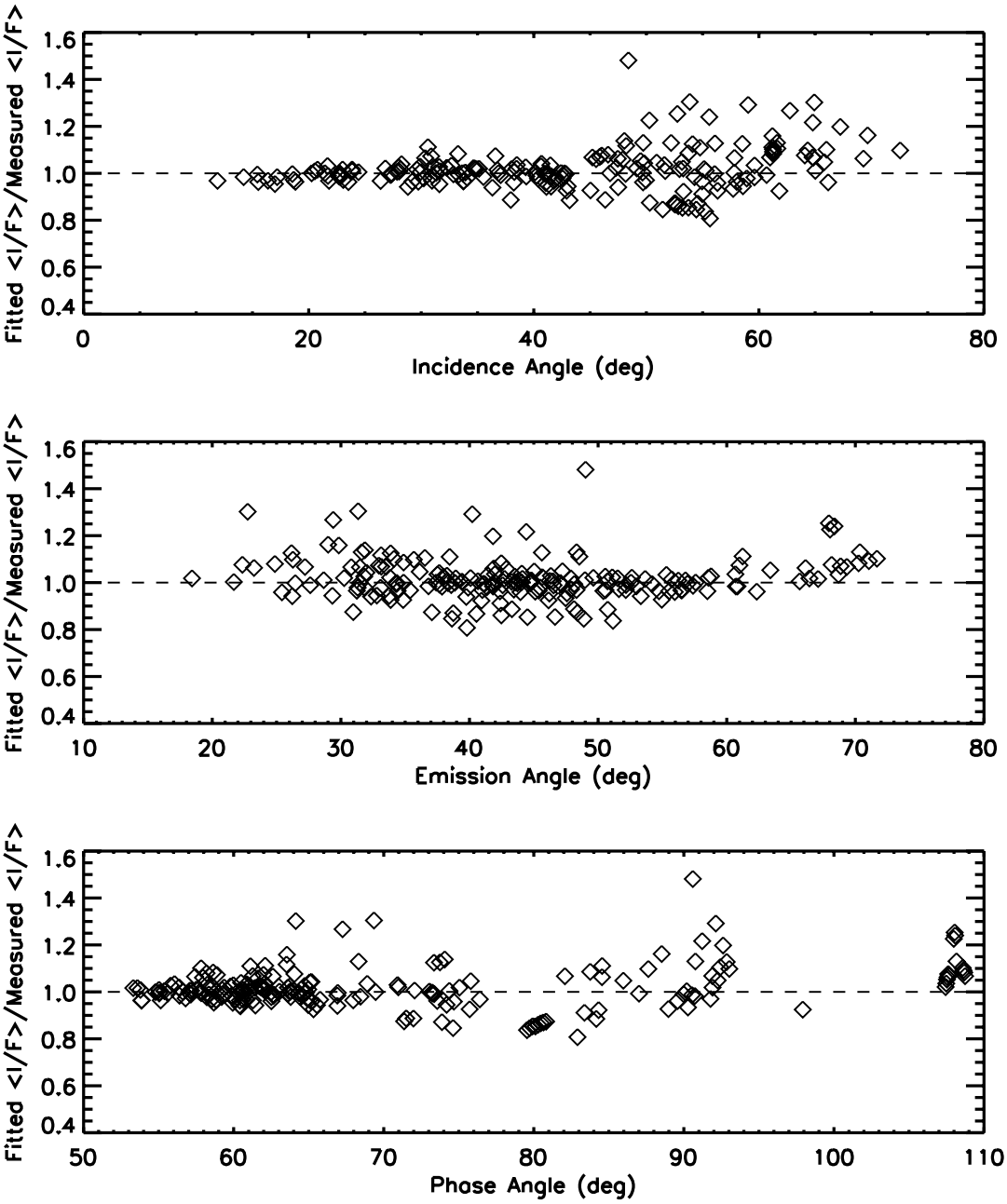

Figure 4.7 The ratio of fitted reflectance to the measured reflectance plotted as a function of incidence angle, emission angle, and phase angle, respectively, for the same dataset as in Fig. 4.6.

illumination and viewing geometry, but we may notice that the data at larger incidence angles scatter more than those at smaller incidence angles, which is possibly due to the $\mu_0/(\mu_0 + \mu)$ dependence of the bidirectional reflectance.

4.4 Discussions

To show the consistency of our derived values of Hapke's parameters with previous ones, we compare them in this section, especially with the values found from Domingue et al. (2002) and Clark et al. (2002). But it has to be kept in mind that none of them can be compared directly. The data resolution and the analysis technique in our study are very similar to those used in Clark et al. (2002). However, the wavelengths studied in Clark et al. (2002) only have a small overlap with the wavelengths of our work. The wavelength dependence of the model had to be used to make the connection. In comparing our results with the values found by Domingue et al. (2002), it has to be kept in mind that the averaged reflectance over the very irregular disk of Eros was used in Domingue et al. (2002), and a spherical shape was assumed, which may cause a systematic difference from this work. The simulations presented in last chapter are important for evaluating the difference, and for connecting the resultant models in comparison, although the wavelengths are similar for both of them. All values referred to in the following discussions are summarized in Table 4.2.

4.4.1 Single-scattering albedo

The properties of single-particle scattering are directly related to the physical and mineralogical properties of the surface particles that comprise the regolith. To compare with the values from Clark et al. (2002), we took the spectrum of Eros covering the wavelength range from 450 nm through 1200 nm, as reported by Murchie et al. (2002a), to establish the necessary connection in wavelength (Fig. 4.8). The spectrum was rescaled in the plot so that at 950 nm the value of the spectrum was set to be the value of the SSA (0.42) found by Clark et al. (2002) at that wavelength. The majority of the spectral wavelength dependence is due to the wavelength dependence of the SSA. So we expect relatively close agreement between the SSA and the spectrum, as is found in the comparison in Fig. 4.8. Furthermore, as indicated by our simulations (Chapter 3.4), for Eros's shape model, if the SSA is fitted from the disk-integrated phase function, either constructed from lightcurve means or lightcurve maxima, it will tend to be overestimated. This explains why our resultant SSA value is smaller than the value found by Domingue et al. (2002). The smaller value of the SSA is more consistent with the value found for a typical S-type asteroid than the earlier one, although still higher than average S-type asteroids. Compared with two other S-type asteroids that have been studied from spacecraft data, (951) Gaspra (Helfenstein et al., 1994), and (243) Ida (Helfenstein et al., 1996), the SSA of Eros is between their values but much closer to Gaspra's.

Typical S-type asteroids are covered by an olivine-pyroxene mixture, with the mixing ratio varying with subtypes (Gaffey et al., 1993). Based on its spectrum, the composition of the regolith of Eros is dominated by olivine (McFadden et al., 2001; Bell et

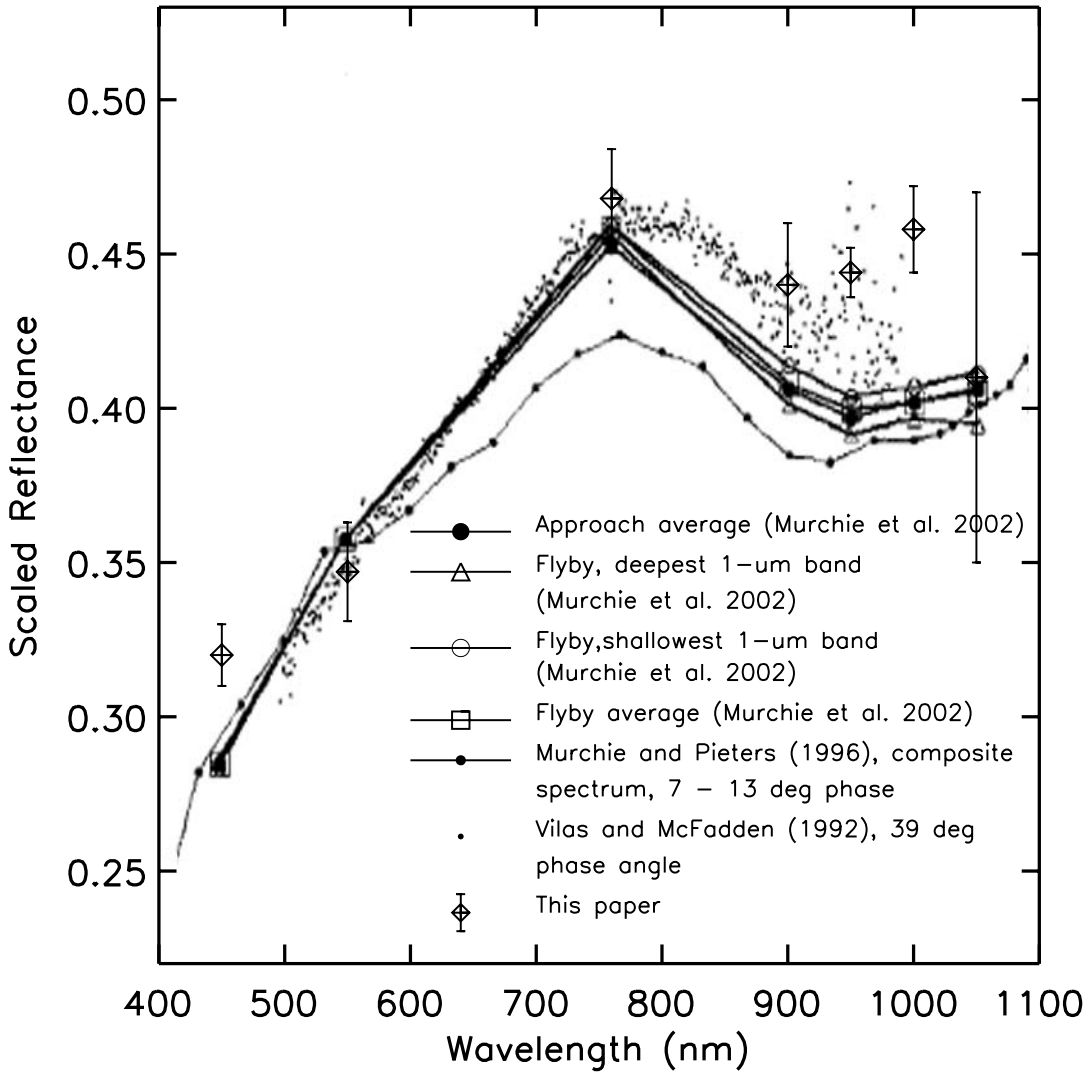

Figure 4.8 The spectrum of Eros as taken from Murchie et al. (2002a) but rescaled so that the reflectance at 950 nm is about the the value of the SSA (0.42) as found by Clark et al. (2002) at 950 nm. The diamonds show our deduced values of w at each of the wavelengths sampled by MSI images. The error bars shown here are the $\pm 2\sigma$ as estimated from the residuals of fit.

al., 2002; Izenberg et al., 2003), which is consistent with the result of Lucey et al. (2002) using the spectrum-temperature relationships. The corresponding ordinary chondrite type was estimated to be L6 type by Izenberg et al. (2003), although previous studies did not exclude the possibility of LL types. The SSA of the regolith particles at any given wavelength is determined by both the composition and the grain size (Lucey, 1998; Hapke, 1993, p.171). If we adopt equations (8a-8c) in Lucey (1998), the average real refractive indices n over the crystallographic axes are expressed as functions of the Mg number, the ratio of Mg to Mg+Fe on a mole percent basis. The imaginary parts, k, of the refractive indices for three minerals (olivine and two pyroxenes) were fitted linearly in the same paper as functions of the Mg number at some selected wavelengths. Therefore, if we take the mixing formula for the SSA (Hapke, 1993, p.283), and assume that the particle sizes of olivine, orthopyroxene, and clinopyroxene components are all the same in the mixture, then the SSA of the mixture can be simplified as,

$$\frac{1-w}{w} = \Sigma_i f_i \frac{1-w_i}{w_i} \tag{4.1}$$

where w and w_i are the SSA of the mixture and the SSA of its ith component, and f_i is the weight percent of the ith component, respectively. Following the theories of reflectance spectroscopy (Hapke, 1993, Ch.6) and the assumptions therein, the SSA of the mixture can be written as a function of particle size and Mg number at a particular wavelength. Unfortunately, the fit of k at 550 nm was not given by Lucey (1998), instead, we used the results at the closest wavelengths, *i.e.*, at 520 nm for olivine, and at 750 nm for both orthopyroxene and clinopyroxene. The weight fraction of olivine was estimated to be 0.6 for Eros's regolith particles, although it was concluded from one-pyroxene hypoth-

esis (McFadden et al., 2001; Bell et al., 2002). The weight fractions for orthopyroxene and clinopyroxene were assumed to be 0.3 and 0.1, respectively, as estimated for L-type ordinary chondrites (McSween et al., 1991). The Mg number fractions of pyroxenes were calculated to be 0.25 from the estimate of mole fractions of Fe and Ca contents found by McFadden et al. (2001) for Eros regolith particles. We use this number for both orthopyroxene and clinopyroxene in our calculation (Adams, 1974), although it was originally obtained assuming a single pyroxene. Assuming the Mg number in the olivine that comprises Eros's regolith is 0.75, which is typical for the olivine from L-type ordinary chondrites (Gomes and Keil, 1980, p.82), we calculate the SSA as a function of grain size and plot it in Fig. 4.9 as the solid line.

Based on the fitted SSA at 550 nm for Eros, the grain size of the regolith particles on the surface of Eros was estimated to be about 160 μm. If one considers other types of ordinary chondrites, the Mg number could range from 0.4 to 0.85, and the size range will be from 100 to 200 μm (dashed lines in Fig. 4.9). However, comparison between the background surface of Eros in and around Psyche crater shows that Eros's surface has been darkened, presumably due to space weathering (Clark et al., 2001; Murchie et al., 2002a). The albedo contrast of 32-40% indicates that the SSA of Eros's regolith particles has been decreased by at least 40%. Because of the small variation of the spectrum over the surface of Eros, the unaltered SSA at 550 nm would be about 0.50. This leads to an estimate of the range of grain size from 50 to 100 μm. In modeling the space weathering on Eros, Clark et al. (2001) also present nominal compositional models for the dark and bright materials in and around Psyche crater to account for their different albedos and spectra in the near IR. The grain size (63 μm for bright material, 77 μm for dark material)

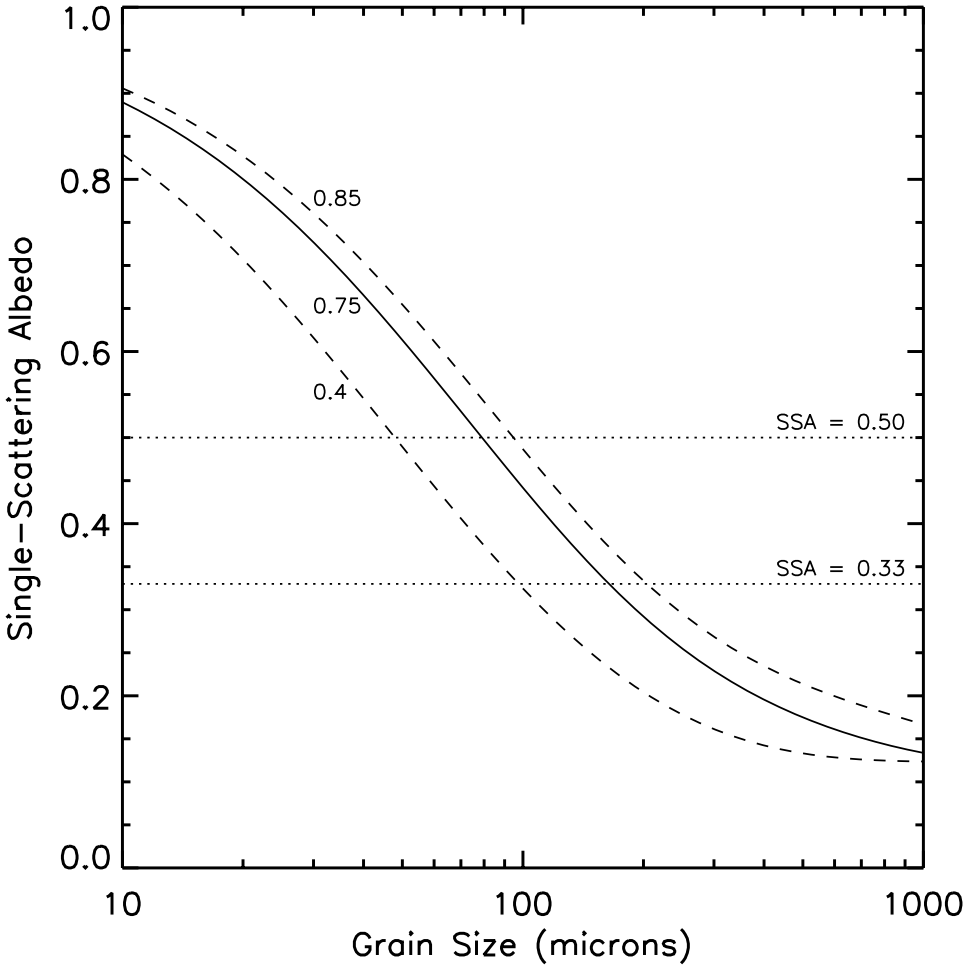

Figure 4.9 The theoretical single-scattering albedo of the cpx-opx-ol mixture as functions of grain size for various Mg numbers in olivine component at 550 nm wavelength. The weight fraction of olivine, orthopyroxene, and clinopyroxene are assumed to be 0.6, 0.3, and 0.1, respectively. The Mg number in pyroxene is assumed to be 0.25 for both orthopyroxene and clinopyroxene. The solid line denotes the calculated SSA with the Mg number 0.75 for the olivine component as estimated from L-type ordinary chondrites. Two dashed lines are the calculated SSA for Mg numbers of olivine 0.40 and 0.85, respectively. The dotted lines represent the fitted value of SSA for Eros, 0.33 at 550 nm, and the estimated SSA that is unaltered by space weathering, 0.50, at the same wavelength.

in their model is right in the above range derived from V-band albedo.

4.4.2 Single-particle phase function

The single-particle phase function describes the direction of the energy scattered from a single particle. Described by empirical formulae, the most commonly used prescription is the Henyey-Greenstein (HG) function. As suggested by Hartman and Domingue (1998), a two-term form of the HG function is a good approximation to describe the single-particle phase behavior for most asteroidal regoliths. Domingue et al. (2002) found that, for Eros's regolith, the two-term form would be reduced further to one-term with their best-fit parameters. In the photometric analysis of Eros in the near-IR carried out by Clark et al. (2002), the single-term HG function seemed to be adequate for describing the single-particle phase behavior. Therefore the single-term HG function was used in our analysis, and the sole parameter, g, in the single-term HG function may or may not be wavelength dependent, which is not predicted or assumed by any currently used theories. However, it happens for Eros that the trend of its wavelength dependence is very weak in the near-IR (Clark et al., 2002). Our results indicate that the weak wavelength dependence trend still remains true for wavelengths between 450 nm and 1050 nm, with values comparable to those found at longer wavelengths.

To compare our resultant value of asymmetry factor with the value found in Domingue et al. (2002), it has to be noted that disk-resolved data were used in our analysis, while whole-disk data were used in Domingue et al. (2002). Although it has been demonstrated that these different approaches are not likely to lead to differences in the resultant models of the single-particle phase function (Hartman and Domingue, 1998), this similarity only

referred to the photometric properties of the disk-integrated phase function, with the assumption that there was no geometric effect introduced either by illumination and viewing geometries, or by irregular shapes. As shown by our modeling, simulations suggest that the g factor estimated by fitting the whole-disk lightcurve means of Eros would be slightly more forward-scattering. However, our result is even more forward-scattering than the value found from Domingue et al. (2002), which must be explained. It was brought to our attention that in the composite phase function used in Domingue et al. (2002), there was a slight discontinuity in the phase function between the segment at phase angles smaller than 60° and the segment at larger phase angles that came from the MSI images during the NEAR Eros flyby in 1998. Not likely to be a random measurement error, the latter part appeared to be systematically below the smooth extrapolation from the former part (See Fig. 5 and 6 in Domingue et al., 2002). The reason for this discontinuity has been determined to be the possible underestimate in the calculated phase angles of the NEAR flyby images, and confirmed by recalculation of the phase angles from spacecraft, Eros and Sun positions. Therefore the smaller reflectance values that should have been at higher phase angles were brought to lower phase angles, which effectively produced a phase function that was more back-scattering than the true one, and caused the overestimate of back-scattering in the fitted g factor. This overestimate of back-scattering dominated the possible underestimate caused by the method of fitting lightcurve means with spherical shape assumption, and gave an even more back-scattering g factor. Furthermore, the slope of the phase curve for the predicted lightcurve maxima of Eros with the g factor of -0.29 is steeper than that for the actual measured lightcurve maxima (Fig. 4.2), also favoring a more forward-scattering g factor.

As an empirical expression, the parameters of the HG function are not directly correlated to the physical characteristics of the actual particles, although some attempts have been made to establish the connection (McGuire and Hapke, 1995; Hartman and Domingue, 1998). The back-scattering regolith (with a negative g factor) is an indication of irregular particles and the existence of large amount of interior imperfection (McGuire and Hapke, 1995), or of complex composition in the regolith particles. However, this is not necessarily the only explanation, because of both the lack of data at phase angles higher than 110° to detect forward scattering of any strength, and the empirical nature of the HG function.

4.4.3 Opposition effect

The opposition parameters are the least constrained of all five parameters. One reason is due to the difficulties in theoretical modeling. The theory modeling the opposition effect was described by Hapke (1993, Ch.8H), Muinonen (1990), Hapke (2002), *etc.*, and a good discussion can be found in Domingue et al. (2002). In addition to the widely accepted shadow hiding opposition effect (SHOE) mechanism known to cause the opposition effect, another mechanism was demonstrated to contribute simultaneously in both high albedo samples (Nelson et al., 1998, 2000) and low albedo lunar samples (Hapke et al., 1993, 1998) at visible wavelengths, namely the coherent backscatter opposition effect (CBOE). In contrast to the SHOE, which is a single-scattering, wavelength independent phenomenon, dominating the reflectance signature, the CBOE is a multiple-scattering, wavelength dependent phenomenon, dominating the polarization signature (Hapke et al., 1998; Hapke, 2002). Reliable detection of the existence of CBOE relies on the mea-

surement of the reflectance of polarized incident light at phase angles near opposition. Theoretically, in the traditional and most widely used formulation of Hapke's equations, as used in Domingue et al. (2002) and Clark et al. (2002), only the SHOE has been taken into account, and the amplitude is limited not to exceed unity. However, only a few objects show an amplitude of the opposition surge that is smaller than unity as fitted directly from the phase function, while many others would have resulted in values greater than one if the theoretical constraint had not been applied (see, *e.g.* Bowell et al., 1989; Helfenstein and Veverka, 1989; Thomas et al., 1996; Helfenstein et al., 1994, 1996; Clark et al., 1999; Simonelli et al., 1998). This is also a strong indication that, in addition to the SHOE, other opposition effect mechanisms may be present simultaneously, or even jointly and interacting with each other. Therefore it is often the case that the amplitude is allowed to exceed unity in the fit to approximate the opposition effect caused by all mechanisms, and the final parameters can be interpreted as equivalent parameters as if the opposition effect were caused by the SHOE only but amplified by other unspecified mechanisms.

In addition to the theoretical difficulties in modeling the opposition effect, the lack of asteroid photometric data near opposition often limits analysis even more. NEAR MSI data do not have any phase angle coverage at less than 50°. The only available visible photometric data for Eros near opposition come from the earlier ground-based observations (Krugly and Shevchenko, 1999), which were also used by Domingue et al. (2002). On the other hand, the NIS data cover a large range of phase angles from near opposition up to 110° at wavelengths from 900 nm through 2400 nm, and these were used in the first attempt to detect the CBOE solely through the photometric analysis by Clark et al. (2002). The wavelength dependence of the width parameter of the opposition effect

was confirmed as the amplitude was limited not to exceed unity, implying the existence of the CBOE component. However, caution has to be used before the two mechanisms can be separated if the result is to be interpreted in terms of surface physical properties such as the porosity and the grain size distribution because those properties have very different contributions to the SHOE and the CBOE (Hapke, 2002, 1993, Ch.8H).

In our studies of the opposition effect, we chose to allow the amplitude to exceed unity. Therefore our results would be the equivalent amplitude and width of the opposition effect and interpreted as the SHOE only. To evaluate how accurate this approach is from the newest opposition effect theory that includes both the SHOE and the CBOE (Hapke, 2002), we applied some mathematical analysis and numerical calculation for Eros's photometric model. The effect of the CBOE can be included in the bidirectional reflectance or the disk-averaged reflectance by multiplying the $1 + B_{CB}(\alpha) = 1 + B_{C0}B(\alpha)$ term of the CBOE with the expression that does not include the CBOE,

$$< r > = < r >_{SH} \left[1 + B_{C0}B(\alpha)\right] \tag{4.2}$$

where $< r >_{SH}$ is reflectance only including the SHOE as in Eq. 2.62; B_{C0} is the amplitude of CBOE, and the $B(\alpha)$ is the shape function, which we assumed the same as that for SHOE. If we change the disk-averaged reflectance function with CBOE in the form of Eq. 4.2 so that it has exactly the same form as Eq. 2.62, then the equivalent amplitude parameter of the opposition effect is,

$$B_e = B_{S0} + B_{C0} + B_{C0}\frac{1}{p(\alpha)}\left[\frac{4}{(1+\gamma)^2}\left(1 - r_0 + \frac{4r_0G(\alpha)}{3F(\alpha)}\right) - 1\right] + B_{S0}B_{C0}B(\alpha) \tag{4.3}$$

where B_{S0} is the amplitude of the SHOE, $F(\alpha)$ and $G(\alpha)$ are defined in Eq. 2.63 and

2.64, respectively, and $\gamma = \sqrt{1-w}$. The equivalent amplitude of the opposition effect can be seen as the total of the amplitudes of the two components, plus a correction term caused by the CBOE, as a function of the SSA w, the asymmetry factor g, and phase angle α. Fig. 4.10 shows the correction term for our fitted values of Hapke's parameters for Eros for two extreme cases that both B_{S0} and B_{C0} are 1, and a zero B_{S0} with $B_{C0} = 1$. If the CBOE is weak, then obviously the correction will be small. When the CBOE is strong, but the SHOE is weak, the correction is less than 0.2, and rather constant over the phase angles smaller than 60°. So for both cases we can conclude that the total amplitude of both opposition effects is about 1.2 to 1.4 for Eros. However, if both components are strong, then this approach is a poor approximation to the real case. An attempt to quantitatively separate the CBOE from SHOE using the ground-based photometric data following the above analysis has not been successful, and the main reason is probably that the approximation that both components have the same shape and width is not true. The data quality may not be high enough to do this either. Reliable conclusions need the help from polarimetric data.

4.4.4 Roughness parameter

The global roughness parameter $\bar{\theta}$ models the roughness of the surface as the average of the slope deviations within each unresolved surface patch as measured from the local horizon, the plane of the unresolved surface patch that defines the average local surface normal, and in turn the incident and emission angles with respect to the patch. If the average surface normal is understood as the zeroth order approximation of the unresolved surface patch, then the roughness parameter can be interpreted as the first order correction

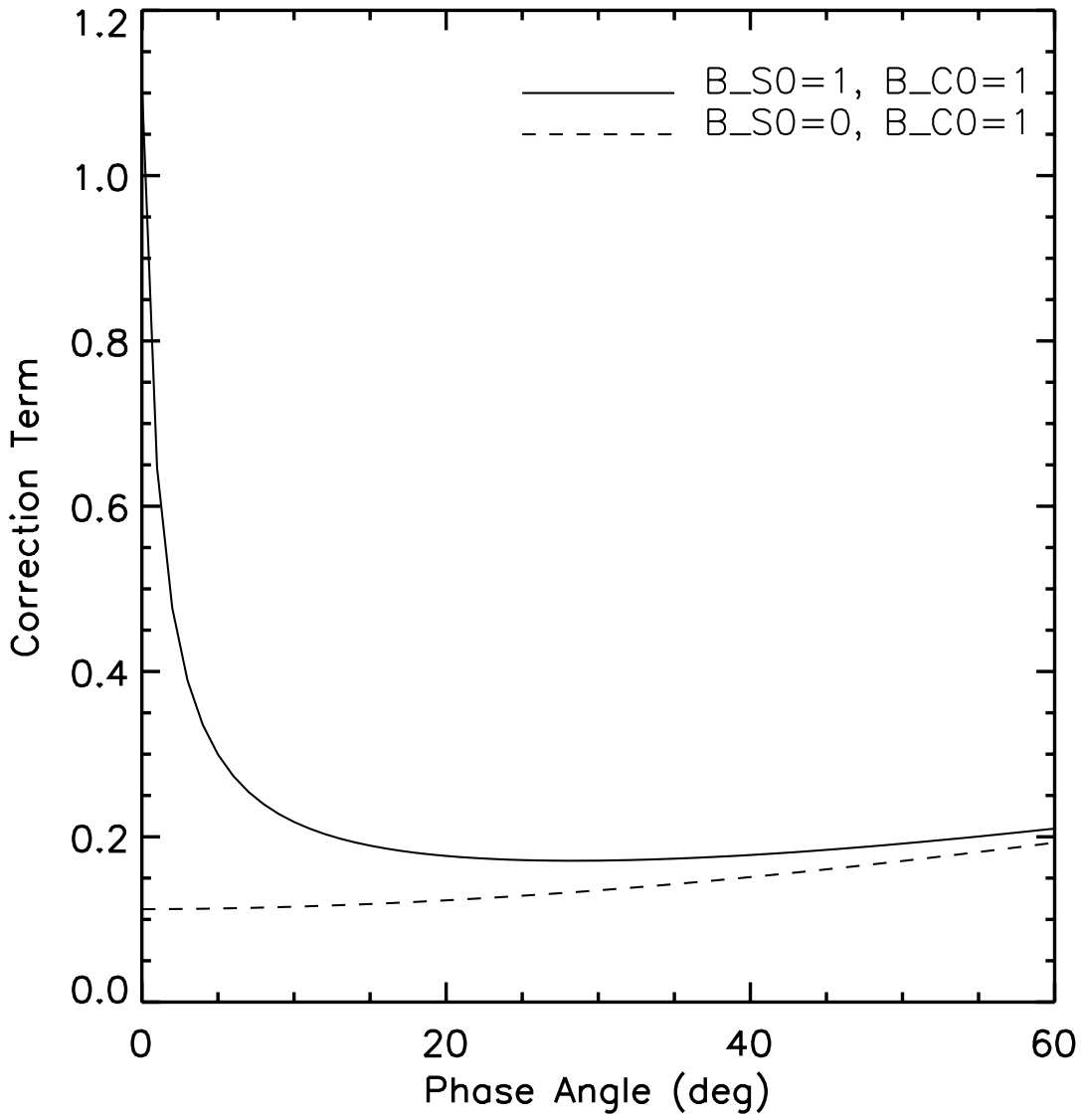

Figure 4.10 The correction term for the two extreme cases of Eq. 4.3. The solid line is for the case in which both opposition effect components are very strong, and the dashed line is for the case with strong CBOE only.

superimposed on the local normal, reflecting by how much the surface slope deviates from the averaged local normal. Since the roughness parameter is purely a geometric parameter, it should be completely independent of wavelength. In Hapke's model for rough surfaces, the slope distribution is assumed to be independent of the azimuth angle and identical over the surface, *i.e.*, homogeneous and isotropic at all scales (Hapke, 1993, p.326). This is why it was traditionally called the *global* roughness parameter. However, considering real asteroid surfaces, such as that of Eros, it is clear that the distributions and the sizes of craters and boulders are not homogeneous (Robinson et al., 2001; Thomas et al., 2001), and therefore the slope distribution changes with location. It is thus equally important to realize that the value of the roughness parameter may also depend on the size of the surface area over which the average was taken, which may in turn indicate that any difference between the values of the roughness parameter fitted from data at different resolutions may not be totally due to the measurement error or uncertainties from the fit. The differences may be real, and correlated with the statistical characteristics of the surface roughness at different scales (Shepard et al., 2001). Some information, such as the size distribution of craters, mountains, and/or their height to size ratio, may be able to be inferred from this parameter.

With this in mind, we compared the values of our roughness parameters derived from images with three different resolutions at 550 nm (Table 4.1), and with the previously published values (Table 4.2). While similar values of the SSA and the asymmetry factor g were obtained from the two datasets at wavelength 550 nm, and S/C ranges about 50 km (line 1, Table 4.1) and 100 km (line 2, Table 4.1), the difference of the two fitted roughness parameters was obvious and much greater than the uncertainties of fit ($< 0.1°$).

The data of the same wavelength but at S/C range about 200 km (line 3, Table 4.1) are very scattered, possibly because the large field of view resulted in many images containing the limb and shadow, therefore the errors of the averaged incidence angles, emission angles, and phase angles used for each image are large. But to confirm the trend of $\bar{\theta}$, we preset the asymmetry factor g to the value obtained from the two other datasets, and held it fixed in the fit. The fitted value of SSA is found to be very close to the values from the other two datasets (line 1 and 2, Table 4.1), and the value of roughness parameter is still following the trend. This result is not so conclusive because of the limited number of measurements at different resolutions in our analysis, and the data quality in the third dataset (line 3, Table 4.1). On the other hand, if we look at the fitted values of the roughness parameter at different wavelengths but similar resolution (line 2, and 4 to 9, Table 4.1), we notice that the fitted values are all very close to each other, with an average of 28° and a standard deviation of only 1.2°, strongly suggesting that the roughness parameter does not depend on wavelength, at least between 450 nm and 1050 nm.

Compared with previous results, the values we found at spacecraft range about 50 km and 100 km are very close to those found by Clark et al. (2002), which can be explained by the similarity between the image footprint size of the MSI data in our studies (2 - 5 km) and the spectral footprint size of the NIS data used in Clark et al. (2002) (2.5 - 5.5 km). It is also noticed that in Clark et al. (2002), the bidirectional reflectance data that comprises the upper envelope as they were plotted as a function of phase angle were selected to fit in order to avoid the possible decrease of reflectance caused by shadows in the spectral footprints. Because of the complexity of the regolith on the surface of Eros (Veverka et al., 2001), this selection rule might have effectively disregarded the data

that could have resulted in a larger roughness parameter, which explains why our value from the data with similar resolution is greater than was found by Clark et al. (2002). In Domingue et al. (2002), the roughness parameter was found using the disk-averaged reflectance as a function of phase angles, thus the irregularity of the global shape of Eros affects the data as well as the small scale roughness down to a few meters. Therefore their resultant value is even larger than our value from the data at S/C range about 200 km.

The variability of roughness parameter with resolution suggests that large scale shadows cast by craters with size comparable to the radius of Eros are as significant in determining Eros's disk-integrated brightness as is the global shape. At small scales, on the order of several kilometers, the surface of Eros is rather smooth, with a roughness parameter of only about 23°. Caution has be to used in correlating the surface roughness parameter estimated from disk-integrated phase function or low resolution images to the statistical characteristics of local surface features such as small craters and boulders. The global shape may also affect the roughness parameter inferred from whole-disk photometry.

4.4.5 Global properties

Our photometric model results in a geometric albedo of 0.23 at 550 nm, smaller than previous results, which is related to the low SSA. Therefore the above discussions about the low single-scattering albedo are still valid here. The phase integral does not vary greatly since the shape of our modeled phase function does not, especially because we used the same dataset as used in Domingue et al. (2002) at phase angles smaller than 60°, the range which primarily determines the phase integral. This in turn results in a Bond

albedo of 0.093, smaller than previously reported at 550 nm. The lower Bond albedo means a decrease in the total radiative energy reflected from the surface of Eros, followed by an increase of the theoretical surface temperature. But this change is very subtle and much smaller than the error in measuring the surface temperature of Eros (Lucey et al., 2002).

Eros is a typical S-type asteroid in terms of its albedo and phase function properties. Fig. 4.11 shows the histogram of the visual geometric albedos of 244 S-type asteroids in Tholen's asteroid taxonomic classification (Tholen, 1984) as cataloged in Neese (2002b), measured during the IRAS Minor Planet Survey and archived in NASA PDS (Neese, 2002a). The geometric albedo of Eros (0.23) is very close to the average of the geometric albedo of S-type asteroids (0.21), but slightly larger. The scatter plot of the asymmetric factor g as a function of the SSA w is shown in Fig. 4.12 for several objects with the Hapke's parameters available. Eros shares the medium high SSA and the moderate backscattering phase function of S-type asteroids.

The reflectance variation over the northern hemisphere of Eros was investigated by Murchie et al. (2002a) at 760 nm and 950 nm. A factor of two variation of albedo was found for most of the surface studied, with a full range of variation a factor of 3.5, which is almost twice that observed on Ida (Helfenstein et al., 1996). In contrast, the variation of 950nm/760nm color ratio of Eros was found to be very subtle (10%), with an average of about 0.85. Bell et al. (2002) reached a similar conclusion, arguing that the uppermost layer of Eros's regolith is compositionally/mineralogically homogeneous. If the albedo variation is the result of different grain sizes of the regolith particles with the same composition, then it may be tested, if enough data are available, by fitting the

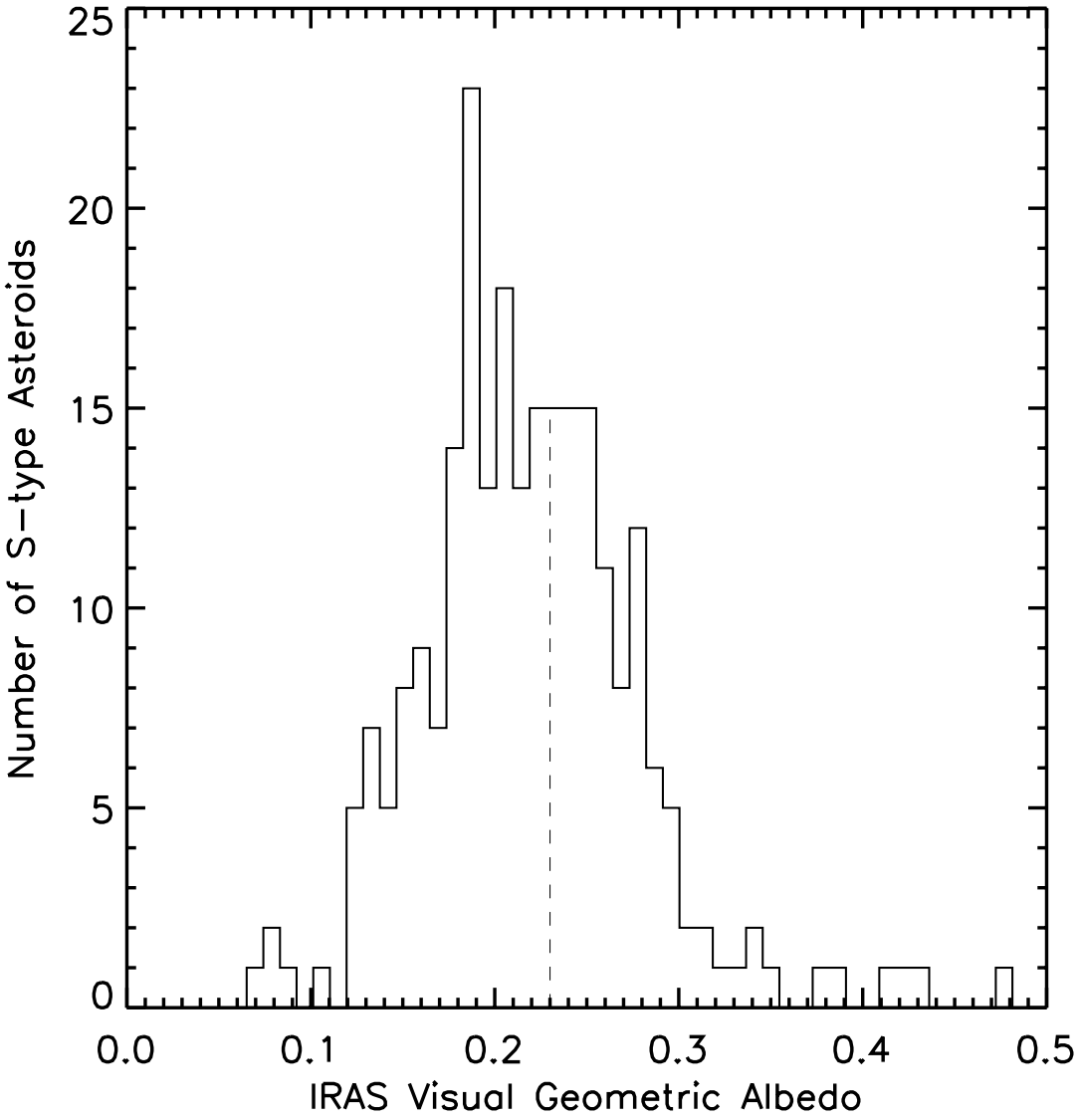

Figure 4.11 The histogram of the visual geometric albedos of 244 S-type asteroids measured by IRAS Minor Planet Survey and archived in NASA PDS (Neese, 2002a). The dashed line shows the geometric albedo of Eros (0.23) at 550 nm as derived in this paper.

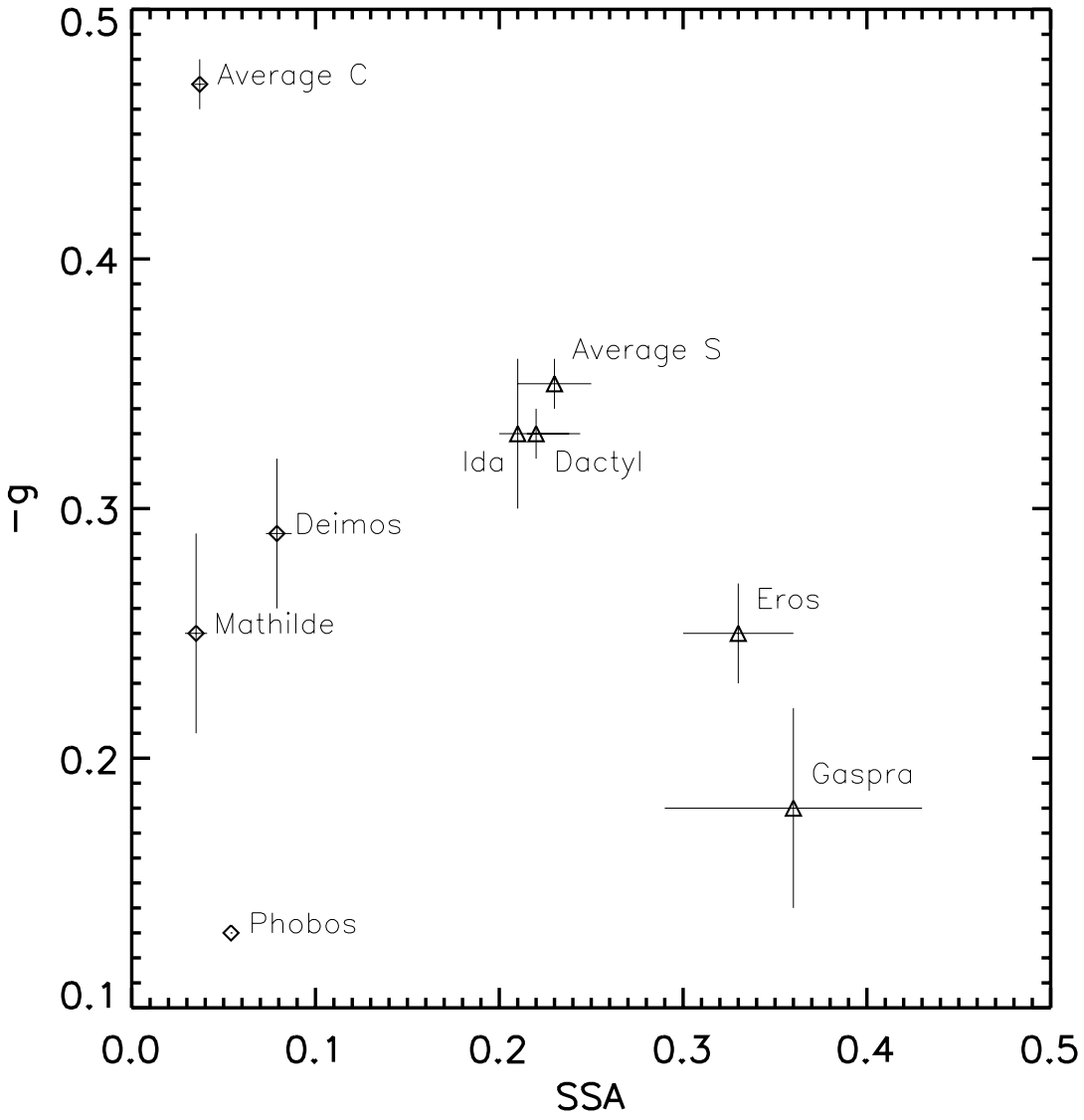

Figure 4.12 The asymmetry factor g as a function of SSA for several S-type asteroids (triangles) and C-type asteroids (diamonds). The error estimates for Phobos are not available. Eros is a typical S-type asteroid sharing the medium high SSA and moderate backscattering phase function of other S-type asteroids. The values for objects other than Eros used in this plot are found from: (253) Mathilde, Clark et al. (1999); Deimos, Thomas et al. (1996); Phobos, Simonelli et al. (1998); Ida and Dactyl, Helfenstein et al. (1996); Gaspra, Helfenstein et al. (1994); average S and C, Helfenstein and Veverka (1989).

roughness parameters at different locations. If no large grain size change is detected, then it will have to be attributed to a spectrally bland mineral with different albedo added into the regolith at different locations. Of course this could also be tested by measuring the reflectance spectra at locations which show albedo variations, but the possible different temperatures resulted from the illumination conditions may also affect the spectra in the similar manner as the grain size does.

4.5 Summary

The photometric parameters of Eros have been improved in this chapter using almost all the available historical data at visible wavelengths. Theoretical forward modeling is used to take into account the highly irregular shape of Eros in fitting the disk-integrated lightcurves from ground observations. The data we used, the main procedures we followed, and the important results and conclusions we reached are summarized below.

1. The ground-based lightcurves have been used to construct a phase function from their primary maxima. The amplitude and the width of opposition effect are found to be 1.4 ± 0.1 and 0.010 ± 0.004, respectively. According to the results from the model simulations, these are the best modeled opposition parameters of Eros's disk-integrated surface. Other parameters fitted in this step should be taken only for instructive purpose for the following steps and not kept as final results.

2. The disk-resolved bidirectional reflectance data are obtained from the NEAR MSI images taken through seven filters centered from 450 nm to 1050 nm, and at about 100 km spacecraft range from Eros. Coupled with Eros's shape model, these data are used

to fit Hapke's parameters other than the opposition effect parameters because the phase angles of these data are from 53° to 110°, where the opposition surge almost disappears.

3. The fit to the disk-resolved data yields Hapke's parameters for Eros at seven wavelengths. The parameters at 550 nm include an SSA of 0.33±0.03, an asymmetry factor g of -0.25±0.02, and a roughness parameter of 28°±3°. Combined with the opposition parameters obtained from fitting the ground-based data, a geometric albedo of 0.23 and a Bond albedo of 0.093 at V-band are calculated.

4. Hapke's parameters of Eros are similar with those of other S-type asteroids. Our resultant SSA, geometric albedo, and Bond albedo are smaller than previously found, but still consistent with the spectrum of Eros and the albedo of Eros at longer wavelengths. These values move Eros very close to the values of typical S-type asteroids. Compared to the other two S-type asteroids that were studied intensively, Eros is slightly darker than Gaspra, but brighter than Ida by about 20% in terms of the SSA.

5. From the mixing ratio of the minerals on Eros's surface regolith from its near-IR spectra (McFadden et al., 2001; Bell et al., 2002; Izenberg et al., 2003), and previous laboratory studies of the single-scattering albedo of the olivine-pyroxene mixture (Lucey, 1998), space weathering on Eros taken into account, the grain size of Eros's surface regolith particles is estimated to be between 50 and 100 μm.

6. The effect of CBOE is estimated from a formulation that only considers the SHOE as an approximation. The CBOE component contributes comparably with, if not dominantly to, the SHOE for the opposition effect of Eros, and the total amplitude of the opposition surge of Eros is likely to be about 1.2 to 1.4, if either, SHOE or CBOE, is weak relative to the other.

7. The roughness parameters fitted at seven different wavelengths but at the same resolution are almost the same, but a trend with spatial resolution has been noticed. This is an indication that the roughness parameter is a local parameter instead of a global parameter, which can be affected by the resolution of the photometric data. Further confirmation is needed both experimentally and theoretically. For Eros, the large scale roughness is very important in determining the disk-averaged reflectance of Eros, and on the scale of the order of several kilometers, Eros's surface is dominated by macroscopic roughness from its regolith.

Chapter 5

The Nucleus of Comet 19P/Borrelly

5.1 Background

Comet 19P/Borrelly is a Jupiter Family Comet (JFC). Some of its primary characteristics are summarized in Table 5.1. NASA's Technology Demonstration Program's Deep Space 1 flew past comet Borrelly in Sept. 22, 2001 with a close approach distance of 2171 km, took a dozen spatially resolved images of its nucleus (Soderblom et al., 2004a), making this comet the second to be imaged by spacecraft after comet 1P/Halley in 1986. Comet Halley, as an intermediate-period comet, is believed to represent the composition of distant long-period comets in the Oort cloud. In contrast, comet Borrelly is believed to have formed in the Kuiper Belt, and had its surface processed by heating in the inner solar system for a long time since being perturbed by Jupiter into its current orbit. Borrelly appears to be considerably depleted in carbon-chain molecules compared to most long-period comets and Halley (A'Hearn et al., 1995). This difference is thought to be an indication of the compositionally distinct regions where they formed. Comet Borrelly then is the first and currently the only JFC that we can study in great detail.

The DS1 flyby occurred 8 days after comet Borrelly passed perihelion. During the last 90 minutes, the nucleus, inner coma, and jets were resolved. Images at visible-wavelength and spectra in the near-IR from 1.3 to 2.6 μm were collected with the Miniature Integrated Camera and Spectrometer (MICAS) onboard the DS1 spacecraft. The nu-

Table 5.1. Some primary characteristics of comet Borrelly

Properties	Values
Geometric albedo	0.084[a]
Size	$4.0\pm0.1 \times 1.58\pm0.06$[b]
Rotational Period	25 ± 0.5 hours[c]
Orbital period	7 years
Perihelion	1.36 AU
Orbital inclination	30°
Orbital eccentricity	0.62
Water production rate	2.5×10^{28} molecules/s at perihelion[d]

[a]this work

[b]Buratti et al. (2004)

[c]Lamy et al. (1998)

[d]Schleicher et al. (2003)

cleus of comet Borrelly is shown to be a dark bowling pin shaped object with large brightness variations across the surface (Fig. 5.1). Those images provide stereoscopic views of the nucleus, from which the shape of the illuminated part was constructed (Kirk et al., 2004a; Oberst et al., 2004). Two collimated jets are observed, and their directions are determined (Soderblom et al., 2004a), consistent with ground-based observations (Farnham and Cochran, 2002; Schleicher et al., 2003). The spectrum of Borrelly's nucleus shows a dry and hot surface, but contains no identifiable spectral features (Soderblom et al., 2004b). The disk-resolved images turned comet Borrelly from a celestial body into a geological object. Its surface geology was discussed on the basis of morphological features, and several geological units have been defined, correlated with particular geological processes (Britt et al., 2004).

The photometry of Borrelly's nucleus has been discussed by Buratti et al. (2004) from both earlier ground and HST observations and the DS1 images. Disk-resolved photometric analysis has been carried out for a cometary nucleus for the first time by Buratti et al. (2004), although a simple biaxial ellipsoidal shape model was used to approximate the nucleus. The surface is very dark, and the phase function of Borrelly is similar to those of dark C- or D-type asteroids. A very large reflectance variation is observed on the surface of Borrelly's nucleus, which is not likely purely due to shadowing. Different explanations have been proposed. Buratti et al. (2004) and Oberst et al. (2004) considered the reflectance variation as the intrinsic variation of albedo, while Kirk et al. (2004a) showed that roughness variation over the surface accounts better for the variations at different phase angles (Fig. 5.2).

With the help of a real shape model, we can improve models of the photometric

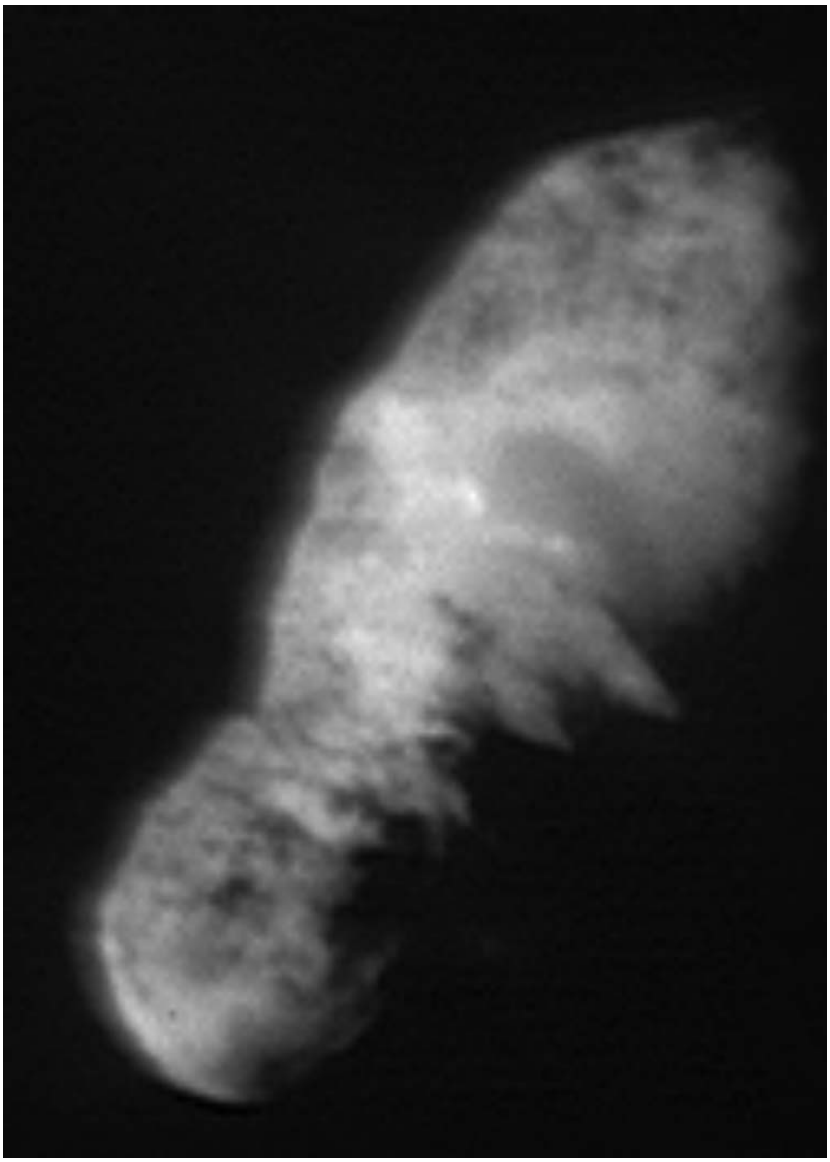

Figure 5.1 The last image of Borrelly's nucleus acquired by DS1. Phase angle is 51.6°. Resolution is 46.7m/pixel. The Sun is to the left of the nucleus, and above image plane by about 38°. Rotational pole is about 45° counter clockwise from up as calculated with ground-based results (Farnham and Cochran, 2002). We see a large brightness variation over the surface.

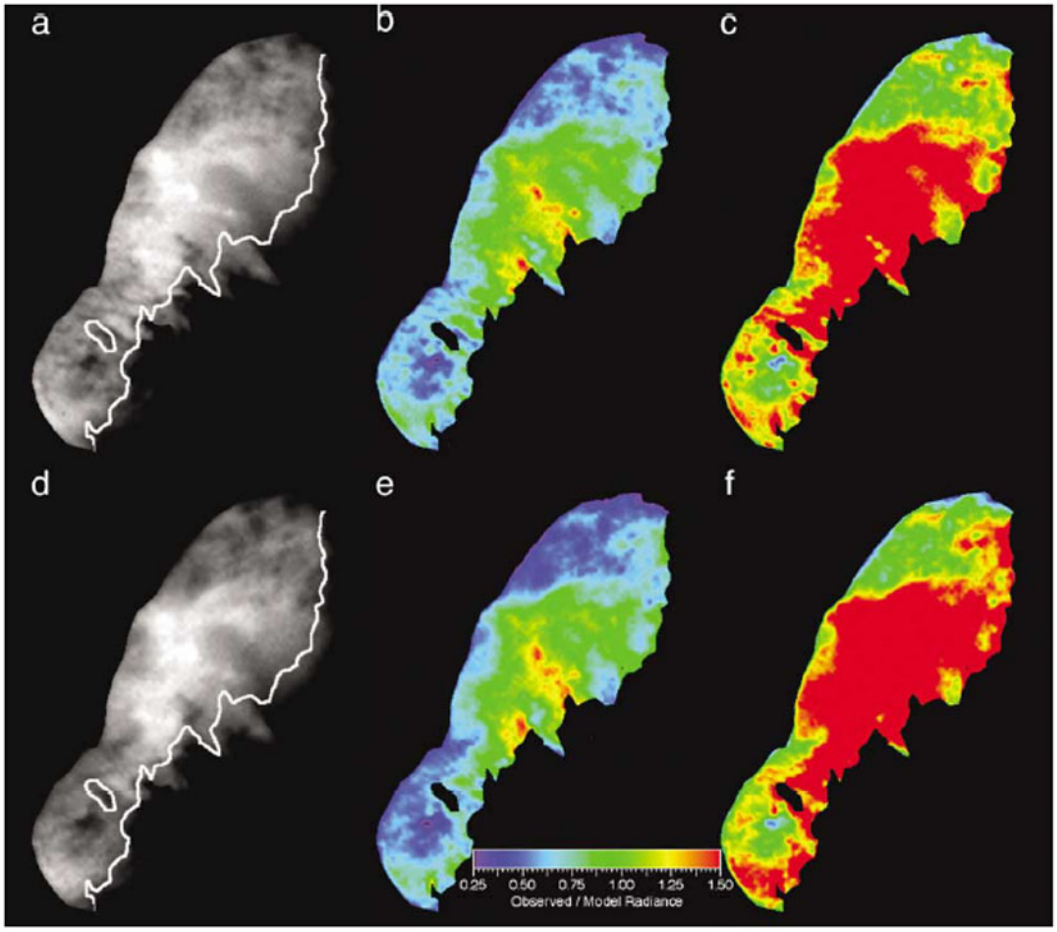

Figure 5.2 The Fig. 9 in Kirk et al. (2004a), showing his modeling with different roughness for smooth terrains and mottled terrains. The first row shows the DS1 image at 51.6° phase angle and models, and the second row 59.6°. The first column shows observed images, second column the ratio of original images and models with 20° roughness parameter, and the third column the ratios with 60° roughness. Green means good modeling.

properties of the surface of Borrelly's nucleus, similar to the disk-resolved photometric analyses for asteroids. I will present my disk-resolved photometric analysis in the following sections, which will be an attempt to apply disk-resolved Hapke's analysis to a cometary nucleus with its real shape model, and expand the technique that has been widely used for asteroids to the regime of comets. It will help explain the photometric variations over the surface of Borrelly, and finally correlate the photometric variation to cometary activity. In addition to comet Borrelly, the similar spatially resolved data for the nucleus of comet Wild 2 have become available from Stardust, and we are expecting those kind of images of comet Tempel 1 from Deep Impact (DI), another of NASA Discovery Program mission. Therefore, this work will provide necessary guidelines and comparisons with future work.

In the following section, the disk-integrated phase function constructed from earlier ground-based observations and DS1 images will be discussed and modeled. Then disk-resolved images are used to perform disk-resolved photometric modeling for each photometrically distinct terrain in the next section. I will present the disk-resolved thermal modeling for the surface of Borrelly's nucleus with the shape model in the next section, and compare it with DS1 observations. Then possible correlations between cometary activities and the photometric heterogeneity of the surface are discussed.

5.2 Disk-integrated Phase Function

Previously the brightness of the nucleus of comet Borrelly was observed both from the ground and from HST (Weissman et al., 1999; Rauer et al., 1999; Lamy et al., 1998).

The disk-integrated phase function can be constructed from those observations and DS1 images (Fig. 5.3). The images used in our studies were downloaded from USGS website, and have been calibrated to standard reflectance unit $< I/F >$ (Soderblom et al., 2004a), where for a 100%-reflecting Lambert disk, the $< I/F >$ is 1, or equivalently, I is the irradiance received by a detector, and πF is the incident flux. The total reduced magnitude $M(1, 1, \alpha)$ of Borrelly is measured by integrating the I/F values for each image, and scaled by the apparent magnitude of the Sun and R-band, -27.29 (Cox, 1999), corresponding to the equivalent wavelength of DS1 clear filter through which all images were acquired. The disk-integrated phase function from DS1 images and earlier ground-based observations is shown in Fig. 5.3, where the data points for ground-based observations are the magnitudes of lightcurve maxima as used in Buratti et al. (2004).

However, as shown in the plot, our measurements from DS1 images are inconsistent with the values measured by Buratti et al. (2004), with a factor of about 3 difference, which prevent our data points from making a smooth phase function together with earlier ground-based observations. The contamination of coma is only responsible for a tiny fraction of it, because as estimated from the ambient dark sky surrounding the nucleus, we found that less than 2% total brightness is contributed by coma. This is consistent with the estimate of coma made by Buratti et al. The cause of the discrepancy is still under investigation, and one possibility could be the confusing π factor in defining the reflectance unit I/F (see Chapter 2). For this reason, we did not perform Hapke's modeling to the disk-integrated phase function presented here.

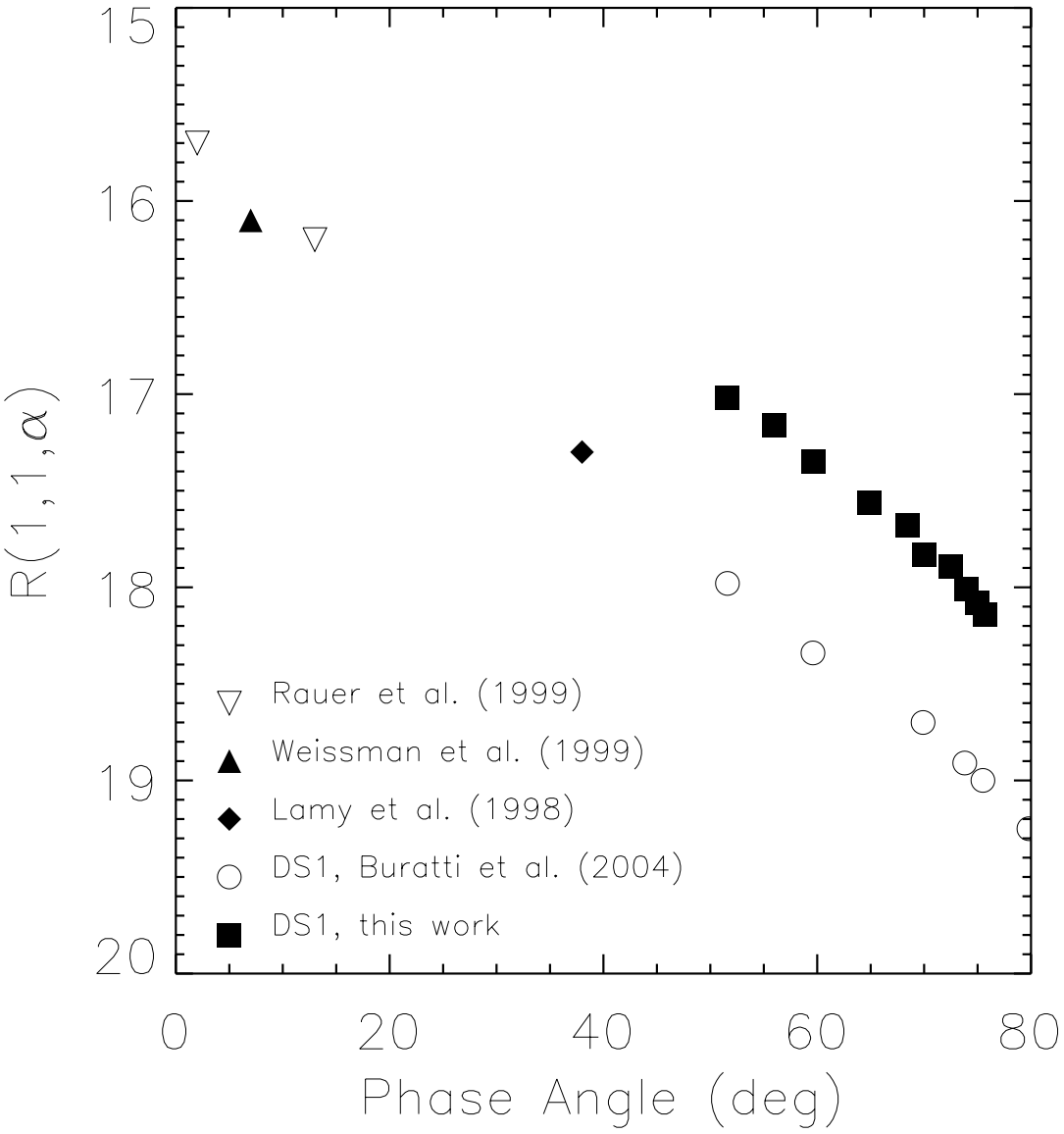

Figure 5.3 Whole-disk phase function of comet Borrelly's nucleus.

5.3 Disk-Resolved Photometry

From the disk-resolved images of comet Borrelly's nucleus obtained from DS1's flyby, the Hapke's parameters can be modeled better than from the disk-integrated phase function, especially for the surface roughness, $\bar{\theta}$, and for the asymmetry factor of single particle phase function, g. However, due to the large photometric variations seen on Borrelly's disk (Fig. 5.1), a single photometric model cannot describe the whole surface well enough, and we have to use different parameter sets to model the different terrains on Borrelly.

5.3.1 Terrain partitioning

The surface of Borrelly has been divided into several geological units according to their brightness and appearance by Britt et al. (2004) (Fig. 5.4). But comparing the terrain map with the phase ratio map constructed from the image at 51.6° phase angle and 59.6° phase angle (Fig. 5.5) as shown in Kirk et al. (2004a), we found that even within a single terrain as defined by Britt et al. (2004), the phase ratio varies. For example, the mottled terrain on the large end of the nucleus show two distinct phase ratios. Phase ratio is a measurement of the change of reflectance with respect to phase angle, determined primarily by the surface roughness, $\bar{\theta}$, and the asymmetry factor, g. Thus different phase ratios indicate different photometric properties of those two different areas, although they have similar brightness as seen from the image at 51.6° (Fig. 5.1). For the purpose of photometric modeling, a terrain partitioning with each terrain having the same photometric properties across, and being able to be modeled by a single set of Hapke's parameters is desired. For

this purpose, we modified the terrain partitioning from Britt et al. (2004) to produce our map of photometric terrains (Fig. 5.6).

5.3.2 Hapke's modeling

With this photometric terrain partitioning, we performed Hapke's fitting to each terrain with the disk-resolved images from 51.6° to about 74°. However, with the data at this range of phase angles, the opposition effect is not able to be modeled, and we assumed the amplitude and the width of opposition effect B_0=1.0 and h=0.01, which are close to the values found from disk-integrated phase function (Buratti et al., 2004). Calculations show that the the uncertainties in other three parameters caused by the uncertainties of B_0 and h will not exceed one tenth of the uncertainties of B_0 and h. *i.e.*, if the error of B_0 and h is 10%, then this will cause no larger then 1% error in the modeled three other parameters. In addition, for those small terrains such as #14, #16, #17, #21-#25, the variations of scattering geometry does not change much over each terrain, making the fitting difficult with large uncertainties in modeled parameters.

In our Hapke's modeling, the basic unit of reflectance data is pixel. We used the radiometric calibrated disk-resolved images downloaded from USGS website, specifically, from image `mid_1_2` through image `near_1` in the original sequence names. The reflectance reading of each pixel in the I/F images is one data point in our photometric modeling. The SPICE data of DS1's flyby archived in NASA PDS Small Bodies Node (SBN) (Semenov et al., 2004c) are used, coupled with the USGS Digital Elevation Map (DEM) shape model (Kirk et al., 2004a) archived in SBN as well (Kirk et al., 2004b), to calculate the incidence angle and emission angle for each pixel. Then the reflectance data

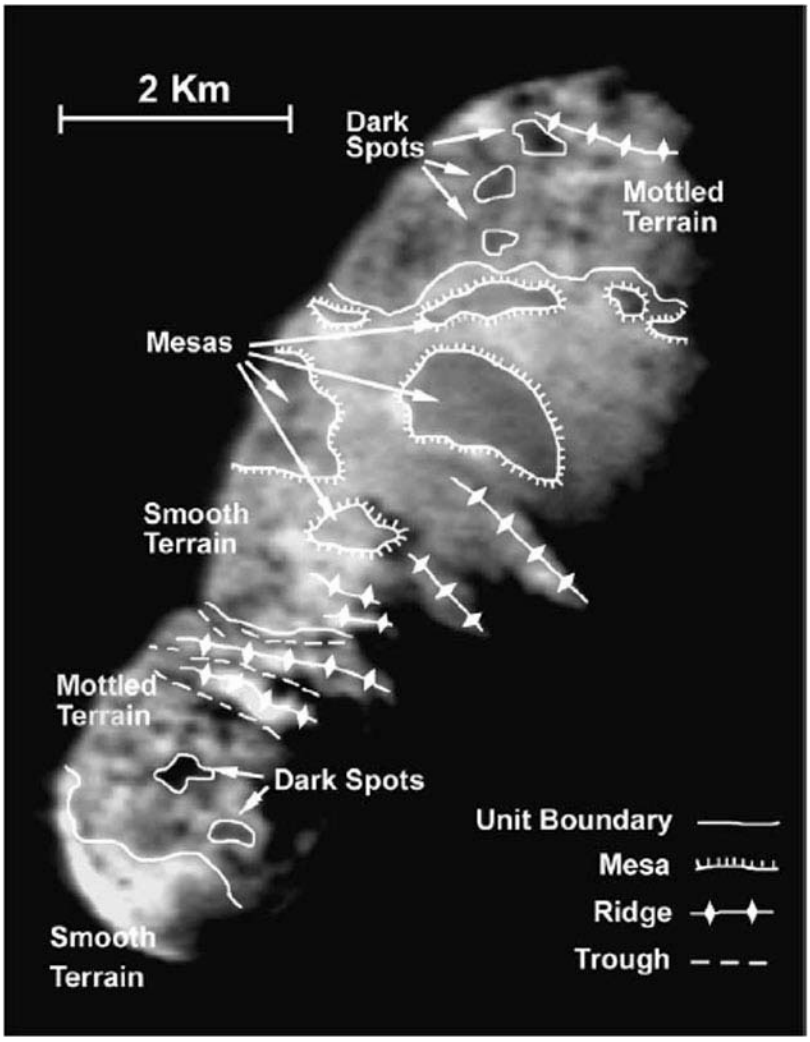

Figure 5.4 Geological terrains on Borrelly's nucleus as defined in Fig. 4, Britt et al. (2004).

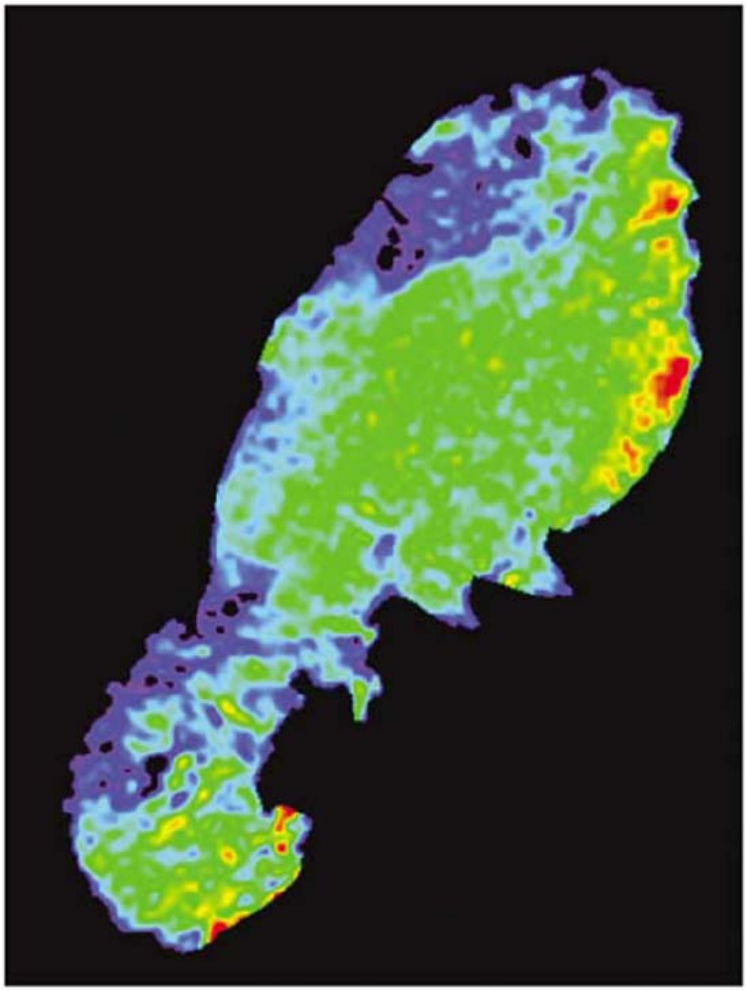

Figure 5.5 Phase ratio map as shown in Fig. 8, Kirk et al. (2004a), representing the ratio map of brightness at phase angle 59.6° and 51.6°.

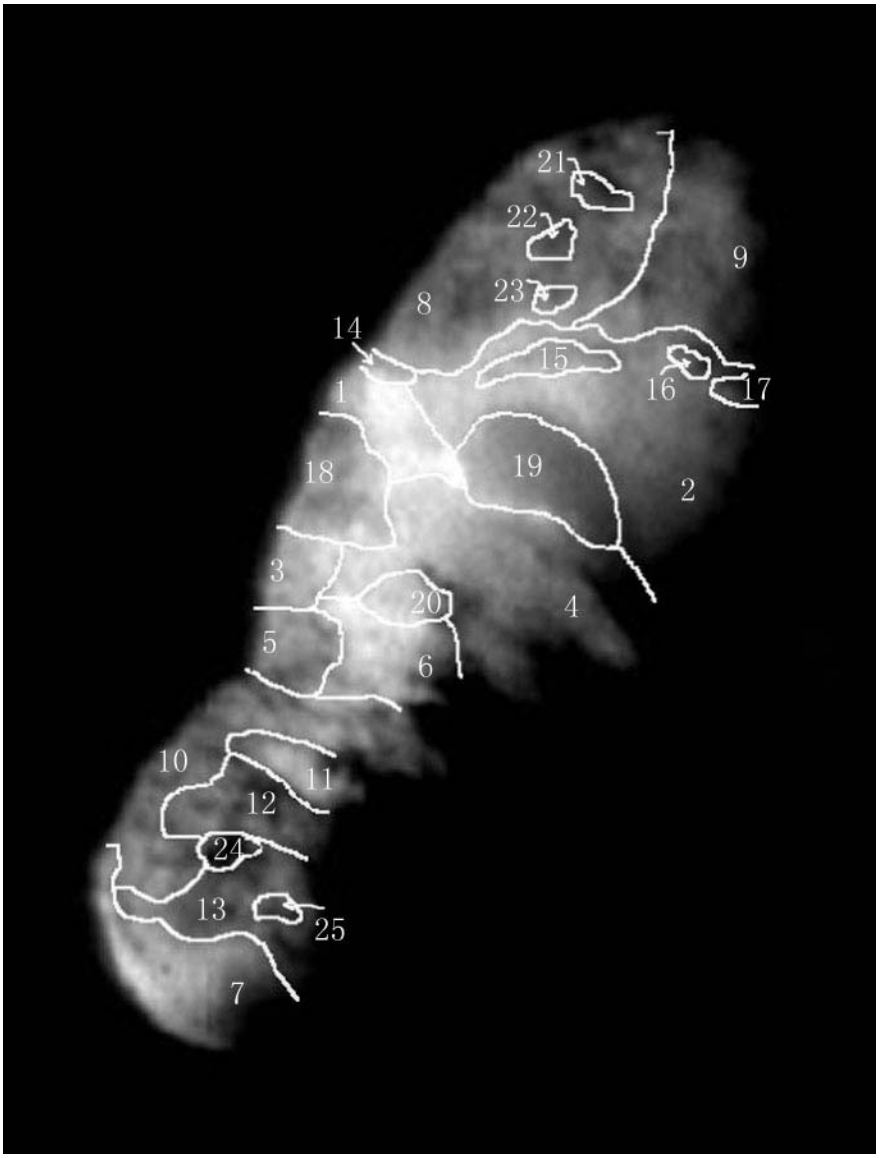

Figure 5.6 Our photometric terrain partitioning. Each terrain shows different photometric properties from others and is modeled as one unit. Totally 25 terrains are identified, numbered from 1 to 25. #1-#7 are in smooth terrains in the definition of Britt et al. (2004), #8-#13 mottled terrains, #14-#20 mesas, and #21-#25 dark spots.

as a function of incidence angle, emission angle, and phase angle, are ready to be fitted with Hapke's model. The modeling is then carried out for every terrain in our 25-terrain partitioning.

The best fitted Hapke's parameters for those large terrains are listed in Table 5.2. Also listed are the RMS of the corresponding fitted parameter sets. The goodness of a typical Hapke's fitting for terrain #2 is plotted in Fig. 5.7 and 5.8. The residual for this terrain is about 18%, and the systematic variation of residuals with respect to incidence angle and emission angle is tiny. The modeled parameter maps for w, g, and $\bar{\theta}$ are shown in Fig. 5.9, 5.10, and 5.11, respectively, with their histograms plotted below.

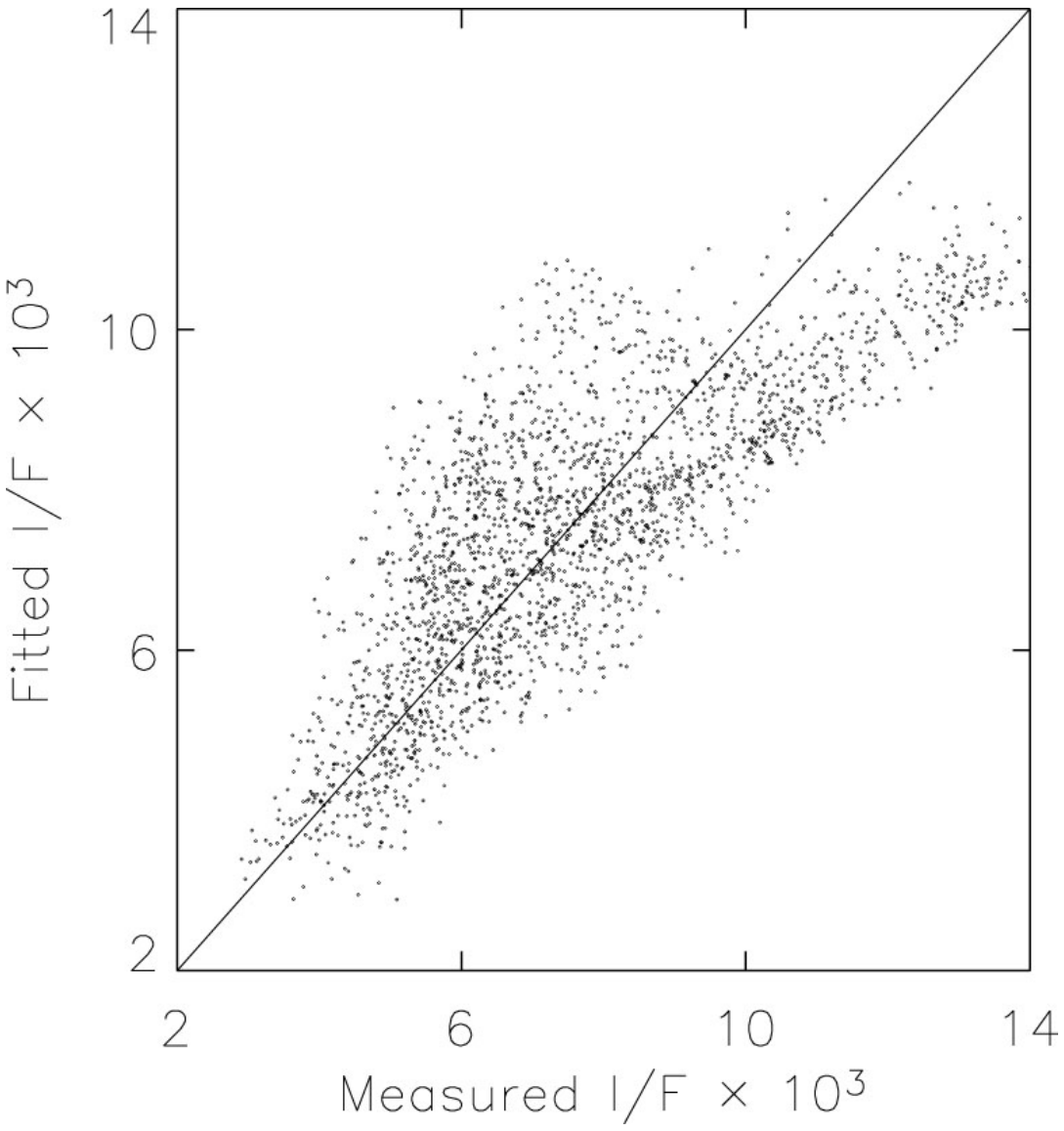

Figure 5.7 The goodness plot of Hapke's modeling for terrain #2 as an example. Shown here is the modeled bidirectional reflectance plotted as a function of measured values. The solid line represents perfect matching between model and observation. The RMS error for this modeling is about 18%.

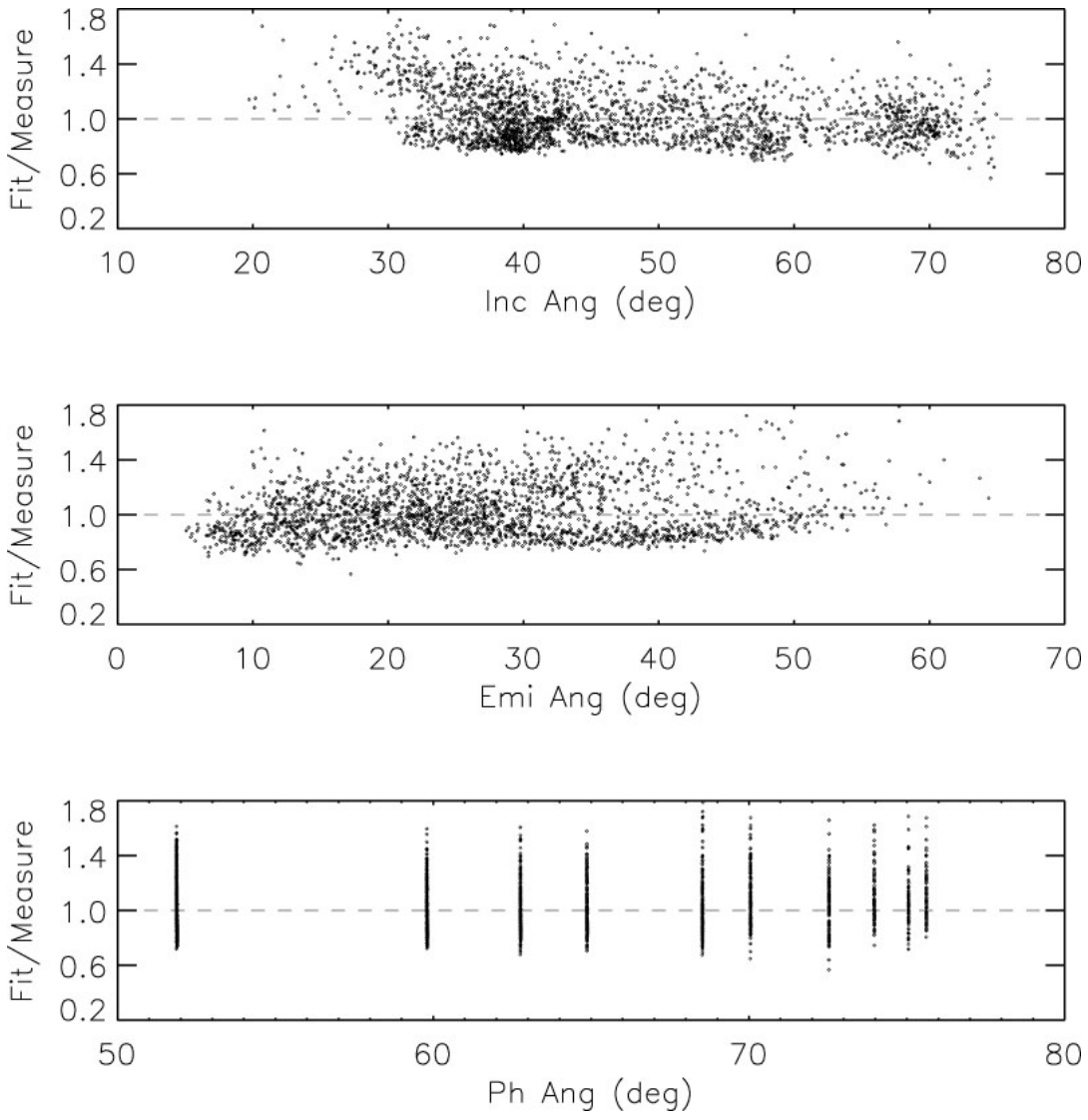

Figure 5.8 Another goodness plot of Hapke's modeling for terrain #2 as an example. The ratio of modeled reflectance to observed reflectance is plotted as a function of incidence angle i (upper panel), emission angle e (middle panel), and phase angle α (lower panel).

Table 5.2. Modeled Hapke's parameters for the 25 terrains on Borrelly's surface as shown in Fig. 5.6.

Index	Number of data points	w	g	$\bar{\theta}$	RMS	A_{geo}	A_{Bond}
1.	350	0.067	-0.40	21.	13.1	0.066	0.020
2.	2264	0.054	-0.35	13.	18.4	0.044	0.016
3.	153	0.052	-0.42	22.	10.7	0.055	0.016
4.	2101	0.068	-0.33	22.	23.2	0.051	0.019
5.	290	0.044	-0.47	23.	15.0	0.058	0.014
6.	606	0.072	-0.35	30.	23.8	0.058	0.019
7.	664	0.059	-0.24	40.	17.9	0.032	0.012
8.	1949	0.052	-0.68	19.	19.1	0.214	0.021
9.	972	0.078	-0.15	55.	12.0	0.032	0.011
10.	758	0.050	-0.66	6.5	22.7	0.183	0.020
11.	144	0.062	-0.70	11.	15.6	0.300	0.026
12.	124	0.031	-0.46	8.	16.3	0.039	0.010
13.	596	0.038	-0.40	30.	21.2	0.038	0.010
14.	22	0.054	-0.37	25.	5.0	0.046	0.015
15.	202	0.053	-0.42	18.	11.6	0.057	0.016
16.	90	0.057	-0.10	34.	11.0	0.020	0.011
17.	No fit						
18.	448	0.055	-0.54	25.	16.6	0.101	0.018
19.	1102	0.057	-0.30	18.	14.2	0.038	0.016
20.	199	0.063	-0.35	18.	10.1	0.051	0.018

Table 5.2—Continued

Index	Number of data points	w	g	$\bar{\theta}$	RMS	A_{geo}	A_{Bond}
21.	107	0.039	-0.65	0.	17.7	0.128	0.015
22.	83	0.039	-0.61	16.	13.6	0.101	0.014
23.	44	0.041	-0.54	22.	8.4	0.075	0.014
24.	87	0.031	-0.27	35.	23.8	0.019	0.007
25.	48	0.063	-0.11	54.	11.3	0.023	0.008

Overall, the scatter in modeling is about 17% on average. The residual map of the modeled disk for image `near_1` is shown in Fig. 5.12, and the corresponding histogram compared with the histogram of the original image is shown in Fig. 5.13. We notice that the greatest residual appears close to the edge of each terrain, and the residual is small close to the interior of each terrain. This could be due to a slight misalignment between the photometric terrain partitioning and the real terrain boundary during photometric modeling. Because the phase angle and viewing geometry for each image change from one image to another, while the photometric terrain partitioning is defined only through the last two images at phase angle 51.6° and 59.6°, the misalignment of defined terrain boundaries and real boundaries is possibly magnified for images at large phase angles and S/C ranges, given Borrelly's very irregular shape and large incidence and emission angles for part of the surface. This introduces uncertainties in the modeled parameters. Of course the large residual close to terrain boundaries could also be because photometric properties on the surface vary from terrain to terrain gradually, and there does not exist a definitive boundary of photometric properties between terrains. This is true for some terrains such as #8 and #9, where we do not see a clear boundary in any single image, but their photometric difference is revealed from fitting several images at different phase angles. Finally, in addition to the fact that we found a large variation of photometric properties across the surface, some large residuals in small parts of a terrain element probably indicates small scale photometric variations that we actually missed in defining photometric terrains.

The uncertainties of Hapke's parameters are dominated by both the uncertainty of absolute radiometric calibrations and the noise in reflectance data. The former has been determined to be better than 10-15% (Buratti et al., 2004). The latter presents itself as

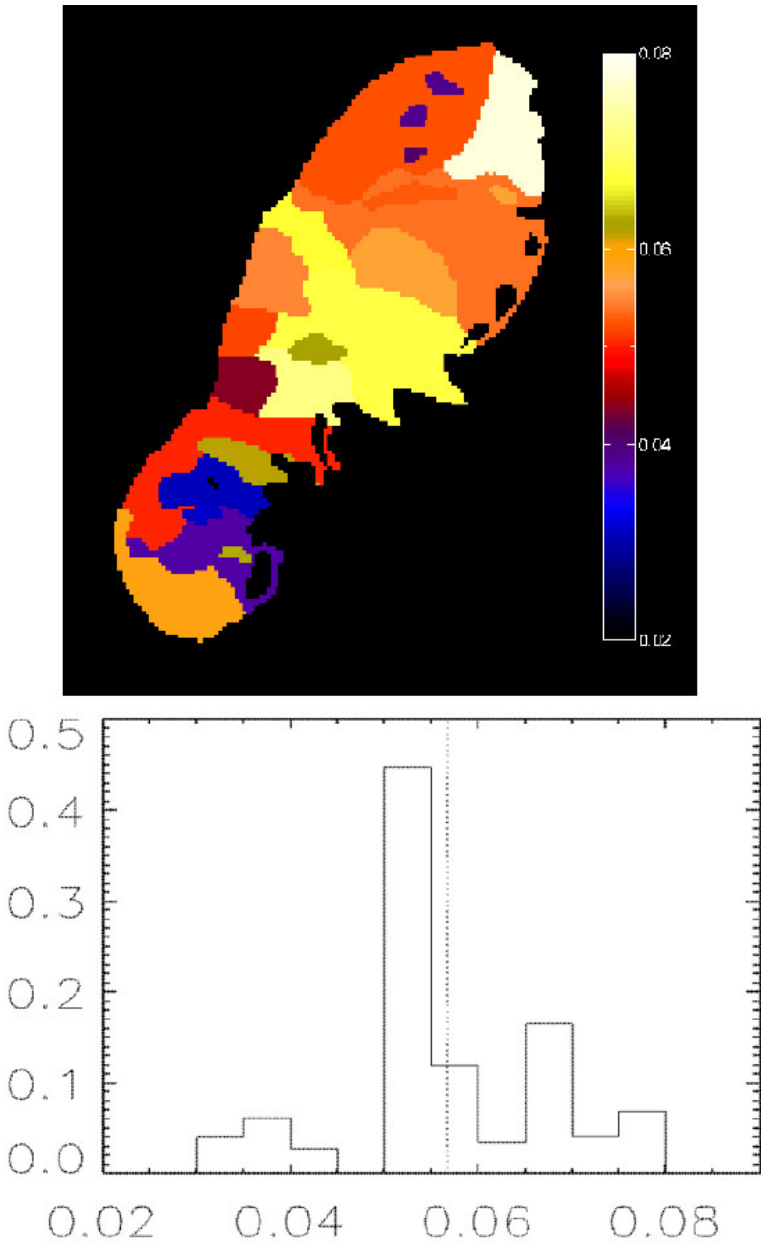

Figure 5.9 The map of modeled SSA (upper panel) and its histogram (lower panel). The dotted line marks the average SSA over the imaged disk.

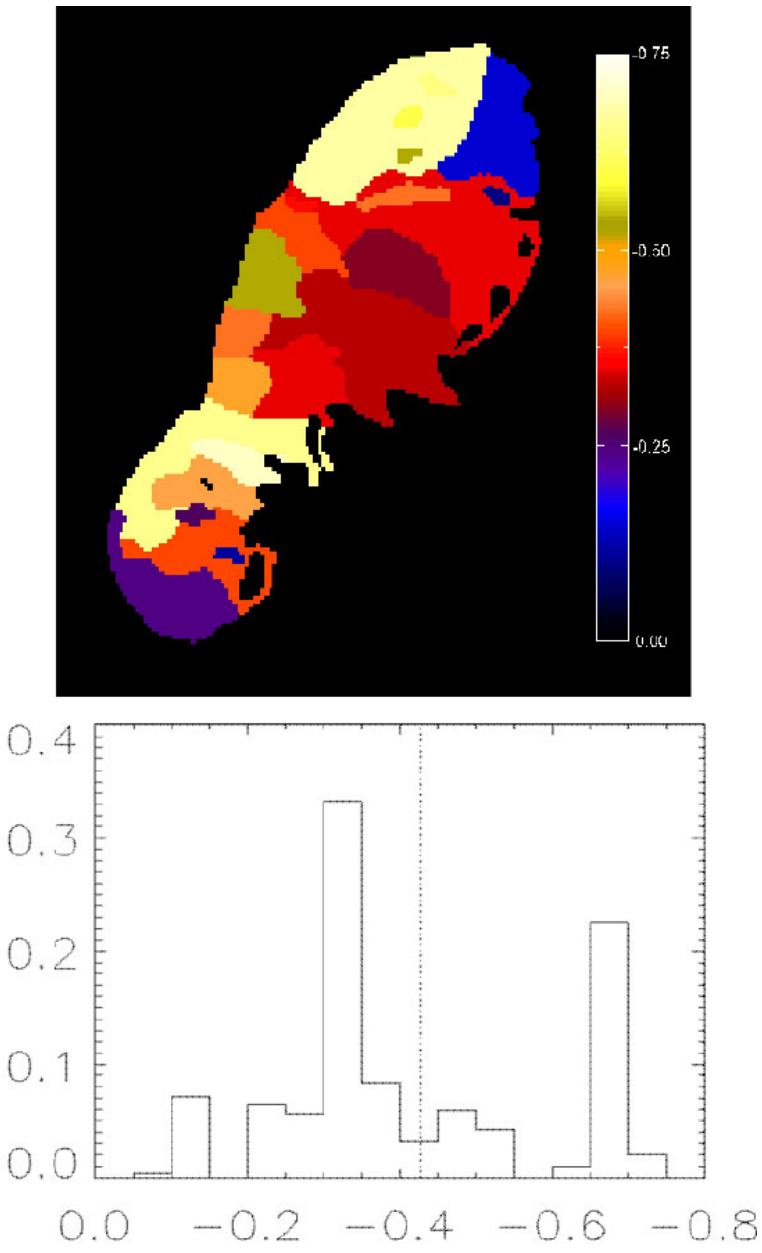

Figure 5.10 The map of modeled asymmetry factor g (upper panel) and its histogram (lower panel). The dotted line marks the average asymmetry factor over the imaged disk.

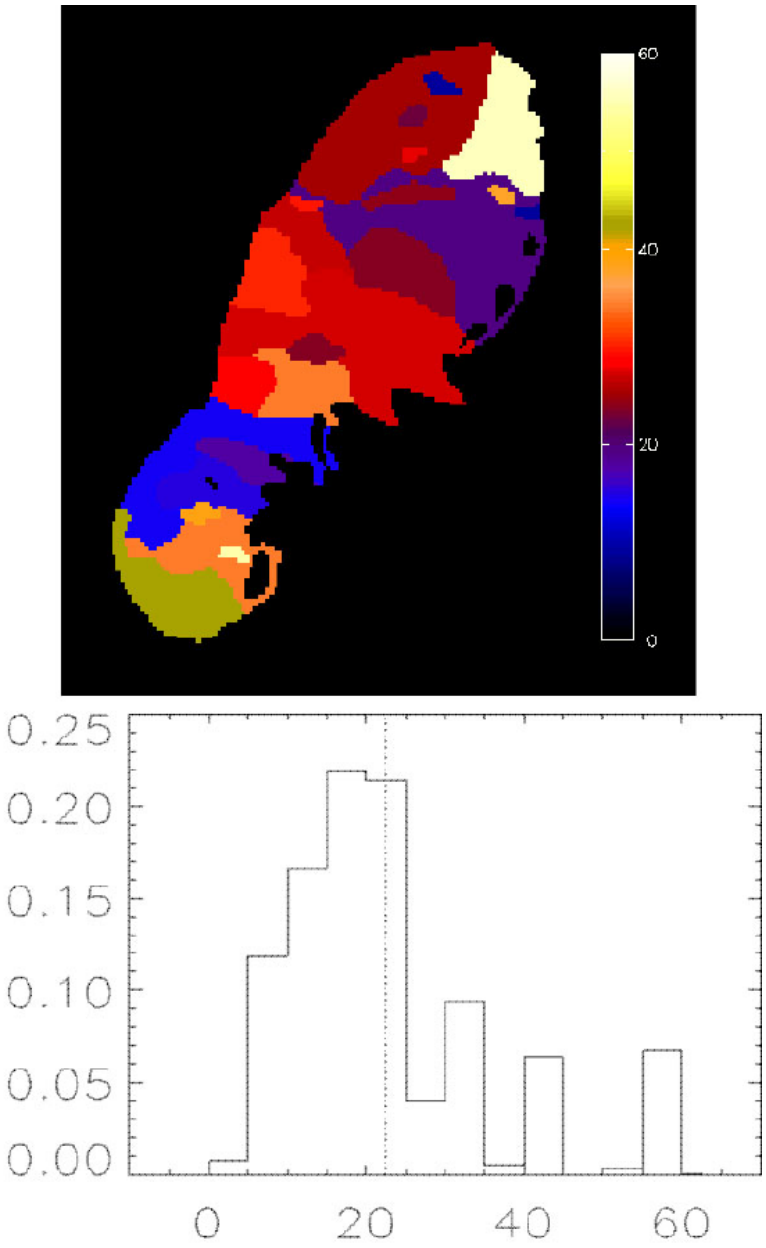

Figure 5.11 The map of modeled roughness (upper panel) and its histogram (lower panel). The dotted line marks the average roughness over the imaged disk.

the scatter of the residuals of fitting as shown in Table 5.2, with an average about 17%. The overall uncertainties of the modeled Hapke's parameters are thus between 15% and 25%, varying from terrain to terrain. Another possible source of uncertainty is the coma, which we have not had any successful attempt to remove. The total intensity from coma is only 1-2% as estimated from ambient dark sky, and much less than 1% on the last image, `near_1`. Therefore the average photometric properties of the disk are not significantly affected by the coma. But in fitting individual terrains, coma could affect the reflectance measurement by up to 10%, increasing the uncertainties of the fitted parameters for some terrains that are obviously affected by coma, such as terrain #1, #4, which are possibly affected by the two collimated jets, and #19, which is certainly affected by the fan jet. The overall uncertainties for terrain #4 could be as large as 28%.

Another goodness check of the photometric model is the phase ratio map as shown in Fig. 5.14 overlapped with terrain partitioning. We have made the color bar used in our modeled ratio map as similar with the one used in Fig. 5.5 as possible, so that the model and the observations can be directly compared through colors. The agreement is reasonably good, and some large features in the phase ratio map are modeled very well. Some photometrically distinct terrains in the middle of the disk produce very smooth boundaries in the modeled phase ratio map, agreeing very well with the real map, and demonstrating the ability of photometric modeling to distinguish surface photometric heterogeneity. The large phase ratio apparent in the observed phase ratio map (Fig. 5.5), close to the terminator to the right of Borrelly's disk, is probably due to artifacts introduced by registering two images with different viewing geometries in constructing the phase ratio map. Those artifacts are not present in the modeled map. On the neck close to the small end in the

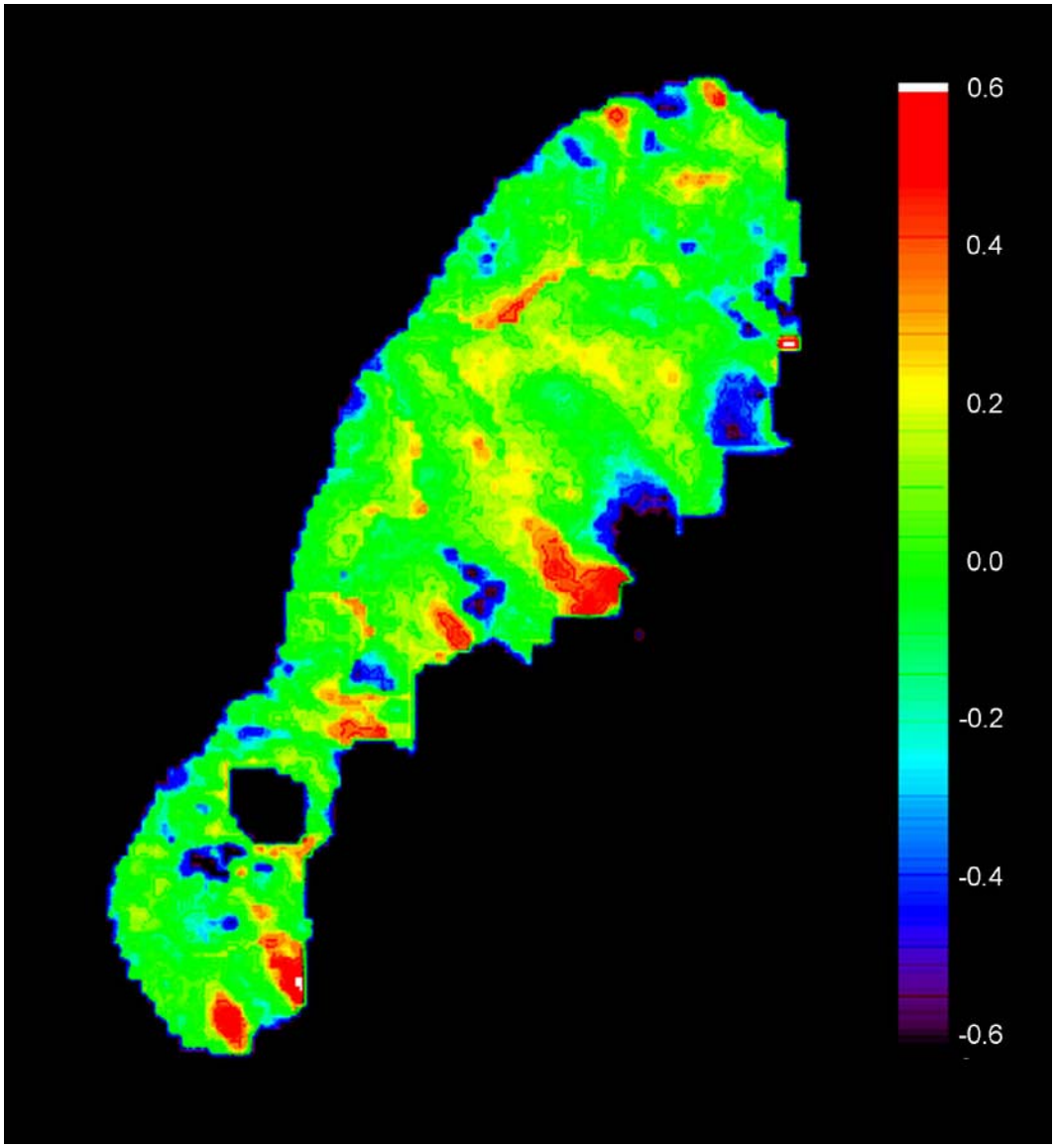

Figure 5.12 Residual map of our photometric model for the `near_1` image (Fig. 5.1).

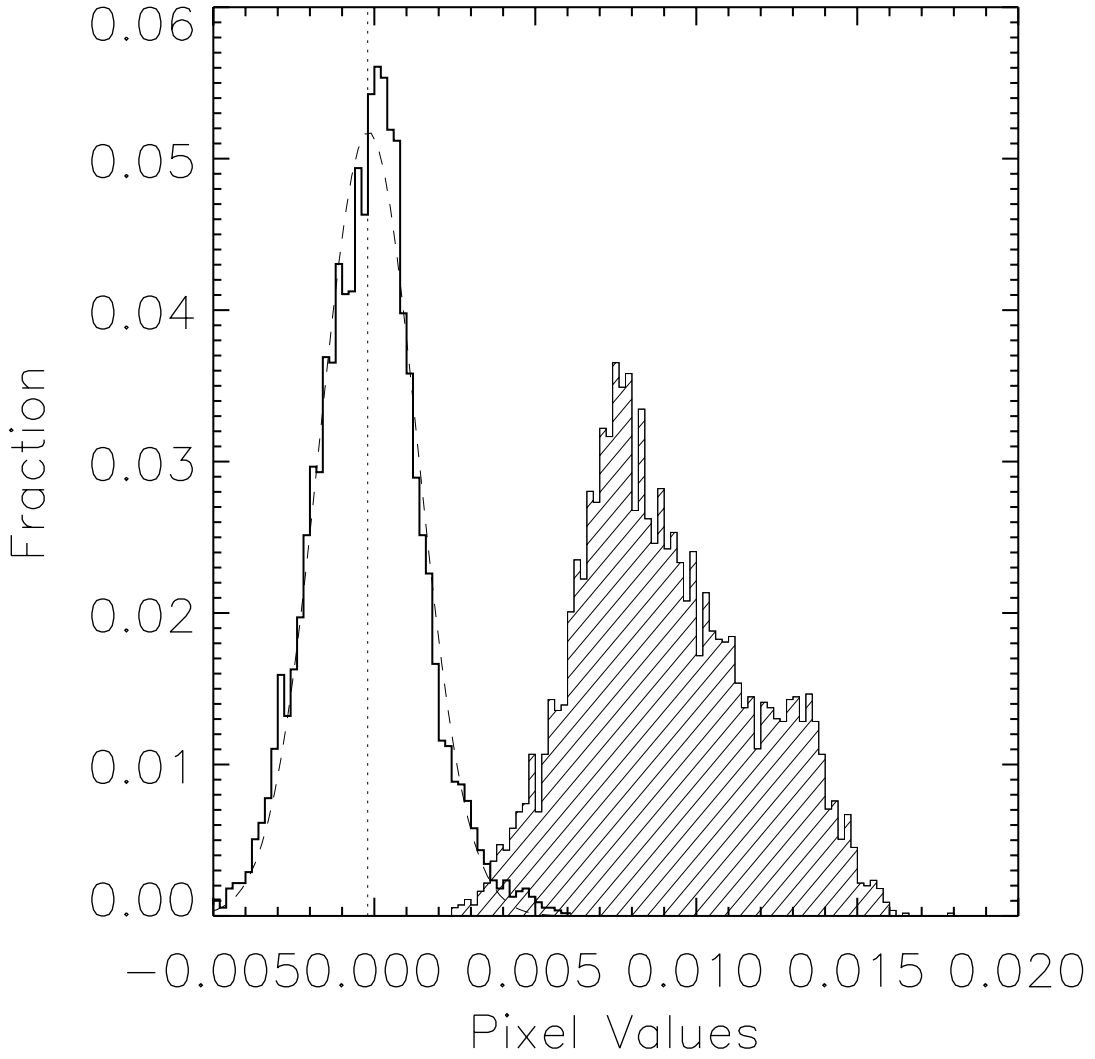

Figure 5.13 The histogram of the residual map (Fig. 5.12) is plotted. A dashed line represents the Gaussian fit to the residual, with a mean of -0.0001, and standard deviation of 0.0015. Plotted as a shaded histogram are the pixels of the original image, `near_1`, as a quantitative comparison.

lower half of the disk, where the surface looks very complicated, our model is not good as shown by the complicated pattern in the residual map (Fig. 5.12) and by the comparison of observed and measured phase ratio map (Fig. 5.5 and 5.14). Possible causes include, 1) terrains are too small, 2) our terrain partitioning is not well aligned with real terrains, and 3) complexity existed within each terrain. Photometric modeling for other large terrains on the central and upper part of the disk, as well as on the small end, is good in terms of reconstructing the phase ratio map.

From our modeled parameter maps for the SSA (w), asymmetry factor (g) of the single-particle phase function, and roughness ($\bar{\theta}$), it is obvious that all three parameters have large variations over the surface of this cometary nucleus. A question to ask is, with the noisy data and the large RMS error of fitting, whether or not the variations in different parameters can really be distinguished, given the extremely non-linearity of Hapke's model? As discussed in Chapter 2, in the case of the disk-integrated phase function, more backscattering (more negative g) and higher roughness ($\bar{\theta}$) have a very similar effect in making the phase curve steeper (see Fig. 2.7). Therefore they cannot be distinguished well. However, in disk-resolved cases, we have a limb darkening profile at any particular phase angle in addition to the phase function indicated by images at various phase angles. For dark surfaces, multiple scattering is usually very weak compared to single scattering. For Borrelly, if we assume 4% SSA, and the other Hapke's parameters as found by Buratti et al. (2004), calculation shows that multiple scattering is less than 2% of the total scattering. Thus in Eq. 2.53, we can safely ignore multiple scattering, and write the bidirectional

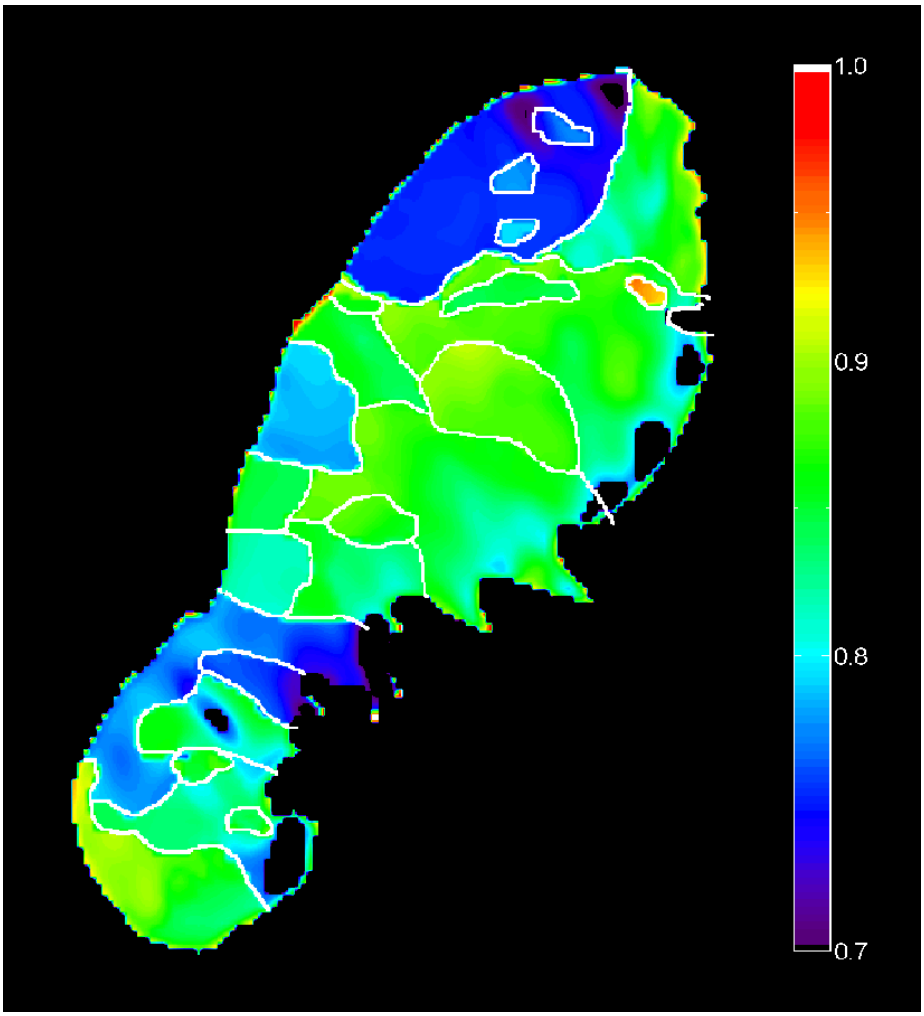

Figure 5.14 Modeled phase ratio map to compare with the observed phase ratio map in Fig. 5.5. Very similar color table is used, so that they can be compared directly.

reflectance as

$$r(i,e,\alpha) = \frac{w}{4\pi}\frac{\mu_{0e}}{\mu_{0e}+\mu_e}[1+B(\alpha)]p(\alpha)S(i,e,\alpha) \tag{5.1}$$

where the limb darkening is determined by the $\mu_{0e}/(\mu_{0e}+\mu_e)\times S(i,e,\alpha)$ as a function of i, e, and α, and is in turn totally controlled by the roughness parameter $\bar{\theta}$ (μ_{0e} and μ_e are the cosines of the effective incidence angle and emission angle, respectively, both depending on $\bar{\theta}$ as shown in Eq. 2.43-2.48). The asymmetry factor g only affects the phase function part, but does not enter limb darkening at all. Therefore, in Borrelly's case, the information we used to model $\bar{\theta}$ is different from and almost orthogonal to that we used to model g. The conclusion is that with disk-resolved images, g and $\bar{\theta}$ can be distinguished well as long as the incidence angle and emission angle of the bidirectional reflectance data are observed over a large range. Noisy data probably lead to large modeling errors, but that does not change the independence between parameters.

Is our result consistent with earlier photometric analyses? What was possibly missed in earlier analyses leading to the conclusion that the reflectance variation is only attributed to the change of one parameter?

In Buratti et al. (2004), semicircular arcs between limb and terminator along the Sun line are used to approximate the shape of Borrelly to perform geometric correction and model a normal reflectance map. This step will bring in uncertainty in estimating normal reflectance, because Borrelly's shape is highly irregular. In modeling the phase function, reflectance is expressed as the product of albedo, a phase function, and a limb darkening profile. The limb darkening profile is approximated by the Lommel-Seeliger function, an approximation that usually works well for dark surfaces. The phase function

is then obtained by comparing the averaged brightness of the whole disk under various phase angles. However, the limb darkening is implicitly assumed to be constant over the surface, so that possible variations in roughness, which affects limb darkening according to Hapke's model, are not taken into account. Variation of the asymmetry factor (g) over different terrains has been noticed by Buratti et al. (2004), which is consistent with our results. Another potential limitation in Buratti's result is that an accurate shape model was not available when the analysis was carried out, thus the uncertainty of normal reflectance map produced from geometric correction with the approximate shape and the uncertainty in the value of the asymmetry factor are large.

In Oberst et al. (2004), a shape model is applied to the photometric analysis. Similar to the analysis of Buratti et al. (2004), the reflectance is expressed as the product of albedo, a phase function, and a limb darkening profile. Here the limb darkening profile is approximated by a linear combination of a Lommel-Seeliger function and a Lambert function, with a constant weight factor, which actually contains the information of surface roughness. Therefore, a possible variation of surface roughness is not taken into account by the weight factor in its limb darkening model, either. Moreover, the variation of phase function is only studied by taking the ratio map of last two resolved DS1's images, and not quantized. In our work, we have used all resolved images to model the phase function parameters g.

Kirk et al. (2004a) utilized an accurate shape model of Borrelly in performing photometric analysis as did Oberst et al. (2004). By comparing the brightness of the last two resolved images, at 51.6° and 59.6°, Kirk et al. (2004a) concluded that albedo variation does not dominate the reflectance variation over the surface because the effect of albedo

variations should cancel in the ratio map for a dark surface (see Eq. 5.1), and the ratio map should have shown less variation. But this is not what is seen in the ratio map (Fig. 5.5), leading them to deduce the variation of $\bar{\theta}$. However, possibly included in the phase ratio map is also the variation of phase function, or g parameter, in addition to roughness variation. Kirk et al. (2004a) made no attempt to differentiate those two different properties.

A summary of the variations of the modeled parameters from terrain to terrain can be found in Table 5.3. The variation of single-scattering albedo is more than a factor of 2 (Fig. 5.9), from the darkest part close to the night side of the small end to the brightest part on the right corner of the large end. And basically there is no direct correlation between the SSA and the reflectance we see in those images. With very different SSA for the two terrains on the large end, their similarly observed reflectances at large phase angles are due to their very different single-particle phase functions, which are also indicated in the phase ratio map. SSA variation, together with the variation in asymmetry factor, g, usually indicates variations in the size, shape, and composition, *etc.*, of the scattering particles on the surface. In addition, high SSA regions seem to be low backscattering (Fig. 5.15), indicating small but transparent particles, such as ice grains or fine particles with large ice content. This is not supported by the spectra of Borrelly's surface from DS1 spacecraft (Soderblom et al., 2004b), which do not show any signatures of water ice. However, since those spectra are averages along each of their scanlines across the surface of this low activity comet (Schleicher et al., 2003), it is very possible that they missed ice concentrated in very small regions compared to the size of nucleus. The evidence from photometric analysis probably shows the existence of ice grains on the surface. The same

Table 5.3 A summary of the variations of modeled Hapke's parameters.

	w	g	$\bar{\theta}$
Range of Hapke's parameters	0.08 to 0.03	-0.1 to -0.7	55° to 5°
Trend or distribution[a]	1. Upper right end	1. Lower end	1. Upper right end
	2. Lower central smooth terrain	2. Upper right end	2. Lower end
	3. Mesas, upper central smooth	3. Upper central, mesa	3. Lower central
	4. Upper left end, Sunward neck	4. Lower central, anti-Sun neck	4. Mesa, upper left end
	5. Anti-Sun neck	5. Sunward neck, upper left end	5. Neck, upper central

[a] w and $\bar{\theta}$ from high to low, g: from isotropic to strong backscattering

conclusion has also been drawn by Buratti et al. (2004).

5.3.3 Global properties from disk-resolved modeling

The average values of those three parameters over the projected disk are calculated to be w=0.057$\pm$0.009, g=-0.43$\pm$0.07, and $\bar{\theta}$=22°$\pm$5°, respectively. The average SSA is consistent with the value 0.056 found by Kirk et al. (2004a), but much larger than the value found by Buratti et al. (2004). The average g factor and roughness $\bar{\theta}$ are consistent with the values found by Buratti et al. using the spherical shape approximation, but our averaged g factor is more backscattering than that found by Kirk et al. (-0.32). Our average roughness parameter $\bar{\theta}$ is consistent with what was found by Kirk et al. for smooth terrain (20°), but not for mottled terrain (60°), although in our model, the roughness over the surface varies in a large range from 5° to 55°, but being $<$35° for more than 4/5 of the projected cross-section area.

The modeled bidirectional reflectance at opposition for the imaged portion of Borrelly's surface is shown in Fig. 5.16, and a geometric albedo of 0.084 is derived from this map. However, this geometric albedo is strongly model dependent, although it is consistent with the value derived from the disk-integrated phase function. It has to be kept in mind that the asymmetry factor g is modeled only from DS1 images within phase angles from 51° to 75°, and we only have one single data point from the ground that can be used to determine the opposition effect parameters effectively. An interesting phenomenon as seen from Fig. 5.16 is the inversion of brightnesses of terrains at opposition compared to the image at high phase angle (Fig. 5.1). The brightest areas seen at high phase angles are dark at opposition, and the dark areas at the neck and part of the large end seen at high

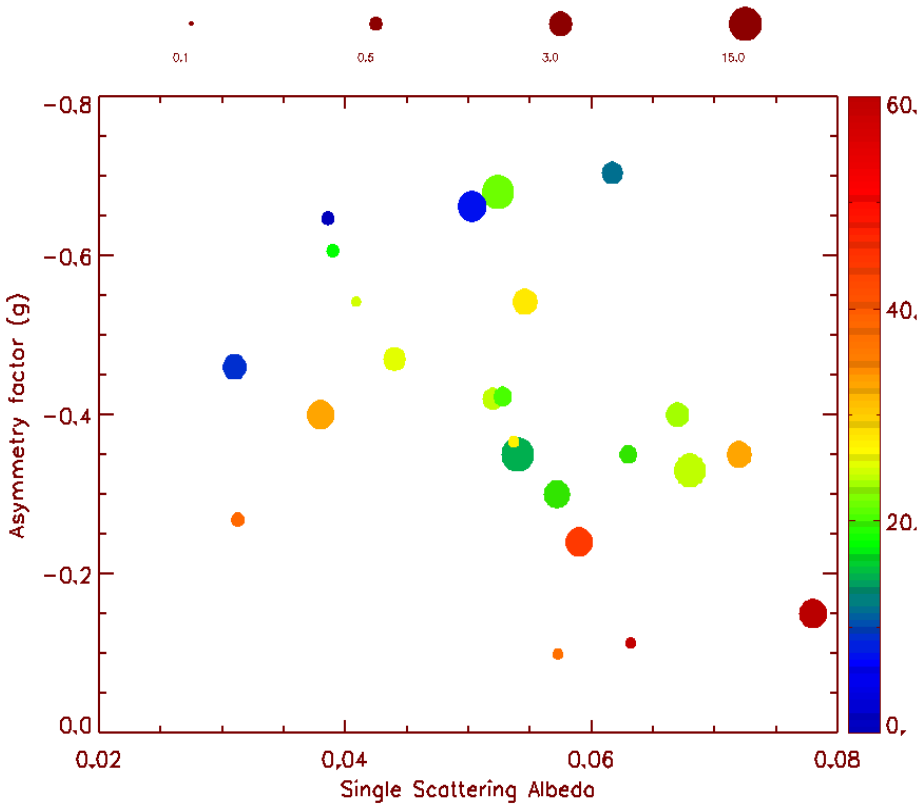

Figure 5.15 A plot of the modeled asymmetry factor g *vs.* SSA w for all terrains. The color of each symbol represents the roughness for that terrain as scaled in the color bar to the right. The size of symbols represents the projected size of that terrain as a percentage of total projected cross-section area of the disk.

phase angles are the brightest at opposition. Of course this is also highly model dependent because we are extrapolating the brightness from high phase angles with the model derived from only a small range of phase angles.

The global photometric properties of Borrelly as we derived are very similar to those from earlier work except for the large discrepancy in albedo. As summarized by (Buratti et al., 2004), comet Borrelly has photometric properties that are very similar to those of dark C- and D-type asteroids, but not the moon or any bright type asteroids. Our work shows that its single scattering albedo could be high, but this is pending on our investigation to the discrepancy between our resultant value and that of Buratti et al.

5.4 Disk-Resolved Thermal Modeling

With the shape model available, we are able to calculate a more detailed, disk-resolved thermal model for the surface of this cometary nucleus. Unlike asteroids, comets usually have ice sublimation on their surface or close below the surface. Not all around the surface of cometary nucleus, sublimation is usually happening only from a small fraction of nuclear surface. For comet Halley, that fraction is about 25% (A'Hearn et al., 1995). For the case of Borrelly, it is only about 4% (Schleicher et al., 2003). Heating from sunlight is the only energy source driving sublimation, which in turn participates determining the temperature distribution over the surface. Therefore, disk-resolved thermal modeling, which provides the temperature distribution over Borrelly's surface, will help us understand the sublimation activity on this cometary nucleus. Together with the jet morphology as indicated by the spatially resolved images from DS1, it is possible to

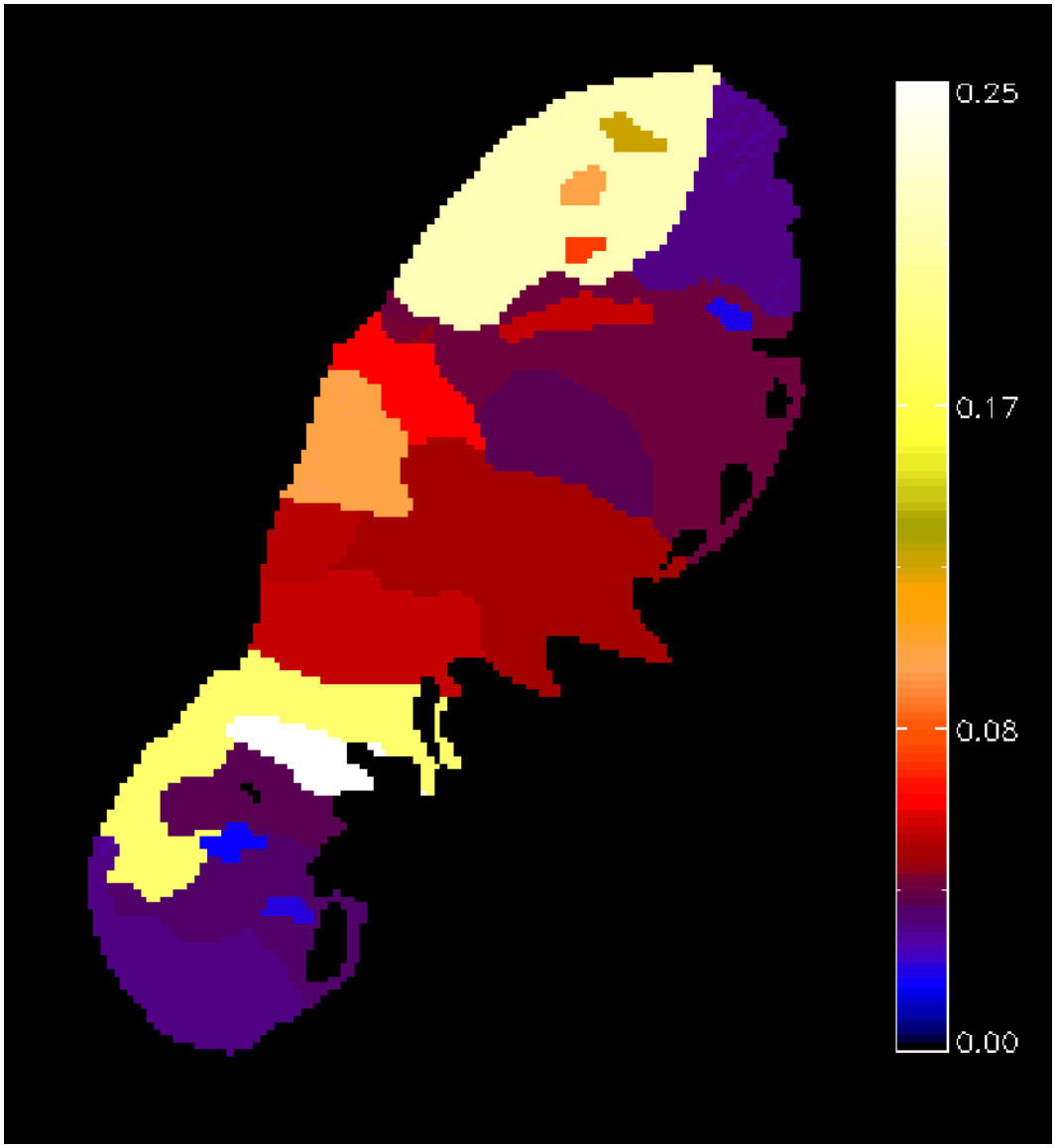

Figure 5.16 The modeled geometric albedo map. Note the non-linear stretch of color table. Some terrains have very high geometric albedo (0.2) that are not likely to be physical. But the average geometric albedo is about 0.084, consistent with whole-disk phase function modeling.

provide some clues about the source regions of jets.

The temperature distribution on Borrelly's surface has been measured from its thermal spectra (Soderblom et al., 2004b). The short-wavelength IR (SWIR) imaging spectrometer integrated into MICAS had its long slit aligned with the vertical direction in Fig. 5.1, and scanned along the horizontal direction. 46 near-IR spectra covering Borrelly's nucleus were obtained, from which the thermal spectrum were modeled, yielding an effective temperature along each slit position (Fig. 5.17). However, one must remember that the temperature distribution derived from the integrated spectra along horizontal lines is dominated by the hottest area along each line. Because thermal flux is very sensitive to temperature ($\propto T^4$), the integrated spectrum along a line will be dominated by the highest temperature areas. Because the effective temperature along each line is derived by fitting the shape of thermal spectrum, it is also dominated by the highest temperature along the scan line. We will take the shape model of the nucleus, and try to reproduce the temperature distribution as measured from SWIR spectra (Fig. 5.17).

The thermal balance of a small element on Borrelly's surface can be represented by the equation below, following the standard thermal model (Brown, 1985; Lebofsky et al., 1986),

$$(1 - A_B)\mu_0 \frac{F_\odot}{r^2} = \epsilon\sigma T^4 + ML(T) + k\nabla T + c\dot{T} \tag{5.2}$$

where $F_\odot$ is solar constant, or solar flux at 1 AU, r is heliocentric distance in AU, A_B is the hemispherical bolometric albedo, ϵ is thermal emissivity, σ is Stefan-Boltzmann constant, T is the local equilibrium temperature on the surface, M is the water production rate per unit area, L is latent heat of ice sublimation at temperature T, k is thermal conductivity,

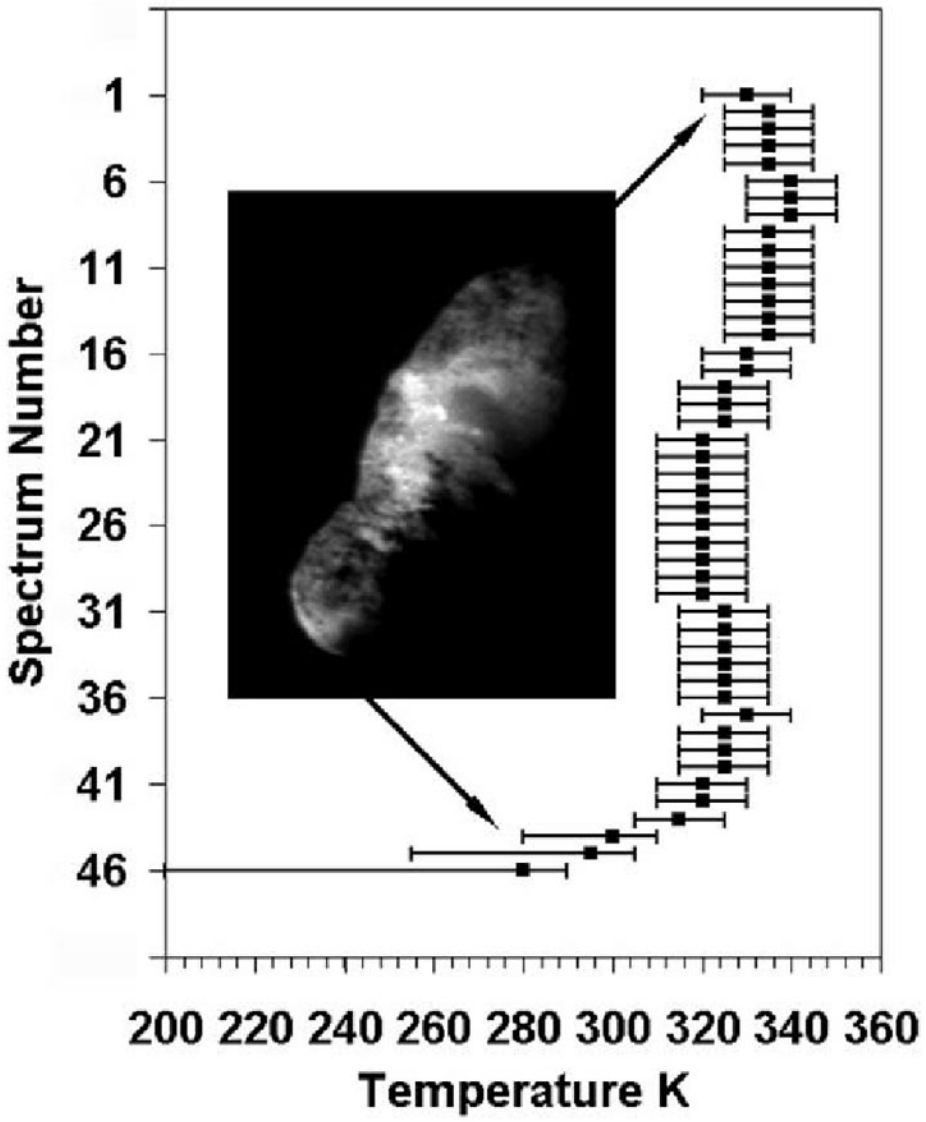

Figure 5.17 Fig. 7 in Soderblom et al. (2004b). The temperature distribution of Borrelly's nucleus along vertical direction as measured from short-IR thermal spectra detected by SWIR instrument.

∇T is temperature gradient, c is thermal capacity, and $\dot{T}$ is temperature change rate.

In Eq. 5.2, the lefthand side is the power received from sunlight by unit area. The first term on righthand side is thermal radiation flux. The second term on righthand side is the heat used to sublimate ice, which we assume to be mainly water ice because first, the latent heat of water is at least $5\times$ that of other volatile materials (mainly CO_2) in comets (Cowan and A'Hearn, 1979; Delsemme and Miller, 1971; Smith, 1929); and second, all observations near a cometary nucleus show H_2O dominant. The third term is the heat conducted to adjacent areas or inside the surface. This term is very complex. It can be due to the true thermal conduction of solid surface, and/or the convection of vapor flow. It could also include the part of heat that is transferred inside by water ice sublimation at depth and water vapor condensation in subsurface. We neglect this term in our modeling because on average, if the heat conduction of solid surface of comets is low, as for most dust particles in space, this term mainly changes the temperature distribution vertically, and is equivalent to the increase of thermal capacity or thermal inertia of the surface. The last term is heat lost or gained due to local temperature change, and is the real thermal inertia, which is usually very low for the surface of comets, and negligible. However, as stated above, we can take an equivalent thermal inertia for the third term on righthand side of Eq. 5.2, and fold it into this term, it is very possible that this term could be large for active areas where there is much water vapor transporting heat inside very effectively, causing thermal lag for fast rotating comets. In our thermal modeling, we neglect this term, too, because first, Borrelly rotates very slowly with a rotational period 25 hours (Lamy et al., 1998), and second, all DS1 resolved images were taken within the last 1.5 hours of close encounter (Soderblom et al., 2004a), a time interval that is too short to

resolve diurnal temperature variation on a rotating body.

Our thermal modeling will be a 2-step procedure. First, we only consider energy loss due to thermal radiation because this term usually dominates for low to moderately active comets. In the case of Borrelly, thermal radiation emits about 95% of the energy it receives from sunlight as calculated from its water production rate of 2.5×10^{28} molecules/sec (Schleicher et al., 2003). If we assume that ice sublimation is uniformly distributed over the surface, then the 5% energy used to sublimate ice will only cause a few percent drop in surface temperature, less than the uncertainty in the temperature measurement from thermal spectrum by DS1 (Soderblom et al., 2004b). So even only the thermal radiation energy lost is considered, we can still get the overall temperature distribution for most of Borrelly's surface. Taking A_B=2%, ϵ=0.9, and the heliocentric distance of Borrelly at the DS1 encounter as 1.36 AU, the subsolar temperature is calculated to be 346 K, and a temperature map is constructed from the map of solar incidence angle. From the temperature map, the thermal flux is integrated for each pixel along horizontal scan lines, and the integrated flux for each scan line is modeled by a blackbody thermal radiation spectrum to find an effective temperature for this scan line. This is the procedure used by Soderblom et al. (2004b) to produce the temperature plot (Fig. 5.17) from Borrelly's spectra. The 1-D temperature distribution model for a dry surface is then produced, and plotted in Fig. 5.18 as a thick solid line. This temperature model overall agrees with measurement within error bars, with some discrepancies for the scanlines that cross active areas, mainly the lower one fifth of the nucleus at the small end, where the predicted temperature is substantially higher than measured temperature by 20° to 40°, and has to be accounted for by including ice sublimation in the thermal modeling.

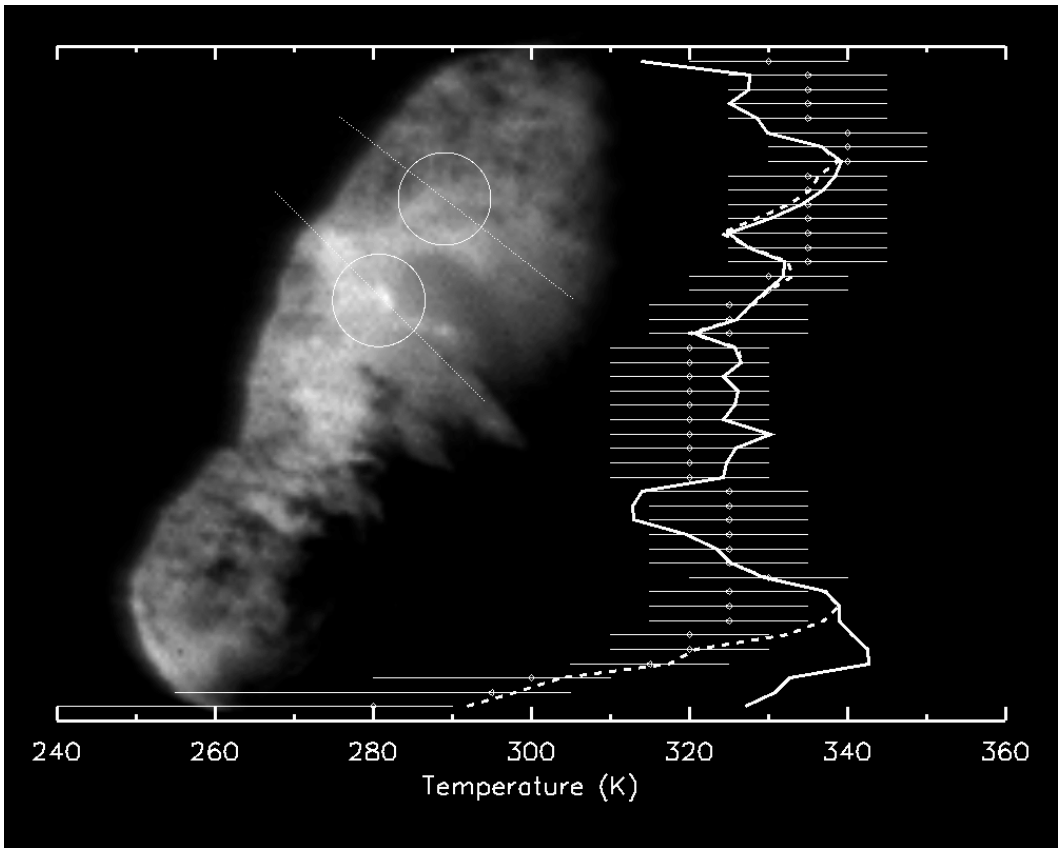

Figure 5.18 Modeled 1-D temperature distribution of Borrelly to simulate the SWIR observation as plotted in Fig. 5.17. Solid line represents the STM model without considering ice sublimation, and dashed line is the model considering ice sublimation occurring for the small end terrain #7 and the possible base areas of the two collimated jets. Also shown is the projected lines of two collimated jets (thin dotted lines) and our modeled source areas (thin circles).

The second step in thermal modeling is then to take into account ice sublimation. Although only 5% of total sunlight power contributes to sublimating water ice, it can still substantially decrease local temperature if concentrated within relatively small active areas. This could also provide an explanation for the discrepancy between observed temperature distribution and the temperature model without considering sublimation. However, a detailed model requires much more information than currently available, such as an observed 2-D temperature map rather than a 1-D plot, thermal characteristics of cometary surface, and even the structure of the interior. Thus what has been done here is not to model it accurately with Eq. 5.2, but to find a solution for the temperature distribution that produces the observed temperature curve as shown in Fig. 5.17, and is consistent with the observed water production rate. Or in other words, to find a self-consistent solution that is not necessarily unique. We also need to assume that the visible surface of this comet is in local thermal equilibrium, where, first, there is no energy flow between local area elements, and second, we only need to consider the thermal balance on the surface, not anything else beneath. The first assumption is probably not true because with the convection of vapor, there must be energy exchange horizontally within the surface. But for our purpose, it should be good enough. The second assumption of course has no problem because of the low thermal inertia and the slow rotation of Borrelly. Therefore, the thermal balance equation used here will only include the lefthand side and the first two terms on the righthand side of Eq. 5.2.

Our solution is obtained, first by correcting the modeled temperature map without considering ice sublimation by the discrepancy between the model and observations. Since photometric modeling has concluded that, fan jet activity, which is associated with

ice sublimation, very likely only occurs on terrain #7 at the small end, we will only modify the modeled temperature for this terrain. Then from the modified temperature map, an effective temperature plot is produced with the method stated above, and shown by the dashed line for the small end of nucleus shown in Fig. 5.18, agreeing with DS1 measurement (Fig. 5.17) very well, as expected. Now the question is, whether or not this model temperature map produces as many water molecules as observed for this fan jet. The estimate of water production rate from temperature model can be made by

$$M = \frac{\epsilon\sigma(\mu_0 T_{ss}^4 - T^4)}{L(T)} \tag{5.3}$$

where M is water production rate per unit area. Water latent heat is calculated following the linear formula in Cowan and A'Hearn (1979),

$$L(T) = 12420 - 4.8T \tag{5.4}$$

(L in cal-mole^{-1}, T in Kelvin) which in turn used the data given by Delsemme and Miller (1971). With the available map of μ_0, the cosine of solar incidence angle i, a distribution map of M can be constructed. Then integrating M within terrain #7 after it is weighted by $1/\cos e$ to take into account the projected area change of Borrelly's surface, the total production rate for the visible part of this active area is estimated to be about 2×10^{27} molecules/sec. Considering the phase angle of about 51.6°, there should be about one third active area invisible on the other side of the nucleus, therefore the total production rate for this active area is about 3×10^{27} molecules/sec, or about 12% of the total production rate for this comet. This is a fairly good agreement with the estimate that about 20% dust is within the fan at the small end (Boice et al., 2002), considering that fraction of dust may not exactly represent the fraction of water production rate. The average water

production rate per unit area in this active area is about 1.3×10^{17} molecules $cm^{-2}s^{-1}$, consistent with the calculation in Cowan and A'Hearn (1979) for comparable heliocentric distance.

In addition to the fan jet active area at the small end, we also constructed a temperature model that includes the possible active areas at the bases of two collimated jets of Borrelly. The directions of two collimated jets have been determined from stereo pair images (Soderblom et al., 2004a), but the sources of collimated jets could only be constrained to lie somewhere along the two projected lines centered on the jets in the DS1 images. We plotted the angles between jets and Borrelly's surface normal along the two projected lines of collimated jets (Fig. 5.19), and decided to take the regions of local minimum angles as the bases of collimated jets because this is the most likely case. The model temperature plot turns out not to change much with the minimum temperature and the sizes of the base areas in temperature models, but the total water production rate for this area depends on them strongly. If taking the minimum temperature in the two base areas to be between 190 K and 200 K, as calculated in Cowan and A'Hearn (1979) for comparable heliocentric distance, then in order to account for about 35% total water production rate for these two jets (Boice et al., 2002), the total area for the bases of those two jets is about 1.5 km^2, and the average water production rate per unit area is about 5×10^{17} molecules $cm^{-2}s^{-1}$, also in a good agreement with the calculation in Cowan and A'Hearn (1979). Fig. 5.18 also shows the thermal modeling discussed here including the two collimated jet base areas in dashed line.

The thermal modeling including the last two terms of Eq. 5.2 can only be done with data covering a considerable fraction of a rotational period. DS1 images do not provide

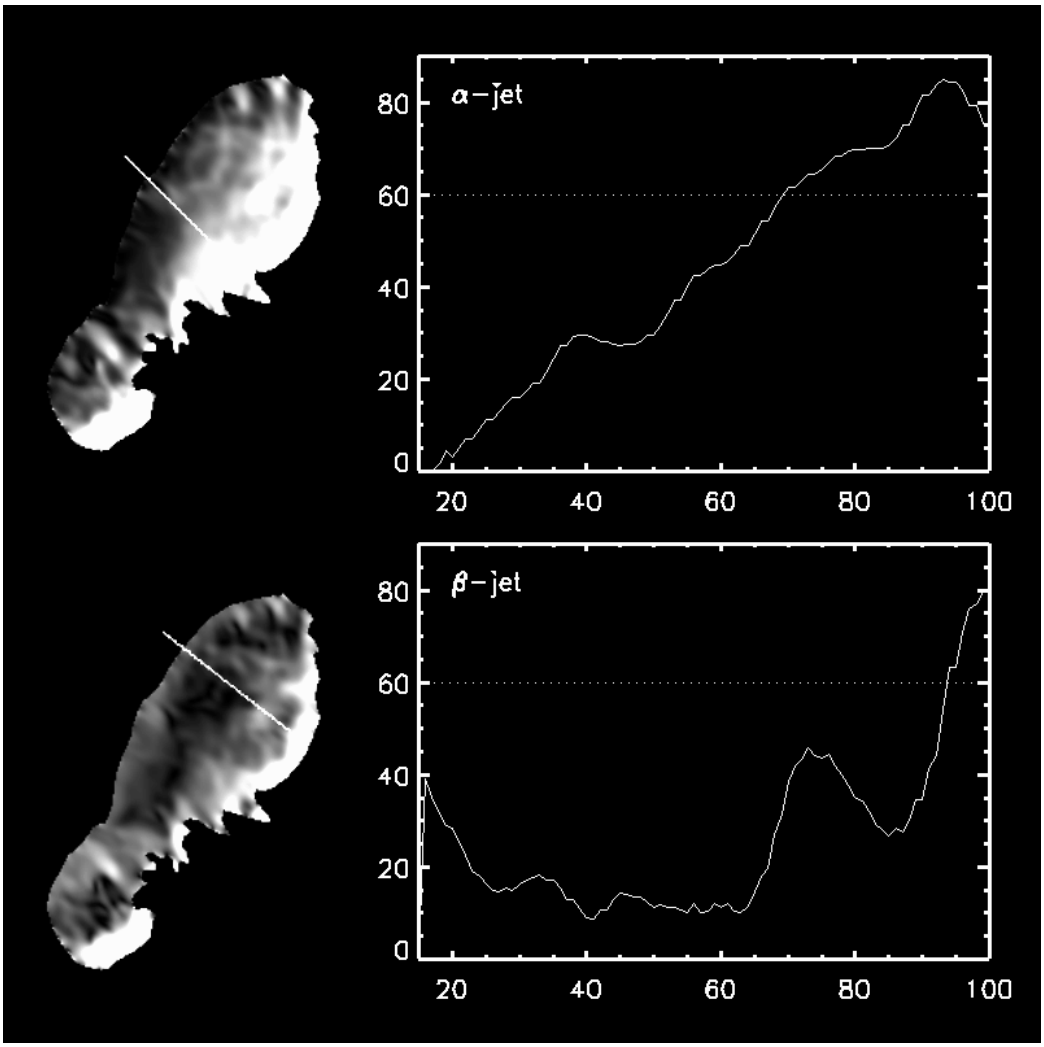

Figure 5.19 The maps of the angles between the directions of two collimated jets and the normals of surface, and the plots of those angles along the projected lines of two jets. Maps are stretched with a maximum angle of 60°, corresponding to the dotted lines in plots. Dark tone corresponds to small angles.

that data coverage. But since the thermal inertia of cometary surface is usually very small, and the active area fraction for Borrelly is also very small, the model ignoring those two terms has been good enough here.

5.5 Discussions

5.5.1 High roughness

Despite the overall moderate roughness parameters ($\leq 35^\circ$) modeled for most terrains, we found very high roughness for some terrains (40°-55°). However, Hapke's photometric model was derived with the assumptions of low albedo and low surface roughness. While the albedo of Borrelly's surface is low everywhere, the modeled high roughness parameters for some terrains are not consistent with the assumptions of the theoretical model. As shown in Chapter 2, and stated above, the bidirectional reflectance is determined by two parts, including the limb darkening properties, and the phase function properties, and the roughness parameter can be determined from both. In our Hapke's modeling, the scattering geometries of the two terrains with particularly high roughness (#7 and #9) cover almost the full range of incidence angle and emission angle from a few degrees to the preset cutoff at 75°. The phase angle coverage (51°-75°) is fair, although not large, for the determination of roughness parameter. Therefore, with their modeling RMS of 18% and 12% for terrain #7 and #9, respectively, the best-fit roughness parameters have small uncertainties from data modeling point of view. Hapke's models with high roughness parameters are still able to describe observations data well in this case. Caution has to be used, however, to interpret the modeled roughness parameters as the physical roughness

of surface for those two terrains. It is possible that the high roughness is caused by some other unknown physical conditions on the surface. Or the surface topography of those two terrains is very different from the roughness structure as assumed in Hapke's model, where the orientations of the normals of the facets of a rough surface are distributed isotropically with a Gaussian distribution function for the tangents of their zenith angles. For example, it is evident from Wild 2's image that the surface materials of a cometary nucleus can have some kind of internal strength (Brownlee et al., 2004). If this is also the case for Borrelly, then a large fraction of the surface could be in very complicated shadows, increasing the roughness that is not modeled by Hapke's model. This possible complication is discussed in the following section.

Even though the physical interpretation of the modeled high roughness parameters for the two terrains deserves further investigations, it is clear that the roughness structure, even if not described quantitatively by the roughness parameter, varies substantially over the surface, causing distinctive photometric variations across the surface of Borrelly's nucleus. In the next step we will made some attempts to correlate the photometric variations to, and study the physical processes that possibly cause the roughness variations. We will not distinguish between the variations of roughness structure and those of roughness parameter in the following text, but it has to be kept in mind that high roughness parameters may or may not have the same physical interpretations as low roughness parameters.

5.5.2 Possible correlation between photometric properties and cometary activity

With the large photometric heterogeneity on the active surface of a comet, it is reasonable to think that the photometric variation is an indication of compositional variation that

originally is caused by cometary activity. For example, as shown above, it is possible that ice sublimation can bring ice grains or dust with high ice content from the deep interior to the surface, or that vapor from inside the active areas condenses on its way out, and forms ice frost just below the surface. High ice content in and near active areas may cause high albedo and more isotropic scattering. In addition, cometary activity may also cause geological change of the surface, such as some particular texture or appearance (Britt et al., 2004), which is tied with surface roughness.

It is obvious that the small end of the nucleus, where we actually see the fan jet emerges, possesses relatively high albedo, low backscattering, and high roughness (Fig. 5.9, 5.10, and 5.11). We do not see any other areas possessing those properties except for the upper right end of the nucleus, where, however, there is no jet activity shown in the resolved images. Is it possibly another source area of fan jet, but was inactive at the time those DS1 images were taken? As shown in DS1 images acquired 10.4 hours before close encounter (Fig. 5.20), when, given Borrelly's rotational period of about 25 hours (Lamy et al., 1998), and the rotational geometry, the big end is at the position of the small end at close encounter and toward the Sun, there was an even stronger sunward fan jet emitted. Thus, the big end is also a source of fan jet, but not active at the time of DS1 close encounter because it was away from the sunward direction.

However, there are two very different terrains on the big end, of which only one shares similar photometric properties with the small end. To explain this phenomenon, we fixed the direction of the Sun and the rotational axis of Borrelly as determined from the ground (RA=214°, Dec=-6°, from Farnham and Cochran, 2002; Schleicher et al., 2003), which is actually very consistent with the value determined from the direction of its pri-

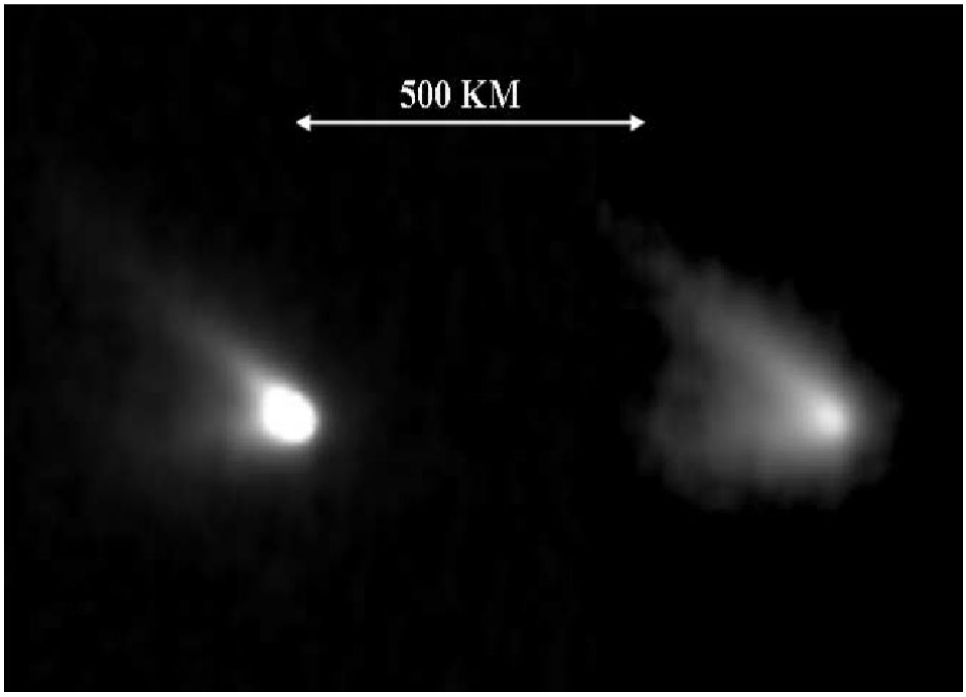

Figure 5.20 Fig. 7 in Soderblom et al. (2004b). A DS1 image acquired 10.4 hours before close encounter at a range of 0.62 million km shows a strong fan jet emitted sunward. The image on the right is a log stretch of the original image on the left, emphasizing the faint jets. Sun is to the left. The two jets shown here remained fixed in orientation for at least a full rotation.

mary jet (Soderblom et al., 2004a), and let the nucleus rotate. A polar day region for the sunward pole at the time of DS1 encounter is determined by the shape of Borrelly, as shown in Fig. 5.21. We found that the boundary of polar day region almost coincides with the boundary of the two photometrically different terrains at the large end. This tends to indicate that only the area that is not in polar day region is active and emitting fan jet when the big end rotates towards the Sun. Because Borrelly has been in a simple rotational mode and very stable, and its orbit has been stable for a long time (Belyaev et al., 1986; Carusi et al., 1985), the polar day region has been heated by sunlight continuously during many perihelion passages, so either the volatile materials in that region have been depleted, or an inert crust has formed that insulates the volatile-rich interior from sunlight, and the area does not show any activity during current perihelion passages. The neighboring region that does not receive continuous sunlight during perihelion passages still keeps active, and displays diurnal changes in activity. This explanation is consistent with the fact that we do not see any activity from the polar day region at the big end, but it does not explain why the upper right region does not show any activity even if it is partially sunlit in the resolved images. The histograms of solar elevation angles for the terrain at small end (#7) and the two terrains at large end (#8 and #9) at the time of DS1 flyby are shown in Fig. 5.22. The fractions of area with solar elevation angle higher than 60° are 41% for small end terrain, 44% for the upper left terrain, and only 4% for upper right terrain. It is clear that at the time of DS1 encounter, the solar elevation for the upper right region (#9) is probably not high enough to trigger fan jet activity, and the upper left terrain (#8) is indeed inactive even if it seems to receive the same amount of sunlight as does the small end, which is actively emitting a fan jet.

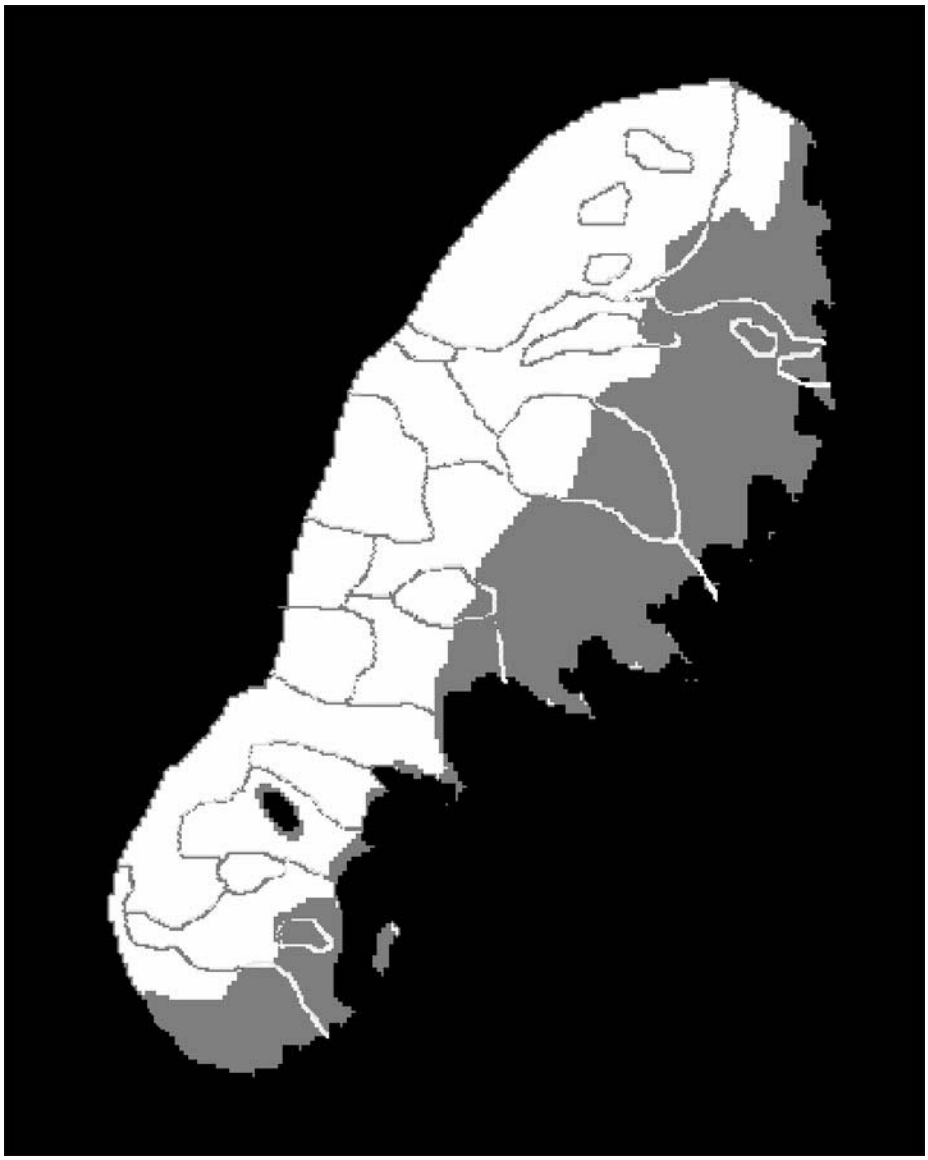

Figure 5.21 The polar day region at the time of DS1 close encounter is marked in white, overlapped with photometric terrain partitioning. Note that the boundary of the polar day region almost coincides with the boundary between the two different terrains at the large end.

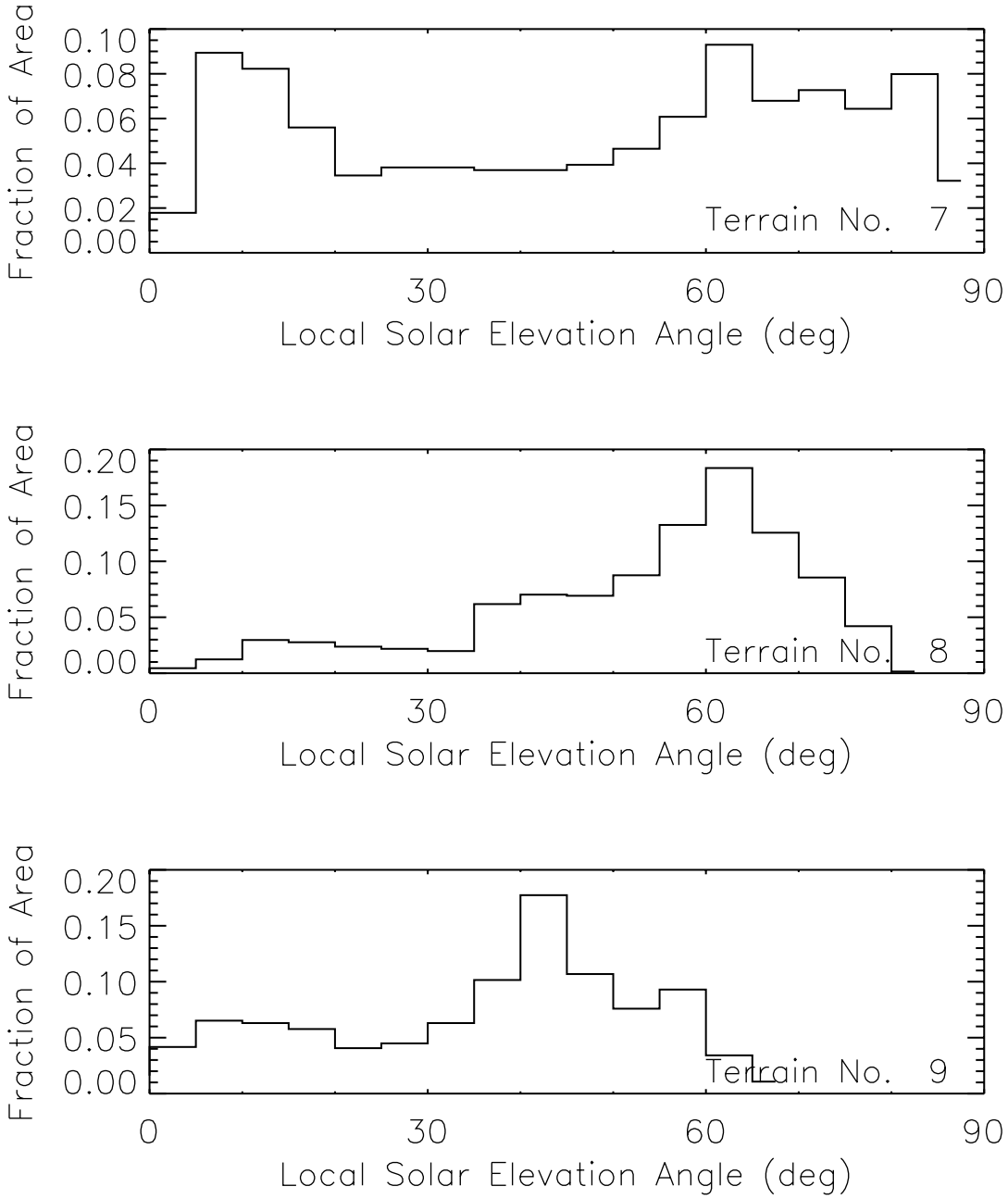

Figure 5.22 Solar elevation angle histograms for the terrains at the small end (#7), upper left of large end (#8), and upper right end (#9).

Therefore, we can draw the conclusion that fan jet activity tends to correlate with high albedo, relatively isotropic scattering, and high roughness. And vise versa, if we found those photometric properties in an area on the surface of a comet, even if no fan jet is observed to emerge from that area, there was probably fan jet activity in the near past or when conditions were met for it.

As stated earlier, it is not hard to interpret high albedo and relatively isotropic scattering for active areas, but how to interpret their high roughness is not so obvious. One way is to think about melting snow on the Earth. The surface of snow is heated by sunlight, melting to liquid. When the liquid flows inside through pores between snow particles, it possibly condenses again, transporting heat inside. During this process, the surface of the snow is eroded, forming all kinds of depressions, holes, frosts, aggregates, *etc.* in many shapes. Those structures actually increase the roughness of the surface of melting snow, and cause a very steep decrease of reflectance with increasing phase. The process occurring on active areas of a cometary nucleus could be very similar, except water ice on a comet is mixed with a large fraction of dust particles, or dirt. When ice in subsurface sublimates, some gas is released outward, blowing up some small dust particles through pores in the surface, and leaving large dust particles on the surface. Also there is another part of vapor moving inward through pores, and condensing again to transport heat to the inside. But the overall erosion by ice sublimation would be like that of melting snow described above, leaving behind a very rough surface with a very steep phase function. Recent images of comet Wild 2 from Stardust encounter reveal a cometary surface composed of some kind of sticky material (Brownlee et al., 2004). With material having some kind of internal strength, it will be relatively easy to form very rough surface

during the complicated sublimation process stated above. However, it is equally possible that an originally rough surface helps produce fan jet because it has more pores in between particles, and water vapor can penetrate from anywhere on a big area without being collimated.

In addition to a fan jet, we also observed two collimated jets from comet Borrelly. However, we could not identify any possible source regions of collimated jets that share similar photometric properties with the source regions of fan jets. This probably means that the properties of source regions of collimated jets are very different from those of fan jet sources, and a different mechanism is responsible for forming collimated jets than forming fan jets. A model of collimated jet formation is proposed by Yelle et al. (2004), in which a single vent structure is responsible for producing a collimated jet, where the jet comes out from a small opening. While it is an effective way of collimating the jet, if this is true, then the area of opening on the surface will be small compared to that of fan jets, and its photometric difference is probably averaged out by surrounding areas in modeling, and undetectable. In another formation mechanism proposed by Britt et al. (2004), collimated jets come from the receding walls of mesas when the volatile material under their top crust evaporates. In this case, the jet should affect a considerably large surrounding area and change its photometric properties, because the area where sublimation occurs is relatively open. Thus the results from photometric analysis seem not to support this mechanism because no area with relative bright and transparent particles is found for the possible source regions in center bright terrains.

5.6 Summary

The DS1 encounter with comet Borrelly made this comet the second to be visited by spacecraft, and imaged closely to resolve its nucleus. The close-up images reveal many more details about a cometary nucleus than seen at Halley. Another comet, Wild 2, was visited by Stardust two and a half years later in January 2004. But Wild 2 has been captured to its current orbit by Jupiter for only a few apparition (Sekanina and Yeomans, 1985), and is considered to still represent the typical surface and composition of comets in Kuiper Belt. While Borrelly has been stable in its current orbit for a very long time (Belyaev et al., 1986; Carusi et al., 1985), and thus displays an evolved surface in inner solar system, it can be compared with Wild 2 in the future when the photometric analysis of Wild 2 are studied from Stardust images. Also Borrelly is thought to be different from comet Halley, which formed in Kuiper Belt, but is very active currently. The detailed study of Borrelly is therefore of great importance.

Disk-integrated analysis from about a dozen disk-resolved images acquired by DS1 shows a highly photometrically heterogeneous surface. The large brightness variation of a factor greater than 2 is due to the variations of both surface physical properties and/or compositions, and large scale (much larger than wavelengths and particle size or pore size) surface roughness. The SSA (w) ranges from 0.03 to 0.08. The asymmetry factor (g) varies from almost isotropic (-0.1) to strongly backscattering (-0.7). And the surface roughness ($\bar{\theta}$) can be as smooth as 5°, to as rough as 55°. In other words, the surface of this cometary nucleus is by no means uniform as the dead surfaces of asteroids. The averages of above parameters over the disk are, w=0.057$\pm$0.009, g=-0.43$\pm$0.07, and $\bar{\theta}$=22°$\pm$5°.

The temperature of Borrelly's surface is measured by DS1 spacecraft using its thermal radiative spectra. Our model shows that, for a low activity comet like Borrelly, the surface thermal balance is dominated by solar elevation angle, except for the active areas with fan jet emitted, where water sublimation may substantially decrease surface temperature by about 20 K to 40 K. A self-consistent temperature model is constructed to reproduce the 1-D temperature distribution observed by DS1, and the water production rate for its active areas. Even though, the surface temperature of Borrelly is still much higher than the sublimation temperature of water ice (about 200 K), indicating very low heat conductivity of Borrelly's surface. Another implication about the bases of fan jets and collimated jets is that fan jets probably emerge from a large area on the surface, but collimated jets possibly have very small source regions.

The calculation of solar elevation change when Borrelly rotates along its stable rotational axis shows that fan jet activities may correlate with some particular surface photometric properties such as high albedo, isotropic scattering, and high roughness. It is hard to say if fan jet activity causes those particular properties or vise versa. But the correlation between fan jet activity and the particular surface properties can be used in the future to identify areas on a cometary nucleus that have been active. The same analysis also shows that the big end of the nucleus displays two compositionally different terrains, one of which is basically dead, while the other emits a fan jet when the overall local solar elevation is high enough.

Chapter 6

HST Observations of Asteroid 1 Ceres

6.1 Background and Data Description

6.1.1 About Ceres

Unlike small asteroids, which are probably the products of disruptive collisions, the largest main belt asteroids are protoplanets that were too large to be shattered and dispersed. Their growth to full sized terrestrial planets was choked off when the asteroid belt was depleted in mass due to the rapid formation of Jupiter very early in the history of the solar system. Furthermore, among all kinds of small bodies, of particular importance are bodies near the expected dew point where water starts to condense to liquid or solid ice, thus where the innermost icy bodies form. Current observational evidence shows that the boundary between rocky bodies and icy bodies is probably somewhere within the asteroid belt or a little further. The composition of inner mainbelt asteroids is more silicate-rich, while that for outer mainbelt asteroids is more carbon-hydrogen-oxygen-nitrogen-rich (CHON-rich) (Tholen, 1984). Further small bodies such as the satellites of giant planets are rich in ice. Because of the biological importance of water, the boundary of its stable existence is of particular interest.

The first asteroid discovered in 1801, asteroid 1 Ceres, is the largest of these planetary embryos, and is located in the main asteroid belt with a semi-major axis 2.77 AU. De-

spite its relatively large apparent angular size as observed from the Earth, little is known about its composition, current evolutionary status, or history, because of the difficulty in interpreting its reflectance spectrum, and the failure to find any spectral match from available meteorite samples (Chapman and Salisbury, 1973; Johnson and Fanale, 1973). The shape and size of Ceres has been determined from earlier observations to be an oblate spheroid (Millis et al., 1987; Parker et al., 2002; Drummond et al., 1998; Saint-Pé et al., 1993), with the effective radius ranging from 471 km to 489 km. The mass of Ceres is measured by observing the perturbations of Ceres on other asteroids, and is consistently estimated to be about 9.4×10^{20} kg (Viateau and Rapaport, 1998; Michalak, 2000; Standish, 2001). The visual geometric albedo of Ceres is reported to be 0.073 (Millis et al., 1987) and 0.01 (Tedesco et al., 1983), higher than the albedo of carbonaceous chondrite material (3-5%), which is considered to be the main compositional material of Ceres.

NASA has selected the Dawn mission to orbit Ceres starting in 2015 for eleven months to investigate in detail its role in the early evolution of terrestrial planets, and to characterize the conditions and processes of the solar system's earliest epoch (Russell et al., 2004).

6.1.2 HST observations

In support of this mission, we observed Ceres with HST's High Resolution Channel of the Advanced Camera for Surveys (ACS/HRC) over the complete rotation of Ceres. The aspect data of the observations are listed in Table 6.1. The observations were carried out before its opposition in December 2003, and after in January 2004. Three broadband filters centered at 555 nm (F555W, V-band), 330 nm (F330W, U-band), and 220 nm (F220W,

Table 6.1. The aspect data of our HST observations. Three filters F555W, F330W, and F220W were used for all three runs.

UTC Date and Time	r[a](AU)	Δ[b](AU)	α[c](°)	# of Images
27-Dec-2003 22:52:30 to 28-Dec-2003 07:35:38	2.61	1.65	6.2	153
30-Dec-2003 03:39:23 to 30-Dec-2003 04:18:45	2.61	1.65	5.4	20
23-Jan-2004 11:37:30 to 23-Jan-2004 15:28:08	2.61	1.65	7.4	44

[a]Heliocentric distance

[b]Earth range

[c]Phase angle

UV-band) were used, where we expected strong absorption in Ceres' spectrum at UV. The pixel scale at Ceres is about 30 km, corresponding to about 3.5° longitude/latitude at equator. The heliocentric distance (r) and geocentric distance (Δ) of Ceres at that time were 2.6 AU and 1.6 AU, respectively, and phase angles (α) are from 5.4° to 7.4°.

From these HST observations, Thomas et al. (2005) have precisely determined the size, shape, and polar orientation of Ceres. The shape of Ceres has been modeled by fitting the limbs of projected ellipses when rotating , and determined to be a rotationally symmetric oblate ellipsoid within about 2 km, with an equatorial radius of 487$\pm$1.8 km and a polar radius of 455$\pm$1.6 km. The smoothness of the limbs of projected ellipses also indicates that Ceres is a fully relaxed body. The orientation of Ceres' rotational pole has been determined from the orientation of its short axis, and also by tracking the motion of

a bright spot on the HST images, to be at the direction of RA=291° and Dec=59°, with about 5° uncertainties. From the reported masses of Ceres (Viateau and Rapaport, 1998; Michalak, 2000; Standish, 2001), the mean density of Ceres is estimated to be 2.0×10^3 kg/m^3, with 3.2% uncertainty including the uncertainties in the estimated mass and in the volume determined above. The oblate shape and its estimated mean density is consistent with such a body if Ceres has a central rocky core surrounded by water ice. The water fraction estimated from the mean density of Ceres, the densities of other common compositional materials in big asteroids, and a simple model incorporating a differentiated internal structure, is from 18% to 28%. This is a reasonable value for objects at the solar distance of Ceres (Wilson et al., 1999; Grimm and McSween, 1989). The possible differentiation during its thermal evolution is described by some models (McSween et al., 2002; McCord and Sotin, 2005). But the distribution of water in different forms such as ice mantle, liquid ocean, or hydrated minerals, inside the body is highly model dependent.

6.2 Data Reduction

In order to perform photometric analysis to the HST images, they need to be calibrated to absolute photometric scale, either reduced magnitude with both heliocentric distance r and Earth range Δ 1 AU, or the standard reflectance unit I/F, where I is the intensity detected by HST, and πF is the incident flux received by the surface of Ceres.

The HST images were first corrected for geometric distortion and rotated north-up (E. F. Young, private communication) prior to any further photometric calibration, which was done in two steps. First, all images are calibrated to reduced magnitude at

r=1 AU and δ=1 AU. The procedure has been standardized and summarized in relevant HST documentation (Pavlovsky et al., 2005). Three keywords in the image headers were used to carry out this step: the exposure time, EXPTIME, and two photometry keywords, PHOTFLAM, the inverse sensitivity in ergs/cm^2/Ang/DN, and PHOTZPT in magnitude, the HST magnitude zero point. The formula we followed is

$$M = -2.5 \log \left(\frac{\text{DN}}{\text{EXPTIME}} \times \text{PHOTFLAM} \right) + \text{PHOTZPT} - 5 \log r - 5 \log \Delta \quad (6.1)$$

where DN is pixel value, r and Δ are the heliocentric distance and Earth range, respectively, measured in AU.

The second step is to convert reduced magnitude to reflectance unit I/F, with the formula derived to be

$$I/F = \frac{1}{A} 10^{(M_0 - M)/2.5} \quad (6.2)$$

where A is the pixel scale in km^2/pixel, and M_0 is a constant resulting from the apparent magnitude of the Sun $m_\odot$ at corresponding bandpass,

$$M_0 = m_\odot + 2.5 \log \pi + 5 \log(1\text{AU}/1\text{km}) = 42.12 + m_\odot \quad (6.3)$$

The apparent magnitude of the Sun through F555W filter was obtained by applying the 0.04 mag correction (Pavlovsky et al., 2004, Table 10.2) to the V-band magnitude of the Sun, -26.75 (Cox, 1999). M_0 is calculated to be 15.41 mag for F555W fitler. Combining Eq. 6.1, 6.2, and 6.3, the formula we used to convert DN number of HST images to I/F reads

$$I/F = r_0 \times \frac{\text{DN}}{\text{EXPTIME}} \times \frac{r^2 \Delta^2}{A} \quad (6.4)$$

where

$$r_0 = 10^{(42.12 + m_\odot - \text{PHOTZPT})/2.5} \times \text{PHOTFLAM} \quad (6.5)$$

is a constant for each filter, meaning the required reflectance for a 1-km^2 area at 1 AU from both the Sun and HST in order to produce one DN per one second exposure time as imaged by ACS/HRC through the corresponding filter. r_0 at 555 nm is calculated to be 1.21×10^{-4} (Table 6.2).

In order to calculate r_0 through F330W and F220W filters, the brightnesses of the Sun as seen through the two filters have to be calculated respectively. This is done by taking a high resolution spectrum of the Sun (A'Hearn et al., 1983; Lean et al., 1992), and modulating it by the throughput of the whole ACS/HRC imaging system including optics, filters, and CCD response, as found from relevant HST documentations (Pavlovsky et al., 2004), and then calculating the average flux per unit wavelength:

$$F_i = \frac{\int F(\lambda)T_i(\lambda)d\lambda}{\int T_i(\lambda)d\lambda} \tag{6.6}$$

Where F_i is the average solar flux per unit wavelength through filter i, $T_i(\lambda)$ is the total throughput of the imaging system, $T_i(\lambda) = T_o \times T_{fi} \times T_{CCD}$, including the throughput of optics (T_o), filter i (T_{fi}), and CCD response (T_{CCD}). After the average solar fluxes per unit wavelength through F330W filter and F220W filter relative to that through F555W filter are calculated, the magnitudes of the Sun through those two filters can be calculated. However, it has to be noted that there exists about 10% red leak for ACS/HRC F220W filter when imaging the Sun (Pavlovsky et al., 2004, Table 4.7). Thus in the calculation of the inband magnitude of the Sun through F220W filter, we put a spectral cutoff at 320 nm to avoid including out-of-band flux. The calculated apparent magnitudes of the Sun and corresponding r_0's are summarized in Table 6.2. According to the ACS Instrument Handbook (Pavlovsky et al., 2004), the absolute photometric calibration of ACS/HRC images

Table 6.2. Calibration constants for Ceres HST images

Filter	PHOTFLAM (ergs/cm^2/Ang/DN)	PHOTZPT (mag)	$m_\odot$ (mag)	r_0
F555W	3.020×10^{-19}	-21.1	-26.71	1.22×10^{-4}
F330W	2.237×10^{-18}	-21.1	-25.85	1.97×10^{-3}
F220W	8.113×10^{-18}	-21.1	-22.60	0.144

should be generally better than 2%. Considering the uncertainties of the high resolution solar spectra we used, and the throughput characteristics of ACS imaging system, the absolute photometric calibration for images through other two filters should be better than 3%.

The resultant I/F of Ceres through the F220W filter obtained using the above procedure of calibration also contains a considerable amount of red leak, which can be estimated with the following analysis. Let the throughput function of F220W filter to be $T(\lambda) = T_0(\lambda) + T_1(\lambda)$, where $T_0(\lambda)$ is the inband throughput, and $T_1(\lambda)$ is the out-of-band throughput. For a solar spectrum, the total flux received by detector through this filter can be writen as the sum of inband flux, F_0, and out-of-band flux F_1, where

$$F_\# = \int F_\odot(\lambda) T_\#(\lambda) d\lambda \text{ , \# = 0 or 1} \tag{6.7}$$

$F_\odot(\lambda)$ is solar flux spectrum prior to entering the filter. Table 4.7 in Pavlovsky et al. (2004) shows that F_0=90.2%$\times(F_0 + F_1)$. For Ceres, the total flux through the F220W

filter also contains two components, an inband flux, F'_0, and an out-of-band flux, F'_1, expressed as,

$$F'_{\#} = \int r(\lambda) F'_{\odot}(\lambda) T_{\#}(\lambda) d\lambda \text{ , \# = 0 or 1} \tag{6.8}$$

where $r(\lambda)$ is the reflectance of Ceres as a function of wavelength, and $F'_{\odot}$ is solar flux spectrum, different from $F_{\odot}$ in Eq. 6.7 by a constant scaling factor, C. If we write the average reflectance of Ceres through the F220W filter as

$$r_{220} = \frac{\int r(\lambda) F'_{\odot}(\lambda) T_0(\lambda) d\lambda}{\int F'_{\odot}(\lambda) T_0(\lambda) d\lambda} \tag{6.9}$$

then the F'_0 for Ceres is, $F'_0 = r_{220} \times C \times F_0$, where F_0 is defined in Eq. 6.7. In addition, because the spectrum of Ceres is flat within $\pm$10% at wavelengths longer than 400 nm, we can write the F'_1 term for Ceres as $F'_1 = r_1 \times C \times F_1$, where F_1 is also defined in Eq. 6.7. If we assume that r'_{220} is the average reflectance of Ceres calculated from the total flux through F220W filter,

$$r'_{220} = \frac{\int r(\lambda) F'_{\odot}(\lambda) (T_0(\lambda) + T_1(\lambda)) d\lambda}{\int F'_{\odot}(\lambda) T_0(\lambda) d\lambda} \tag{6.10}$$

then the total flux of Ceres through F220W filter is $r'_{220} F_0$ times the constant C, and we have

$$r'_{220} F_0 = r_{220} \times F_0 + r_1 F_1 \tag{6.11}$$

Simple manipulation shows that

$$\frac{r_{220}}{r'_{220}} = 1 - 0.109 \times \frac{r_1}{r'_{220}} \tag{6.12}$$

If take $r_1 = r_{555}$, the reflectance at V-band, and measure r_{555} and r'_{220} from our HST images, we found that the real reflectance of Ceres through F220W filter is 80.2% of the

value without considering red leak as directly obtained from the photometric calibration. The uncertainty in the absolute photometric calibration for images through F220W filter was estimated to be about 8%, including the uncertainties of the estimate of red leak.

Another possible source of uncertainty of the absolute photometric calibration comes from the imperfect charge transfer efficiency (CTE) of ACS/HRC CCD (Pavlovsky et al., 2004). It is estimated that the uncertainty caused by CTE is less than 1% for absolute photometry, and about 4×10^{-4} across the disk of Ceres. Therefore this part does not dominate.

6.3 Disk-Integrated Photometry

6.3.1 Lightcurve

The total magnitude of Ceres plotted *vs.* sub-Earth longitude is shown in Fig. 6.1. The magnitude, shape and the amplitude of the lightcurve through F555W filter consistently agrees with earlier ground based observations in V-band at similar phase angles (Tedesco et al., 1983; Taylor et al., 1976; Schober, 1976; Gehrels and Owings, 1962; Ahmad, 1954). The average magnitude of Ceres $M(1,1,\alpha)$ through F555W filter is 3.92$\pm$0.02 mag. Because of the flat spectrum of Ceres at wavelengths longer than 400 nm, the 0.04 mag correction to convert solar magnitude from V-band to F555W fitler (Pavlovsky et al., 2004) is still valid for Ceres, yielding a V-band magnitude of Ceres 3.88$\pm$0.02 mag at 6.2° phase, in an excellent agreement with the value obtained by Tedesco et al. (1983). The 0.04 magnitude lightcurve amplitude, which is roughly 4% of the average brightness, although small compared to the lightcurve amplitudes of other asteroids, cannot be

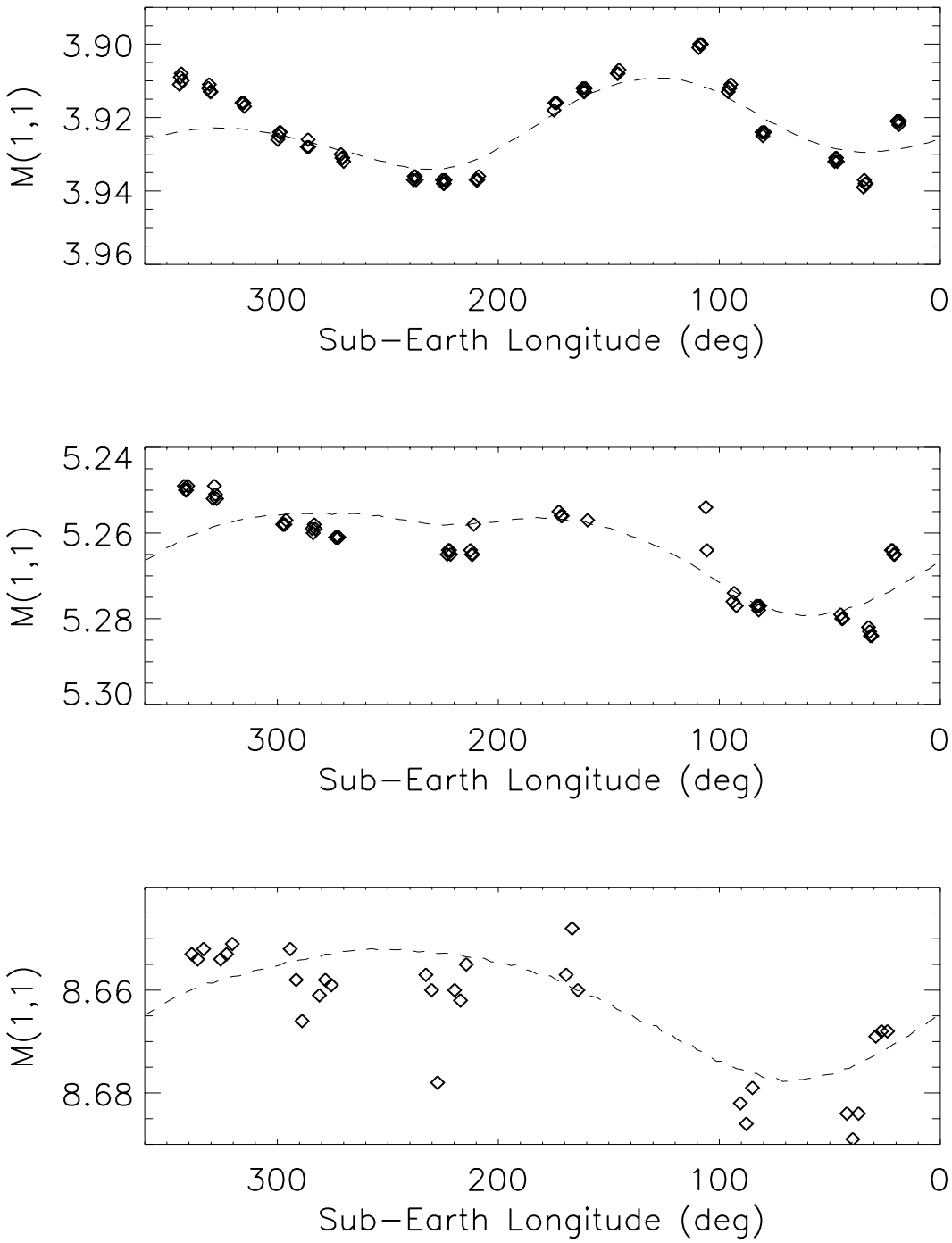

Figure 6.1 The lightcurves of Ceres are plotted in symbols for V-band (upper panel), U-band (middle panel) and UV-band (lower panel) as functions of sub-Earth longitude. The synthetic lightcurves constructed from our SSA maps are plotted as dashed lines (see later text).

produced by Ceres' rotationally symmetric shape (Thomas et al., 2005). The only explanation is that the surface of Ceres shows some non-randomly distributed albedo pattern, either big areas with small variations of reflectance relative to the average, or small areas with big reflectance variations.

6.3.2 Spectrum

The HST observations provide whole-disk reflectance at three wavelengths, complementing earlier measurements to construct a spectrum covering UV wavelengths for Ceres. From the total brightnesses of Ceres at the three wavelengths as measured from the HST images, the geometric albedo can be calculated by

$$p(\lambda) = \frac{r^2\Delta^2}{R_{Ceres}^2}\frac{F_{Ceres}(\lambda)}{F_{\odot}(\lambda)}f_{\alpha} \tag{6.13}$$

r and Δ are the heliocentric (in AU) and geocentric (in km) distances of Ceres. R_{Ceres} is the equivalent radius of Ceres, which we used 470.7 km from the two axes of its best fit oblate spheroidal shape model (Thomas et al., 2005). $F_{Ceres}(\lambda)$ is the measured total flux of Ceres through each filter, and $F_{\odot}(\lambda)$ is the solar flux at 1 AU over the same filter. The phase correction factor f_{α}=1.6 was calculated using the equations of the IAU-adopted HG system (Bowell et al., 1989) with a slope parameter G=0.12 (Lagerkvist and Magnusson, 1990).

Combining our observations with earlier ones (Parker et al., 2002; Chapman and Gaffey, 1979), the spectrum of Ceres is shown in Fig. 6.2, where the spectrum at visible wavelengths from the 24-color asteroid survey is rescaled so that its value at V-band is equal to the geometric albedo measured in our analysis. The most prominent feature in the

spectrum of Ceres is a strong absorption band centered at about 280 nm, with a FWHM of about 120 nm, and about 30% reflectance relative to 555 nm. With the large uncertainty of the geometric albedo at 162 nm wavelength from Parker et al., the blue side of the band is not well defined. But the existence of an absorption band is consistent with the different mechanisms for the absorption features as discussed by Gaffey et al. (1989).

The wavelength position of the Hartley band of O_3 (290 nm vicinity) falls in the the wavelength regions of our analysis. We have to consider the possibility that this spectral feature is affected by terrestrial atmospheric ozone. In order to do this, we calculated the angular separation between the line of sight of HST and the direction of Earth's limb as seen from HST, as a function of the altitude of the closest point from Earth limb to the line of sight of HST (line AB in Fig. 6.3). To prevent the scattered light from Earth's limb and terrestrial atmosphere, HST is not allowed to point within 7.1° to the Earth limb during nighttime, and 15° during daytime. Therefore, from Fig. 6.3, we see that the line of sight of HST is never closer than 295 km from Earth's limb. This is much higher than the altitude of terrestrial atmospheric ozone, which is less than about 100 km from Earth's surface. Therefore, all HST observations are free of ozone contamination from terrestrial atmosphere. And for our observations, the spectral feature is from the surface of Ceres.

Spectral absorption bands at similar wavelengths have been detected for Jupiter's icy satellites, Europa and Ganymede. A broad absorption feature in the UV spectrum of Europa was first noted by Lane et al. (1981), and confirmed by Noll et al. (1995). It was attributed to an SO band, caused by the implantation of sulfur ions from Jupiter's magnetosphere into the water-ice surface on the trailing hemisphere (Lane et al., 1981; Sack et al., 1992; Noll et al., 1995). An absorption band at similar wavelength has been

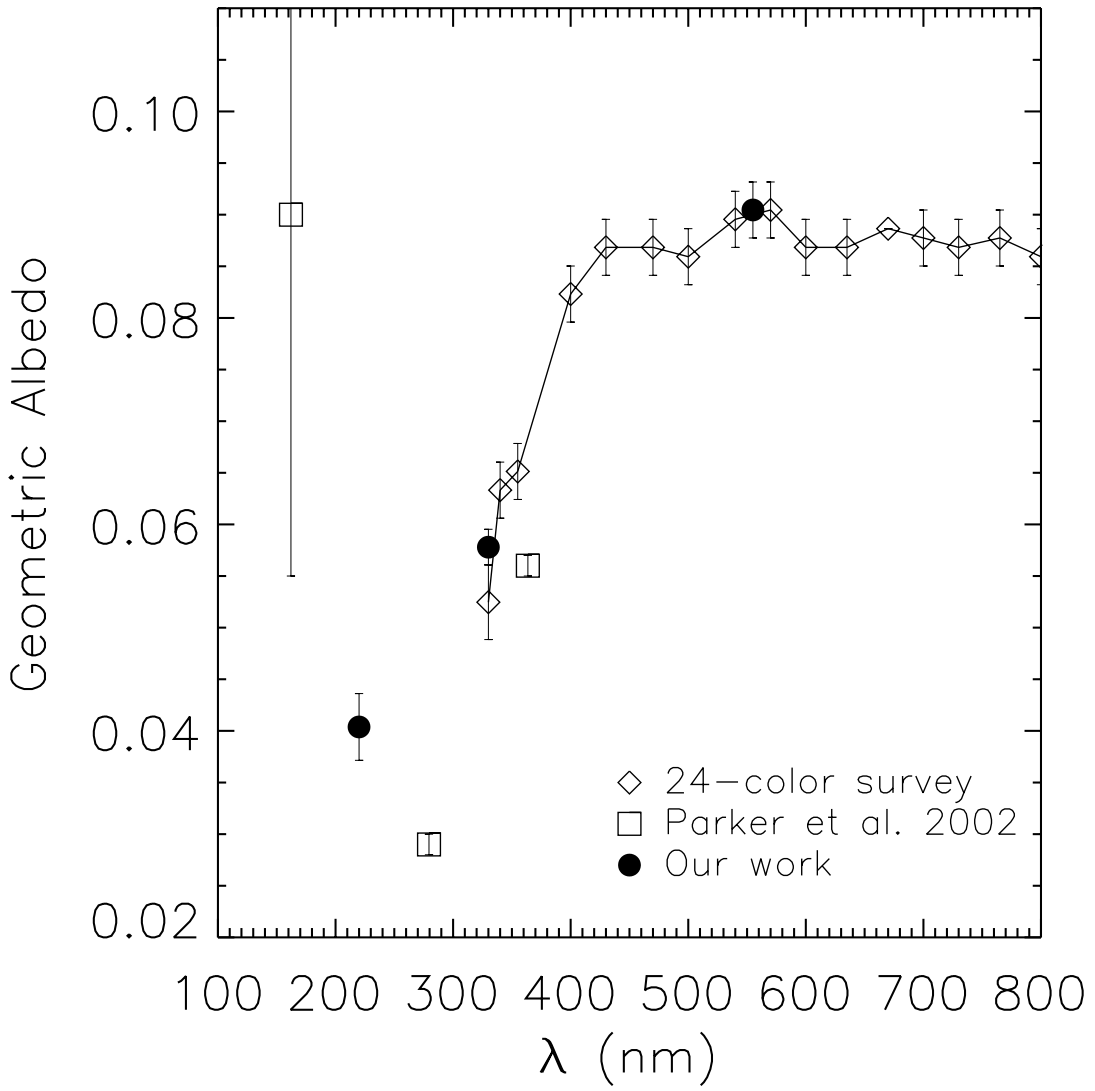

Figure 6.2 The spectrum of Ceres constructed from our measurement and earlier observations. Plotted as y-axis is the geometric albedo at various wavelengths. The uncertainties for our measurements are about 3%.

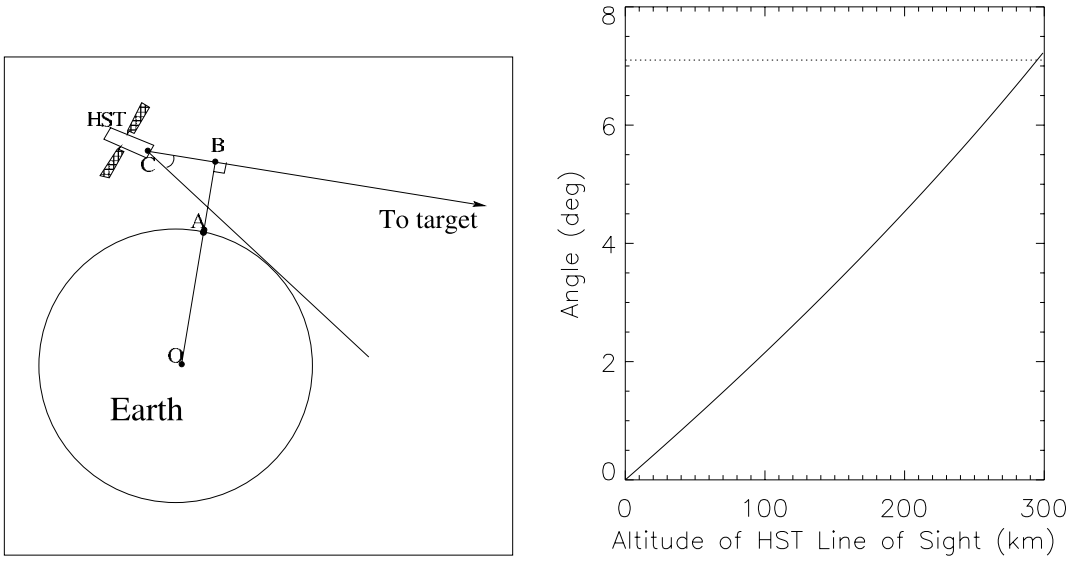

Figure 6.3 The angular separation between the line of sight of HST and Earth limb as seen from HST (angle ACB), is plotted as a function of the altitude (line AB) of the closest point (point B) along HST line of sight (line CB). The minimum allowed angular separation of the line of sight of HST from Earth limb, 7.1°, determines that the lowest altitude of the light of sight of HST is much higher than the altitude of terrestrial atmospheric ozone, which is about 100 km.

observed on Ganymede, and is identified to be the Hartley band of ozone (Noll et al., 1996). The value of the density ratio of $[O_3]/[O_2]$ has been estimated to be 10 times of the peak ratio of the Earth's atmosphere in the same paper. Although the UV absorption band in Ceres' spectrum could also be due to ozone or SO_2 trapped in Ceres' surface, it is much stronger than those in the spectra of Jupiter's satellites. And unlike Europa and Ganymede, Ceres is not in a highly radiative environment with continuous supply of sulfur and oxygen as are Europa and Ganymede. We have compared the absorption band with available laboratory measured UV spectra (Wagner et al., 1987), but found none of them matches the absorption band in both the strength and the wavelength. More observations with higher spectral resolution are needed to confirm the strong UV absorption feature in Ceres' spectrum, and more analyses are needed for the spectrum of Ceres to reveal its nature.

6.4 Disk-Resolved Analysis

6.4.1 Hapke's model

With the sunlit disk of Ceres resolved into about 750 pixels, and the precisely determined but simple shape (Thomas et al., 2005), the normal direction of a surface element imaged in each pixel can be analytically calculated, and the reflectance can be modeled on a pixel-by-pixel basis. The excellent signal-to-noise ratio of greater than 1000 for the images of Ceres enables us to study its reflectance variations, which are expected to be at least 4% as indicated by the lightcurve amplitude.

The HST observations only cover a small range of phase angles (5.4° to 7.5°).

According to Hapke's photometric model, phase parameters such as asymmetry factor (g) and opposition parameters (B_0 and h) cannot be determined from the small range of phase angles covered by our HST observations (see Chapter 2). Therefore we took the values for those parameters from Helfenstein and Veverka (1989), g=-0.4, B_0=1.6, h=0.06, in our analysis, and only modeled the single scattering albedo (SSA), w, and the roughness parameter, $\bar{\theta}$. On the other hand, since the HST images cover the whole rotation of Ceres, we can construct surface maps from those images. For this purpose, the geometric effects in all images have to be removed with the modeled limb darkening profile. According to Hapke's theory, the bidirectional reflectance of a rough surface is expressed as Eq. 2.53. For the dark surface of Ceres with an SSA of about 0.06 (Helfenstein and Veverka, 1989), multiple scattering is always less than 3% of the total scattering under any geometries, thus we can safely ignore the multiple scattering term in Eq. 2.53 here, too, as for comet Borrelly, yielding Eq. 5.1. The bidirectional reflectance is now proportional to the SSA, w; limb darkening profile, ($\mu_{0e}/(\mu_{0e} + \mu_e)S(i, e, \alpha)$), which only depends on one parameter, $\bar{\theta}$; and a phase function, $[1 + B(\alpha)]p(\alpha)$, that is only a function of phase angle α once g, B_0, and h are preset and kept unchanged in modeling. Furthermore, to prevent the uncertainties in phase parameters (g, B_0, and h) from affecting our modeling of limb darkening profile, and in turn the SSA maps, we decided to only use the images taken in the first HST observing run that are almost at one single phase angle (6.1°-6.2°), but cover the whole rotation of Ceres, to perform Hapke's modeling, and to construct albedo maps.

Hapke's fitting shows that at all three wavelengths, only the central portion of Ceres' disk with incidence angles i and emission angles e less than about 50° (V and U) or 40°

(UV) can be modeled with small residuals of about ±2%, consistent with the lightcurve amplitude, and without any systematic deviation associated with particular incidence and emission angles (Fig. 6.4). The modeled parameters are listed in Table 6.3. For the outer annulus, Hapke's model will give out a fit that has large residuals, and systematic bias with respect to geometry. Other empirical models, including the Minnaert's model, and a modified Minnaert's model, are employed to fit the outer annulus, with the model residual shown in Fig. 6.4, too (see later text for details). The SSA at V-band is about 0.073±0.002, yielding a modeled geometric albedo of 9.2%. The SSA at 330 nm and 220 nm is determined to be 0.046±0.002, 0.032±0.003, respectively. The V-band SSA of Ceres is low compared to both mafic silicate-rich asteroids and icy moons of giant planets, but high relative to the most common type of asteroids, C-types, and comets that contain large fractions of water ice.

The roughness parameter of Ceres is fitted by Hapke's model to be 48° from 555 nm images, and 38° from images at the other two wavelengths. Because surface roughness is a topographical parameter, it should not depend on wavelength except for bright surfaces, for which multiple scattering probably illuminates shadows to mimic the effect of low roughness. We take the average of the fitted values for roughness, 40°±6°, as our modeled roughness parameter. The high roughness of Ceres is not consistent with earlier results using a disk-integrated phase function observed from ground (Helfenstein and Veverka, 1989), which is only within 20° phase, thus not good for modeling roughness. Radar observations indicate that Ceres' surface is very rough at scales larger than meters to tens

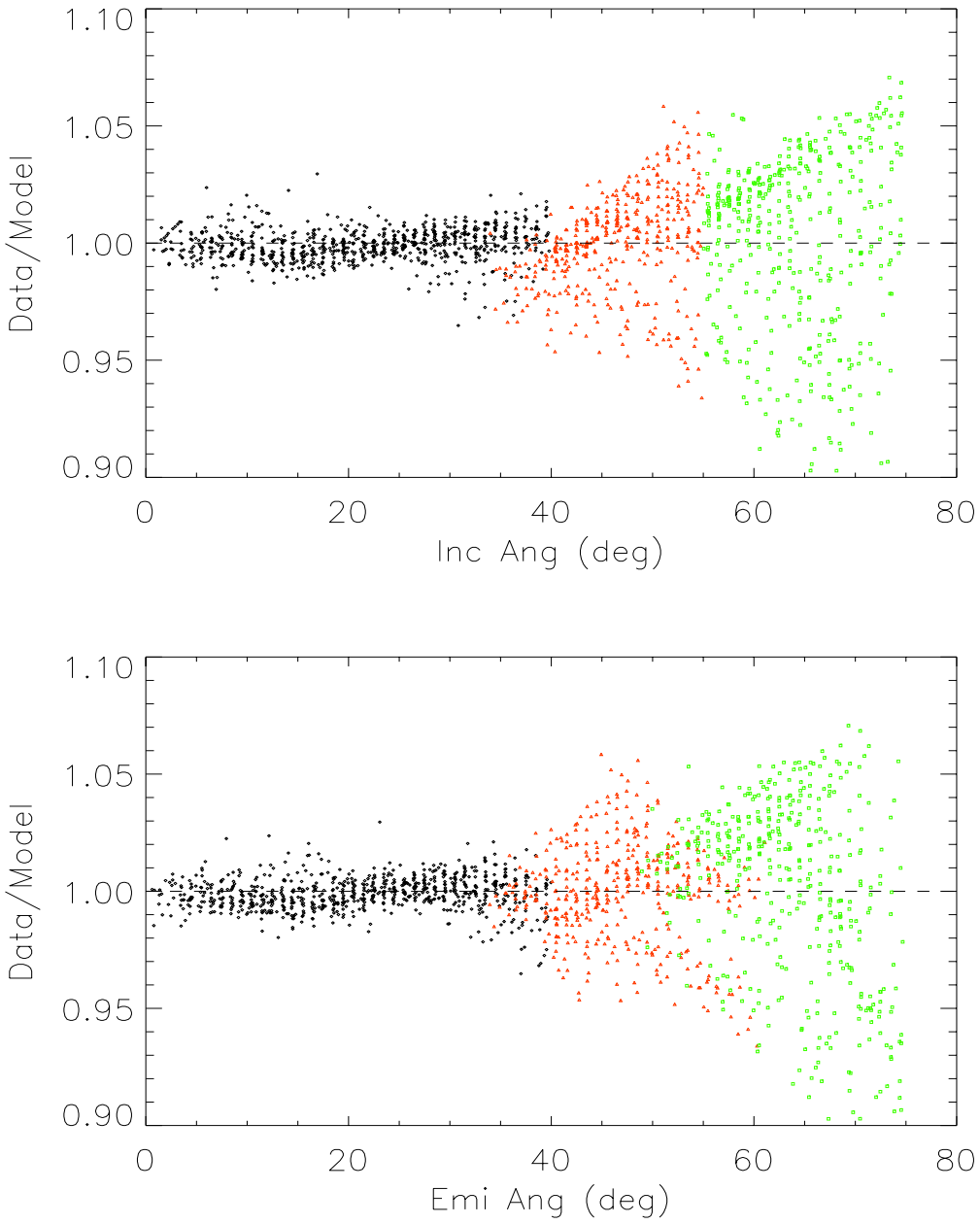

Figure 6.4 The ratio of the measured reflectance to modeled reflectance for the HST images through filter F555W, plotted as functions of incidence angle and emission angle. Black dots represent the fit with a Hapke's model, red dots a Minnaert's model, and green dots a modified Minnaert's model (see later text). The scatter for small i's and e's with Hapke's models is below $\pm$2% level.

of meters, with an RMS slope θ_{rms} of 20°-50° (Mitchell et al., 1996), which is defined as,

$$\tan\theta_{rms} \equiv < \tan^2\theta >^{1/2} = [\int_0^{\pi/2} \tan^2\theta p_P(\theta) \sin\theta d\theta]^{1/2} \tag{6.14}$$

where $p_P(\theta)$ is the slope probability distribution. The RMS slope of Ceres translates to a photometric roughness parameter $\bar{\theta}$ about the same value. But the polarization characteristics of the same radar echos also indicate that the surface of Ceres is very smooth at centimeter to decimeter scales.

6.4.2 Minnaert's model

Another commonly used, however empirical, limb darkening model is the Minnaert's model (Minnaert, 1941), where the reflectance of a surface is described by

$$r = A \cos^k i \cos^{k-1} e \tag{6.15}$$

with a constant A called Minnaert's albedo, and a constant k. Usually both Minnaert's parameters depend on phase angle. Unlike Hapke's model, Minnaert's model does not yield the SSA of the surface. Parker et al. (2002) found that, different from other asteroids and the Moon, Ceres has a very high Minnaert's k of about 0.9, meaning a strong brightness drop from disk center towards the limb. However, near-IR observations in H and K bands (1.55-1.80μm and 1.95-2.40μm, respectively) show a flatter brightness profile for the center 60% of the disk, indicating a Minnaert's parameter k close to 0.5 (Saint-Pé et al., 1993).

We used Minnaert's model to fit Ceres, and found that, at all three wavelengths, Minnaert's model yields a good fit in the places where Hapke's model does, and is also good for the immediate outer annulus until i and e about 60°, as shown by the red dots in

Table 6.3. Modeled Hapke's parameters and Minnaert's parameters for the central portion of Ceres' disk.

λ (nm)	Number of Data Points	w or A[a]	$\bar{\theta}$ or k[b]	RMS (%)
		Hapke's model		
555	1088	0.073	48	1.4
330	667	0.046	38	1.1
220	545[c]	0.032	38	1.6
		Minnaert's model		
555	1088	0.095	0.62	0.95
330	667	0.059	0.58	1.0
220	545	0.042	0.55	1.6

[a]For Hapke's model, the SSA is listed in this column. Otherwise the modeled Minnaert's albedo A for is listed.

[b]For Hapke's model, the roughness parameter $\bar{\theta}$ is listed in degrees, otherwise the modeled constant k for Minnaert's model is listed.

[c]Only include data with i and e less than 40°.

Fig. 6.4, but not the outermost annulus of Ceres' disk. For the central portion of the disk, the value of Minnaert's parameter is found to be about 0.6 for all three wavelengths (Table 6.3), a better agreement with the value found from the mid-IR observations. Since the phase angle of our observations is 6.2°, which is closer to that of the mid-IR observations (α=9°) than to that of Parker et al. (α=19°), it is very likely that the difference between the modeled k is due to phase angle change. If this is true, then it indicates that the limb darkening properties of Ceres strongly depend on phase angle, but not on wavelength. And the phase angle dependence of Minnaert's parameter is even stronger than that of icy satellites of Uranus (Veverka et al., 1989). But whether this dependence is due to a geometrical origin or particle's single-scattering properties cannot be determined.

6.4.3 Modified Minnaert's model

In addition to the above models to fit the central part of Ceres' disk, we also attempted to model the outer rim where either Hapke's model or Minnaert's model failed, to see whether the limb darkening can be described by any other model. By observing the bidirectional reflectance as a function of incidence angle and emission angle, we noticed that, for the rim of Ceres' disk where i and e are higher than 50° (40° for 220 nm images), the reflectance depends on both i and e strongly, but with different dependence. The dependence is not like that which is predicted by a Minnaert's model with a k parameter close to 1, in which case the reflectance depends on $\cos i$ strongly, while on $\cos e$ rather weakly. Thus we tried a model that is modified from the Minnaert's model, where

$$r = A \cos^k i \cos^j e \tag{6.16}$$

Table 6.4. The modeled parameters of the modified Minnaert's model to the outer annulus of Ceres.

λ (nm)	Range of i and e	Number of data points	A	k	j	RMS (%)
555	$50 < e \leq 75$	606	0.110	0.39	0.18	3.1
330	$50 < i, e < 60$	150	0.058	0.48	-0.19	1.3
	$i, e > 60$	237	0.073	0.52	0.10	3.3
220	$40 < i, e \leq 60$	170	0.050	0.37	-0.049	1.8
	$i, e > 60$	237	0.059	0.42	0.16	3.7

A is a constant, equivalent to Minnaert's albedo. k and j are two different power indices, representing different dependence of the reflectance on incidence angle i and emission angle e. If $j = k - 1$, then this model reduces to Minnaert's model.

χ^2 fitting to this model for the outer rim of Ceres' disk shows that this model actually works better than both Hapke's model and Minnaert's model in this region (Fig. 6.4, green dots), although the residual is still greater than those of any models for the central part of the disk. The modeled parameters are listed in Table 6.4 at all three wavelengths. It is noticed that for the outer annulus, especially close to the edge of the disk, reflectance depends on both i and e with positive power law indices, meaning decreasing reflectance with both i and e.

6.4.4 Albedo maps

As stated earlier, for the dark surface of Ceres, the bidirectional reflectance is approximated to be proportional to w. If one assumes 10% SSA variation for Ceres, which is reasonable as found later, the variation in multiple scattering will be about 4% for a roughness parameter $\bar{\theta}$=40°, and is only responsible for 1% of the total reflectance variation given that multiple scattering is always less than 3% of the total scattering for a surface with only 7% SSA. In other words, for Ceres' surface, more than 99% reflectance variation is accounted for by the variation in single scattering, which is proportional to the SSA, w. Therefore, the deviation maps of bidirectional reflectance derived from the ratio of real images to the models with disk-averaged photometric parameters (Table 6.3) actually represent the deviations of the SSA from its average. The assumption of constant multiple scattering results in correct SSA map at 555 nm within an uncertainty of less than 1%, and even less for the SSA maps at other two wavelengths because of the lower SSA.

Thus our procedure to find the SSA maps was that, first, for each HST image, we generated a model image using the disk-averaged parameters at the corresponding wavelength and the geometry of that image. Then we calculated the ratio of the real image to the model to find a map of the SSA deviation from the global average. The SSA deviation map is equivalent to the SSA map by a constant factor, which is the disk-averaged SSA at the corresponding wavelength. Therefore, in our following analysis and presentation of our results, we only refer to the deviation maps in the unit of percentage deviation from the corresponding average SSA at that wavelength. Because of the small SSA variations

of Ceres as shown later, this method of representing the SSA maps emphasize subtle variations. In our next step, the SSA map as a disk in the imaging plane is projected onto a planetocentric longitude-latitude coordinate system that is modified from the definition in Thomas et al. (2005), with its west longitude system changed to an east longitude system. After the projection maps have been made for all images, at each wavelength, we combine them, for each pixel, by taking the median of all maps covering that pixel, to construct a final SSA map in Ceres' longitude-latitude system. SSA maps at three wavelengths are shown in Fig. 6.5. All these maps only contain low-latitude area on Ceres (lower than $\pm 50^\circ$ for V and U maps, and $\pm 40^\circ$ for UV), because only these parts on the disk can be fitted with Hapke's model. These maps are close to model-independent in the sense that we do not see any dependence of the residual on incidence and emission angles, thus no dependence on the relative locations in the imaged disk. The resolution in these maps is enhanced compared to the original images.

A pseudo-color map from the three maps is also constructed with V-, U-, and UV-band SSA deviation maps representing red, green, and blue, respectively (Fig. 6.6). Thus a red area in the pseudo-color map represents an area with high albedo relative to the average at V-band, but relatively dark at other two bands; if an area is yellow, a combination of red and green, then that area is relatively dark at only UV-band, but relatively bright at other two wavelengths; and a white area means an area that is relatively bright at all three wavelengths. This map includes not only low-latitude areas where Hapke's model works well, but also high-latitude areas where the modified Minnaert's model was used. For the high-latitude area, we used the resultant model parameters from the Minnaert's model and the modified Minnaert model. Therefore keep in mind that for high-latitude

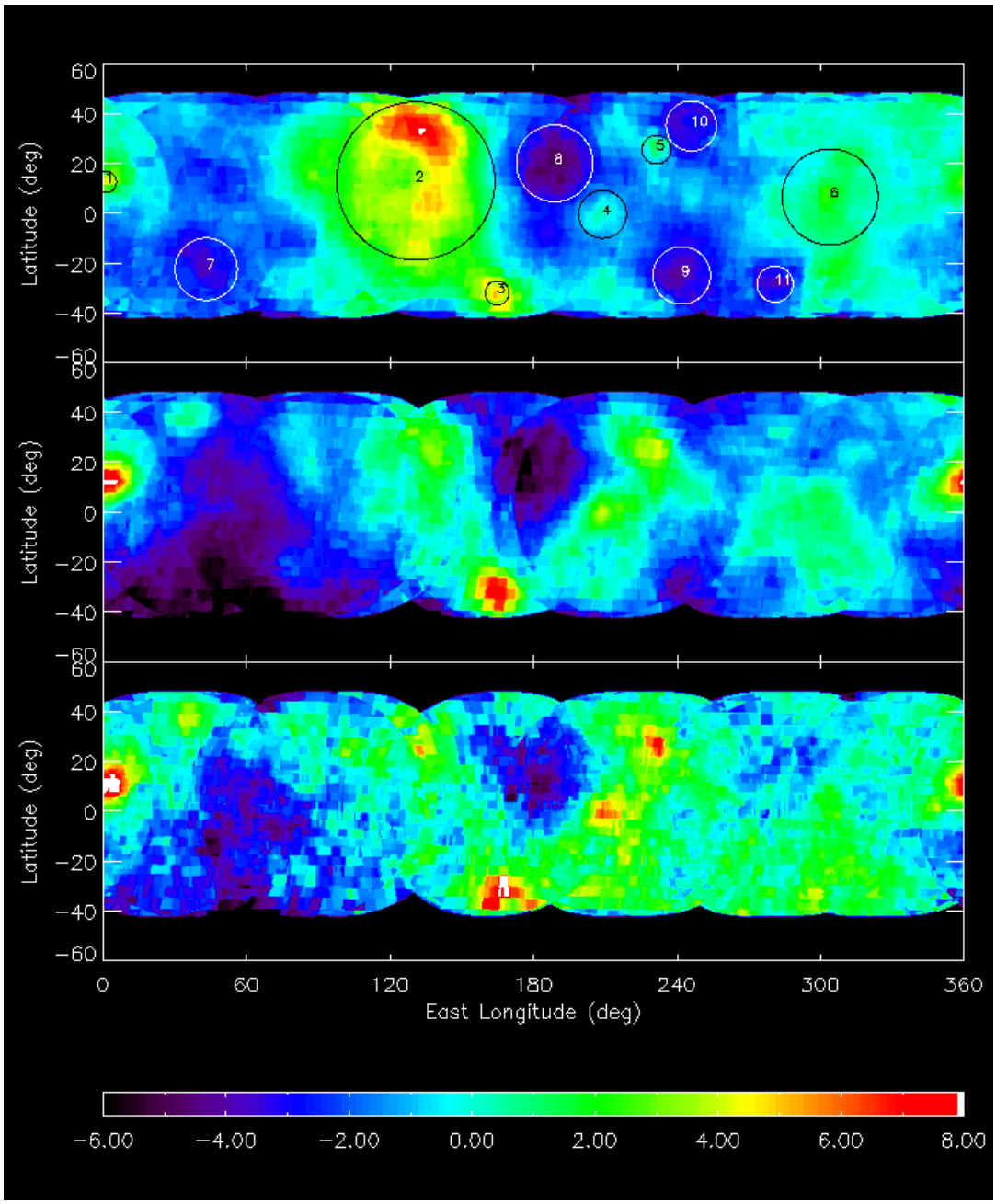

Figure 6.5 The SSA deviation maps of Ceres at V- (upper panel), U- (middle panel), and UV-band (lower panel). The color bar represents the percentage deviation of the SSA from their corresponding average values at three wavelengths (V: 0.073, U: 0.046, UV: 0.032). Circles with numbers in the upper panel mark the features we identified. From #1 to #6 are bright features, and from #7-#11 are dark features.

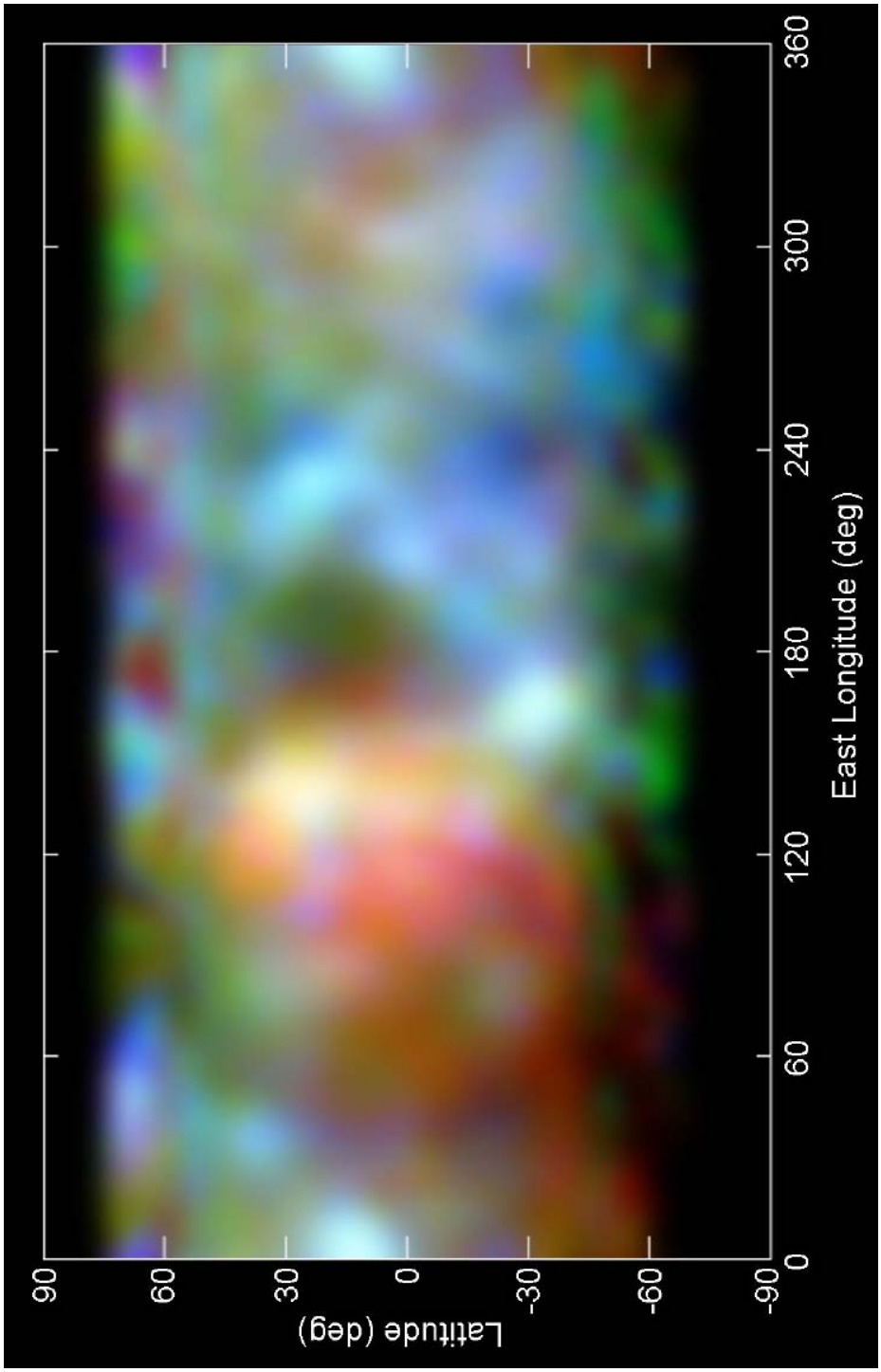

Figure 6.6 The pseudo-color map of Ceres constructed from three albedo deviation maps at 555 nm (red channel), 330 nm (green channel), and 220 nm (blue channel).

area, the uncertainties in the SSA maps will be relatively large, and could be greater than the SSA variation for some areas. This pseudo-color map has been enhanced in contrast and color, and blurred by a scale of 3.5°, which is the corresponding pixel scale of our HST images at the equator on the surface of Ceres.

Since the SSA variation over Ceres' surface is only a few percent, we have to consider if the features seen on the maps are real or possibly due to artifacts from data processing, or even just random noise. For this purpose, we performed three tests. First, we made sure that the noise level in the original images is low compared to the variation of features so that they are not confused with surface features. To do this, the noise levels from raw images are estimated by the statistics of the background sky in those images, to be about 0.02%, 0.04%, and 0.4% of the average pixel readings over Ceres' disk for V-, U-, and UV-band images, respectively. This level is much smaller than the SSA variation of about 2% at both V-band and U-band, and is about 1/5 of the SSA variation at UV. Furthermore, the calculated standard deviation of the SSA measured from different images for each longitude-latitude grid point is usually 1/5 to 1/4 of the SSA variation. As shown above, the uncertainties caused by our approximation of constant multiple scattering is less than 0.3%. The uncertainty of relative photometry for HST/ACS images is usually better than 1%. Therefore although the distribution of the SSA at any wavelength is unimodal like a Gaussian, it does not necessarily mean that the features are totally random like noise, especially when we do not observe any random spatial distribution of features from the SSA maps. The absolute photometric calibration error has the same effect for all pixels, thus does not affect the relative brightness of features. The photometric modeling is free of systematic deviations associated with incidence or emission angle, therefore is

not likely to introduce artifacts.

Next, for each filter, we linked the images before being projected into longitude-latitude coordinate, while they are still disks, in the order of the time of observations, generating an animation showing the rotation of Ceres' disk. Then we linked the corresponding projected SSA maps in longitude-latitude plane into another animation, showing how the projection of the imaged hemisphere in each image moves in the fixed longitude-latitude coordinate when sub-Earth point moves around Ceres. Comparing these animations, we found that, while in the first animation, features like bright spots or dark spots move across the disk when Ceres rotates, the corresponding features in the second animation just sit still in their own longitude-latitude positions, with almost the same brightness level from frame to frame. This gives us confidence of two aspects: first, we do see features in the raw HST images that are moving across the disk as Ceres rotates; and second, the same features in all images are mapped into their correct location on the longitude-latitude plane, and are positively enhanced to show themselves in the projections.

The third test is to use our SSA map and the shape of Ceres to produce disk-integrated lightcurves, and compare them with the observed lightcurves at three wavelengths. The synthetic lightcurves are plotted in Fig. 6.1 as dashed curves. We did not try to calibrate the absolute scale of the observed lightcurve and the synthetic lightcurve because the uncertainty in modeling the outer annulus is comparable with the lightcurve amplitude, so that it is hard to calibrate absolute brightness scale. Instead, the synthetic lightcurves were aligned with the observed ones to compare the shapes. We notice that the synthetic lightcurves almost simulate the observed ones, indicating that the overall distribution of bright and dark terrains are retrieved correctly. The biggest difference ap-

pears at longitude about 0° at all three wavelengths, where the observed brightness are higher than model predicted by 0.015 mag compared to the 0.04 mag total lightcurve amplitude. The underestimate of modeled lightcurve amplitude could be due to features at high latitude that cannot be modeled well. The slightly smaller lightcurve amplitude of synthetic lightcurves indicates that, at least to the scale comparable to the size of disk, we do not create features, and on the other hand, we may lose some features and fail to simulate their effect on the disk-integrated lightcurves.

To estimate the relative error of the SSA deviation maps quantitatively, we calculated the standard deviation for each longitude-latitude location according to the total number of images for that location weighed by its cosine of emission angle in each image. This takes into account the pixel resolution change due to the projection from disks to the longitude-latitude plane. We found that for the area with latitude less than 50°, the error does not exceed 3% in the V-band map, and peaked at 1% level. At U-band, the same analysis shows a maximum error of 4% for low-latitude areas, with most at 1.3%. The SSA map at UV shows some large errors greater than 10% and up to 50% for less than 3% of the total area of the low-latitude surface, but most of it is at 2% level. All those tests and the error estimate convinced us that, for areas with latitude lower than 50°, at least the big features seen on the maps are real. Small features could also be real, but their shapes may have been circularized due to the limited spatial resolution.

6.4.5 Albedo features

The SSA features show local heterogeneity on Ceres, although variations from average are very small. The features are quite consistent but with different relative strengths at

three wavelengths (Fig. 6.5, Table 6.5). The most obvious, #2, the big bright area, is centered at 130° longitude and 15° latitude, about 60° across, with an elongated shape. Other small features appear to be circular, including the one at 0° longitude (#1), and the series of features (#3-#5) along a diagonal line to the right of the biggest bright area. A dark area (#7) to the left of the biggest bright area is open toward the South pole. Another dark area (#8) close to the equator and to the right of #2 has a bright rim around it, and is consistently dark at all three wavelengths. Its latitude is consistent with the "Piazzi" feature reported previously (Parker et al., 2002), but an identification cannot be made due to insufficient longitude constraints of the earlier observations.

Comparing the SSA maps at three wavelengths, or looking at the pseudo-color map, we see that the features can be divided into at least two different spectral groups. One is #2, which is relatively redder by 8% than the second group, including #1 and #3-#5. This difference is confirmed by the different shapes of lightcurves at three wavelengths (Fig. 6.1), and in the later sections by the different trends of their spectra. The spectral variation between those two groups of features, and their different shapes, may indicate different compositions and origins.

6.5 Discussions

6.5.1 Roughness parameter

Hapke's theory was developed with the assumptions of low albedo and low roughness (Hapke, 1993). The roughness parameter of Ceres is modeled to be as high as 48°, therefore it is probably not physical. Nevertheless, the modeled parameters provide good de-

Table 6.5. Summary of features on Ceres' surface. Their SSA at 555 nm for #1 to #6 are brighter than surrounding background, and for #7-#11 darker than surrounding area.

Index	Longitude (°)	Latitude (°)	Size (°)	V-band SSA (×0.073)	330nm-555nm Color (mag)
1	1	12	4	1.04	0.40
2	130	13	33	1.04	0.47
3	164	-32	5	1.04	0.41
4	208	-1	10	1.00	0.42
5	231	25	6	1.01	0.41
6	303	-23	13	1.02	0.46
7	43	-23	13	0.96	0.47
8	188	20	16	0.96	0.44
9	241	-25	12	0.96	0.44
10	245	35	10	0.97	0.43
11	280	-29	7	0.96	0.43

scriptions of the limb darkening properties of Ceres' disk, at least for the central part. Since we did not see any systematic deviations with respect to incidence angle and emission angle, with the small scattering of model, it is fair to say that the geometric effects in the reflectance associated with μ_0 and μ have been removed, and the average normal reflectance of the surface has been measured accurately. In this sense, the deviation maps of reflectance as derived above are valid. The modeled roughness parameter, $\bar{\theta}$, may or may not be the real roughness of the surface, and so is the single scattering albedo, w, because it is derived together with the roughness parameter.

However, from earlier results by other observational means, the surface roughness of Ceres is indeed high at scales larger than meters as detected by radar (Mitchell et al., 1996). In addition, both the radar observations of Mitchell et al. and thermal modeling (Saint-Pé et al., 1993) suggests the possible existence of a complex roughness structure such as fractal topography. Thus the high roughness of Ceres could be real, but in a form that is not consistent with the underlying assumptions in Hapke's model, where the distribution of the normal directions of surface facets on a rough surface was treated as isotropic with a Gaussian distribution (Hapke, 1993). The fit to Ceres' limb shows that the highest relief on Ceres could not exceed 5 km (Thomas et al., 2005), if the high photometric roughness is real, it must be at scales between tens of meters and kilometers, and widespread all over the surface. The surface of Ceres is probably made of very smooth materials at small scales as suggested by radar observations (Mitchell et al.), either like the surface of some kind of crystal structure, or deposited by very fine grained particles, but saturated with craters, or a blocky, chaotic surface at the sizes of tens of meters to kilometers, even while it is relaxed at a global scale. Both Mitchell et al. and Saint-Pé et

al. (1993) suggested the possibility of fractal topographical structure on Ceres' surface. Unfortunately, the size scale of roughness cannot be directly observed by photometric methods from our current HST images. Dawn will provide images at resolutions as high as 10 m/pixel (Russell et al., 2004), showing more details about surface topography.

A related questions is, whether or not the modeled single scattering albedo, w, is real. From data modeling point of view, the covariance factor of the two modeled parameter, w and $\bar{\theta}$, from our data is about 0.15, meaning that the models of those two parameters are almost orthogonal. Therefore the interpretation of roughness $\bar{\theta}$ almost does not affect the interpretation of w. And again, compared with earlier observations, the modeled geometric albedo from our fitted parameters is consistent with earlier results modeled from the IAU-adopted HG system (Tedesco et al., 1983; Lagerkvist and Magnusson, 1990). Thus the modeled single scattering albedo should be real.

6.5.2 Color variations

The distributions of the SSA of Ceres at three wavelengths all show a unimodal shape with very narrow ranges (Fig. 6.7). From the albedo maps, we can derive the color variations of Ceres' surface by dividing any two of them. Such ratio maps are shown in Fig. 6.8, and the histogram of those color ratio maps are show in Fig. 6.9. But note that, because the error in the SSA maps is about 2%, the error in the color ratio maps is about 3%. Given the small color variations of Ceres of about 3% standard deviation, comparable with the error, we have to be cautious about the color features we see on these color ratio maps. Only big features with very distinctive color ratios, and consistent with the difference of lightcurves at different wavelengths are considered to possibly be real. For example, in

the color ratio map of 330nm/555nm, we believe that the big red region at about 100° longitude and the big blue region at about 220° longitude are spectrally different. But we may not say for sure that the variations within the above two features are real.

As stated in the last section, the eleven features can be grouped into two different spectral types as shown in Fig. 6.10 where the average deviation of the SSA from its corresponding SSA of each feature is plotted as a functions of wavelength. Thus what are shown here are not the spectra of each features, but their deviation from the globally averaged spectrum. It is clearly shown that the eleven features can be divided into two spectral distinct groups. One includes features #2, #6, and #7, with their spectra almost aligned with the average spectrum of Ceres, but slightly redder (2%). Another group includes all other features, with their spectra slightly bluer than average by up to 6%. But caution has to be used when interpreting the spectral difference between features because the uncertainties within the SSA deviation maps is about 2-3% as shown in the upper right corner of Fig. 6.10, the subtle difference between the spectra of features is probably not really resolved. Since we have not found good interpretations for the UV spectral absorption band in Ceres' spectrum, the interpretations for the subtle variation of the spectra of those features have not been available.

6.5.3 The uniform surface of Ceres

Fig. 6.11 shows the range of single scattering albedo or the normal reflectance if the former is not available. The variations of reflectance are proportional to those of SSA for dark surfaces, but not for bright surfaces. But they usually do not differ by much. At the resolution of our HST observations, the SSA variations of Ceres are much smaller than

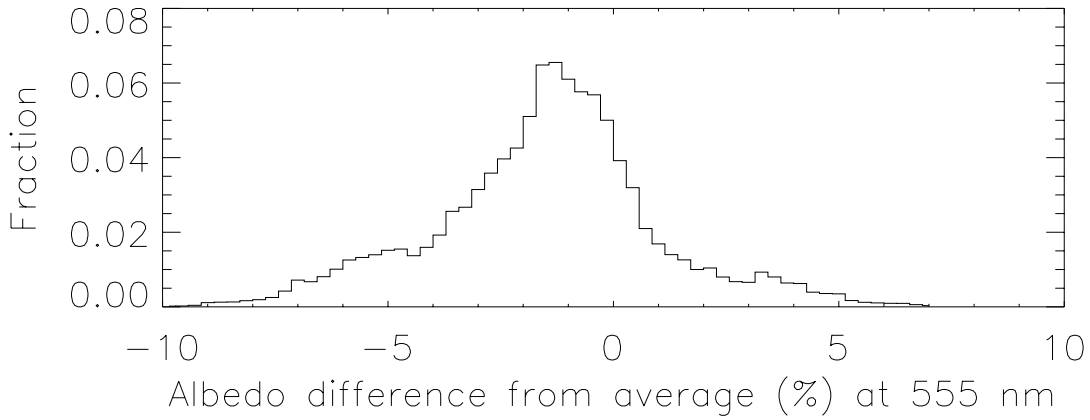

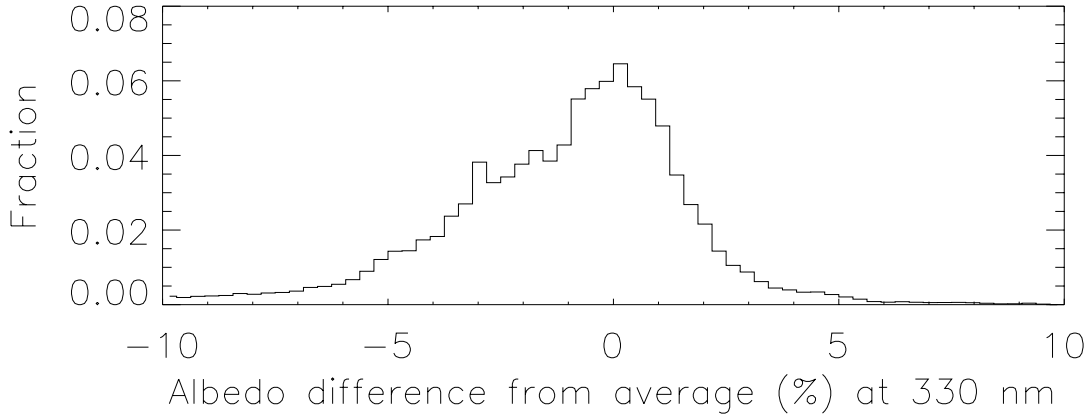

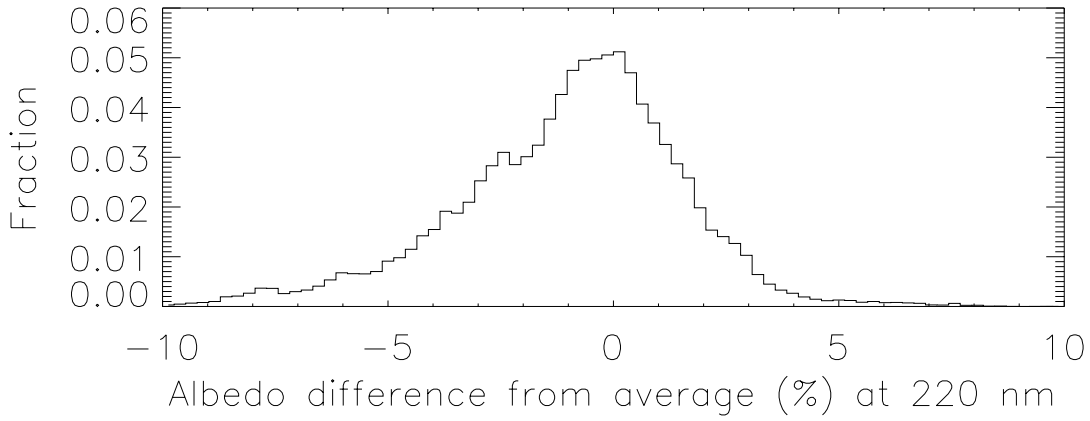

Figure 6.7 The histogram of the SSA deviation from averages of Ceres at three wavelengths.

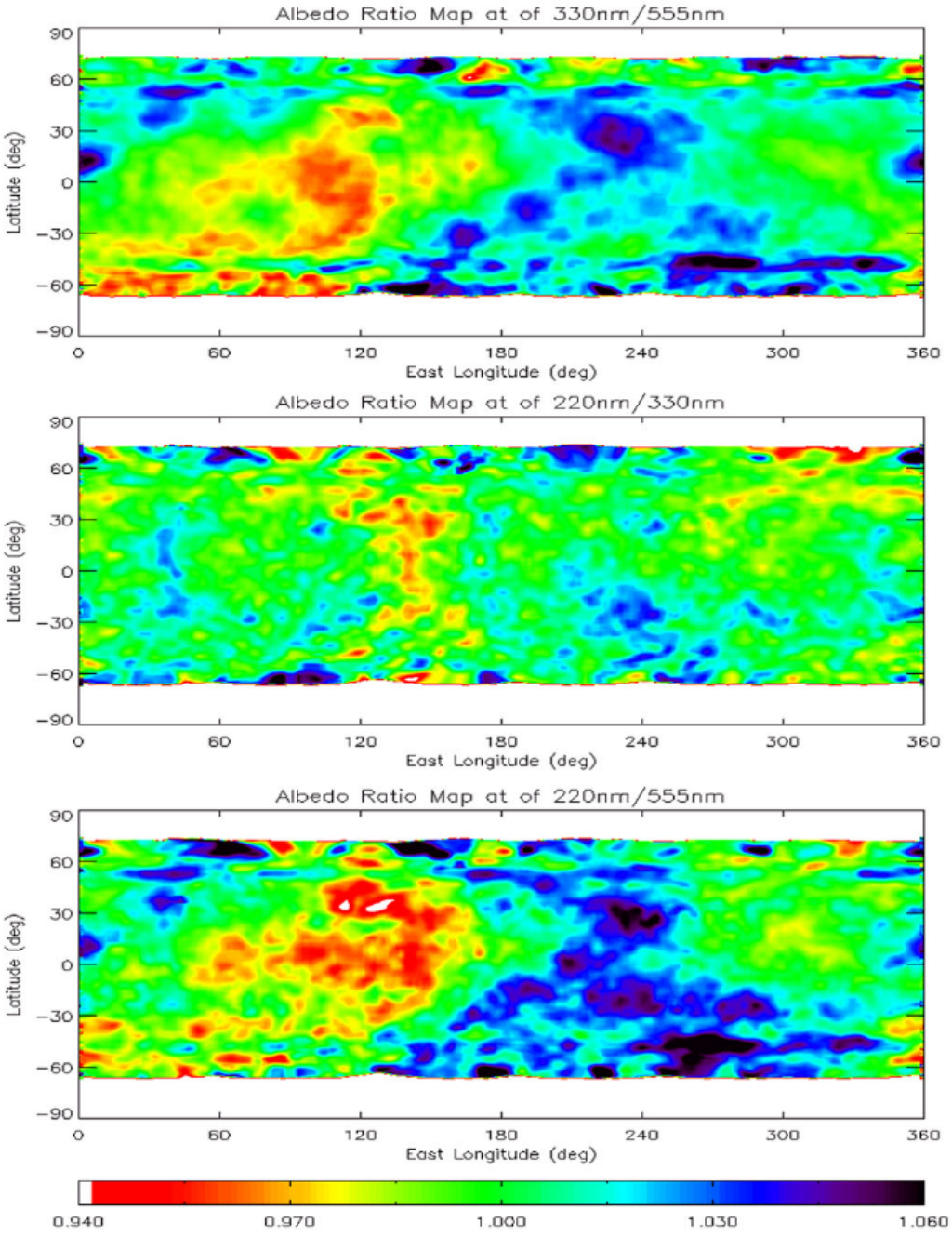

Figure 6.8 The color ratio maps of Ceres, derived by dividing the SSA deviation maps at two wavelengths. Note, however, because the uncertainties in the color ratio maps are comparable with the standard deviations of the color ratio (Fig. 6.9), caution has to be used when considering whether features in these maps are real or not.

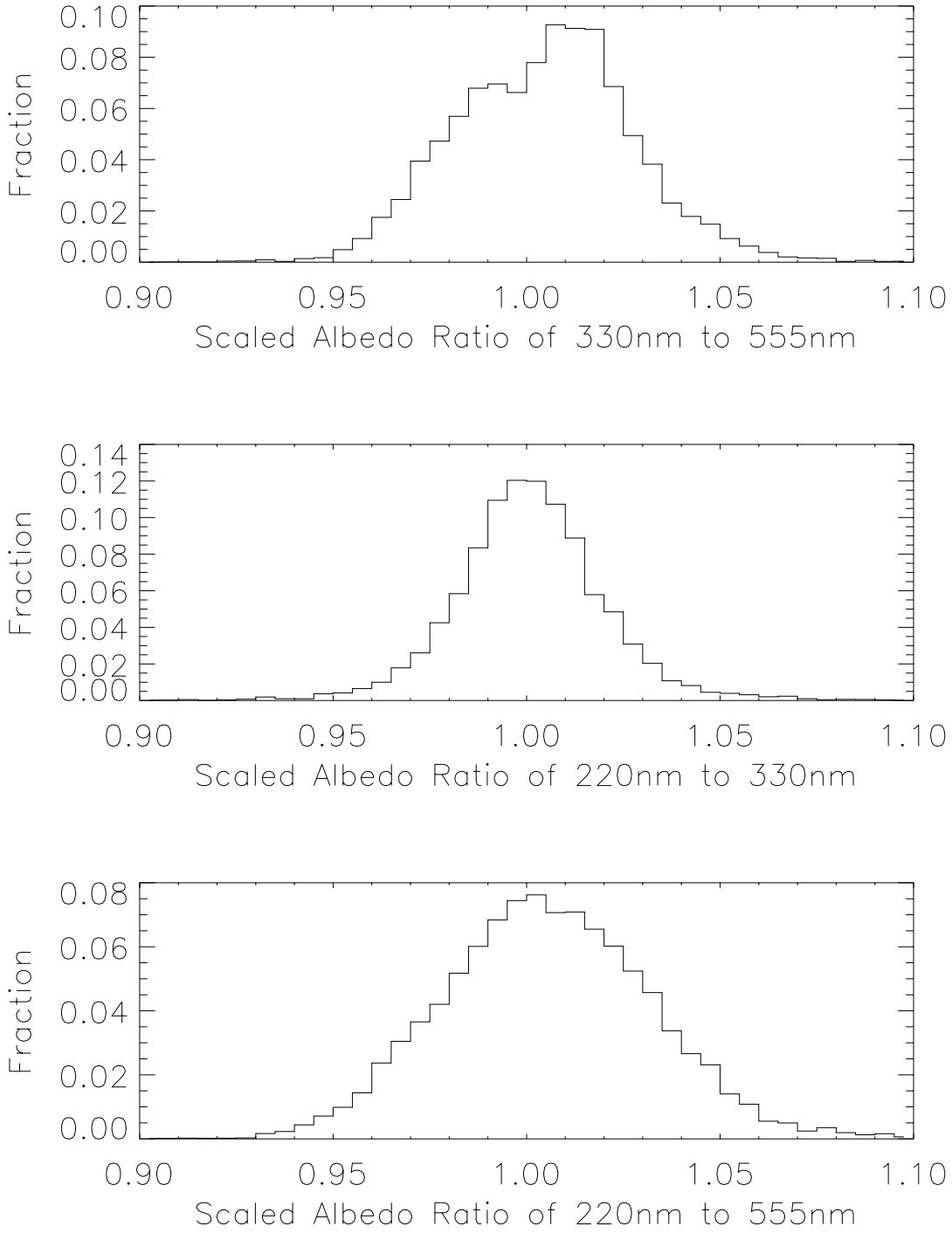

Figure 6.9 The histograms of the color ratio maps (Fig. 6.8).

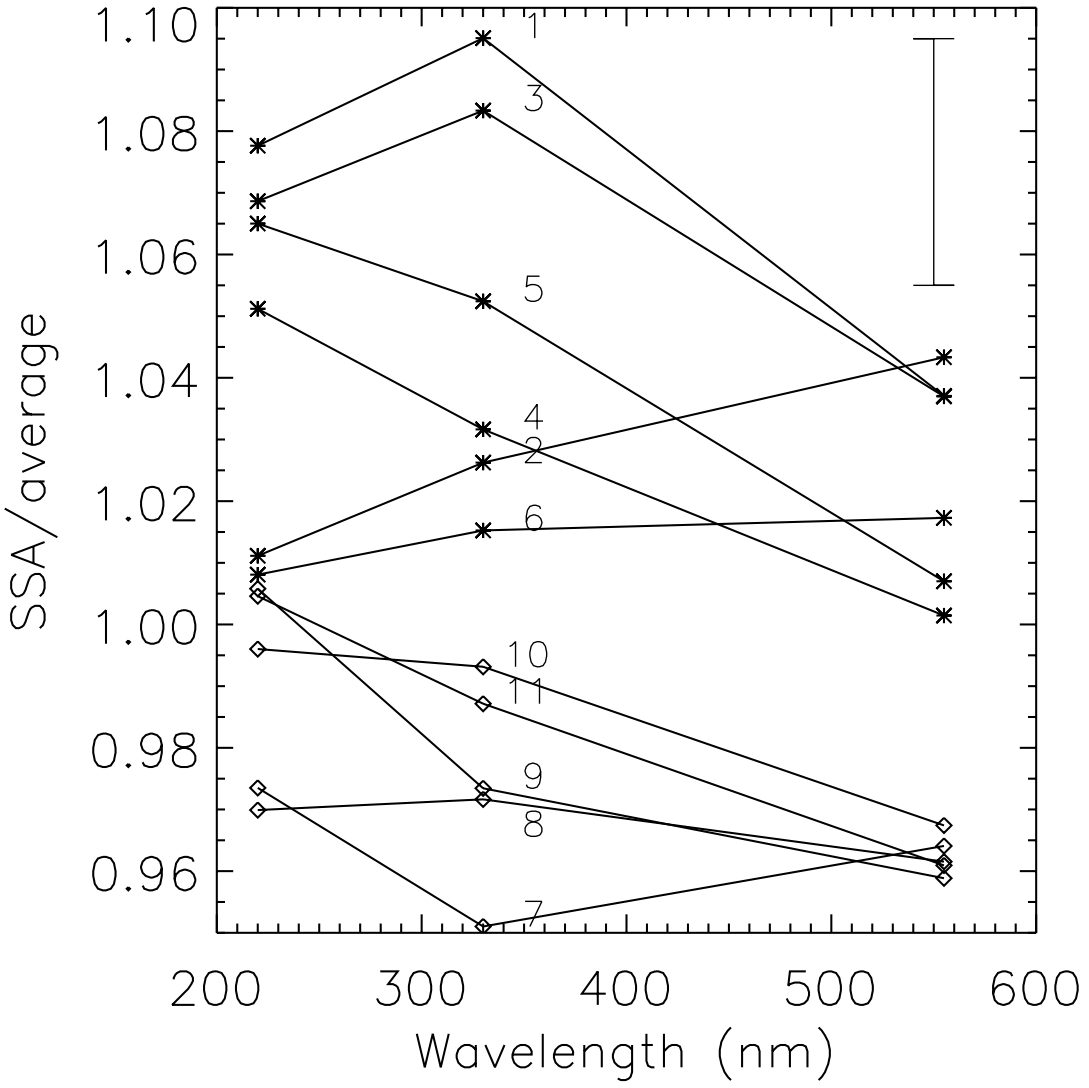

Figure 6.10 The plot of spectral deviation from average spectrum of Ceres for the eleven features as identified in Table 6.5. These spectra are plotted as the percentage deviation from the average spectrum of Ceres (Fig. 6.2). What is emphasized here is the subtle deviations of the spectra of features from the average. However, note that the typical error bar of the SSA as shown in the plot are about 2%, which is comparable with the spectral difference between some features.

those of other asteroids, but close to some icy moons of giant planets. Below our resolution, there could exist albedo patterns with large variations but within small size scale such as a few kilometers. But given the size of Ceres about 1000 km across, and imaged to more than 750 pixels in our observations, it is not likely that such patterns spread all over the surface to affect the global albedo distribution significantly so that the albedo distribution could be substantially different if imaged at a higher resolution, although the range could be possibly extended by a small fraction. Therefore, Ceres' surface is probably one of the most uniform surfaces of solar system small bodies measured to date. With its unique spectrum, and a possibly high water fraction, Ceres has clearly taken a different evolutionary path than other rocky asteroids.

Although there is a lack of spectral evidence for water ice on Ceres' surface (Larson et al., 1979), the presence of a UV emission at 308 nm to the north of Ceres' limb indicates the existence of a tiny amount of OH molecules that can only be produced by photodissociation of water in sunlight, and the corresponding H_2O production rate of 10^5 to 10^6 times smaller than that of an active comet may be the evidence of the existence of water ice on or beneath the surface (A'Hearn and Feldman, 1992). The strong absorption feature at about 3 μm (Lebofsky et al., 1981) was interpreted as being caused by water molecules or structural OH groups embedded in between layers of clay minerals (Lebofsky et al., 1981; Feierberg et al., 1981), and later thought to be an ammoniated clay mineral (King et al., 1992). The best estimated density of Ceres implies about 25% water fraction (Thomas et al., 2005). Thus the most acceptable composition of the surface layer of Ceres is thought to consist of metamorphosed and/or aqueously altered clay minerals, and a large amount of water inside. Starting from those results, the most recent model of

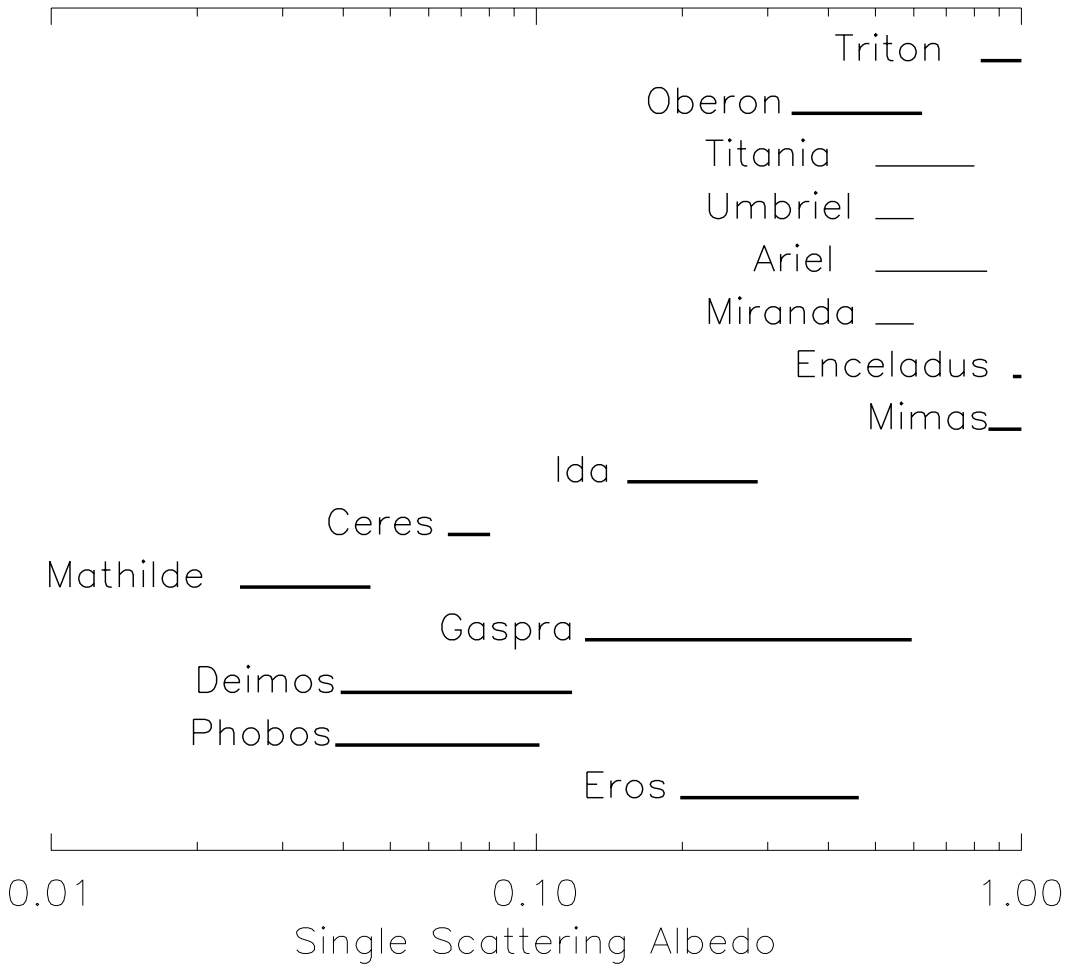

Figure 6.11 The SSA or normal reflectance range of some asteroids and satellites, scaled at the SSA. Objects are ordered by heliocentric distance from bottom to top. Thin lines are for those objects without their SSA available. Data are all V-band unless otherwise specified below. Eros: Li et al. (2004); Murchie et al. (2002a); Phobos: Simonelli et al. (1998); Deimos: Thomas et al. (1996); Gaspra (410 nm): Helfenstein et al. (1994); Mathilde: Clark et al. (1999); Ceres: this work; Ida: Helfenstein et al. (1996). The measurement for the following objects are at 470 nm: Mimas: Verbiscer and Veverka (1992); Enceladus: Buratti et al. (1990); Miranda, Ariel, Umbriel, Titania: Buratti and Mosher (1991) Oberon: Helfenstein et al. (1991); Triton: Hillier et al. (1994).

evolution (McCord and Sotin, 2005) predicts that water has played an important role in heat transport and redistribution inside Ceres in its early evolutionary history.

Heated by the energy from gravitational accretion and probably radioactive decay such as ^{26}Al (Grimm and McSween, 1989) shortly after its formation, Ceres probably differentiated, with water ice reaching its surface (McCord and Sotin, 2005), formed an icy crust globally, and may have had ice tectonics or water volcanism, like what is happening today on, *e.g.*, Europa. Such geological activity would resurface Ceres by mixing and/or depositing minerals on the surface, erasing major albedo and morphological features. The lack of a dynamical family of small asteroids associated with Ceres, unlike Vesta's vestoids, is consistent with an icy crust that would not produce such a family. The surface of Ceres was hydrated and/or ammoniated during this time. However, unlike Europa, which has continuous energy input from Jupiter's tidal perturbation to sustain activity today, Ceres has cooled down as its internal energy sources depleted quickly, and all activities tapered off as its temperature decreased. This does not necessarily imply that water ice exists on its surface today. At least one comet, 19P/Borrelly, containing a large fraction of interior water ice, has a dry and hot surface (Soderblom et al., 2004a). Actually water ice should not be expected on the surface of Ceres, because it is always within 3 AU (perihelion 2.55 AU, aphelion 2.99 AU), a canonical distance within which water is not stable on the surface of any small body (Cowan and A'Hearn, 1979). The actual temperature of the warmest area on Ceres was measured to be 235 ± 4 K (Saint-Pé et al., 1993), not favoring the existence of amorphous water ice or crust. Water ice on Ceres' surface, if existed, must have been sublimated over time and escaped from its weak gravity, leaving behind hydrated and ammoniated silicates. If there is still some water ice on its surface

today, it must be on the poles where the least sunlight is received. Unlike comets, which have periodical violent activity during perihelion passages to alter their surfaces, Ceres' surface is geologically dead today, with a hydrated but uniform surface left behind.

In 2015, the Dawn mission is scheduled to observe Ceres' surface morphology, determine the crater density, and thereby infer the age of the surface. Dawn can measure the mineral composition with visible-IR spectroscopy, and the water-related hydrogen fraction both on the surface and underneath with gamma-ray/neutron spectroscopy. This will help us very much in understanding the history of Ceres.

6.6 Summary

In conclusion, Ceres is observed with HST ACS/HRC through three broadband filters centered at 555 nm, 330 nm, and 220 nm. Images were taken at phase angles from 5.4° to 7.5°, covering more than one full rotation of Ceres. The resolution of HST observation is 30 km/pix, with the disk of Ceres imaged into more than 750 sunlit pixels, enabling disk-resolved photometric analysis. The lightcurve of Ceres from the HST observations is found to be well consistent with earlier observations (Tedesco et al., 1983). A spectrum of Ceres is constructed from our HST observations and earlier ones, showing a very possible strong absorption band centered at about 280 nm with 30% reflectance of that at 555 nm. This spectral feature is not due to terrestrial atmospheric ozone contamination, but its nature has not been identified. Hapke's modeling yields good fit to the central portion of Ceres' imaged disk, and Minnaert's model and a model that is modified from the Minnaert's model yields better fitting to the reflectance at outer annulus of Ceres'

disk. The single scattering albedo of Ceres at 555 nm, 330 nm, and 220 nm are modeled to be 0.073 ± 0.002, 0.046 ± 0.002, and 0.032 ± 0.003, respectively. The surface of Ceres is found to be very rough at the scales between ten kilometers to meters, with a roughness parameter $40^\circ \pm 6^\circ$. The deviation maps of single scattering albedo from the averages at three wavelengths are produced, showing a very uniform surface, at least at the resolution of our observations. Eleven surface features defined by albedo and spectrum, are identified. The uniformity of albedo, together with the large water content as indicated by its mean density (Thomas et al., 2005), suggests that Ceres could have been resurfaced, probably by melted water or ice, after the heavy bombardment phase of solar system formation, although small craters or other topographic features below the resolution ($<$60km) of these data may exist. In short, Ceres is proving to be a very important solar system object, a key to understanding the early solar system processes occurred in the proto-terrestrial planets.

Chapter 7

Summary and Future Work

7.1 Summary

In summary, Hapke's model has been briefly reviewed; some numerical simulations were carried out to study the effect of irregular shapes on disk-integrated phase function modeling; photometric properties of three objects, asteroid Eros, comet Borrelly, and asteroid Ceres, were modeled with Hapke's model, utilizing disk-resolved images mainly returned from spacecraft, and from HST.

Hapke's theoretical model (Hapke, 1993) is the most widely used model that correlates the physical properties of a planetary surface with its photometric behavior. From the bidirectional reflectance of a surface as a function of incidence angle, emission angle, and phase angle, or from the phase function of an object, the photometric properties such as albedo, roughness, porosity, particle scattering properties, *etc.*, can be inferred. Some hints of further physical properties such as the composition, particle size and size distribution, and evolutionary history can also be found. The model has been applied to the photometric data of many atmosphereless satellites and asteroids, including very bright icy satellites and very dark C- and D-type asteroids, and has proved to be able to describe the photometric data fairly well.

For small bodies in the solar system, shapes are almost never close to a sphere, and the apparent disks are almost never spatially resolved from ground-based observations.

Due to the complexity of Hapke's theoretical model, it is impossible to integrate the total brightness over the surface of an irregular shape analytically, so usually a spherical shape is assumed in modeling any ground-based small body photometric data. We have carried out numerical simulations to study the assumption of spherical shape in modeling the disk-integrated phase function of irregularly shaped asteroids. The method is that, with an assumed non-spherical shape and uniform Hapke's parameters across the whole surface, the reflectance of each surface element can be calculated under a particular Sun-object-observer geometry, then integrated over the illuminated and visible surface under that geometry to find the disk-integrated brightness. Repeating the above procedure for a whole rotation of the body gives a rotational lightcurve. Then we calculate such lightcurves under all possible aspect angles and whichever phase angles we want. Taking those lightcurves as our input "data", just like the observed lightcurves from the ground for asteroids, but covering all possible geometries, we can study the phase function constructed from those theoretical lightcurves of an asteroid with "known" Hapke's parameters. Hapke's disk-integrated phase function theoretical model is then applied to the calculated disk-integrated phase functions, and the modeled parameters can be compared with the original, or "true", parameters to find out the effect of irregular shape on the Hapke's modeling in terms of the modeled parameters, or to evaluate the spherical shape assumption in Hapke's modeling to the studied irregular shape.

In our simulations, we assumed two non-spherical shapes, a triaxial ellipsoid and Eros's real shape, and assumed Hapke's parameters for Eros as published by Domingue et al. (2002). The main results derived from our simulations are, 1. For triaxial ellipsoidal bodies, the assumption of spherical shape works well at the small phase angles that can be

reached from the Earth, but not for large phase angles. and 2. If the shape is more irregular than a triaxial ellipsoid, with large concavities, then the phase angle range within which the spherical assumption works decreases dramatically, and usually has to be dealt with case by case. Our simulation method can be taken as a forward simulation method to be used with Hapke's modeling iteratively in analyzing photometric data of small bodies with known shapes.

With the help of numerical simulations using Eros's real shape, we modeled the ground-based phase function of Eros, and analyzed the goodness of our model. The opposition height and width parameters are found from this model. Other photometric parameters of Eros were then determined from disk-resolved images returned from NEAR Shoemaker spacecraft at seven wavelengths from 450 nm to 1050 nm. The single scattering albedo, w, is a strong function of wavelength, and its value at 550 nm is found to be 0.33$\pm$0.03. The asymmetry factor, g, and the roughness parameter, $\bar{\theta}$, are almost independent of wavelength, and their values are found to be -0.25$\pm$0.02 and 28°$\pm$3°, respectively. The opposition height and width are modeled, only from ground-based data, to be 1.4$\pm$0.1 and 0.010$\pm$0.004, respectively. At V-band the modeled geometric albedo is 0.23 and the Bond albedo is 0.093. The fitted Hapke's parameters of Eros indicate that Eros is a typical S-type asteroid in terms of photometric properties. From earlier estimate of the composition of Eros from its IR reflectance spectrum and laboratory measurement of the optical properties of pyroxene and olivine, two compositional components of Eros, the particle size is estimated from its single scattering albedo to be between 50 and 100 μm. This estimate is an example of estimating the physical properties of surface regolith on an asteroid from its Hapke's parameters.

Similar photometric analysis has been performed for comet Borrelly, too, with the disk-resolved data returned from DS1 flyby. Since the data are very limited both in quality and phase angle coverage, the uncertainty of photometric modeling is relatively large. But as an attempt to apply Hapke's disk-resolved modeling technique to a comet, it successfully resolved the photometric heterogeneity on Borrelly's surface. The variations of photometric properties are studied by modeling Hapke's parameters for each terrain in a terrain partition modified from the version proposed by Britt et al. (2004) from a geological point of view. The maps of Hapke's parameters are constructed for single scattering albedo (w), asymmetry factor (g), and roughness ($\bar{\theta}$). The single scattering albedo of Borrelly varies by a factor of 2.5, with an average of about 0.057$\pm$0.009. The single-particle phase function of Borrelly's surface varies from an almost isotropic one (g=-0.1) to a very backscattering one (g=-0.7), averaging g=-0.43$\pm$0.07. The roughness of most of the surface of Borrelly is smaller than 35°, but in some areas the modeled roughness can be as large as 55°, which may or may not be true because Hapke's theory may fail for high roughness. Nevertheless, those areas have different roughness properties from those of others. The average surface roughness is about 22°$\pm$5°. Analysis with the geometry of the Sun and the rotation of Borrelly shows that the large photometric variations are probably correlated with cometary activity. The formation of fan jets is probably related to a relatively high single scattering albedo, a strong backscattering phase function, and a rough surface, indicating possible exposed or concentrated ice content on the surface layer of the nucleus. Thermal modeling assuming a dry surface without sublimation of ice gives a fit that agrees well with the simple 1-D temperature measurement from DS1 except for the small end, where the discrepancy can be fully explained by including ice

sublimation that is consistent with the observed water production rate and the brightness of the fan jet. The source regions of collimated jets can not be constrained well because of the limited spatial resolution of temperature measurement, but a self-consistent temperature model is proposed to accommodate the 1-D temperature plot and water production rate.

Ceres, the first asteroid discovered, is a target of Dawn, another NASA Discovery Program mission scheduled to launch in 2006 to characterize two of the largest asteroids in the Solar System, Ceres and Vesta. HST images at three wavelengths, 555 nm, 330 nm, and 220 nm, covering more than one rotation of Ceres, were acquired in December 2003 and January 2004 to map the surface of Ceres. The lightcurves of Ceres are constructed from those images at three wavelengths. The V-band lightcurve is highly consistent with earlier observations in its magnitude, amplitude, and shape. An average reduced V-magnitude of Ceres at 6.2° phase is measured to be 3.88 ± 0.02 mag. The lightcurve magnitude is 0.04 mag. Since the oblate spheroidal shape of Ceres is rotationally symmetric, the lightcurve is expected to be produced by variations of surface albedo. The difference of the shapes of lightcurves at three wavelengths indicates color variations over the surface. Combined with earlier HST observations (Parker et al., 2002) and the 24-color asteroid survey (Chapman and Gaffey, 1979), the spectrum of Ceres at UV is constructed, and a strong absorption band centered at 280 nm is identified. The reflectance at band center is only about 30% of the reflectance outside the band, and the width of the band is about 120 nm. The attempts to match this absorption band with laboratory vacuum UV spectra or the similar spectra observed for Europa and Ganymede have been unsuccessful. With the disk of Ceres resolved into more than 750 sunlit pixels, disk-resolved

photometric study is enabled. These images are modeled with Hapke's model, Minnaert model, and a modified Minnaert model, coupled with the precisely determined shape and size from the same dataset (Thomas et al., 2005), to find Ceres' disk-averaged albedo and surface roughness. The single scattering albedo of Ceres is modeled to be 0.073 ± 0.002, 0.048 ± 0.002, and 0.050 ± 0.002 at 555 nm, 330 nm, and 220 nm, respectively. Then the disk-averaged photometric model is combined with original images to retrieve the single scattering albedo variation over the surface, and to construct single scattering albedo maps in longitude-latitude projection. The albedo variation across Ceres' disk in only about 13% from minimum to maximum. The albedo maps show differences at three wavelengths that is consistent with the color variations as indicated by different shapes of lightcurves at three wavelengths. The surface of Ceres is uniform within 3% standard deviation for albedo, and within 5% for color, making Ceres one of the solid bodies in the solar system with the most uniform surface.

It is worth pointing out that the surfaces of asteroids and cometary nuclei reflect different physical processes active throughout their evolutionary history. In our samples, Eros has been dominated by collisions and cratering, Borrelly's surface is controlled by sublimation and outgassing, and it is not yet clear what process occur on Ceres as the primary agents to determine the photometric properties of Ceres' surface. Once we have more and more asteroids and cometary nuclei with their photometirc properties studied, we expect to understand their evolution better and better, and to know more about the formation of the Solar System.

7.2 Future Work

Thesis work is never the end, it is only the starting point of one's scientific career. From my graduate research work, I managed to master the expertise of photometric analysis with Hapke's model. Very naturally, the next step is to apply the techniques I learned to more objects to study their physical properties, with the continuous support from the data returned from space exploration missions, and to support future space missions. In this section, some possible future work is projected as an extension from my thesis work. Comet 81P/Wild 2, visited by Stardust in January, 2004, with 72 disk-resolved close-by images of its nucleus acquired, is one of my next steps. Another object is comet 9P/Tempel 1, the target of Deep Impact mission. With our knowledge base of cometary photometry extended, we can make some comparisons among comets and between comets and asteroids.

7.2.1 Comet 81P/Wild 2

Comet Wild 2 was captured into its current orbit only 30 years ago as the result of a close encounter with Jupiter (Sekanina and Yeomans, 1985). Its surface probably retains the records of processes occurred at about 5 AU from the Sun, which was its perihelion distance of the previous orbit for hundreds of years. There is no much recent processing occurred after Wild 2 was captured to its current orbit. It is thus a Jupiter Family Comet (JFC) that best represents the comets with longer periods and more primordial surfaces. On January 2, 2004, Stardust successfully encountered comet Wild 2 with a closest distance of 236 km. The spacecraft returned 72 disk-resolved images of the nucleus (Fig.

7.1) covering solar phase angles from 2° up to 110° (Brownlee et al., 2004). The resolution and phase angle coverage of those images make the dataset valuable in studying the photometric properties of the surface of the nucleus of comet Wild 2.

All raw images of comet Wild 2 at the encounter, as well as the ephemeris data, have been made available on NASA's PDS SBN in University of Maryland College Park (Semenov et al., 2004a,b). A triaxial ellipsoidal shape model is available (Duxbury et al., 2004; Duxbury and Farnham, 2004), and a high resolution shape model has been developed (Kirk et al., 2005) as well. The radiometric calibration of the Stardust images is still ongoing, but will be available soon.

Photometric analysis of comet Wild 2, similar with that of comet Borrelly, can be done for both disk-integrated phase function and disk-resolved images. Although ground-based disk-integrated photometric data for the nucleus of Wild 2 are not available, the whole-disk phase function can still be calculated by integrating the flux over the disk in the Stardust disk-resolved images, and a very preliminary average brightness that only includes the illuminated and visible part of the imaged disk, directly derived from raw images, is shown in Fig. 7.2 as a function of phase. Clearly we see divergence between inbound leg and outbound leg at about 60° phase angle. Our analysis shows that this is not caused by geometric effects, nor is it caused by large shadows because they have been excluded in calculating the disk-averaged brightness. It is most likely caused by the effect of image doubling due to the optical system configuration. A quick-and-dirty Hapke's fitting to the outbound leg phase function yields its Hapke's parameters except for w: B_0=1.4, h=0.052, g=-0.42, and $\bar{\theta}$=19° (dashed line in Fig. 7.2). The modeling of these disk-integrated photometric data is of importance as a connection between disk-resolved

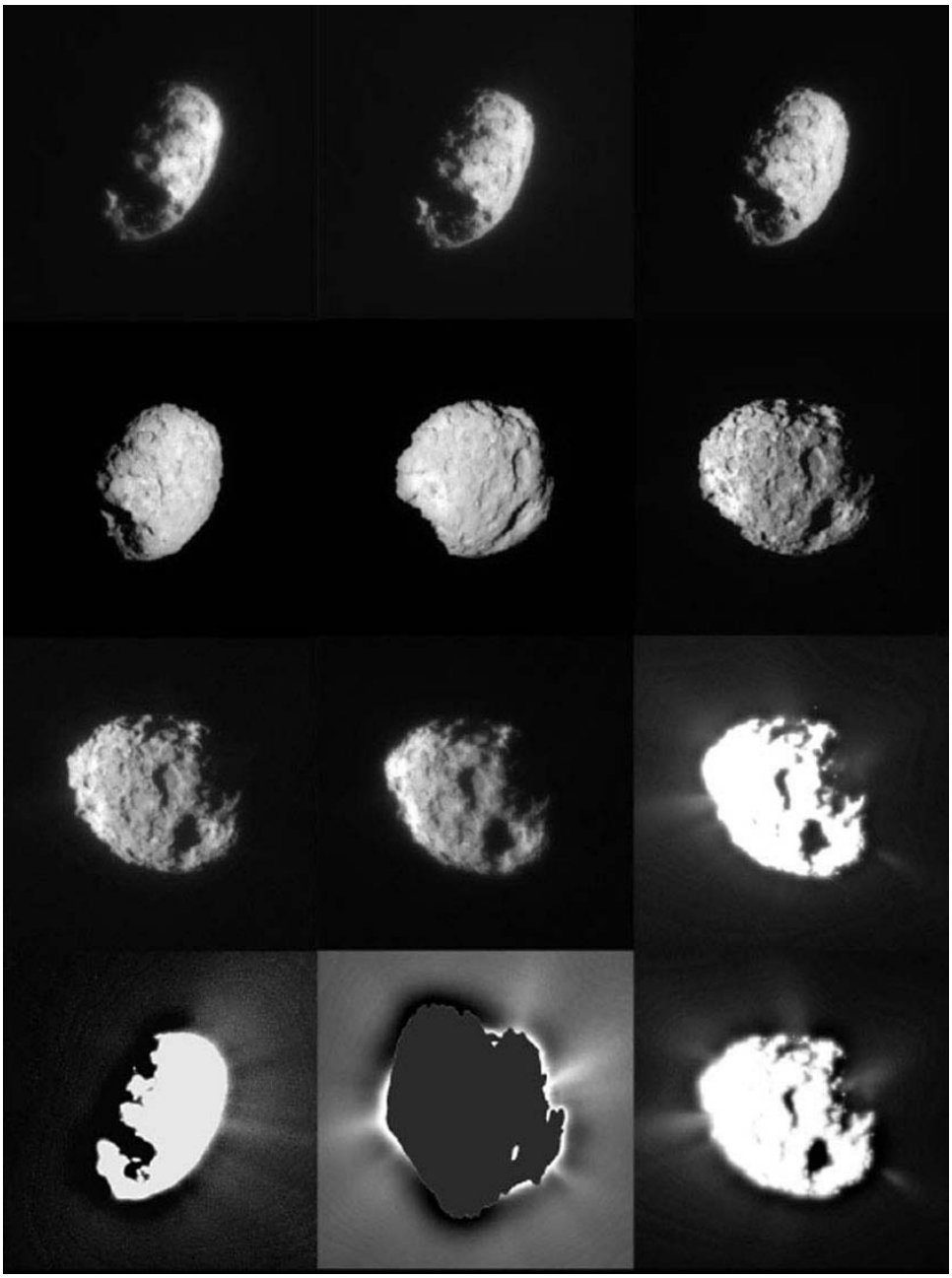

Figure 7.1 Images of comet Wild 2 from Stardust spacecraft (Brownlee et al., 2004).

analysis and ground-based phase function analysis. Since when analyzing ground-based phase function, we have to assume spherical shape, which is obviously untrue for almost all small bodies, the modeled parameters will be biased. The bias can be estimated by comparing the disk-integrated phase function modeling and disk-resolved analysis from the same dataset. Therefore the photometric parameters modeled from ground-based data can be compared with disk-resolved analysis, and evaluated and/or corrected.

The shape of Wild 2 has been modeled with an oblate spheroid (Duxbury et al., 2004), which can be used in disk-resolved photometric modeling. A shape model with less than 100 m spatial resolution in the projected disk of Wild 2 and including big craters on Wild 2 has been developed by Kirk et al. (2005), and will be more helpful. As a JFC that has been perturbed close to the Sun for only a short time, the photometric properties of Wild 2 will represent those of more primordial surfaces relative to Borrelly or Tempel 1, whose surfaces are believed to have been eroded for a long time in the inner solar system.

There is another unique significance of studying the photometric properties of Wild 2. Stardust is still an ongoing mission with its primary scientific goal being to return the first sample of cometary dust particles collected from the inner coma of comet Wild 2 to Earth scheduled in January 2006. The photometric analysis of Wild 2 will disclose the properties of surface where those particles are emitted, and help understand the processing and modification history of those particles, providing a scientific background for any future analyses of those returned particles.

The photometric analysis of comet Wild 2 from Stardust images is also very useful in the preparation for Deep Impact, which is scheduled to arrive at comet Tempel 1 in just

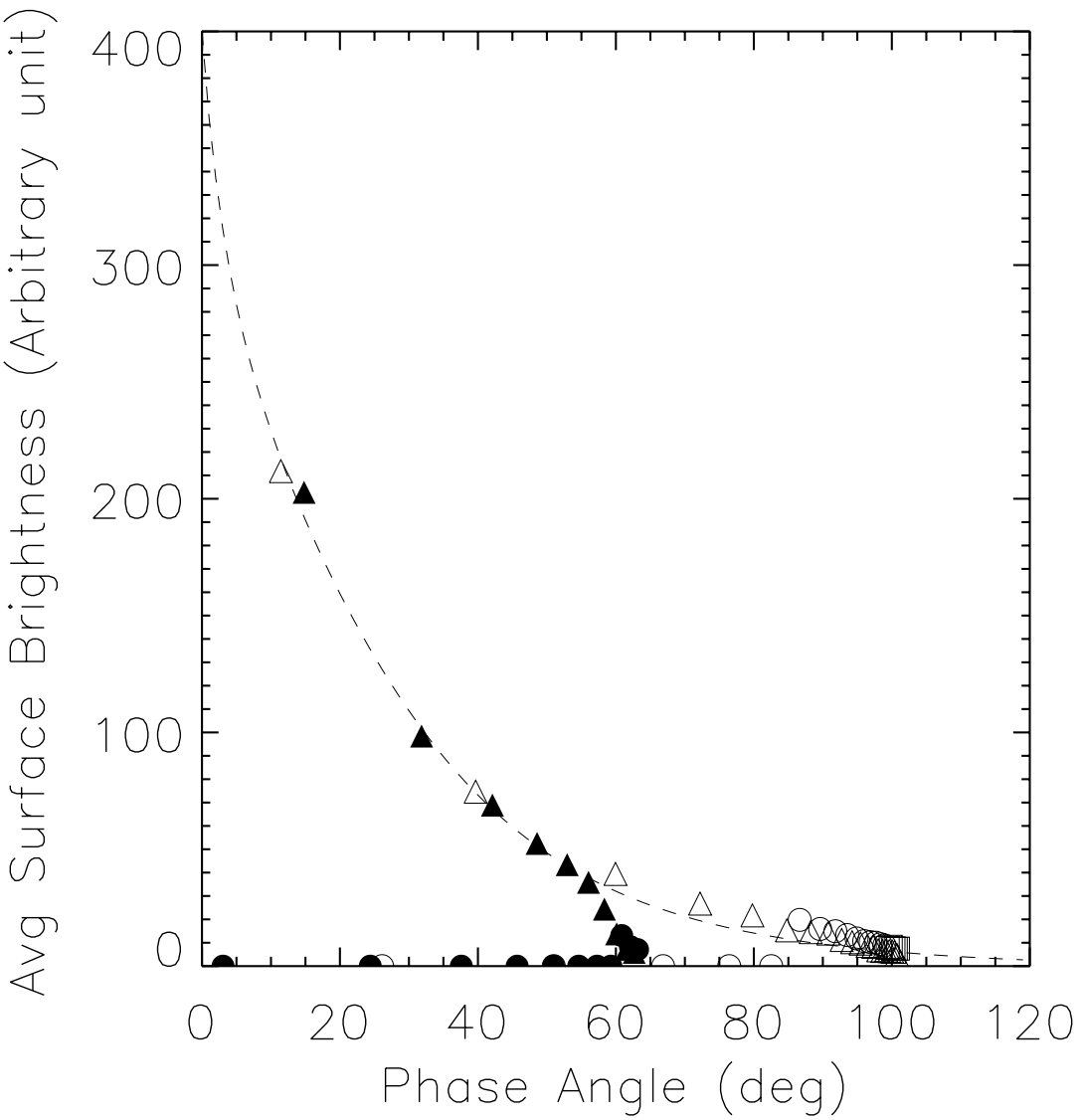

Figure 7.2 The average surface brightness of comet Wild 2 as a function of phase angle. Note that this is a very preliminary phase function directly integrated from raw images of Wild 2 from Stardust spacecraft. The y-axis is in uncalibrated arbitrary reflectance unit. All solid symbols are for inbound leg, open symbols outbound leg. Shapes of symbols represent exposure time: triangles 10 ms, circles 100 ms, and squares 35 ms. Dashed line shows a quick-and-dirty Hapke's fit to the outbound leg phase function. Symbols on x-axis are satuated, and should be ignored.

a few months, to do a unique experiment with the nucleus (A'Hearn et al., 2005, and next section). From the point of view of both auto-navigation and scientific data acquisition, the imaging sequence planning relies on the estimate of the photometric properties of comet Tempel 1. Wild 2 provides an excellent analogue to DI close encounter with a cometary nucleus. Therefore the photometric analysis of comet Wild 2 is not only a practice of the similar work to comet Tempel 1 in the future, but extremely helpful in the imaging sequence planning of DI.

7.2.2 Comet 9P/Tempel 1

Comet 9P/Tempel 1 is the target of Deep Impact, which will have a close approach with the comet on July 4, 2005, and release an impactor to collide with its nucleus, creating a crater, and excavating the fresh materials from the interior to study the primordial composition and characterizations of this old JFC. The Medium Resolution Imager (MRI) and High Resolution Imager (HRI) onboard DI's flyby spacecraft and the imager onboard the impactor will return images of the nucleus with resolutions better than ten meters per pixel. The phase angle coverage of the disk-resolved images will be between 27° and 63°, much larger than that of ground-based observations, enabling us to study the photometric properties of the nucleus.

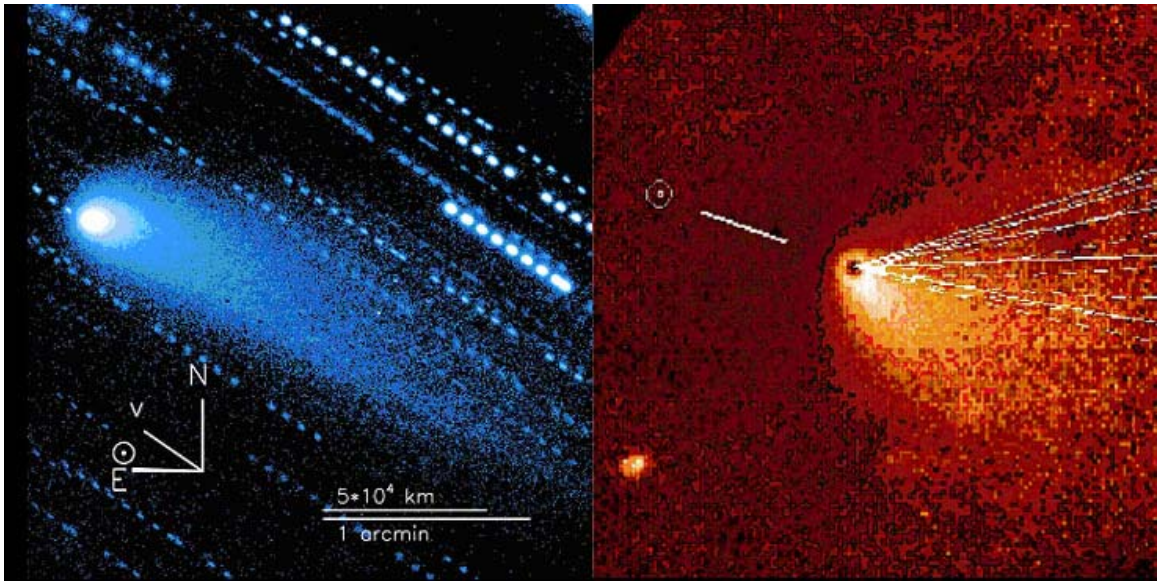

Figure 7.3 The CCD images of comet Tempel 1 from 2004 apparition (left) and 1994 apparition (right). (Figure 4 of Lisse et al., 2005).

Table 7.1. Available ground-based photometric data for comet Tempel 1, not including the data from DI observing campaign.

Telescope	UT date	Filters	Heliocentric distance (AU)	Phase angle (deg)	Reference
JKT 1m	1995 Aug	R, V, B	3.51	14.9	Lowry et al. (1999)
HST	1997 Dec	F675W	4.48	3.8	Lamy et al. (2001)
WHT 4.2m	1998 Dec	R	3.36	13.94	Lowry and Fitzsimmons (2001)

Table 7.2. Past phase function observing windows during DI observing campaign. Photometric data are expected from observations during these windows. (Table 4 of Meech et al., 2005)

Dates	r (AU)	Phase angle (deg)	Mag
08/13/01-02/02/02	4.13-4.53	14.2-1.4	23.5-21.9
10/01/03-01/03/04	4.27-4.00	13.4-1.8	23.0-21.9

An extensive ground-based observing campaign has collected many data of comet Tempel 1 for years (Meech et al., 2005). Some data suitable for constructing a phase function are listed in Table 7.1 and 7.2. Two images of comet Tempel 1 are shown in Fig. 7.3. Its rotational lightcurve in both visible and IR are available from HST and Spitzer Space Telescope (SST) (Belton et al., 2005), respectively. The size of nucleus is estimated to be $14.4\times4.4\times4.4$ km from lightcurves, and the V-band albedo is about 4%. More results about the nucleus have been summarized in Belton et al. (2005).

With a large amount of ground-based and *in situ* data that either have been available or will be made available soon for comet Tempel 1, the photometric analysis of this comet can be done fairly well. The nucleus extraction technique mentioned in Chapter 1 can be employed to find the brightness of nucleus from ground-based images taken when the comet had developed coma. The disk-integrated phase function can then be constructed and modeled. From the disk-resolved images that will be returned by DI, the disk-integrated photometry of Tempel 1 can also be obtained and modeled, and compared with that of ground observations.

From DI data a shape model for Tempel 1 will be constructed as has been done for Borrelly, and the disk-resolved analysis is then possible. Very likely we will observe large photometric variations on the surfaces of Tempel 1 like what we saw on Borrelly (Fig. 5.1) because both of them are old JFCs. If so, similar to Borrelly, the surface of Tempel 1 can be divided into several photometric terrains, and the photometric analysis can be carried out individually for each of them. By doing this, the variations of photometric parameters can be retrieved, and further analyses such as their correlation with active areas can be carried out.

The spectrometer onboard DI covers a wavelength range from 1μm to 4.8μm, covering enough thermal spectrum to enable good thermal modeling. A 2-D temperature map of Tempel 1's surface will be obtained, which is much better than the 1-D temperature scan for Borrelly from DS1 (Fig. 5.17). The thermal modeling of this comet can be done much better than of Borrelly, and the ice sublimation occurred on Tempel 1 that contains much information about jet formation can be studied. This will also help us to understand any photometric variations that are possibly correlated with cometary activity. With ground-based data obtained for this comet for a couple of apparitions, and continuous monitoring for the most recent apparition, hopefully the thermal modeling can be correlated with diurnal and seasonal variations occurred on this comet. This will also provide some clues about the thermal properties of the cometary surface.

Just as for Wild 2, the studies of the physical properties of Tempel 1's surface also have a unique significance, which is to support the primary scientific objectives of DI mission. Tempel 1 will be the first comet whose interior is excavated for *in situ* observations, and the fresh materials without much thermal processing will be characterized. The spacecraft is equipped with instruments that are able to comprehensively study the properties and compositions of the fresh materials from imaging and spectroscopy. The photometric studies of its surface then allow us to study the environment where the excavation occurs, helping thoroughly characterize the surface together with other observations such as spectroscopy. The comparison between the old surface and fresh interior help put the primary scientific goal of DI into a broad context. The observations of crater formation will help constrain the strength, density, porosity of surface, all of which are also correlated with the photometric properties, and therefore can be compared and validated with photometric

analysis. Long term monitoring of comet Tempel 1 in both the physical properties and the chemical compositions of coma and nucleus, if available, will help model the formation of jets, ice sublimation, and determine the evolution of cometary surfaces. The results can also be compared and possibly correlated with that of Wild 2, a JFC whose surface may well represent a transition stage from more primordial materials from formation to the thermally processed surfaces.

7.2.3 Comparisons of photometric properties among comets and with dark asteroids

With the knowledge base of photometric properties of cometary nuclei expanded, we can compare among comets, and with dark C- or D-type asteroids. The three comets with photometric properties studied are all JFCs. But they have different dynamical histories. Comet Borrelly and Tempel 1 are old JFCs, with their surfaces exposed to relatively intensive heating from the Sun for a long time (Belyaev et al.; Carusi et al.). Comet Wild 2 is newly captured to its current orbit, with many topographic features on the surface that have not been eroded (Brownlee et al., 2004). The comparison between them will present a rough picture of the evolution of photometric properties of cometary surfaces due to thermal modification.

On the other hand, comets are considered to form from beyond the asteroid belt, where water ice condenses and is stable, out to the Kuiper belt. Dark C- or D-type asteroids are thought to form within an adjacent region at the outer rim of the asteroid belt. Therefore we expect to see some similarities and transitions from dark asteroids to comets (Hartmann et al., 1987). Some transitional objects such as comet 107P/Wilson-Harrington (Fernández et al., 1997; Bowell et al., 1992), asteroid 3200 Phaethon (Williams and Wu,

1993), comet 133P/Elst-Pizarro (Hsieh et al., 2004), and C/2001 OG108 (Abell et al., 2003; Fernández et al., 2003), reinstate the connection and possible transition between asteroids and comets. Comparisons of the photometric properties of comets and dark asteroids will establish some connections between these two kinds of objects.

The photometric properties of some dark asteroids have been studied from both spacecraft data (Clark et al., 1999) and ground data (*e.g.* Lazzarin et al., 1995; Barucci et al., 1994; Fitzsimmons et al., 1994, *etc.)*, and the property of dark meteorites have been studied in the laboratory (Britt and Consolmagno, 2000). The photometric properties of comets and asteroids can then be compared in terms of albedo, color, single-particle phase function, porosity, and surface roughness. The albedo, color, and single-particle phase function may relate to the compositions, the roughness may be affected by evolution history and the size of objects, and the porosity may be related to both.

BIBLIOGRAPHY

A'Hearn, M. F., Ohlmacher, J. T., and Schleicher, D. G. 1983, A High Resolution Solar Atlas for Fluorescence Calculations, *Tech. Report, Univ. of Maryland Astronomy Program: College Park*, AP, 83-044

A'Hearn, M. F., Campins, H., Schleicher, D. G., and Millis, R. L. 1989, The Nucleus of Comet P/Tempel 2, *Astrophys. J.*, **347**, 1155-1166

A'Hearn, M. F., and Feldman, P. D. 1992, Water Vaporization on Ceres, *Icarus*, **98**, 54-60

A'Hearn, M. F., Millis, R. L., Schleicher, D. G., Osip, D. J., and Birch, P. V. 1995, The Ensemble Properties of Comets: Results from Narrowband Photometry of 85 Comets, *Icarus*, **118**, 223-260

A'Hearn, M. F., Belton, M. J. S., Delamere, A., and Blume, W. H. 2005, Deep Impact: The Mission, submitted to *Space Science Reviews*

Abell, P. A., Fernández, Y. R., Pravec, P., French, L. M., Farnham, T. L., Gaffey, M. J., Hardersen, P. S., Kusnirak, P., Sarounova, L., and Sheppard, S. S. 2003, Physical Characteristics of Asteroid-like Comet Nucleus C/2001 OG108 (LONEOS), *34th LPSC*, abstract no. 1253

Adams,J. 1974, Visible and Near-Infrared Diffuse Reflectance Spectra of Pyroxene as Applied to Remote Sensing of Solid Objects in the Solar System, *J. Geophys. Res.*, **79**, 4829-4836

Ahmad, I. I 1954, Photometric Studies of Asteroids IV. The Light-Curves of Ceres, Hebe, Flora, and Kalliope, *Astrophys. J.*, **120**, 551-559

Ambartsumian, V. 1958, The Theory of Radiative Transfer in Planetary Atmospheres, in *Theoretical Astrophysics*, Ed. Ambartsumian, V., 550-564

Barucci, M. A., and Fulchignoni, M. 1983, On the Inversion of Asteroidal Lightcurve Functions, in *Asteroids, Comets, Meteors*, 101-105

Barucci, M. A., Capria, M. T., Harris, A. W., and Fulchignoni, M. 1989, On the Shape and Albedo Variegation of Asteroids - Results from Fourier Analysis of Synthetic and Observed Asteroid Lightcurves, *Icarus*, **78**, 311-322

Barucci, M. A., Lazzarin, M., Owen, T., Barbieri, C., and Fulchignoni, M. 1994, Near-Infrared Spectroscopy of Dark Asteroids, *Icarus*, **110**, 287-291

Bell, J. F., Davis, D. R., Hartmann, W. K., and Gaffey, M. J. 1989, Asteroids - The Big Picture, in *Asteroids II*, Ed. Binzel, R. P., Gehrels, T., and Matthews, M. S., 921-945

Bell, III, J. F., and 20 colleagues, 2002, Near-IR Reflectance Spectroscopy of 433 Eros from the NIS Instrument on the NEAR Mission. I. Low Phase Angle Observations, *Icarus*, **155**, 119-144

Belskaya, I. N., and Shevchenko, V. G. 2000, Opposition Effect of Asteroids, *Icarus*, **147**, 94-105

Belton, M. J. S., Veverka, J., Thomas, P., Helfenstein, P., Simonelli, D., Chapman, C.,

Davies, M. E., Greeley, R., Greenberg, R., and Head, J. 1992, Galileo Encounter with 951 Gaspra - First Picture of an Asteroid, *Science*, **257**, 1647-1652

Belton, M. J. S., and 19 colleagues, 1994, First Images of Asteroid 243 Ida, *Science*, **265**, 1543-1547

Belton, M. J. S., Chapman, C. R., Klaasen, K. P., Harch, A. P., Thomas, P. C., Veverka, J., McEwen, A. S., and Pappalardo, R. T. 1996, Galileo's Encounter with 243 Ida: An Overview of the Imaging Experiment, *Icarus*, **120**, 1-19

Belton, M. J. S., and 15 colleagues, 2005, Deep Impact: Working Properties for the Target Nucleus - Comet 9P/Tempel 1, submitted to *Space Science Reviews*

Belyaev, N. A., Kresák, L., Pittich, E. M., and Pushkarev, A. N. 1986 *Catalogue of Short-Period Comets*, (Slovak Acad. Sci.), Bratislava

Bendjoya, Ph. and Zappalà, V. 2002, Asteroid Family Identification, in *Asteroids III*, Ed. Bottke, W. F. Jr., Cellino, A., Paolicchi, P., and Binzel, R. P., 613-618

Beyer, M. 1953, Der Lichtwechsel und die Lage der Rotationsachse des Planeten 433 Eros während der Opposition 1951-52, *Astron. Nachr.*, **281**, 121

Birkett, C. M., Green, S. F., Zarnecki, J. C., and Russell, K. S. 1987, Infrared and Optical Observations of Low-Activity Comets, P/Arend-Rigaux (1984K) and P/Neujmin 1 (1984C), *MNRAS*, **225**, 285-296

Bohren, C., and Huffman, D. 1983, *Absorption and Scattering of Light by Small Particles*, New York: Wiley.

Boice, D. C, Britt, D. T., Nelson, R. M., Sandel, B. R., Soderblom, L. A., Thomas, N., and Yelle, R. V. 2002, The Near-Nucleus Environment of 19P/Borrelly During the Deep Space One Encounter, *33th LPSC*, abstract no. 1810

Born, M., and Wolf, E. 1980, *Principles of Optics*, 6th ed., New York: Pergamon Press

Bowell, E., Hapke, B., Domingue, D., Lumme, K., Peltoniemi, J., and Harris, A. W. 1989, Application of Photometric Models to Asteroids, in *Asteroids II*, Ed. Binzel, R. P., Gehrels, T., and Matthews, M. S., 524-556

Bowell, E., Skiff, B. A., West, R. M., Heyer, H.-H., Quebatte, J., Marsden, B. G., and Bus, S. J. 1992, (4015) 1979 VA = Comet Wilson-Harrington (1949 III), *IAU Circ.*, , 5585

Britt, D., and Consolmagno, G. J. S. J. 2000, The Porosity of Dark Meteorites and the Structure of Low-Albedo Asteroids, *Icarus*, **146**, 213-219

Britt, D. T., Boice, D. C., Buratti, B. J., Campins, H., Nelson, R. M., Oberst, J., Sandel, B. R., Stern, S. A., Soderblom, L. A., and Thomas, N. 2004, The Morphology and Surface Processes of Comet 19/P Borrelly, *Icarus*, **167**, 45-53

Brooke, T. Y., and Knacke, R. F. 1986, The Nucleus of Comet P/Arend-Rigaux, *Icarus*, **67**, 80-87

Brown, R. H. 1985, Ellipsoidal geometry in Asteroid Thermal Models - The Standard Radiometric Model, *Icarus*, **64**, 53-63

Brownlee, D. E., and 12 colleagues 2003, Stardust: Comet and Interstellar Dust Sample Return Mission, *J. Geophys. Res.*, **108**, SRD 1-15

Brownlee, D. E., and 11 colleagues 2004, Surface of Young Jupiter Family Comet 81P/Wild 2: View from the Stardust Spacecraft, *Science*, **304**, 1764-1769

Buratti, B. J., and Veverka, J. 1985, Photometry of Rough Planetary Surfaces: The Role of Multiple Scattering, *Icarus*, **64**, 320-328

Buratti, B. J., Mosher, J. A., and Johnson, T. V. 1990, Albedo and Color Maps of the Saturnian Satellites, *Icarus*, **87**, 339-357

Buratti, B. J., and Mosher, J. A. 1991, Comparative Global Albedo and Color Maps of the Uranian Satellites, *Icarus*, **90**, 1-13

Buratti, B. J., Hicks, M. D., Soderblom, L. A., Britt, D., Oberst, J., and Hillier, J. K. 2004, Deep Space 1 Photometry of the Nucleus of Comet 19P/Borrelly, *Icarus*, **167**, 16-29

Bus, S. J., A'Hearn, M. F., Bowell, E., and Stern, S. A. 2001, (2060) Chiron: Evidence for Activity near Aphelion, *Icarus*, **150**, 94-103

Campins, H., A'Hearn, M. F., and McFadden, L.-A. 1987, The Bare Nucleus of Comet Neujmin 1, *Astrophys. J.*, **316**, 847-857

Carcich, B., NEAR MSI Shape Model for 433 Eros V1.0, NEAR-A-MSI-5-EROS-SHAPE-MODEL-V1.0, NASA Planetary Data System, 2001

Carusi, A., Kresák, L., Perozzi, E., and Valsecchi, G. B. 1985, *Orbital Elements and Long-term Evolution of Short-Period Comets*, Hilger, Bristol

Chakrabarti, S. K. 1992, Properties of the Oort Cloud and the Origin of Comets, *MNRAS*, **259**, 37-46

Chamberlin, A. B., McFadden, L.-A., Schulz, R., Schleicher, D. G., and Bus, S. J. 1996, 4015 Wilson-Harrington, 2201 Oljato, and 3200 Phaethon: Search for CN Emission, *Icarus*, **119**, 173-181

Chandrasckhar, S. 1960, *Radiative Transfer*, Dover Publications, New York.

Chapman, C. R., and Salisbury, J. W. 1973, Comparisons of Meteorite and Asteroid Spectral Reflectivities, *Icarus*, **19**, 507-522

Chapman, C. R., and Gaffey, M. J. 1979, Spectral Reflectances of the Asteroids, in *Asteroids*, 1064-1089

Cheng, A. F. 2002, Near Earth Asteroid Rendezvous: Mission Summary, in *Asteroids III*, Ed. Bottke, W. F. Jr., Cellino, A., Paolicchi, P., and Binzel, R. P., 351-366

Clark, B. E., Veverka, J., Helfenstein, P., Thomas, P. C., Bell, III, J. F., Harch, A., Robinson, M. S., Murchie, S. L., McFadden, L. A., and Chapman, C. R. 1999, NEAR Photometry of Asteroid 253 Mathilde, *Icarus*, **140**, 53-65

Clark, B. E., and 11 colleagues, 2001, Space Weathering on Eros: Constraints from Albedo and Spectral Measurements of Psyche Crater, *Meteorit. Planet. Sci*, **36**, 1617-1637

Clark, B. E., Helfenstein, P., Bell, III, J. F., Peterson, C., Veverka, J., Izenberg, N. I.,

Domingue, D., Wellnitz, D., and McFadden, L. A. 2002, NEAR Infrared Spectrometer Photometry of Asteroid 433 Eros, *Icarus*, **155**, 189-204

Coradini, A., Capaccioni, F., Capria, M. T., de Sanctis, M. C., Espianasse, S., Orosei, R., Salomone, M., and Federico, C. 1997a, Transition Elements between Comets and Asteroids, *Icarus*, **129**, 317-336

Coradini, A., Capaccioni, F., Capria, M. T., de Sanctis, M. C., Espinasse, S., Orosei, R., Salomone, M., and Federico, C. 1997b, Transition Elements between Comets and Asteroids, *Icarus*, **129**, 337-347

Cowan, J. J., and A'Hearn, M. F. 1979, Vaporization of Comet Nuclei - Light Curves and Life Times, *Moon and the Planets*, **21**, 155-171

Cox, A. N. 1999, *Allen's Astrophysical Quantities*, 4th ed, Ed. Cox, A. N., The Athlone Press, Ltd. London

Davis, D. R., Durda, D. D., Marzari, F., Campo Bagatin, A., and Gil-Hutton, R. 2002, Collisional Evolution of Small-Body Populations, in *Asteroids III*, Ed. Bottke, W. F. Jr., Cellino, A., Paolicchi, P., and Binzel, R. P., 545-558

Delahodde, C. E., Meech, K. J., Hainaut, O. R., and Dotto, E. 2001, Detailed Phase Function of Comet 28P/Neujmin 1, *Astron. Astrophys.*, **376**, 672-685

Delsemme, A. H., and Miller, D. C. 1971, The Continuum of Comet Burnham (1960 II): The Differentiation of a Short Period Comet, *Planet. Space Sci.*, **19**, 1229-1257

Domingue, D., and Hapke, B. 1989, Fitting Theoretical Photometric Function to Asteroid Phase Curves, *Icarus*, **74**, 330-336

Domingue, D. L., Robinson, M., Carcich, B., Joseph, J., Thomas, P., and Clark, B. E. 2002, Disk-Integrated Photometry of 433 Eros, *Icarus*, **155**, 205-219

Donn, B. D. 1990, The Formation and Structure of Fluffy Cometary Nuclei from Random Accumulation of Grains, *Astron. Astrophys.*, **235**, 441-446

Drummond, J. D., Fugate, R. Q., Christou, J. C., and Hege, E. K. 1998, Full Adaptive Optics Images of Asteroids Ceres and Vesta: Rotational Poles and Triaxial Ellipsoid Dimensions, *Icarus*, **132**, 80-99

Duncan, M., Quinn, T., and Tremain, S. 1988, The Origin of Short-Period Comets, *Astrophys. J.*, **328**, L69-73

Ďurech, J., and Kaasalainen, M. 2003, Photometric Signatures of Highly Nonconvex and Binary Asteroids, *Astro. Astrophys.*, **404**, 709-714

Duxbury, T. C., Newburn, R. L., and Brownlee, D. E. 2004, Comet 81P/Wild 2 Size, Shape, and Orientation, *J. Geophys. Res.*, **109**, E12S02

Duxbury, T., and Farnham, T. L., Tri-Axial Ellipsoid Model of Comet Wild 2, SDU-C-NAVCAM-5-WILD2-SHAPE-MODEL-V1.0, NASA Planetary Data System, 2004

Farnham, T. L., and Cochran, A. L. 2002, A McDonald Observatory Study of Comet 19P/Borrelly: Placing the Deep Space 1 Observations into a Broader Context, *Icarus*, **160**, 398-418

Farnham, T. L., and Schleicher, D. G. 2005, Physical and Compositional Studies of Comet 81P/Wild 2 at Multiple Apparitions, *Icarus*, **173**, 533-558

Feierberg, M. A., Lebofsky, L. A., and Larson, H. P. 1981, Spectroscopic Evidence for Aqueous Alteration Products on the Surfaces of Low-Albedo Asteroids, *Geochim. Cosmochim. Acta*, **45**, 971-981

Fernández, J. A. 1980, On the Existence of a Comet Belt beyond Neptune, *MNRAS*, **192**, 481-491

Fernández, J. A., and Ip, W.-H. 1981, Dynamical Evolution of a Cometary Swarm in the Outer Planetary Region, *Icarus*, **47**, 470-479

Fernández, J. A., and Gallardo, T. 1994, The Transfer of Comets from Parabolic Orbits to Short-Period Orbits: Numerical Studies, *Astron. Astrophys.*, **281**, 911-922

Fernández, Y. R., McFadden, L.-A., Lisse, C. M., Helin, E. F., and Chamberlin, A. B. 1997, Analysis of POSS Images of Comet-Asteroid Transition Object 107P/1949 W1 (Wilson-Harrington), *Icarus*, **128**, 114-126

Fernández, Y. R. 1999, Ph.D. dissertation, University of Maryland

Fernández, Y. R., Lisse, C. M., Ulrich Käufl, H., Peschke, Sibylle, B., Weaver, H. A., A'Hearn, M. F., Lamy, P. P., Livengood, T. A., and Kostiuk, T. 2000, Physical Properties of the Nucleus of Comet 2P/Encke, *Icarus*, **147**, 145-160

Fernández, Y. R., Jewitt, D. C., and Sheppard, S. S. 2001, Low Albedos Among Extinct Comet Candidates, *Astrophys. J.*, **553**, L197-200

Fernández, Y. R., Abell, P. A., Pravec, P., French, L. M., Farnham, T. L., Gaffey, M. J., Hardersen, P. S., Kusnirak, P., Sarounova, L., and Sheppard, S. S. 2003, Physical Characteristics of the Asteroid-Like Nucleus of Comet LONEOS C/2001 OG108, *35th DPS*, session 47.04

Fitzsimmons, A., Dahlgren, M., Lagerkvist, C.-I., Magnusson, P., and Williams, I. P. 1994, A Spectroscopic Survey of D-type Asteroids, *Astron. Astrophys.*, **282**, 634-642

Gaffey, M. J., and McCord, T. B. 1978, Asteroid Surface Materials - Mineralogical Characterizations from Reflectance Spectra, *Space Sci. Rev.*, **21**, 555-628

Gaffey, M. J., Bell, J. F., Cruikshank, D. P. 1989, Reflectance Spectroscopy and Asteroid Surface Mineralogy, in *Asteroids II*, Ed. Binzel, R. P., Gehrels, T., and Matthews, M. S., 98-127

Gaffey, M. J., Bell, J. F., Brown, R. H., Burbine, T. H., Piatek, J. L., Reed, K. L., and Chaky, D. A. 1993, Mineralogical Variations within the S-Type Asteroid Class, *Icarus*, **106**, 573-602

Gehrels, T., and Owings, D. 1962, Photometric Studies of Asteroids IX. Additional Light-Curves, *Astrophys. J.*, **135**, 906-924

Gombosi, T. I., and Houpis, H. L. F. 1986, An Icy-Glue Model of Cometary Nuclei, *Nature*, **324**, 43-44

Gomes, C. B., and Keil, K. 1980, *Brazilian Stone Meteorites*, University of New Mexico Press

Grimm, R. E., and McSween, H. Y. Jr. 1989, Water and the Thermal Evolution of Carbonaceous Chondrite Parent Bodies, *Icarus*, **82**, 244-280

Grimm, R. E., and McSween, H. Y. Jr. 1993, Heliocentric Zoning of the Asteroid Belt by Aluminum-26 Heating, *Science*, **259**, 653-655

Hameen-Anttila, K. 1967, Surface Photometry of the Planet Mercury, *Ann. Acad. Sci. Fenn.*, **Ser., A6, 252**, 1-19

Hapke, B. 1981, Bidirectional Reflectance Spectroscopy. I - Theory, *J. Geophys. Res.*, **86**, 3039-3054

Hapke,B. 1984, Bidirectional Reflectance Spectroscopy 3. Correction for Macroscopic Roughness, *Icarus*, **59**, 41-59

Hapke, B. 1986, Bidirectional Reflectance Spectroscopy IV - The Extinction Coefficient and the Opposition Effect, *Icarus*, **67**, 264-280

Hapke, B. 1993, *Theory of Reflectance and Emittance Spectroscopy*, Cambridge University Press, Cambridge, UK

Hapke, B. W., Nelson, R. M., and Smythe, W. D. 1993, The Opposition Effect of the Moon: The Contribution of Coherent Backscatter, *Science*, **260**, 509-511

Hapke, B., Nelson, R., and Smythe, W. 1998, The Opposition Effect of the Moon: Coherent Backscatter and Shadow Hiding, *Icarus*, **133**, 89-97

Hapke, B. 2002, Bidirectional Reflectance Spectroscopy 5: The Coherent Backscatter Opposition Effect and Anisotropic Scattering, *Icarus*, **157**, 523-534

Harris, A. W., Young, J. W., Poutanen, M., Bowell, E., Tholen, D. J., and Nicholson, P. D. 1995, Photoelectric Lightcurves of 433 Eros, *LPI*, **26**, 553

Harris, A. W., Young, J. W., Bowell, E., and Tholen, D. J. 1999, Asteroid Lightcurve Observations from 1981 to 1983, *Icarus*, **142**, 173-201

Hartman, B., and Domingue, D. 1998, Scattering of Light by Individual Particles and the Implications for Models of Planetary Surfaces, *Icarus*, **131**, 421-448

Hartmann, W. K., Tholen, D. J., and Cruikshank, D. P. 1987, The Relationship of Active Comets, "Extinct" comets, and Dark Asteroids, *Icarus*, **69**, 33-50

Helfenstein, P., and Veverka, J. 1987, Photometric Properties of Lunar Terrains Derived from Hapke's Equation, *Reports of Planetary Geology and Geophysics Program*, **1986**, 217-218

Helfenstein, P., and Veverka, J. 1989, Physical Characterization of Asteroid Surfaces from Photometric Analysis, in *Asteroids II*, Ed. Binzel, R. P., Gehrels, T., and Matthews, M. S., 557-593

Helfenstein, P., Hillier, J., Weitz, C., and Veverka, J. 1991, Oberon: Color Photometry from Voyager and Its Geological Implications, *Icarus*, **90**, 14-29

Helfenstein, P., and 23 colleagues, 1994, Galileo Photometry of Asteroid 951 Gaspra, *Icarus*, **107**, 37-60

Helfenstein, P., and 10 colleagues, 1996, Galileo Photometry of Asteroid 243 Ida, *Icarus*, **120**, 48-65

Henyey, C., and Greenstein, J. 1941, Diffuse Radiation in the Galaxy, *Astro. J.*, **93**, 70-83

Hillier, J., Veverka, J., Helfenstein, P., and Lee, P. 1994, Photometric Diversity of Terrains on Triton, *Icarus*, **109**, 296-312

Hsieh, H. H., Jewitt, D. C., and Fernández, Y. R. 2004, The Strange Case of 133P/Elst-Pizarro: A Comet Among the Asteroids, *Astro. J.*, **127**, 2997-3017

Huss, G. R., MacPherson, G. J., Wasserburg, G. J., Russell, S. S., and Srinivasan, G. 2001, Aluminum-26 in Calcium-Aluminum-Rich Inclusions and Chondrules from Unequilibrated Ordinary Chondrites, *Meteorit. Planet. Sci.*, **36**, 975-997

Izenberg,N.R., Murchie,S.L., Bell, III,J.F., McFadden,L.A., Wellnitz,D.D., Clark,B.E., and Gaffey,M.J. 2003, Spectral Properties and Geologic Processes on Eros from Combined NEAR NIS and MSI Data Sets, *Meteorit. Planet. Sci*, **38**, 1,053-1,077

Jewitt, D., and Meech, K. J. 1985, Rotation of the Nucleus of Comet P/Arend-Rigaux, *Icarus*, **64**, 329-335

Jewitt, D., and Meech, K. 1987, CCD Photometry of Comet P/Encke, *Astro. J.*, **93**, 1542-1548

Jewitt, D. C., and Meech, K. J. 1988, Optical Properties of Cometary Nuclei and a Preliminary Comparison with Asteroids, *Astrophys. J.*, **328**, 974-986

Jewitt, D. C., and Luu, J. X. 1995, The Solar System Beyond Neptune, *Astro. J.*, **109**, 1867-1876

Johnson, T. V., and Fanale, F. P. 1973, Optical Properties of Carbonaceous Chondrites and Their Relationship to Asteroids, *J. Geophys. Res.*, **78**, 8507-8518

Kaasalainen, M., Lamberg, L., Lumme, K., and Bowell, E. 1992a, Interpretation of Lightcurves of Atmosphereless Bodies. I. General Theory and New Inversion Schemes, *Astron. Astrophys.*, **259**, 318-332

Kaasalainen, M., Lamberg, L., and Lumme, K. 1992b, Interpretation of Lightcurves of Atmosphereless Bodies. II. Practical Aspects of Inversion, *Astro. Astrophys.*, **259**, 333-340

Kaasalainen, M., and Torppa, J. 2001, Optimization Methods for Asteroid Lightcurve Inversion. I. Shape Determination, *Icarus*, **153**, 24-36

Kaasalainen, M., Torppa, J., and Muinonen, K. 2001, Optimization Methods for Asteroid Lightcurve Inversion. II. The Complete Inverse Problem, *Icarus*, **153**, 37-51

Keil, K. 2002, Geological History of Asteroid 4 Vesta: The “Smallest Terrestrial Planet”, in *Asteroids III*, Ed. Bottke, W. F. Jr., Cellino, A., Paolicchi, P., and Binzel, R. P., 573-584

Keller, H. U., and 17 colleagues, 1986, First Halley Multicolour Camera Imaging Results from Giotto, *Nature*, **321**, 320-326

King, T. V. V., Clark, R. N., Calvin, W. M., Sherman, D. M., and Brown, R. H. 1992, Evidence for Ammonium-Bearing Minerals on Ceres, *Science*, **255**, 1551-1553

Kirk, R. L., Howington-Kraus, E., Soderblom, L. A., Giese, B., and Oberst, J. 2004a

Comparison of USGS and DLR Topographic Models of Comet Borrelly and Photometric Applications, *Icarus*, **167**, 54-69

Kirk, R. L., Oberst, J., and Biese, B., DS1 Digital Elevation Maps of Comet 19P/Borrelly V1.0, DS1-C-MICAS-5-BORRELLY-DEM-V1.0, NASA Planetary Data System, 2004b

Kirk, R. L., Duxbury, T. C., Hörz, F., Brownlee, D. E., Newburn, R. L., Tsou, P., and Stardust Team 2005, Topography of the 81/P Wild 2 Nucleus Derived from Stardust Stereoimages, *36th LPSC*, abstract no. 2244

Królikowska, M. 2001, A Study of the Original Orbits of "Hyperbolic" Comets, *Astron. Astrophys.*, **376**, 314-321

Krugly, Yu. N., and Shevchenko, V. G. 1999, Magnitude Phase Dependence of Asteroid 433 Eros, *LPI*, **30**, 1595

Kuiper, G. P. 1951, On the Origin of the Solar System, in *Proceedings of a topical symposium, commemorating the 50th anniversary of the Yerkes Observatory and half a century of progress in astrophysics*, Ed. Hynek, J. A., 357

Lagerkvist, C.-I. and Magnusson, P. 1990, Analysis of Asteroid Lightcurves. II - Phase Curves in a Generalized HG-System, in *Astron. Astrophys. Suppl.*, **86**, 119-165

Lagerkvist, C.-I., and Magnusson, P., Asteroid Photometric Catalog V1.0, EAR-A-3-DDR-APC-LIGHTCURVE-V1.0, NASA Planetary Data System, 1995

Lamy, P. L., and Toth, I. 1995, Direct Detection of a Cometary Nucleus with the Hubble Space Telescope, *Astro. and Astrophys.*, **293**, 43-45

Lamy, P. L., Toth, I., and Weaver, H. A. 1998, Hubble Space Telescope Observations of the Nucleus and Inner Coma of Comet 19P/1904 Y2 (Borrelly), *Astro. and Astrophys.*, **337**, 945-954

Lamy, P. L., Toth, I., A'Hearn, M. F., and Weaver, H. A. 1999, Hubble Space Telescope Observations of the Nucleus of Comet 45P/Honda-Mrkos-Pajdusakova and Its Inner Coma, *Icarus*, **140**, 424-438

Lamy, P. L., Toth, I., A'Hearn, M. F., Weaver, H. A., and Weissman, P. R. 2001, Hubble Space Telescope Observations of the Nucleus of Comet 9P/Tempel 1, *Icarus*, **154**, 337-344

Lane, A. L., Nelson, R. M., and Matson, D. L. 1981, Evidence for Sulphur Implantation in Europa's UV Absorption Band, *Nature*, **292**, 38-39

Larson, H. P., Feierberg, M. A., Fink, U., and Smith, H. A. 1979, Remote Spectroscopic Identification of Carbonaceous Chondrite Mineralogies Applications to Ceres and Pallas, *Icarus*, **39**, 257-271

Lazzarin, M., Barbieri, C., and Barucci, M. A. 1995, Visible Spectroscopy of Dark, Primitive Asteroids, *Astro. J.*, **110**, 3058-3072

Lean, J., VanHoosier, M., Brueckner, G., Prinz, D., Floyd, L., and Edlow, K. 1992, SUSIM/UARS Observations of the 120-300 nm Flux Variations of the Sun During the Maximum of the Solar Cycle: Inferences for the 11-year Cycle, *GRL*, **19**, 2203-2206

Lebofsky, L. A., Feierberg, M. A., Tokunaga, A. T., Larson, H. P., and Johnson, J. R. 1981, The 1.7- to 4.2-micron Spectrum of Asteroid 1 Ceres - Evidence for Structural Water in Clay Minerals, *Icarus*, **48**, 453-459

Lebofsky, L. A., Sykes, M. V., Tedesco, E. F., Veeder, G. J., Matson, D. L., Brown, R. H., Gradie, J. G., Feierberg, M. A., and Rudy, R. J. 1986, A Refined "Standard" Thermal Model for Asteroids Based on Observations of 1 Ceres and 2 Pallas, *Icarus*, **68**, 239-251

Levison, H. F., Dones, L., and Duncan, M. J. 2001, The Origin of Halley-Type Comets: Probing the Inner Oort Cloud, *Astro. J.*, **121**, 2253-2267

Li, J., A'Hearn, M. F., and McFadden, L. A. 2004, Photometric Analysis of Eros from NEAR Data, *Icarus*, **172**, 415-431

Lisse, C. M., Fernández, Y. R., Kundu, A, A'Hearn, M. F., Dayal, A., Deutsch, L. K., Fazio, G. G, Hora, J. L., and Hoffmann, W. F. 1999, The Nucleus of Comet Hyakutake (C/1996 B2), *Icarus*, **140**, 189-204

Lisse, C. M., A'Hearn, M. F., Farnham, T. L., Groussin, O., Meech, K. J., Fink, U., and Schleicher, D. G. 2005, The Coma of Comet 9P/Tempel 1, submitted to *Space Science Reviews*

Lowry, S. C., Fitzsimmons, A., Cartwright, I. M., and Williams, I. P. 1999, CCD Photometry of Distant Comets, *Astron. Astrophys.*, **349**, 649-659

Lowry, S. C., and Fitzsimmons, A. 2001, CCD Photometry of Distant Comets II, *Astron. Astrophys.*, **365**, 204-213

Lucey, P. G. 1998, Model Near-Infrared Optical Constants of Olivine and Pyroxene as a Function of Iron Content, *J. Geophys. Res.*, **103**, 1,703-1,713

Lucey, P. G., Hinrichs, J., Urquhart, M. L., Wellnitz, D., Izenberg, N., Murchie, S., Robinson, M., Clark, B. E., and Bell, III, J. F. 2002, Detection of Temperature-Dependent Spectral Variation on the Asteroid Eros and New Evidence for the Presence of an Olivine-Rich Silicate Assemblage, *Icarus*, **155**, 181-188

Lumme, K., and Bowell, E. 1981a, Radiative Transfer in the Surfaces of Atmosphereless Bodies. I - Theory, *Astro. J.*, **86**, 1694-1721

Lumme, K., and Bowell, E. 1981b, Radiative Transfer in the Surfaces of Atmosphereless Bodies. II. Interpretation, *Astro. J.*, **86**, 1705-1721

Lyttleton, R. A. 1948, On the Origin of Comets, *MNRAS*, **108**, 465-475

MacPherson, G. J., Davis, A. M., and Zinner, E. K. 1995, The Distribution of Aluminum-26 in the Early Solar System - A Reappraisal, *Meteorit. Planet. Sci.*, **30**, 365-386

McCord, T. B., and Sotin, C. 2005, Ceres: Evolution and Current State, *J. Geophys. Res.*, , In press

McFadden, L.-A. 1993, The Comet-Asteroid Transition, in *Asteroids, Comets, Meteors*, 210

McFadden, L. A., Cochran, A. L., Barker, E. S., Cruikshank, D. P., and Hartmann, W. K. 1993, The Enigmatic Object 2201 Oljato - Is It an Asteroid or an Evolved Comet, *J. Geophys. Res.*, **98**, 3031-3041

McFadden, L. A., Wellnitz, D. D., Schnaubelt, M., Gaffey, M. J., Bell, III, J. F., Izenberg, N., Murchie, S., and Chapman, C. R. 2001, Mineralogical Interpretation of Reflectance Spectra of Eros from NEAR Near-Infrared Spectrometer Low Phase Flyby, *Meteorit. Planet. Sci,* **36**, 1711-1726

McGuire, A. F., and Hapke, B. 1995, An Experimental Study of Light Scattering by Large, Irregular Particles, *Icarus*, **113**, 134-155

McSween, H. Y., Bennett III, M. E., and Jarosewich, E. 1991, The Mineralogy of Ordinary Chondrites and Implications for Asteroid Spectrophotometry, *Icarus*, **90**, 107-116

McSween, H. Y. Jr., Ghosh, A., Grimm, R. E., Wilson, L., and Young, E. D. 2002, Thermal Evolution Models of Asteroids, in *Asteroids III*, Ed. Bottke, W. F. Jr., Cellino, A., Paolicchi, P., and Binzel, R. P., 559-571

Meech, K. J., Jewitt, D., and Ricker, G. R. 1986, Early Photometry of Comet P/Halley - Development of the Coma, *Icarus*, **66**, 561-574

Meech, K. J., A'Hearn, M. F., Lisse, C. M., and Weaver, H. A., Biver, N. 2005, The Deep Impact Earth-Based Campaign, submitted to *Space Science Reviews*

Michalak, G. 2000, Determination of Asteroid Masses - I. (1) Ceres, (2) Pallas and (4) Vesta, *Astron. Astrophys.*, **360**, 363-374

Millis, R. L., and 41 colleagues, 1987, The Size, Shape, Density, and Albedo of Ceres from Its Occulation of BD+8 471, *Icarus*, **72**, 507-518

Millis, R. L., A'Hearn, M. F., and Campins, H. 1988, An Investigation of the Nucleus and Coma of Comet P/Arend-Rigaux, *Astrophys. J.*, **324**, 1194-1209

Minnaert, M. 1941, The Reciprocity Principle in Lunar Photometry, *Astrophys. J.*, **93**, 403-410

Mitchell, D. L., Ostro, S. J., Hudson, R. S., Rosema, K. D., Campbell, D. B., Velez, R., Chandler, J. F., Shapiro, I. I., Giorgini, J. D., and Yeomans, D. K. 1996, Radar Observations of Asteroids 1 Ceres, 2 Pallas, and 4 Vesta, *Icarus*, **124**, 113-133

Muinonen, K. 1990, Light Scattering by Inhomogeneous Media: Backward Enhancement and Reversal of Linear Polarization, Ph.D. dissertation, University of Helsinki

Muinonen, K. 1998, Introducing the Gaussian Shape Hypothesis for Asteroids and Comets, *Astron. Astrophys.*, **332**, 1087-1098

Muinonen, K., and Lagerros, J. S. V. 1998, Inversion of Shape Statistics for Small Solar System Bodies, *Astro. Astrophys.*, **333**, 753-761

Müller, G. 1893, Helligkeitsb estimmungen der grossen Planeten und einiger Asteroiden, *Publ. Astrophys. Obs. Potsdam*, **30**, 198-389

Murchie, S., and 17 colleagues, 1999, Inflight Calibration of the NEAR Multispectral Imager, *Icarus*, **140**, 66-91

Murchie, S., and 10 colleagues, 2002a, Color Variations on Eros from NEAR Multispectral Imaging, *Icarus*, **155**, 145-168

Murchie, S., Robinson, M., Domingue, D., Li, H., Prockter, L., Hawkins, S. E., Owen, W., Clark, B., and Izenberg, N. 2002b, Inflight Calibration of the NEAR Multispectral Imager. II. Results from Eros Approach and Orbit, *Icarus*, **155**, 229-243

NEAR Science Data Center, NEAR SPICE Kernels Eros/Orbit, NEAR-A-SPICE-6-EROS/ORBIT-V1.0, NASA Planetary Data System, 2001

Neese, C., Asteroid Albedos V1.0, EAR-A-5-DDR-ALBEDOS-V1.0, NASA Planetary Data System, 2002a

Neese, C., Asteroid Taxonomy V4.0, EAR-A-5-DDR-TAXONOMY-V4.0, NASA Planetary Data System, 2002b

Nelson, R., Hapke, B. W., Smythe, W. D., and Horn, L. J. 1998, Phase Curves of Selected Particulate Materials: the Contribution of Coherent Backscattering to the Opposition Surge, *Icarus*, **131**, 223-230

Nelson, R. M., Hapke, B. W., Smythe, W. D., and Spilker,L. J. 2000, The Opposition Effect in Simulated Planetary Regoliths. Reflectance and Circular Polarization Ratio Change at Small Phase Angle, *Icarus*, **147**, 545-558

Nicodemus, F. 1970, Reflectance Nomenclature and Directional Reflectance and Emissivity, *Appl. Opt.*, **9**, 1474-1475

Nicodemus, F., Richmond, J., Hsia, J., Ginsberg, I., and Limperis, T. 1977, Geometrical Considerations and Nomenclature for Reflectance, National Bureau of Standards Monograph

Noll, K. S., Weaver, H. A., and Gonnella, A. M. 1995, The Albedo Spectrum of Europa from 2200 A to 3300 A, *J. Geophys. Res.*, **100**, 19,057-19,059

Noll, K. S., Johnson, R. E., Lane, A. L., Domingue, D. L., and Weaver, H. A. 1996, Detection of Ozone on Ganymede, *Science*, **273**, 341-343

Press, W. H., Teukolsky, S. A., Vetterling, W. T., and Flannery, B. P. 1992, , in *Numerical Recipes in C: The Art of Scientific Computing* 2nd ed., Cambridge University Press, Cambridge, UK

Oberst, J., Giese, B., Howington-Kraus, E., Kirk, R., Soderblom, L., Buratti, B., Hicks, M., Nelson, R., and Britt, D. 2004, The Nucleus of Comet Borrelly: A Study of Morphology and Surface Brightness, *Icarus*, **167**, 70-79

Oort, J. H. 1950, The Structure of the Cloud of Comets Surrounding the Solar System and a Hypothesis Concerning its Origin, *Bull. Astron. Inst. Neth.*, **11**, 91-110

Ostro, S. J., and Connelly, R. 1984, Convex Profiles from Asteroid Lightcurves, *Icarus*, **57**, 443-463

Ostro, S. J., and Connelly, R. 1986, What can a Lightcurve Tell Us about Asteroid's Shape?, *17th LPSC*, abstract no. 636

Ostro, S. J. 2003, Radar Observations of Asteroids, *35th DPS*, session 32.01

Parker, J. W., Stern, S. A., Thomas, P. C., Festou, M. C., Merline, W. J., Young, E. F., Binzel, R. P., and Lebofsky, L. A. 2002, Analysis of the First Disk-Resolved Images of

Ceres From Ultraviolet Observations with the Hubble Space Telescope, *Astronomical Journal*, **123**, 549-557

Pavlovsky, C. et al. 2004, ACS Instrument Handbook, Version 5.0 (Baltimore: STScI)

Pavlovsky, C. et al. 2005, ACS Data Handbook, Version 4.0 (Baltimore: STScI)

Rauer, H., Hahn, G., Harris, A., Helbert, J., Mottola, S., and Oberst, J. 1999, Nuclear Parameters of Comet P/Borrelly, *31th DPS*, session 37.03

Reinhard, R. 1986, The Giotto Encounter with Comet Halley, *Nature*, **321**, 313-318

Richardson, D. C., Leinhardt, Z. M., Melosh, H. J., Bottke, W. F. Jr., and Asphaug, E. 2002, Gravitational Aggregates: Evidence and Evolution, in *Asteroids III*, Ed. Bottke, W. F. Jr., Cellino, A., Paolicchi, P., and Binzel, R. P., 501-515

Robinson, M. S., Thomas, P. C., Veverka, J., Murchie, S., and Carcich, B. 2001, The Nature of Ponded Deposits on Eros, *Nature*, **413**, 396-400

Russell, H. N. 1906, On the Light-Variations of Asteroids and Satellites, *Astrophys. J.*, **24**, 1-18

Russell, C. R., and 20 colleagues, 2004, Dawn: A Journey in Space and Time, *Planet. Space Sci.*, **52**, 465-489

Sack, N. J., Johnson, R. E., Boring, J. W., and Baragiola, R. A. 1992, The Effect of Magnetospheric Ion Bombardment on the Reflectance of Europa's Surface, *Icarus*, **100**, 534-540

Safronov, V. S. 1969, Evolution of the Protoplanetary Cloud and Formation of the Earth and Planets.

Sagdeev, R. Z., Blamont, J., Galeev, A. A., Moroz, V. I., Shapiro, V. D., Schevchenko, V. I., and Szego, K. 1986a, VEGA Spacecraft Encounters with Comet Halley, *Nature*, **321**, 259-262

Sagdeev, R. Z., and 37 colleagues, 1986b, Television Observations of Comet Halley from VEGA Spacecraft, *Nature*, **321**, 262-266

Saint-Pé, O., Combes, M., and Rigaut, F. 1993, Ceres Surface Properties by High-Resolution Imaging from Earth, *Icarus*, **105**, 271-281

Schleicher, D. G., Woodney, L. M., and Millis, R. L. 2003, Comet 19P/Borrelly at Multiple Apparitions: Seasonal Variations in Gas Production and Dust Morphology, *Icarus*, **162**, 415-442

Schober, H. J. 1976, Photoelectric Photometry of 1 Ceres During the Ceres-Campaign 1975, *Mitteilungen der Astronomischen Gesellschaft*, **40**, 207-210

von Seeliger, H. 1887, Zur Theorie der Beleuchtung der grossen Planeten, insbesondere des Saturn, *Abh. Bayer. Akad. Wiss. Math. Naturwiss.*, **Kl 16**, 405-516

Sekanina, Z., and Yeomans, D. K. 1985, Orbital Motion, Nucleus Precession, and Splitting of Periodic Comet Brooks 2, *Astro. J.*, **85**, 2335-2352

Semenov, B. V., Newburn, R. L., Taylor, H. W., Hash, C., and Acton, C. H., Stardust

NAVCAM Images of Wild 2, SDU-C-NAVCAM-2-EDR-WILD2-V1.0, NASA Planetary Data System, 2004a

Semenov, B. V., Elson, L. S., and Acton, C. H., Stardust SPICE Kernels V1.0, SDU-C-SPICE-6-V1.0, NASA Planetary Data System, 2004b

Semenov, B. V., Elson, L. S., and Acton, C. H., Deep Space 1 SPICE Kernels V1.0, DS1-A/C-SPICE-6-V1.0, NASA Planetary Data System, 2004c

Shepard, M. K., Campbell, B. A., Bulmer, M. H., Farr, T. G., and Gaddis, L. R. 2001, The Roughness of Natural Terrain: A Planetary and Remote Sensing Perspective, *J. Geophys. Res.*, **106**, 32,777-32,796

Shkuratov, Yu. G., and Helfenstein, P. 2001, The Opposition Effect and the Quasi-Fractal Structure of Regolith: I. Theory, *Icarus*, **152**, 96-116

Silva, A. M., and Cellone, S. A. 2001, Cometary Activity in 2060 Chiron at Minimum Brightness, *Planet. Space Sci.*, **49**, 1325-1330

Simonelli, D. P., Wisz, M., Switala, A., Adinolfi, D., Veverka, J., Thomas, P. C., and Helfenstein, P. 1998, Photometric Properties of Phobos Surface Materials From Viking Images, *Icarus*, **131**, 52-77

Smith, A. W. 1929, in *International Critical Tables*, Vol. V., 138

Soderblom, L. A., Boice, D. C., Britt, D. T., Brown, R. H., Buratti, B. J., Kirk, R. L., Lee, M., Nelson, R. M., Oberst, J., and Sandel, B. R. 2004a, Imaging Borrelly, *Icarus*, **167**, 4-15

Soderblom, L. A., Britt, D. T., Brown, R. H., Buratti, B. J., Kirk, R. L., Owen, T. C., and Yelle, R. V. 2004b, Short-Wavelength Infrared (1.3-2.6 um) Observations of the Nucleus of Comet 19P/Borrelly, *Icarus*, **167**, 100-112

Squyres, S. W., and Sagan, C. 1983, Albedo Asymmetry of Iapetus, *Nature*, **303**, 782-785

Standish, E. M. 2001, JPL Interoffice Memorandum, 312. F-01-006 dated April 11, 2001

Stratton, J. 1941, in *Electromagnetic Theory*, New York: McGraw-Hill.

Taylor, R. C., Gehrels, T., and Capen, R. C. 1976, Minor Planets and Related Objects. XXI. Photometry of Eight Asteroids, *Astro. J.*, **81**, 778-786

Taylor, H. W., NEAR MSI Images for Eros/Orbit, NEAR-A-MSI-3-EDR-EROS/ORBIT-V1.0, NASA Planetary Data System, 2001

Tedesco, E. F. 1976, UBV Lightcurves of Asteroid 433 Eros, *Icarus*, **28**, 21-28

Tedesco, E. F., Taylor, R. C., Drummond, J., Harwood, D., Nickoloff, I., Scaltriti, F., Schober, H. J., and Zappala, V. 1983, Worldwide Photometry and Lightcurve Observations of 1 Ceres during the 1975-1976 Apparition, *Icarus*, **54**, 23-29

Tholen, D. J. 1984, Ph.D. dissertation, University of Arizona

Tholen, D. J., and Barucci, M. A. 1989, Asteroid Taxonomy, in *Asteroids II*, Ed. Binzel, R. P., Gehrels, T., and Matthews, M. S., 298-315

Thomas, P. C., Adinolfi, D., Helfenstein, P., Simonelli, D., and Veverka, J. 1996, The Surface of Deimos: Contribution of Materials and Processes to Its Unique Appearance, *Icarus*, **123**, 536-556

Thomas, P. C., Veverka, J., Robinson, M. S., and Murchie, S. 2001, Shoemaker Crater as the Source of Most Ejecta Blocks on the Asteroid 433 Eros, *Nature*, **413**, 394-396

Thomas, P. C., and 18 colleagues, 2002, Eros: Shape, Topography, and Slope Processes, *Icarus*, **155**, 18-37

Thomas, P. C., Parker, J. W., McFadden, L. A., Russell, C. T., Stern, S. A., Sykes, M. V., and Young, E. F. 2005, Size and Shape of 1 Ceres: Implications for Interior Structure, In Preparation

Urey, H. 1955, The Cosmic Abundances of Potassium, Uranium, and Thorium and the Heat Balances of the Earth, the Moon, and Mars, *Proc. Natl. Acad. Sci. U.S.*, **41**, 127-144

Van de Hulst, H. 1957, in *Light Scattering by Small Particles*, New York: Wiley

Van Diggelen, J. 1959, Photometric Properties of Lunar Crater Floors, *Rech. Obs. Utrecht*, **14**, 1-114

Veeder, G. J., Hanner, M. S., and Tholen, D. J. 1987, The Nucleus of Comet P/Arend-Rigaux, *Astro. J.*, **94**, 169-173

Verbiscer, A. J., and Veverka, J. 1992, Mimas: Photometric Roughness and Albedo Map, *Icarus*, **99**, 63-69

Veverka, J., Helfenstein, P., Skypeck, A., and Thomas, P. 1989, Minnaert Photometric Parameters for the Satellites of Uranus, *Icarus*, **78**, 14-26

Veverka, J., Belton, M., Klaasen, K., and Chapman, C. 1994, Galileo's Encounter with 951 Gaspra: Overview, *Icarus*, **107**, 2-17

Veverka, J., and 13 colleagues, 1999, NEAR Encounter with Asteroid 253 Mathilde: Overview, *Icarus*, **140**, 3-16

Veverka, J., and 32 colleagues, 2001, Imaging of Small-Scale Features on 433 Eros from NEAR: Evidence for a Complex Regolith, *Science*, **292**, 484-488

Viateau, B., and Rapaport, M. 1998, The Mass of (1) Ceres from its Gravitational Perturbations on the Orbits of 9 Asteroids, *Astron. Astrophys.*, **334**, 729-735

Wagner, J. K., Hapke, B. W., and Wells, E. N. 1987, Atlas of Reflectance Spectra of Terrestrial, Lunar, and Meteoritic Powders and Frosts from 92 to 1800 nm, *Icarus*, **69**, 14-28

Weidenschilling, S. J. 1994, Origin of Cometary Nuclei as Rubble Piles, *Nature*, **368**, 721

Weidenschilling, S. J. 1997, The Origin of Comets in the Solar Nebula: A Unified Model, *Icarus*, **127**, 290-306

Weissman, P. R. 1986, Are Cometary Nuclei Primordial Rubble Piles?, *Nature*, **320**, 242-244

Weissman, P., Doressoundiram, A., Hicks, M., Chamberlin, A., Sykes, M., Larson, S., and Hergenrother, C. 1999, CCD Photometry of Comet and Asteroid Targets of Spacecraft Missions, *31th DPS*, session 30.03

Weissman, P. R., Bottke, W. F. Jr., and Levison, H. F., 2002, Evolution of Comets into Asteroids, in *Asteroids III*, Ed. Bottke, W. F. Jr., Cellino, A., Paolicchi, P., and Binzel, R. P., 669-686

Weissman, P. R., and Lowry, S. C. 2003, The Size Distribution of Jupiter-Family Cometary Nuclei, *34th LPSC*, abstract no. 2003

Wetherill, G. W. 1988, Where do the Apollo Objects Come From?, *Icarus*, **76**, 1-18

Whipple, F. L. 1950, A Comet Model. I. The Acceleration of Comet Encke, *Astrophys. J.*, **111**, 375-394

Wild, W. J. 1989, Matrix Formalism for Inferring Planetary Surface Albedo Distributions from Light-curve Measurements, *PASP*, **101**, 844-848

Wild, W. J. 1991, Light-curve Inversion Formalism, *Astrophys. J.*, **368**, 622-625

Williams, I. P., and Wu, Z. 1993, The Geminid Meteor Stream and Asteroid 3200 Phaethon, *MNRAS*, **262**, 231-248

Wilson, L., Keil, K., Browning, L. B., Krot, A. N., and Bourcier, W. 1999, Early Aqueous Alteration, Explosive Disruption, and Re-Processing of Asteroids, *Meteor. Planet. Sci.*, **34**, 541-557

Wilson, A., and Gimenez, A. 2004, ESA's Report to the 35th COSPAR Meeting

Yelle, R. V., Soderblom, L. A., and Jokipii, J. R. 2004, Formation of Jets in Comet 19P/Borrelly by Subsurface Geysers, *Icarus*, **167**, 30-36

Zappalà, V., Cellino, A., Dell'Oro, A., and Paolicchi, P. 2002, Physical and Dynamical Properties of Asteroid Families, in *Asteroids III*, Ed. Bottke, W. F. Jr., Cellino, A., Paolicchi, P., and Binzel, R. P., 619-631

Zellner, B. and Bowell, E. 1977, Asteroid Composition Types and Their Distributions, in *Comets, Asteroids, Meteorites: Interrelation, Evolution and Origins*, Ed. Delsemme, A. H., 185-197

Ziolkowski, K. 1995, Comets and Asteroids in the Taurid Complex: Remarks on a Possible Common Origin, *Earth, Moon, and Planets*, **68**, 647-651